Universitat Politècnica de València
I.U.I CMT – Clean Mobility & Thermofluids
PhD Program in Propulsion Systems for Transport

DOCTORAL THESIS

1D LIQUID SPRAY/GAS JET COMBUSTION MODELLING USING DETAILED CHEMISTRY

Presented by:

Jiawei Cao

Supervised by:

Dr. José María García Oliver

In fulfilment of the requirement for the degree of

Doctor or Philosophy

Valencia, October 2024

DOCTORAL THESIS

1D LIQUID SPRAY/GAS JET COMBUSTION MODELLING USING DETAILED CHEMISTRY

Presented by:	Jiawei Cao
Supervised by:	Dr. José María García Oliver

Examination committee:

Chairman:	Dr. José Javier López Sánchez
Secretary:	Dr. Bertrand Naud
Member:	Dr. Benedicte Cuenot

External examiners:

Dr. Xavier Tauzia
Dr. Alexander Marinos Kreton Peter Taylor

Valencia, October 2024

Abstract

The increase in greenhouse gas (GHG) emissions worsens global warming and climate change. Carbon dioxide (CO_2), as the main composition in GHG, is strictly restricted in the emission regulation under the target of carbon neutrality by the middle of this century. In the transportation sector, electrification has been widely recognized as a good pathway to achieve such goals in light-duty applications. Great success in the low power range has built confidence in the employment of large power motors. However, the current shortcomings of battery such as low energy density, or limited recycling of used batteries make it difficult to fully replace the combustion engines in a short time, especially for heavy-duty engines. The utilization of low-carbon/zero-carbon fuels can be a transitional solution for achieving CO_2 emission reduction rapidly.

The present thesis aims to fully predict the specific characteristics of the combustion process of diesel-like reacting sprays fueled with hydrocarbon and oxygenated fuels. To accomplish this objective, a so-called Quasi-1D model is utilized, which integrates an in-house developed one-dimensional spray model with an advanced combustion model based on laminar flamelets at a low computational cost. Subsequently, the combustion metrics and flame structure can be efficiently examined throughout the evaluation of the chemical state obtained along mixing trajectories.

The study mainly focuses on the case of a free spray injected through a single hole into steady environments with the variation of ambient and injection conditions recommended by Engine Combustion Network (ECN). A wide variety of fuels are considered, including n-dodecane, Primary Reference Fuels, and OMEn-type fuels.

In conclusion, the Quasi-1D model delivers an accurate prediction of the main metrics of spray combustion process across the variety of conditions considered in spite of its low computational cost. This results in a promising tool for the calibration of combustion in engines with alternative fuels.

Resumen

El aumento de las emisiones de gases de efecto invernadero (GEI) empeora el calentamiento global y el cambio climático. El dióxido de carbono (CO_2), como principal componente de los GEI, está estrictamente restringido en las normativas que pretenden un objetivo de neutralidad de carbono. En el sector del transporte, la electrificación ha sido ampliamente reconocida como un buen camino para lograr dicho objetivo. El gran éxito en el rango de baja potencia ha generado confianza en el empleo de motores eléctricos de gran potencia. Sin embargo, las deficiencias actuales, como la baja densidad energética y el reciclaje limitado de baterías usadas dificultan la sustitución total de los motores de combustión en poco tiempo, especialmente en el caso de los motores de transporte pesado. La utilización de combustibles limpios puede ser una solución de transición para lograr una reducción rápida de las emisiones de CO_2.

La presente tesis tiene como objetivo predecir las características específicas del proceso de combustión de chorros tipo Diesel en condiciones reactivas alimentados con combustibles hidrocarburos y oxigenados. Para lograr este objetivo, se utiliza una herramienta numérica denominada modelo Quasi-1D, que acopla un modelo de chorro unidimensional desarrollado internamente con un modelo de combustión avanzado basado en flamas laminares de un bajo coste computacional. Posteriormente, las métricas de combustión y la estructura de la llama se pueden examinar de manera eficiente a través de la evaluación del estado químico obtenido a lo largo de las trayectorias de mezcla.

El estudio se centra principalmente en el caso de un chorro libre inyectado a través de un orificio único en un ambiente estacionario, con variaciones de condiciones de dicho ambiente y de inyección recomendadas por la Engine Combustion Network (ECN). Se han considerado una gran variedad de combustibles, incluyendo el n-dodecano, combustibles de referencia primarios y combustibles oxigenados de tipo OMEn.

En conclusión, el modelo cuasi-1D ofrece una predicción precisa de las principales métricas del proceso de combustión en el amplio rango de condiciones consideradas a pesar de su bajo coste computacional. Ello lo constituye en una herramienta prometedora para la calibración de la combustión en motores con combustibles alternativos.

Resum

L'augment de les emissions de gasos d'efecte d'hivernacle (GEI) empitjora l'escalfament global i el canvi climàtic. El diòxid de carboni (CO_2), com a principal component dels GEI, està estrictament restringit en les normatives que pretenen asolir un objectiu de neutralitat de carboni. En el sector del transport, l'electrificació ha sigut àmpliament reconeguda com un bon camí per a aconseguir aquest objectiu. El gran èxit en el rang de baixa potència ha generat confiança en l'ús de motors elèctrics de gran potència. No obstant això, les deficiències actuals, com la baixa densitat energètica i el reciclatge limitat de bateries usades dificulten la substitució total dels motors de combustió en poc temps, especialment en el cas dels motors de transport pesat. La utilització de combustibles nets pot ser una solució de transició per a aconseguir una reducció ràpida de les emissions de CO_2.

La present tesi té com a objectiu predir les característiques específiques del procés de combustió de dolls tipus Dièsel en condicions reactives alimentats amb combustibles hidrocarburs i oxigenats. Per a aconseguir este objectiu, s'utilitza una ferramenta numèrica denominada model Quasi-1D, que acobla un model de doll unidimensional desenvolupat internament amb un model de combustió avançat basat en flamelets laminars d'un baix cost computacional. Posteriorment, les mètriques de combustió i l'estructura de la flama es poden examinar de manera eficient a través de l'avaluació de l'estat químic obtingut al llarg de les trajectòries de mescla.

L'estudi es centra principalment en el cas d'un doll lliure injectat a través d'un orifici únic en un ambient estacionari, amb variacions de condicions d'aquest ambient i d'injecció recomanades per la Engine Combustion Network (ECN). S'han considerat una gran varietat de combustibles, incloent el n-dodecan, combustibles de referència primaris i combustibles oxigenat de tipus OMEn.

En conclusió, el model Quasi-1D oferix una predicció precisa de les principals mètriques del procés de combustió en l'ampli rang de condicions considerades malgrat el seu baix cost computacional. Això el constitueix en una ferramenta prometedora per a la calibració de la combustió en motors amb combustibles alternatius.

There is only one true heroism in the world:
to see the world as it is, and to love it.

– Romain Rolland

Acknowledgement

It has been four years since I arrived in Valencia on 21st of November in 2020. We were still suffering from the threat of CARS-CoV-2 at that time, the flying from Amsterdam to Valencia deeply impressed me. When I was at the height of 30,000 feet, I imagined what my PhD career would be. When time went back to Sep 2017, it is the first time for me to come to Valencia for the purpose of participating in the ILASS-Euro conference. I was curious about everything in Valencia, sunshine, beach, blue sky, passionate locals. It looks like everything here is saying 'welcome'. Suddenly, the turbulence brought me back to reality. To be honest, my brain was full of the mind that I am ready to face the challenge, and I will get the degree after several years.

First, I want to thank Dr. Jose Maria Desantes for giving me the opportunity to develop a research work at Instituto Universitario de Investigación CMT – Clean Mobility & Thermofluids. Within four years' work here, this thesis will be completed here.

I would like to express my deepest gratitude to my supervisor, Prof. Dr. José María García-Oliver, for the continuous support of my PhD study and research. His immense knowledge, unwavering patience, and insightful feedback have been invaluable throughout the entire process. At the beginning, I was not familiar with the 1D spray model, Jose Maria had been a constant source of patience and encouragement. Eight months later, I can give some personal understanding in the daily meeting, Jose Maria encouraged me to have deeper and deeper consideration. Even though I always made mistakes and brought trouble to him, he is always kind to help me. He is like a beacon, guiding me on the route to the port. At this moment, I really understand the say from Jose Maria, 'PhD degree is not only yours, but also belongs to a team', which will be in my mind forever. Finally, I could not have asked for a better supervisor to guide me through this journey. Once again express my gratitude to him.

To my colleague, Dr. Daiana De León, I owe a huge thanks for the support to my thesis in the simulation database and thank you for the daily help especially in the matters in the language of Spanish. Wish you have an excellent career as a teacher in your mother university in Uruguay. Dr. Iván Olmeda Ramiro, thank you for your sharing knowledge in the group meeting, it opens my eyesight in the field of combustion.

In the experimental campaign, I want to thank Prof. Dr. José V. Pastor for your guide on the optical techniques. I also want to express my thanks to Dr. Felipe De Vargas, Dr. Francisco Tejada, Dr. David for their valuable support. Technicians, Jose Enrique del Rey and Omar Huerta, thank you for the help in the measurement in IAPAT. Finally, Dr. Gabriela Bracho, thank you for your great work in the measurement and paper preparation.

In the simulation, I want to thank Dr. José Manuel Pastor for the suggestions in the thesis. I also want to thank Dr. Vald Aparece-Scutariu and Dr. Dong-hyuk Shin for your support on the database for the model validation in my thesis.

When I was an intern at Large Engine Competence Center, I would like to thank Gerhard for the permission on my short stay in his team and thank Anton for the daily guide on my work. Thank Herlinde for the preparation of the vast paperwork to close my internship.

When I moved to Valencia, the support from Dr. Weiwei Shang was crucial. Thank you for helping with my accommodation and the new life in Valencia. Hope you have a good time as a visiting researcher in CMT in the following months. In the daily life, my roommate, Xiaodan, Mingda, making a good memory in my living in Spain. Good luck with you and your PhD career. Weisong Zhang, He Jiang, Ruijun Ou, thank you.

Then, I want to express thanks to my friend, Yifeng Qin, who always encouraged me to welcome the new life when I was trapped in a bad mood.

Nine years ago, when I was in the first year of my master's education, Prof. Dr. Zhixia He introduced a brand-new world of combustion to me; Dr. Tiemin Xuan showed me what scientific research should be; Dr. Wenjun Zhong, taught me the skills of optical measurement. Since then, I decided to find my apple in the field of combustion. Thank you for accompanying me at each step of the way.

Finally, I want to thank my family, thanks for the continuous support for my education.

Written in Nanjing, China

2024.09.19

Funding acknowledgements

The respondent wishes to acknowledge the financial support received through a grant from China Scholarship Council (No.201808320236) and Vicerrectorado de Investigación of Universitat Politècnica de València with reference FPI UPV SUBP2 (PAID-06-22).

Technical acknowledgements

Thanks to Dr. Bertrand Naud from CIEMAT for the support in the use and application of the flamelet solver used in this work.

Contents

List of Figures

List of Tables

Nomenclature

Acronyms

ASOI	After Start of Injection
BEVs	Battery-Electric Vehicles
CARTS	Cross-sectionally Averaged Reactive Turbulent Spray
CAS	Cross-sectionally Averaged Spray
CDC	Conventional diesel combustion
CFD	Computational Fluid Dynamics
CH_2O	Formaldehyde
CI	Compression Ignition
CIEMAT	Centro de Investigaciones Energéticas, Medioambientales y Tecnológicas
Cmax	Maximum Normalized Progress Variable across the Spray Domain
CMT	Clean Mobility & Thermofluids – Research Institute
CNG	Compressed Natural Gas
CO	Carbon Monoxide
CO_2	Carbon Dioxide
DDM	Discrete Droplet Method
DI	Direct-injection
DNS	Direct Numerical Simulation
ECN	Engine Combustion Network
EOC	End of Combustion
EOI	End of Injection
EU	Europe Unions
EVs	Electric Vehicles
GCI	Gasoline Compression Ignition
GHG	Greenhouse Gas
HCO	Bicarbonate
HCCI	Homogeneous Charge Compression Ignition
HEVs	Hybrid-Electric Vehicles

HRR	Heat Release Rate
HSDI	High-Speed Direct Injection
H_2O	Water
ID	Ignition delay
IEA	International Energy Agency
IL	Intact Length as an Input for the Transition of Spray Angle in 1D Spray Model
IMO	International Maritime Organization
LES	Large-Eddy Simulation
LL	Liquid Length
LNG	Liquefied Natural Gas
LOL	Lift-off Length
LTC	Low-temperature Combustion
KH	Kelvin-Helmholtz
N_2	Nitrogen
NO	Nitric Oxide
NOx	Nitrogen Oxides
OH	Hydroxide
OME	Polyoxymethylene Dimethyl Ethers
ON	Octane Number
O_2	Oxygen
PAHs	Polycyclic Aromatic Hydrocarbons
PCCI	Premixed Charged Compression Ignition
PLIF	Planar laser-induced fluorescence
PM	Particular matter
PODE3	Polyoxymethylene Dimethyl Ether 3
PPC	Partially Premixed Combustion
Pr	Prandtl Number
PRF#	Primary Reference Fuels
RANS	Reynolds-Averaged Navier-Stokes simulation
RCCI	Reactivity Controlled Compression Ignition

RCM	Rapid Compression Machine
RO_2	Peroxy radicals
ROI	Rate of injection
RT	Rayleigh-Taylor
SDR	Scalar Dissipation Rate
SMD	Sauter Mean Diameter
SNL	Sandia National Laboratory
SOC	Start of Combustion
SOI	Start of Injection
SR	Strain Rate
TKE	Turbulent Kinetic Energy
Tmax	Maximum Temperature across the Spray Domain
TSL	Two-stage Lagrangian
UFPV	Unsteady Flamelet Progress Variable
UHC	Unburned Hydrocarbons
URANS	Unsteady Reynolds-Averaged Navier-Stokes simulation
XO_2	Mole fraction of Oxygen
Wb	Weber number
0D	Zero-dimensional
1D	One-dimensional
2D	Two-dimensional

Greek symbols

$\alpha_{LOL,c}$	Coefficient of Lift-off Length Determined by C
α, θ	Spray Spread Angle
χ	Scalar Dissipation Rate
χ_{cl}	On-axis Scalar Dissipation Rate
χ_{st}	Stoichiometric Scalar Dissipation Rate
ϕ	Equivalence Ratio
ϕ_{max}	Maximum Equivalence Ratio

β-PDF	Beta Function – Probability Density Function
β:	Coefficient for the Near Field and Developed Field
θ_1	Near-field Spray Angle as an Input for 1D Spray Model
θ_2	Far-field Spray Angle as an Input for 1D Spray Model
ζ	Ratio for the Spray Boundary Definition, the Value is 0.01
ρ_i	Density for Component i
$\bar{\rho}$	Cross-sectionally Averaged Density
ρ_f	Fuel Density
ρ_a	Air Density
τ	Characteristic Time
τ_{comb}	Combustion Timing
$\dot{w}_c$	Source Terms in Balance of Progress Variable.
$\dot{\omega}_k$	Net Production Rate of Species k
γ_t	Coefficient in Radial Boundary Definition

Latin symbols

$A(x)$	Cross-sectional Area at the Distance of x
$A_f(0)$	Cross-sectional Area of the Fuel at the Nozzle Outlet
C	Normalized Progress Variable
c_d	Discharge Coefficient
C_S	Penetration Coefficient
C_χ	Coefficient for Scalar Dissipation Rate Fitting
d_{eq}	Nozzle Equivalence Diameter
d_0	Nozzle Diameter
d_s	Sac Chamber Diameter of the Nozzle
d_{SprayD}	Nozzle Diameter of Spray D
d_{SprayA}	Nozzle Diameter of Spray A
D_l	Laminar Diffusivity

D_t	Turbulent Diffusivity
$erfc^{-1}$	Inverse Complementary Error Function
f	Mixture Fraction
$\bar{f}$	Cross-sectionally Averaged Mixture Fraction
f_{cl}	On-Axis Mixture Fraction
f_{evap}	Evaporation Mixture Fraction
*f*st	Stoichiometric Mixture Fraction
H	Spray Height
$h_{f,0}$	Enthalpy of Pure Fuel
$h_{a,\infty}$	Enthalpy of Pure Air
i	Section Index
j	Timing Index
k	Constant Coefficient in Radial Boundary Definition
k_f	Coefficient in Radial Boundary Definition in terms of Mixture Fraction
k_{LL}	Correlation for Liquid Length Calculation
k_u	Coefficient in Radial Boundary Definition in terms of Velocity
L	Orifice Length
L_b	Breakup Length
$\dot{M}$	Fuel Momentum
$\dot{m}_a$	Entrained Gas Rate
m_a	Entrained Air Mass
$mass^i_{ignited}$	Radially Integrated Mass at Ignited State
$mass^i_{tot}$	Cross-sectionally Total Mass
$\dot{m}_{ent}$	Entrainment Rate
m_f	Fuel Mass
$\dot{m}_f$	Fuel Mass Rate
$\dot{m}_{f,evap}$	Evaporation Fuel Mass Rate
n	Engine Speed
P_a	Chamber Pressure

P_{inj}	Injection Pressure
R	Radius at Spray Boundary
r	Radius
R_{evap}	Evaporation Coefficient
r_S	Swirl Ratio
R_{st}	Radius of Stoichiometric Ratio
S	Spray Tip Penetration
Sc	Schmidt Number
S_f	Spray Penetration in The Free Penetration Region
S_r	Spray Radius
S_S	Swirl Spray Penetration
s_{tip}^{j}	Spray Tip at the Timing j
t	Time
T	Temperature
T_a	Ambient Temperature
T_{cl}	On-Axis Temperature
t_{break}	Breakup Time
T_{evap}	Saturation Temperature When the Fuel is fully Vaporized
$T_{f,0}$	Initial Fuel Temperature
u	Axial Convective Velocity
$\bar{u}$	Cross-sectionally Averaged Velocity
u_{cl}	On-Axis Mixture Fraction
u_f	Fuel Velocity
u_j	Effective Velocity
u_0	Spray Initial Velocity
$u(x)$	Velocity at the Distance of x
u_{th}	Theoretical Fuel Velocity at the Nozzle Outlet
$\bar{u}_{tip}^{j-1}$	Cross-sectional Average Velocity at Spray Tip at the Timing $j-1$

v	Radial Convective Velocity
v_{diff}	Radial Diffusion Velocity
$v_{f,0}$	Exit Velocity of the Nozzle
v_{tot}	Total Radial Velocity
x	Axial Distance
$xLOL_C$	Temporal lift-off length by C
$xLOL_{OH}$	Temporal Lift-off Length by OH Mass Fraction
x_0	Beginning of the Spray Domain
XO_2	Mole Fraction of Oxygen
Y_c	Progress Variable
$\dot{Y}_c$	Transient Term in Progress Variable Conservation Equation
Y_c^{inert}	Progress Variable at Inert State
Y_c^{steady}	Progress Variable at Steady State
$Y_{f,evap}$	Evaporation Fraction of the Mixture
Y_f	Fuel Mass Fraction
Y_i	Mass Fraction of Mixture Component i
Y_k:	Species Mass Fraction

Chapter 1

Introduction

Content

1.1 Background and Motivation

The negative effect of greenhouse gas (GHG) emissions on global warming and climate change has gained more attention and brought about a restriction of carbon emission all over the world. As the main composition in greenhouse gases, carbon dioxide (CO_2) emissions from energy combustion and industrial process accounted for 89% of the energy-related GHG emission in 2022 as reported in International Energy Agency (IEA) [1]. As shown in Figure 1.1, in the past decades, as well as in near future ones, fossil fuels continue to serve as the primary energy supply globally, Figure 1.1. Considering the situation that more than 58% of the installed power generation capacity relying on combustion all over the world, the global emissions from fuel combustion dominated by oil and natural gas accounts for 55% [2]. The transport sector, which accounts for about 60% of the oil consumption [3], is currently trying to achieve significant CO_2 reduction targets, as well as on ultra-low nitrogen oxides (NOx) emissions within a general trend towards zero fossilization.

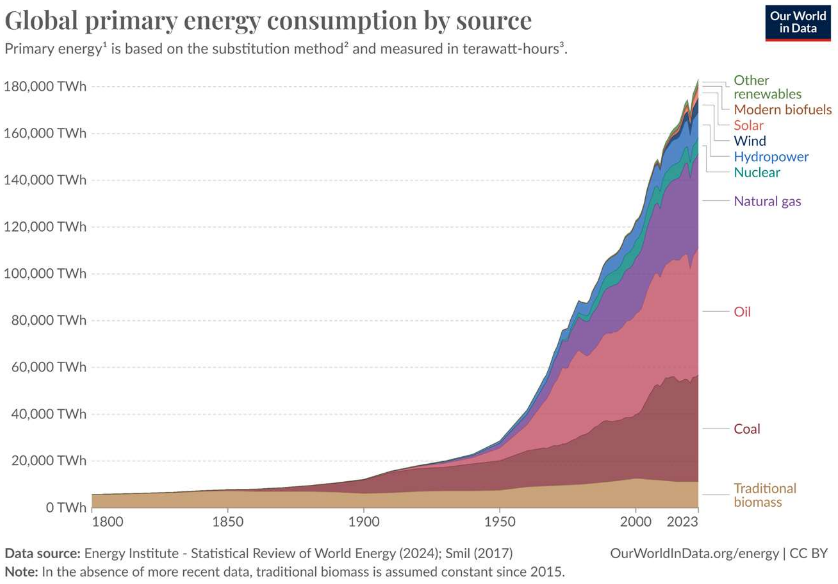
Global primary energy consumption by source

Primary energy¹ is based on the substitution method² and measured in terawatt-hours³.

Data source: Energy Institute - Statistical Review of World Energy (2024); Smil (2017) OurWorldInData.org/energy | CC BY

Note: In the absence of more recent data, traditional biomass is assumed constant since 2015.

Figure 1.1. Global primary energy consumption by source [4]

To meet the demand of Net Zero Emission by 2050 and hence decarbonize road transport, electric vehicles (EVs) are a promising technology. With the fast development of battery and public charging points, as well as the financial support from the local government, the share of electric cars in total sales has increased from ~4% in 2020 to 18% in 2023, where the huge growth was in China [5]. However, current unsolved problems such as the reduced efficiency in cold weather and low energy density makes it hard for a full replacement of internal combustion engine, particularly in large power scenarios, such as heavy-duty road transport, shipping et al. Accounting for more than 25% of road transport and 6% of total GHG emissions in European Unions (EU), heavy-duty vehicles were required to reduce the CO_2 emission by 15% within 5 years since 2019, especially for the heavy lorries over 16 tons [1]. Then, further reduction in CO_2 emission was demanded that a 90% reduction compared to 2019, which covers all the heavy-duty vehicles, including medium lorries, city buses, coaches and trailers. For shipping, it only accounts for around 3% of global CO_2 emission, while the rate was assumed to rise to 17% by 2050 [6]. Meanwhile, an initial strategy adopted by International Maritime Organization (IMO) in 2018, promoted a target of the reduction in total annual GHG emission by at least 50% by 2050 compared to 2008 [7].

To comply with the stricter regulations of CO_2 emissions, much effort has been made in respect to improving thermal efficiency and utilizing low-carbon or zero-carbon fuels. Reported by WEICHAI POWER CO. LTD, diesel engine has reached a record-breaking thermal efficiency of 53.09% [8]. If focusing on the combustion, low-temperature combustion mode, such as Homogeneous Charge Compression Ignition (HCCI) and Reactivity Controlled Compression Ignition (RCCI) has shown great potential on the fuel efficiency improvement, as well as the reduction in emissions of soot particles and NOx [9] [10]. Another method to improve thermal efficiency is electrification which has been primarily associated with light-duty vehicles, while there is also growing interest in electrifying heavy-duty vehicles by battery-electric vehicles (BEVs) and hybrid-electric vehicles (HEVs). HEVs take advantage of both internal combustion engines and electric motors, while it also comes with high initial cost and maintenance complexity due to the dual powertrains.

With the advantage of minimal modifications to current injection systems, the utilization of clean fuels is preferred compared to the employment of HEVs, particularly in large engines. For example, biodiesel, which is a widely used fuel, was estimated to reduce CO_2 emissions by approximately 85% based upon a life-cycle analysis [11]. In addition, oxygenated fuels, such as polyoxymethylene dimethyl ether, are also promising in the CO_2 emission, with a production cost that is also trying to become close to that of fossil fuels [12]. Additionally, investigations on compressed or liquefied natural gas (CNG or LNG) [13] [14], and methanol [15] are also currently underway for marine engines. Meanwhile, the ongoing research of the possible utilization of zero-carbon fuels, such as hydrogen [16] and ammonia [17], can help to hugely reduce CO_2 emission, while the design of infrastructure of injection system and fuel storage is still challenging.

When utilizing these fuel candidates, it is essential to quantify the spray and combustion characteristics. However, experimental testing cannot encompass all required conditions due to facility limitations, and it also entails a significant workload. Additionally, optimizing the production pathway or raw source introduces further complexity. Computational Fluid Dynamics (CFD) offers valuable insights into physical and chemical processes, particularly in scenarios that are challenging to measure. Nevertheless, the computational cost of reliable CFD remains prohibitively high for all fuel candidates. Over the past few decades, fundamental research has delivered detailed characterization of the spray and combustion processes using several parameters obtained from measurements conducted in High Pressure and Temperature vessels. Within this context, phenomenological model/low-dimensional model can also facilitate the evaluation of the effect of operating parameters for multiple new fuel candidates at a lower computational cost. While the current accuracy is still far away from CFD results, such models can also be applied in rapid engine calculations.

1.2 Objective of the study

In the history of one-dimensional spray model proposed by CMT – Clean Mobility & Thermofluids, the prediction to spray penetration, mixing and evaporation processes of inert spray has been established in [18] [19], similar predictions were extended under reacting conditions by means of 1-step chemistry, as well as external user inputs in terms of experimental ignition delay and lift-off length [20]. A more predictive approach was introduced in [21] to enable predictions of combustion metrics based upon detailed chemistry. In this thesis, this approach has been further developed, hence, the main objective of this thesis is to validate the consistency of the predictions of ignition delay and lift-off length over a wide range of operation conditions and fuels. This goal will be achieved through two partial objectives:

- **Optimizations**: the main task in this section is related to the numerical issue. Further reduction in computational cost compared to [21] is demanded throughout the simplification of model description and the corresponding structure of the in-house code written in the language of C++. In parallel, more accurate predictions to combustion metrics are also required, which is mainly on the development on the approach of flamelet integration with one-dimensional (1D) spray model.
- **Applications:** the optimized model will be validated by the experimental database from CMT performed under various steady engine-like conditions recommended by Engine Combustion Network (ECN) [22]. The initial validation is conducted for n-dodecane using different chemical mechanisms. Then, the model will be extended to other fuels, including a binary mixture of hydrocarbon fuels with a wider range of fuel reactivity compared to n-dodecane [19] [23], and polyoxymethylene dimethyl ethers (OME), a sustainable alternative to fossil fuels and kind to reduce greenhouse gas and soot emission rather than diesel [24].

1.3 Approach of the study

An extensive review of the literature will serve as the basis for the development of the thesis. Following recommendations in [25], the interaction between the physical 1D spray model and detailed chemistry should be studied, which will substitute the current coupling of the local density into the axial momentum and mixture fraction equations. The combustion model is based upon an unsteady flamelet progress variable model developed at CMT for CFD applications. Consistently with this approach, off-line tabulated flamelet manifolds contain the mixing and chemistry states from inert to fully reacting in terms of the local mixture fraction f and tabulated progress variables Y_c. Conservation equations including Y_c will be integrated along the temporal mixture trajectories throughout the spray. Additionally, the integration approach in terms of the scalar dissipation rate variation will be utilized.

Under this scheme, the study of the first scenario will allow to provide more accurate predictions, which will be closer to CFD approach and low demand of computational resources will also retain. The validation of applicability will further emphasize the value of the 1D model development.

1.4 Outline of the study

In order to achieve the set objectives with the presented approach, the thesis is structured in seven chapters, and the main content of each chapter is listed as follows:

Chapter 1: the current chapter presents an overview of the thesis, including a brief description of the background, research tool and thesis structures.

Chapter 2: this chapter reviews concepts on spray and combustion process in compression ignition engines, followed by the detailed description of the main subprocess, namely atomization, evaporation, mixing, entrainment, premixed and diffusion combustion. The prediction of characteristic parameters starts from the empirical formulas, then the concept of phenomenological spray model is introduced. Finally, the literature review on the application of phenomenological spray model on the spray and combustion process was presented to close this chapter.

Chapter 3: this chapter introduces the modelling approach in this work, emphasizing the basic concepts, optimizations and the influence on the ignition process under ECN Spray A condition.

Chapter 4: this chapter explores the effect of chemical mechanisms and mixing characteristics on the prediction of n-dodecane reacting sprays. It starts with the model validation for inert ECN Spray A. Then, the effect of strain rate together with three chemical mechanisms on the ignition are discussed, followed by the comparison of single and multiple flamelets. Next, the difference of mixing state generated by different injection pressure and nozzle diameter is investigated. Finally, the model accuracy on the combustion metrics is analyzed throughout the comparison of ECN recommended conditions.

Chapter 5: the effect of fuel reactivity of hydrocarbon fuels on the ignition is studied following the conclusion in the previous chapter. An in-depth analysis on the differences introduced by octane number effects will be done, as well as the comparison of combustion metrics under ECN conditions.

Chapter 6: In an analogous way as the previous chapter, the model application was extended to oxygenated fuels, and the hydrocarbon fuels at a similar fuel reactivity are kept as a reference. An analysis of the mixing and fuel reactivity will be done. Like the previous chapters, the model accuracy on the combustion metrics under a wide range of conditions will be presented.

Chapter 7: this chapter draws the conclusions from the obtained results and suggests the possible future work.

Chapter 2

Fundamentals

Content

2.1 Introduction

As explained in Chapter 1, the role of liquid fossil fuels as an energy source remains challenging to replace, particularly in compression ignition engines. To address the need for maintaining high energy density while achieving carbon dioxide neutrality, one potential solution is to substitute current fossil fuels with renewable alternatives. Consequently, it is essential to understand the combustion characteristics of these fuels to ensure their optimal application in compression ignition (CI) engines. For numerical tools, a phenomenological model aimed at predicting specific quantitative parameters demonstrates reasonable accuracy with low computational costs. This chapter will lay the groundwork for the studies presented in this thesis, beginning with a brief overview of the essential phases of the combustion process in CI engines. Then, it will review research on the spray and combustion processes under quiescent environments. Next, the principles of phenomenological spray model will be given, followed by a literature review of the model application and recent studies to close this chapter.

2.2 Conventional DI diesel engine combustion process

The combustion process in DI diesel engines takes place in a period with a magnitude of milliseconds and comprises complex physical and chemical processes. Heat release rate (HRR) provides an invaluable tool for dissecting the combustion phases of the combustion process, offering insights into the combustion efficiency, emissions formation and the overall performance of the engines. Figure 2.1 presents the combustion phases of a conventional direct-injection (DI) diesel process [26]. From the start of injection (SOI) to the end of combustion (EOC), the HRR evolution can be divided into four phases:

- **Ignition delay period**: the first stage of the combustion process is defined as the time interval between SOI and the start of combustion (SOC) when HRR is first noticeable [27]. As the liquid fuel was ejected into the chamber, it undergoes a series of physical processes, including liquid core break up, atomization, evaporation caused by the energy exchange with the surrounding hot gas. These processes mainly depend on the ambient environment, such as temperature, pressure, et al., and physical fuel properties, such as density, viscosity, surface tension, and vapor pressure et al. [28] In addition, due to the oxygen in the surrounding and high temperature in the air, the low-intensity chemical reaction also takes place, producing of shorter hydrocarbon chains. Therefore, controlling the phase of SOC is seen as an effective way to improve the fuel economy and thermal efficiency of engines, as well as the reduction in pollutant emissions [29]. For example, it is critical to realize low-temperature combustion (LTC). The calculation of ignition delay is also the interest in this thesis.

- **Premixed combustion phase**: after the appearance of combustion (starting at point *b*), the fuel-air mixture formed in the previous stage enters a high-temperature combustion, corresponding to a rapid increase in HRR and reaching the first peak in a short time. This phase is known as premixed combustion, and it usually takes place as fuel injections are in progress, as shown in Figure 2.1. After the first peak, the premixed mixture was burned out, and then the steep decrease in HRR is observed until the first minimum (ending at point *c*). The duration of this phase is usually proportional to the ignition delay period [30]. Some species like CO_2 and H_2O have already been produced during this phase. Besides, the soot precursor polycyclic aromatic hydrocarbons (PAHs) are also quickly formed in the hot flames [31].
- **Mixing-controlled combustion phase**: this phase starts when the fuel-air mixture forms before ignition has been consumed completely. The subsequent combustion process is dominated by the fuel-air mixing rate; hence, this phase is also called mixing-controlled combustion. Compared to premixed combustion phase, HRR in this phase is more progressive, and the second peak can be observed at the end of injection (EOI). By adjusting the injection strategies, like reducing injection duration or modifying injection timing, lower HRR can be obtained and no peaks across the entire phase, especially for a heavy-duty engine [29]. Thus, the soot formation can be significantly reduced [32]. As long as the injection rate is maintained, the diesel jet enters a 'quasi-steady' period, during which the flame structure also remains relatively constant. More details will be presented in the next section. Immediately following the end of injection, the ending of fuel momentum supply rapidly decelerates the flow propagation, leading to a stagnant, fuel-lean region near the nozzle. If the ignition delay occurs after the end of injection, this stagnant region can become too lean to obtain a complete combustion and soot emission can be reduced or even eliminated.
- **Late combustion phase**: this phase typically starts at EOI, when the lack of fuel momentum supply rapidly decelerates the flow propagation, leading to a stagnant, fuel-lean region near the nozzle. At the case of ignition delay occurring after EOI, this stagnant region becomes much lean, hence, soot emission can be reduced or even eliminated [33]. In addition, this late burning of the fuel that ejected during the ramp-down period usually leads to unstable flame (b-c) compared to the mixing-controlled combustion period. The continuous expansion of cylinder volume exacerbates the combustion, resulting in lower heat release, which ultimately ceases until the flame extinguishes. Proper management of the late combustion phase is

essential to ensure complete combustion of unburned hydrocarbons and carbon monoxide, thereby minimizing emissions of these pollutants.

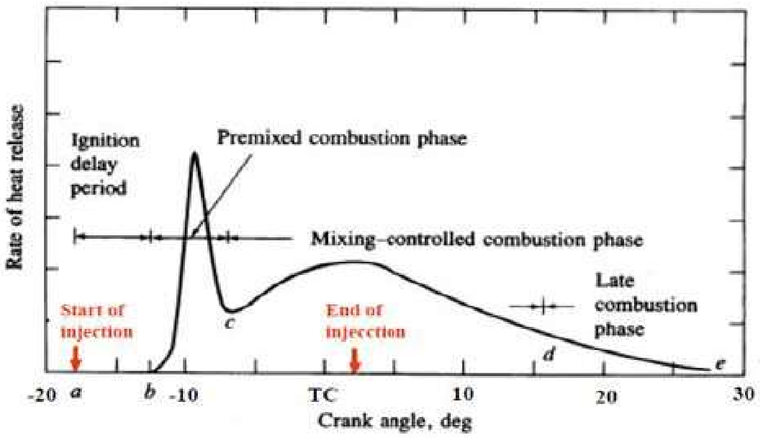

Figure 2.1. Diagram of combustion phases during a typical DI diesel engine combustion process characterized by rate of heat release [26].

2.3 Spray and combustion process under quiescent environment

To further investigate the spray and combustion process fundamentally, most studies have focused on free spray without considering turbulence in the chamber and wall impingement. As shown in Figure 2.2, spray characteristics are typically explored for different processes such as cavitation, atomization, evaporation, fuel-air mixing and entrainment until the ignition, as well as pollutant emission formation. This section will provide a detailed introduction to these processes, serving as a baseline for the subsequent review of phenomenological models.

2.3.1. Atomization

As the high-velocity liquid fuel is ejected into the high-temperature high-pressure combustion chamber, atomization takes place initially by transforming the injected fuel into a fine spray or tiny droplets. In the context of atomization, the surface of the jet becomes perturbed, leading to the formation of waves. These waves grow due to the Kelvin-Helmholtz instability, which amplifies the surface perturbations. Eventually, the jet breaks up into ligaments, which further disintegrate into droplets due to the action of surface tension and aerodynamic forces. The increased contact area with the surrounding gas facilitates better exchange of heat, mass and momentum, ultimately improving the air entrainment and subsequent evaporation process, and promoting a more efficient and complete combustion.

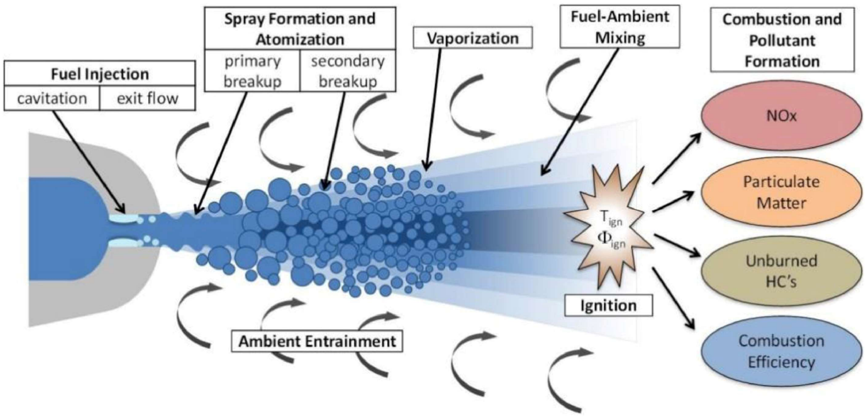

Figure 2.2. Schematic of spray and combustion process [34]

In brief, atomization is the process of converting liquid fuel core into a number of tiny droplets. As the fuel leaves the nozzle, the jet velocity remains constant until it reaches a certain distance downstream from the nozzle outlet, this distance is called intact length. Numerous research has shown that the magnitude of the intact length is comparable to the nozzle diameter, approximately 1 to 3 times the latter [35] [36]. The spray region, characterized by the dispersed phase volume fraction [37], can be classified into two regions, where the first one in the upstream is named as dense region and the latter one is named as diluted region [38], as shown in Figure 2.3.

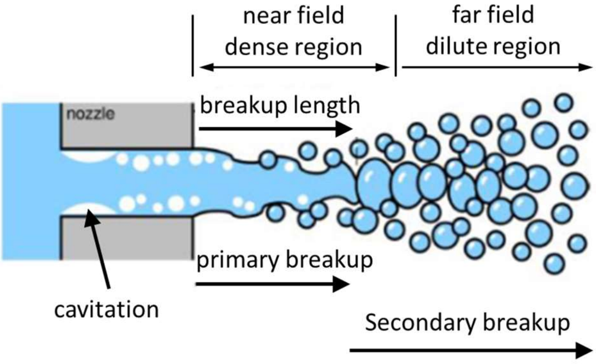

Figure 2.3. Schematic of atomization process of spray

In the dense region, liquid jet disintegrates into large droplets and ligaments, a process known as primary breakup. This phenomenon describes the transformation of the cylindrical liquid column that emanates from the injector nozzle into distinct particles, derived by instabilities arising from surface tension, the geometry of the injector nozzle, and aerodynamic effects [39]. Ultimately, it turns out to be the Kelvin-Helmholtz (KH) instability and the Rayleigh-Taylor (RT) instability at the gas-liquid interface [40]. Depending on the nozzle exit conditions, primary breakup exhibits various regimes categorized by the ratio of the Ohnesorge number to the Reynolds number, relating the viscous forces to the inertial and surface tension forces. As jet velocity increases, the primary breakup mode initially remains in the Rayleigh regime, then transitions to the First Wind-Induced regime, where the droplet diameter is approximately equal to the nozzle diameter. Furthermore, as the droplet size becomes much smaller than the nozzle diameter, air resistance no longer acts as damping factor while increasing perturbations, leading to the Second Wind-Induced regime. Therefore, the resultant droplet diameter becomes a critical parameter in the quantitative investigation of the primary breakup process.

The Sauter Mean Diameter (SMD) is frequently utilized to quantitatively analyze the primary breakup process. Numerous optical techniques have been developed and employed to obtain this value and distribution [41] [42] [43]. Recently, a combination of visible-light scattering and X-ray absorption, called as scattering-absorption measurement ratio, has overcome the limitations of the single technique employed in the real dense spray [44] [45] [46]. Using the tool of CFD, the KH model is commonly applied for modelling the primary breakup, and the effect of cavitation and turbulence have also been also considered. KH-RT model exhibits improved predictions the spray and combustion characteristics [47] [48] [49].

In the diluted region, the volume fraction of the dispersed phase decreases to the range of $10^{-6} - 10^{-3}$ [38], where the influence of dispersed phase turbulence on the continuous phase turbulence becomes pronounced. Thus, the droplets are surrounded by turbulent gas flow, which generates aerodynamic forces on their surface. As a consequence, such forces may overcome the superficial tension and distort the spherical sharp breaking the droplet again into parcels of smaller dimensions [50]. This process is named as secondary breakup, and it is usually quantitatively characterized using Weber number (Wb). As shown in Figure 2.4, bag breakup is observed when the Weber number ranges roughly from 11 to 80, during which aerodynamic forces cause the droplets to shape into a relatively flat disk, eventually transforming into a thin membrane. These membranes ultimately rupture, leading to the formation of numerous small droplets. When the Weber number falls within the range of 80 to 350, a strip breakup is manifested. In this case, the flat disks develop inward, and the membranes collapse at their edges, producing smaller droplets. For Weber number surpassing 850, catastrophic breakup is observed. Extremely high shear rates at the gas-liquid interfaces lead to the elongation of droplets, which eventually fragment due to Rayleigh instabilities [38].

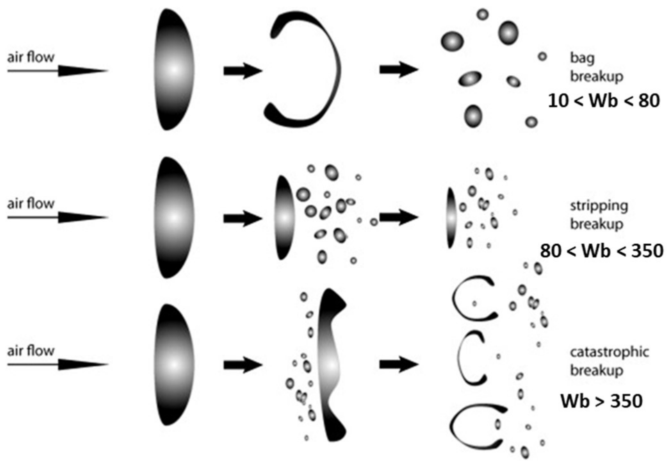

Figure 2.4. Schematic of secondary break regimes [38]

2.3.2. Evaporation

After the atomization process, liquid fuel has broken up into a parcel of small particles. As the spray continues to entrain air, heat is gradually transferred from the ambient gas to the tiny fuel droplets; therefore, their relative velocities decrease as the droplets transfer momentum to the air, leading to an increase in the temperature of the liquid. The temperature rise results in a decrease in the vapor pressure at the surface of droplet, initiating the evaporation process and causing the local mixture to approach adiabatic saturation conditions [51]. As the liquid fuel penetrates, it reaches a distance where the total fuel evaporation rate in the spray equals the fuel injection rate; this distance is called liquid length (LL). Usually, liquid length refers to the maximum length where the liquid phase stabilizes. It has been verified that an excessive LL would cause a wetting of the piston and cylinder wall, contributing to potentially higher emissions [52].

Over the last decades, several optical techniques have been developed for measuring liquid length, such as Mie scattering [53] and Diffused Back-illumination [54] [55]. In non-reacting scenarios, experimental finds indicate that liquid length is significantly influenced by the factors such as nozzle diameter [53], fuel temperature [56] [57], thermodynamic environment [58], and fuel properties [52] [59] [60]. For instance, a shorter LL was observed at higher gas densities, as illustrated in Figure 2.5. Furthermore, it has been validated that injection pressure has little influence on liquid length, due to the simultaneous change in injection rate and evaporation rate [53].

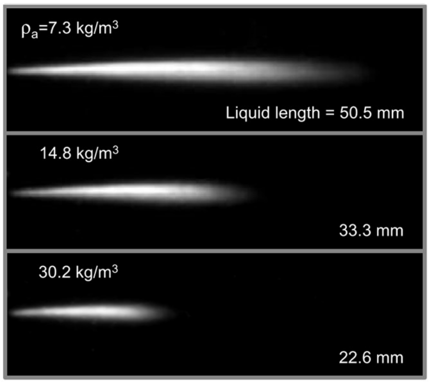

Figure 2.5. Effect of gas density on the liquid length. Time-averaged Mie-scattered light images for three sprays injected from left to right into the different ambient gas densities. The orifice pressure drops and diameter, the ambient gas temperature, the fuel temperature, and the fuel were 135 MPa, 246 μm, 1000 K, 438 K and DF2, respectively [53].

The observation that liquid length is linearly dependent on the nozzle diameter and just little influenced by the injection pressure suggested that vaporization in a diesel spray is controlled by mixing process, as opposed to interphase transport rates of mass, momentum, and energy at droplet surfaces. The ratio of entrained gas rate $\dot{m}_a$ to the fuel mass rate $\dot{m}_f$ is used to examine the mixing process by jet theory [56],

$$\frac{\dot{m}_a}{\dot{m}_f} \propto \frac{\sqrt{\rho_a \cdot \rho_f} \cdot d_0 \cdot u_f \cdot tan\left(\frac{\theta}{2}\right) \cdot x}{\rho_f \cdot d_0^2 \cdot u_f} = \sqrt{\frac{\rho_a}{\rho_f}} \cdot \frac{1}{d_0} \cdot tan\left(\frac{\theta}{2}\right) \cdot x \tag{2.1}$$

where d_0 is the nozzle diameter, ρ_f and ρ_a are the density of fuel and air, respectively, θ is the spray spreading angle and x is the axial distance. With the principle of conservation of mass, momentum and energy, Siebers derived a scaling law to the liquid length under the assumptions [61]:

- Axially uniform spray angles established for the non-head region of transient gas jet, which considers a constant velocity, fuel concentration and temperature across the section.
- Thermodynamic equilibrium between saturated fuel vapor and entrained ambient gas is equivalent to the adiabatic condition.

Therefore, vaporization can be seen as a mixing-controlled process, and the effect of atomization process can be ignored. The problem of two-phase diesel spray can be reduced to a single-phase flow where a fraction of fuel vaporizes instantaneously once there is enough enthalpy in the surrounding gas to heat it up and vaporize it [59]. Under the hypothesis of mixing-controlled spray, spray model was simplified as a one-dimensional model [18] [33], and liquid length can be defined as the location where the fuel concentration reaches the evaporation fraction of the mixture, $Y_{f,evap}$,

$$LL = \frac{k_{LL} \cdot d_0 \cdot \sqrt{\frac{\rho_f}{\rho_a}}}{tan\left(\frac{\theta}{2}\right) \cdot Y_{f,evap}} \tag{2.2}$$

the terms d_0, ρ_a, ρ_f and θ has been explained before. The term k_{LL} is a correlation constant which is partially determined by the area coefficient of the injector. The latter one, $Y_{f,evap}$, can be calculated by the enthalpy difference,

$$\frac{1}{Y_{f,evap}} = 1 + \frac{\Delta h_f\left(T_{evap}, T_{f,0}\right)}{\Delta h_a\left(T_{a}, T_{evap}\right)} \tag{2.3}$$

where T_a is the ambient temperature, $T_{f,0}$ is the initial fuel temperature, and T_{evap} is the saturation temperature when the fuel is fully vaporized. This is in agreement with the experimental observation that LL depends on the fuel properties, i.e., fuel latent heat and fuel temperature.

2.3.3. Fuel-air mixing and entrainment

After the complete vaporization of the fuel, the downstream penetration of liquid length is driven by fuel momentum, which continues to entrain the surrounding hot gas. Typically, the mixing and entrainment processes can be characterized by spray vapor penetration, spray angle and mixture fraction distribution, each of which will be individually discussed in the following sections.

Spray tip penetration

Spray tip penetration, one of the most essential characteristics, determines the degree of air entrainment into the spray, significantly effecting combustion and engine performance. As shown in Figure 2.6, spray penetration is defined as the furthest distance from the nozzle outlet to the spray tip. Shadowgraph or schlieren imaging techniques are predominantly employed to identify the vapor boundary of a penetrating jet [61]. Usually, the conical-shaped region extending from the nozzle to approximately 70% of the total penetration is denoted as steady-state region, and the elliptical region is designated as the transient region. To avoid the complex vortical structures near the spray head, the attention is primarily focused on the steady-state region.

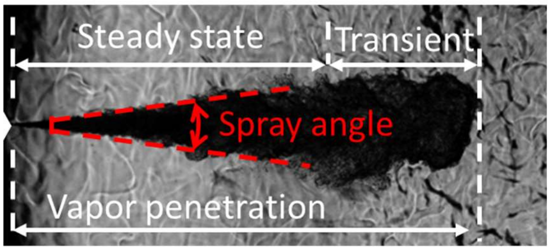

Figure 2.6. Diagram of vapor penetration and spray angle

The research on jet penetration can be retrieved by Sass as early as 1920s under room temperature [62]. Concluded from the measurement results, some empirical formulas have been proposed as a function of the following parameters:

$$S = f(\Delta P, d_0, \rho_a, \theta, t, \rho_f, v_{f,0}, L) \qquad (2.4)$$

where ΔP is the pressure difference between nozzle exit and ambient, $v_{f,0}$ is the exit velocity of the nozzle, t is time, L is the orifice length, the terms of d_0, ρ_a, ρ_f and θ are consistent with the explanation before. Due to the operating conditions or limitations of facilities used in the experiment, not all the parameters in Eq. (2.1) are considered in all the empirical formulas. Table 2.1 presents some correlations proposed in the last century, and the penetration is mainly dependent on nozzle diameter ($d^{0.18}$ – $d^{0.82}$), injection pressure ($\Delta P^{0.25}$ – $\Delta P^{0.39}$) and air density ($\rho_a^{-0.25}$ – $\rho_a^{-0.5}$). For most correlations, penetration is concluded as a function of square root of time dependent. However, these empirical formulas also have the limitation on the conditions. For example, the formula proposed by Dent [63] can only be recommended under the conditions besides large chamber pressure ($P_a > 10\ MPa$), otherwise it would be overpredicted.

Table 2.1. Power of parameters in correlations of Eq.((2.4) [64]

Proposer(s) of Correlation	Power of Parameter							
	ΔP	d	ρ_a	θ	t	ρ_f	v	L
Schweitzer [65]	0.2936	0.4127	-0.4127	-	0.5873	-	-	-
Lyshevskiy [66]	0.3	0.4	-0.5	-	0.5	0.4	0.3	-
Wakuri [67]	0.25	0.5	-0.447	-	0.5	0.197	-	-
Sitkei [68]	0.39	0.82	-0.35	-	0.48	-0.04	-0.3	-
Parks [69]	0.3	0.4	-0.4	0.6	0.6	-	-	-
Oz [70]	-	-	-0.369	-	0.5	-	-	-
Taylor and Walsham [71]	0.34	0.18	-0.32	-	0.64	-	-	0.18
Dent [63]	0.25	0.5	-0.25	0.25	0.5	-	-	-

To further understand this phenomenon, Hiroyasu and Arai [35] proposed a two-phase evolution of penetration in the 1990s, based on measurements conducted under ambient densities of up to 30 kg/m^3 and injection pressures of up to 80 MPa. The penetration was characterized by a linear dependence on time during the initial stage, which transitioned to a dependence on the square root of time in subsequent phases. The formulas can be written as:

$$S(t) = 0.39\sqrt{\frac{2\Delta P}{\rho_f}}t, 0 < t < t_{break}$$

$$S(t) = 2.95\left(\frac{\Delta P}{\rho_a}\right)^{1/4}\sqrt{d_0 t}, t \geq t_{break}$$

$$t_{break} = 28.65 \frac{\rho_f \cdot d_0}{(\rho_a \Delta P)^{1/2}} \tag{2.5}$$

Before the breakup time, t_{break}, the linear dependence on time is mainly caused by the transient nature of the initial injection rate. It is important to note that the empirical formulas discussed above are typically derived from the measurement under non-vaporizing conditions. Thus, the droplet size is larger than that observed under actual engine conditions. In certain instances, a correlation of the form $S \propto t^{3/2}$ may provide a more accurate prediction prior to the breakup time [72] [73]. What's more, empirical correlations derived from diesel may not be applicable for predicting the behavior of alternative fuels, such as biodiesel [74].

To address the impact of gas density and vaporization on spray penetration, especially under engine-like conditions, such as gas density exceeding 25 kg/m^3 at ambient temperature of 1000 K and injection pressure surpassing 100 MPa, Naber and Siebers conducted measurements on both non-vaporizing and vaporizing sprays under a wide range of conditions. They also provided a theoretical correlation for spray penetration. A similar trend was observed for both non-vaporizing and vaporizing sprays as gas density increased, with the maximum reduction in vaporizing penetration relative to non-vaporizing spray occurring at the location where fuel vaporization is complete. In [75], a scaling law for the free turbulent jet is further deduced on the basis of momentum conservation and is also validated by experimental results, allowing the penetration correlation for vaporizing spray to be expressed as follows:

$$S \propto \rho_a^{-0.25} \cdot \dot{M}^{0.25} \cdot tan^{-0.25}\left(\frac{\theta}{2}\right) \cdot t^{0.5} \tag{2.6}$$

where $\dot{M}$ is the fuel momentum, S is the spray penetration. Indicated by the measurements [60] [76], penetration is mainly governed by the momentum.

Spray angle

As stated in Eq. (2.6), the spray angle is a critical parameter that influences both penetration and entrainment mass. As shown in Figure 2.6, spray angle is a measure of the angle in the fitting lines extending from 10% to 60% of the penetration, where the spray is in a steady state [75]. The ranges of the fitting lines can also be scaled from the injector to 50% of the penetration. In the atomization regime, spray is assumed to be symmetrical in the radial direction; thus, spray angle was observed to follow the correlation [77],

$$tan\left(\frac{\theta}{2}\right) = \frac{1}{A} \cdot 4\pi \cdot \left(\frac{\rho_a}{\rho_f}\right)^{0.5} \frac{\sqrt{3}}{6} \tag{2.7}$$

The term A is a constant specific to a given nozzle geometry. However, the density ratio varies according to other research findings, the impact of breakup length is incorporated in the correlation proposed by Hiroyasu and Arai, in agreement with the two-step penetration correlation in Eq. (2.5). The new formulation is written as:

$$\theta = 83.5 \cdot \left(\frac{L_0}{d_0}\right)^{-0.22} \left(\frac{d_0}{d_s}\right)^{0.15} \left(\frac{\rho_a}{\rho_f}\right)^{0.26} \tag{2.8}$$

where L_0 is the orifice length, d_s is the sac chamber diameter of the nozzle, the other terms are the same as the explanation before. In conclusion, various measurements indicate that the spray angle can be significantly affected by the ratio of ambient to fuel density, ambient temperature and injector geometry. Additionally, while the influence of fuel properties may not be as pronounced as that of the aforementioned parameters, it remains a contributing factor [78]. However, turbulence and aerodynamic instabilities introduce considerable uncertainty in the spray angle measuring. Furthermore, discrepancies in optical techniques and image processing method also contribute to this error, making accurate measurement of the spray angle challenging.

Fuel mass fraction/mixture fraction

The mixing of fuel vapor with the surrounding oxidizer is the primary factor that governs the spray combustion in engines. The mixing properties can be characterized by a variable called mixture fraction, a conservative variable that is equal to the fuel mass fraction for inert sprays [18]. It has been known that the gradient of mixture fraction affects the scalar dissipation rate, which in turn affects the reaction rates in diffusion flame [38]. Therefore, quantitative mixing measurement is crucial to understand and improve the combustion process.

Generally, laser-based techniques are employed to obtain mixing characteristics. The widely used method for measuring diesel-like spray is Rayleigh Scattering [79] [80]. However, this technique is limited to the vaporized portion of the spray due to interference from scattering caused by liquid-phase droplets. Raman spectroscopy is another method that can also capture the liquid fraction of the fuel-air mixture, but it faces limitations such as low signal intensity and poor spatial resolution [81]. Planar laser-induced fluorescence (PLIF) with tracers is frequently utilized, although the fluorescence signal is affected by temperature, pressure, and gas composition [82] [83]. Recently, laser-induced breakdown spectroscopy has been proposed and is increasingly used in various flames to measure local composition of element [84] [85], then, the local mixture fraction can be derived using the classic definitions proposed by Bilger [86] and Peters [87].

In terms of the simulation results, a linear function of mixture fraction as the axial distance in the vaporized region is observed. Furthermore, self-similar profiles have been verified for a reasonable description of the radial distribution in the fully developed region [88]. However, it is important to account for the fuel phase near the nozzle, while it will make it more complex in phenomenological spray model, thus, a consideration that was overlooked.

2.3.4. Auto ignition

After the evaporation, the fuel vapor continues to mix with the surroundings, then the ignition takes place at a certain distance where the equivalence ratio is favorable. As discussed in Section 2.1, ignition in real engines is analyzed by means of heat release rate derived from the cylinder pressure evolution, and the ignition is characterized as the beginning of the rapid heat release. As shown in Figure 2.7, the pressure rise in a constant-volume vessel for typically single-hole orifice injectors is smaller than that in engine chambers and the measurement uncertainty also brings potential errors on the analysis of trend. The development of optical techniques facilities the measurement of ignition delay throughout luminosity intensity, while also allowing for the spatial resolution of species within the flame via laser-based techniques. Additionally, shadowgraph enables the analysis of spray profiles.

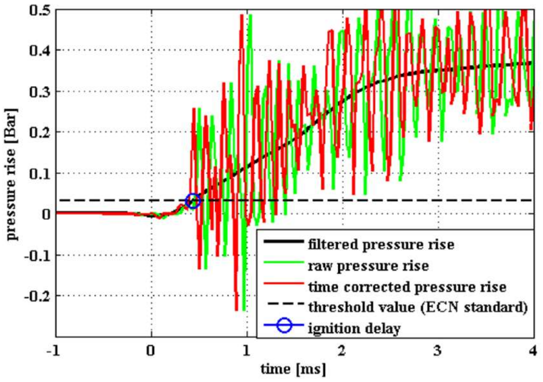

Figure 2.7. Pressure rise after ignition for Spray A in a constant volume vessel [89]

The numerous investigations suggest that the combustion process of liquid hydrocarbon fuel in conventional diesel engines undergoes a two-stage ignition process at specific temperatures and pressures. The first-stage ignition, also known as cool-flame chemistry, produces sufficient reactive fuel fragments with moderate heat release, which significantly influences the second-stage ignition timing. Higgins et al [90] proposed a typical overview of the auto-ignition concept, dividing the period from fuel ejection to ignition into three stages, which are summarized as follows:

- Physical induction period: this period encompasses the duration from the initiation of injection to the phase characterized by a simultaneous rise in pressure and chemiluminescence. During this phase, the ejected fuel undergoes atomization, entrainment, mixing with the surrounding hot air, and vaporization. This vaporization process induces a cooling effect on the gases in the liquid-phase fuel region of the spray, which impedes the ignition process. As hot air continues to penetrate and entrain, the mixing of vaporized fuel and hot air elevates the temperature of the gaseous fuel/air mixture in the non-vaporizing sections of the spray, facilitating the commencement of the initial ignition phase. Obtained from the measurement in [91], the first appearance of pressure rise at approximate 0.2 ms ASOI (After Start of Injection) in Figure 2.7 corresponds with the appearance of CH_2O PLIF signal detected near the liquid length at 0.23 ms ASOI in Figure 2.8. This is also the marker of the phase ending. However, the distinction between the physical induction period and the first stage of ignition is somewhat contingent upon the resolution of the diagnostics employed.

- First stage ignition period: The first stage ignition period extends from the time of initial detectable rise in pressure and chemiluminescence until the onset of rapid heat release, which signifies the commencement of second-stage ignition chemistry. During this period, the reaction quickly spreads downstream, as evidenced by the fully filled CH_2O at a low intensity extending from the liquid length to the spray head at 0.31 ms ASOI. Early in the first stage, chain-branching reactions consume fuel, producing radicals and releasing small quantities of energy that increase the temperature. Consequently, a 'softening' effect in Schlieren begins at the spherical near the field, where a narrower spray tip is observed compared to the inert spray [91] [92] [93]. As the temperature rises to the ambient level, the dissociation of intermediate products back to reactants begins, which reduces chain branching and effectively decreases the fuel consumption rate. The increased temperature further enhances the CH_2O formation, resulting in a higher percentage of intense CH_2O, which nearly fills the spray head. Concurrently, the diminished shadowgraph in the same region is also recognized as indicative of the ending of the first-stage ignition process.
- Second stage ignition period: the continuous entrainment of hot air and the heat release from the first-stage ignition increases the spray temperature until the chemistry dominated by the hydrogen peroxide dissociation reactions occurs, resulting in significant heat release. Similar to the phenomenon depicted in Figure 2.1, this heat release serves as a trigger for premixed combustion. From 0.39 ms ASOI to 0.49 ms ASOI, the area of the CH_2O signal remains constant, while the spray head in schlieren image returns to dark in the spray due to a much higher refractive index gradient and lower density. In the following frames shown in Figure 2.8, CH_2O undergoes oxidation in the high-temperature regions, initiating soot formation.

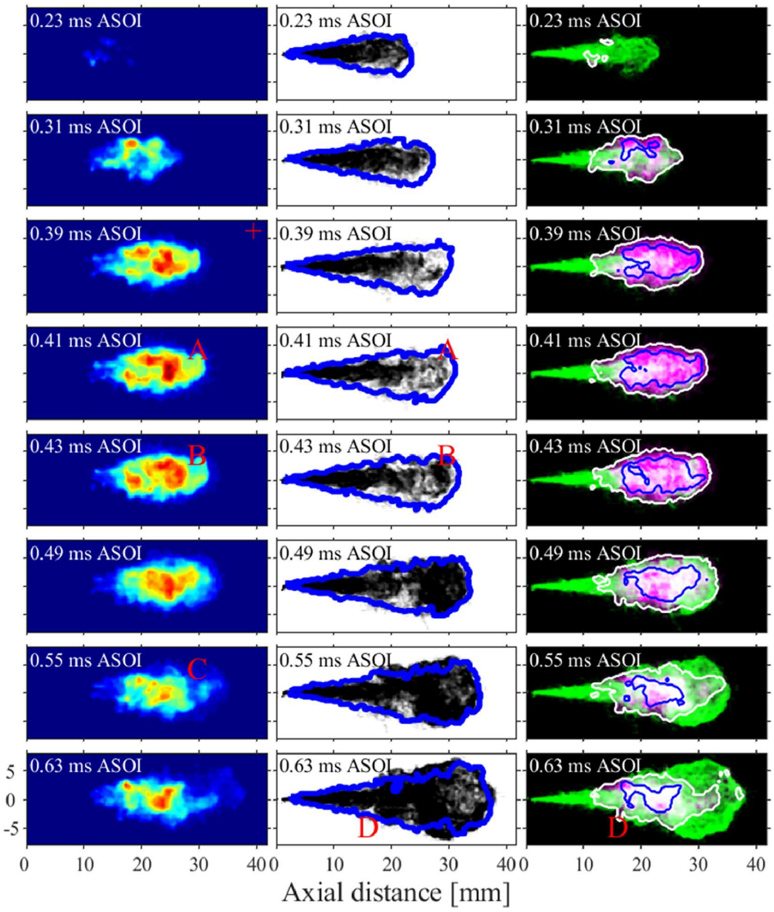

Figure 2.8. Temporal evolution of formaldehyde PLIF, Schlieren images of reacting spray and the imposed boundaries of inert spray in the middle column. In the right column, the boundaries of 10% (white lines) and 50% (blue lines) of the maximum CH_2O intensity (pink color) are superposed on the images of reacting spray shown in green color [91]. A, B , C, D represent different timings.

During the auto-ignition process of a reacting spray, the most critical parameter is the ignition delay, which mostly refers to the instant when low-temperature and high-temperature combustion begins. Adjustments made during the premixed combustion period helps to realize low-temperature combustion, which is advantageous for reducing emission and maintaining engine efficiency. Ignition delay (ID) for both cool and hot flames is directly related to combustion chemistry; hence, the correlation can be modeled using an Arrhenius type equation [22],

$$ID \propto exp\left(\frac{A}{T_a}\right) \cdot \rho_a^B \cdot \Delta P^C \cdot O_{2\%}^D \tag{2.9}$$

The terms of $\rho_a, T_a, \Delta P$ are the same as the ones in previous equations, $O_{2\%}$ is the oxygen concentration. The investigation into the different fuel types showed that not all the exponential coefficients will be considered [94]. Additionally, the variation in optical techniques (i.e., Schlieren, broadband chemiluminescence) employed to obtain ignition delay, results in slight differences in the fitting coefficients [22].

2.3.5. Mixing controlled combustion

After the peak heat release rate of the premixed combustion shown in Figure 2.1, the fuel-air mixture formed in the atomization and evaporation process has been consumed, and the flame is then sustained by the mixing of vaporized fuel with the surrounding, depending on the fuel injection momentum. Thus, the combustion occurring during this phase is named as mixing-controlled combustion, or diffusion flame. During this phase, the flame develops at the periphery of the fuel-rich, high-temperature downstream region of the jet. Before the end of injection, the spray jets exhibit a 'quasi-steady' state that the flame structure remains constant during this phase.

As shown in Figure 2.9, a conceptual model proposed by Dec is widely accepted to describe the mixing-controlled combustion process, encompassing liquid and vapor zones, fuel-air mixing, autoignition, reaction zones, and soot distributions. The diffusion flame extends starting from a certain distance downstream of the nozzle, named as lift-off length (LOL). The magnitude of LOL indicates the amount of air entrainment upstream of the combustion zone; thus, a longer LOL corresponds to a mixture with a lower equivalence ratio. In conventional diesel-like spray combustion modes, soot is formed in regions where the equivalence ratio (ϕ) over 2 [95], and the local equivalence ratio near the LOL is estimated in the range of 2 – 4 [61]. Previous measurement indicates that LOL exhibits a proportional relationship with ignition delay [94], and LOL is also influenced by the factors, such as ambient temperature, density, oxygen concentration, as well as the fuel properties [96]. The correlation of lift-off length as a parametric relationship was developed by Peters [87] and Siebers [96], written as

$$LOL \propto T_a^a \cdot \rho_a^b \cdot u_{th}^c \cdot O_{2\%}^d \qquad (2.10)$$

where u_{th} is the theoretical fuel velocity at the nozzle outlet, obtained as:

$$u_{th} = \sqrt{\frac{2\Delta P}{\rho_f}} \qquad (2.11)$$

It should be noted that the parameter will not exhibit the similar influence on both ID and LOL. For example, LOL is more sensitive to injection pressure compared to ID [97]. In some cases, Z_{st}, representing the stoichiometric mixture fraction is added in Eq. (2.10), accounting for the difference in fuel compositions compared to hydrocarbon fuels [98].

Downstream of lift-off length, the effect of cooling in the vaporization process generates a fuel-rich region where the local temperature is lower than the ambient temperature. Near the lift-off length, several intermediate reaction species (i.e., CH_2O, RO_2) are produced and subsequently consumed in the downstream, as indicated by the combined measurement of CH_2O/PAHs LIF [92]. The products of premixed combustion play a role of reactants in the subsequent diffusion flame. As the temperature increases, PAHs quickly formed in the rich region of the diffusion flame, where flame temperature is ~ 1600 K. Moreover, some emissions, such as carbon monoxide (CO) and unburned hydrocarbons (UHC) are also produced. Extending from the initial soot formation region near the premixed combustion zone, soot appears as small particles, thereafter, soot concentration and particle size increase as the spray travels downstream. Ultimately, the highest concentration and the biggest particles occur at the spray head. Towards the flame periphery, a high concentration of OH radial [99] oxidizes the soot particles. Beyond this zone, the high flame temperature and the availability of oxygen create an almost ideal environment for thermal NO production. Shown in this conceptual model, high NO production rates via the thermal mechanism are expected to occur only around the jet periphery on the lean side of the diffusion flame, where is also favorable to the production of CO_2 and H_2O in complete combustion.

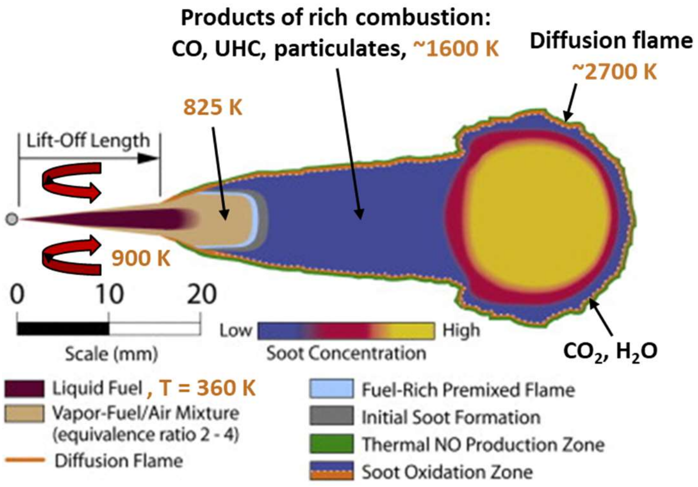

Figure 2.9. Schematic of Dec's conceptual model for conventional direct-injection diesel combustion during mixing-controlled combustion phase [29].

To meet the stricter limitations on pollutant emissions, especially in soot particles and nitrogen oxides, low temperature combustion modes and alternative fuels are increasingly favored for heavy-duty engines. The use of a smaller-orifice nozzle for the injection event, along with earlier injections within an exhaust gas recirculation environment, is preferred to facilitate low-temperature combustion. In contrast to conventional diesel combustion (CDC), the zone of liquid fuel is larger under low-temperature combustion mode, and the conical jet obtained in CDC is indistinguishable. In addition, the longer LOL also causes reduced soot formation at a further distance, with soot primarily forming only in the head vortex. Methanol is usually adopted in marine engines, Kaario et al [100] illustrated the flame structure of methanol as weak combustion in terms of low CH_2O formation in the premixed combustion, and the lean combustion in the spray head also results in a low flame temperature compared to n-dodecane, a surrogate of diesel. Xuan et al [101] explored the difference of ignition process between n-dodecane and polyoxymethylene dimethyl ether 3 (PODE3) and summarized conceptual models under 800 K and 900 K. A narrower high-temperature OH flame is observed at PODE3 due to the high oxygen content, and there is no two-lobes OH structure for the low-temperature case. Furthermore, no PAHS and soot can be found for PODE3 flames. The position of PAH/soot is replaced by CO and HCO within PODE3, which are surrounded by OH radicals. At 800 K, PODE3 shows a greater potential for soot reduction, resulting from a much longer LOL compared to n-dodecane.

2.4 Principles of phenomenological/low dimensional spray models

To aid in the fundamental understanding of the combustion process with alternative fuels under engine-like conditions, both experimental and numerical tools are utilized. The former is usually employed in optical access facilities, where the spray and combustion process are accessible by means of optical technique. Consequently, combustion metrics such as ignition delay, lift-off length, spatial resolution of species, soot formation, and heat release can be accurately obtained.

As for numerical tools, the complexity of model description classifies the tools into three types: *thermodynamic model* shows the lowest computational cost while the accuracy is limited by the ignition behavior of engines; *CFD models* can provide highly detailed predictions to such complex processes, while the computational cost is also high, and it also has the requirements on the users. As a balance of computational cost and calculation accuracy, phenomenological or low-dimensional models stay in this space. Further discussion of these three-type tools is shown in the following.

Thermodynamic models

The principle is based on the first law of thermodynamics and mass balance, while also considering momentum conservation and spatial variations in composition and thermodynamic properties. Upon the intrinsic characteristics of the combustion process, the chamber is divided into one or more homogeneous mixing zones [102]

[103] [104]. Consequently, this model is referred to as a zero-dimensional (0D) model. Typically, this model is adopted to calculate the heat release process, in conjunction with experimental data obtained from pressure-based combustion diagnostics. Concerning the computational cost, this model is the least expensive while the predicted results are also somewhat limited.

Computational Fluid Dynamics models

The simulation of a multi-phase turbulent flow is to find the solutions of Navier-Stokes equations based on different hypotheses. Direct Numerical Simulation (DNS) is a tool that solves these equations without employing any turbulence models, thereby, the entire range of spatial and temporal scales of turbulence must be obtained. This approach yields the most accurate prediction, while it can only be implemented by advanced users managing high performance computing. Large-Eddy Simulation (LES) simplifies calculation by modelling the smallest turbulence scales. Compared to DNS, LES significantly saves computational cost, although it is less effective in modelling in-nozzle flow and near-field spray. Reynolds-Averaged Navier-Stokes simulation (RANS) models all the turbulence scales, and it decomposes an instantaneous quantity into a time-averaged and fluctuating quantities. The accuracy depends a lot on the adopted turbulence model. Relatively to LES, RANS can further reduce the computational cost, while it is still expensive for a wide application.

In turbulent spray modeling, the Lagrangian-discrete droplet method (DDM), which represents the spray as a collection of individual fuel droplets with uniform properties, and the Eulerian approach, which treats the spray as a continuous flow, are commonly utilized in CFD studies. DDM demonstrates a notable drawback in the near-field modelling, where the liquid droplet size may be larger than the cell size. However, the format of partial-differential equations in Eulerian approach makes itself expensive in the calculation. Comparisons between DDM and the Eulerian method in spray modeling indicate that DDM is less effective in predicting liquid length and mixture fraction in the near field [105]. The common solution is to combine Lagrangian and Eulerian method, which takes the advantage of computational efficiency of Lagrangian in the far-field simulation and the accuracy using Eulerian in the near-field simulation [106] [107]. However, CFD requires a significant level of expertise from the user, and the calculation is more performed in workstations or super computers.

Phenomenological/Low-dimensional models

This model is a balanced solution of both requirement of accuracy and computational cost. It does not aim to predict the intricate details of all sub-processes; instead, it only focuses on a few particular quantitative parameters, such as liquid length, spray vapor penetration, ignition delay, lift-off length, heat release rate and pollutant emissions. The derivation of these parameters involves a compromise in accuracy through 'acceptable' simplifications, indicating that the results are inherently non-exact. Nevertheless, they preserve most of the essential physics required to predict these parameters with a significant degree of accuracy. Similar to the spray models used in CFD, phenomenological models can also be categorized into Lagrangian and Eulerian approach. Since the mixing-controlled hypothesis is valid on a developed jet, thus, the combination of CFD with phenomenological spray can improve the accuracy in the prediction to the near-field spray while maintaining the low computational cost [108]. It is important to note that phenomenological models lack a comprehensive description of the turbulent flow field; therefore, they are more suitable for diesel engines, where combustion is primarily mixing-controlled.

2.4.1. Lagrangian models

Lagrangian approach discretizes the spray region into a number of individual droplets or parcels, which travel through time and space along distinct trajectories. As a grid-dependent approach, the cell size must be much larger than the droplet size. Starting from a multi-zone model based on a mathematical model for droplet evaporation, Hiroyasu et al [109] developed it by adding equations for spray penetration. This allows the fuel-air conditions in each zone to be described as one-dimensional flow, instead of homogeneous flow. Therefore, this approach facilitates both temporal and spatial solutions for spray distribution, burning rate, pressure, local temperature and gas composition.

The schematic of this lagrangian spray model is shown in Figure 2.10, where the spray is divided into numerous small packages by an insight of concentric circles from the view of the fuel stream side. Each package is assumed to independently undergo the processes of evaporation, entrainment, and ignition. From the onset of injections, the spray released in small increments of time is partitioned into small packages, each containing an equal mass of fuel, with no interactions among them, such as heat and mass transfer.

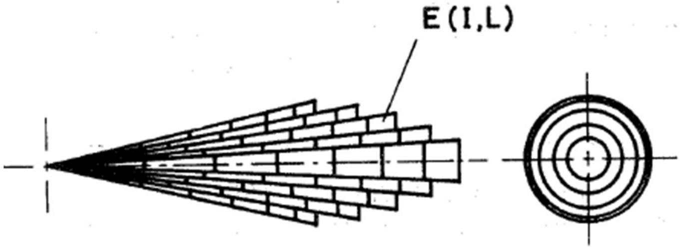

Figure 2.10. Diagram of packages division in spray region proposed by Hiroyasu et al [109].

To describe the spray and combustion process, the following sub models are introduced in the Hiroyasu-type model. First, spray penetration follows the empirical two-portion penetration shown in Eq. (2.5). Thus, the penetration at the Lth package along the radial direction can be described as

$$S_L = S \cdot exp\left(-8.557 \times 10^{-3} \cdot (L-1)^2\right) \tag{2.12}$$

What's more, the effect of swirling is in conjunction with the spray by a coefficient C_S,

$$S_S = C_S \cdot S$$

$$C_S = \left(1 + \frac{\pi r_S n S}{30 u_0}\right)^{-1} \tag{2.13}$$

Thereby, the swirl spray penetration S_S can be calculated if the swirl ratio r_S, engine speed n, and spray initial velocity u_0 are known.

Second, the air entrainment is based on the conservation of momentum, thus, the entrained air mass for each package can be written as:

$$m_f \cdot u_0 = \left(m_f + m_a\right) \cdot u \tag{2.14}$$

Third, evaporation for each package is expressed to start immediately after the fuel ejection, the evaporation is described as the single droplet evaporation together with the number of droplets. Thus, the heat transfer is also the sum of the heat transfer of all the droplets.

Four, combustion rate and amount of burning fuel of each package are calculated by assuming the stoichiometric condition.

It must be mentioned that these correlations were generated by the experiments before the appearance of high-pressure common rail injection system, and the injection pressure is no more than 70 MPa. Thus, the effect of droplet atomization and collision process needs to be considered. Jung et al [103] modified the breakup time in the spray penetration model proposed by Hiroyasu et al. and included a radiative heat transfer model, then achieved a good prediction to heat release rate and engine performance with high fidelity [110]. Poetsch et al [111] introduced the separation of burned combustion zones, which are partly re-entrained to the zones with active chemical reactions. Meanwhile, the effect of zone number is also discussed.

2.4.2. Eulerian models

Eulerian approach treats the diesel-like spray as a continuous flow. In modern diesel engines, the high ambient pressure in the combustion chamber diminishes the impact of fuel atomization on subsequent physical processes. Consequently, turbulent mixing emerges as the dominant factor, rendering the dynamics of individual droplet dynamics relatively insignificant; thus, the vaporization is also regarded as a mixing-controlled process. Beyond the near-nozzle regions, gas theory is applicable for describing the spray characteristics. In addition, the high injection pressure facilitates the formation of finer droplets, thereby further mitigating the significance of droplet dynamics. Depending on the injection rate, spray model based on Eulerian approach can be classified as steady solution where the injection rate is constant and unsteady solution where the injection rate is changed as the time evolution. The details of these two solutions are presented in the following.

Steady solution

Naber et al. proposed a correlation using integral control surface techniques and validated it against measured spray penetration under non-vaporizing conditions, covering a wide range of gas density, injection pressure and orifice diameter, and vaporizing conditions at gas temperature up to 1000 K. The schematic of the spray model is shown in Figure 2.11. Starting from the original point inside the nozzle, the spray is described as a symmetrically triangle profile. Compared to the realistic spray shape shown in Figure 2.6, the region starting from the nozzle to the distance where is approximately 70% of the total penetration can be seen as a conical shape, also named as steady region, while the spray head shown as an elliptical shape, called as transient region. With a primary focus on penetration, the research concentrated on the steady region. Consequently, this triangular spray profile aligns with the findings of [112] [113].

The calculation domain is discretized as a number of cells along the axial direction. For this injection, the spray can be assumed to be incompressible or isothermal, neglecting compressible flow effects near the nozzle outlet. The main hypothesis for this spray model can be listed as:

- Velocity profile along the radial direction: a uniform velocity is assumed in [61] for a primary derivation to the spray propagation speed. In fact, the radial velocity matches well with a Gaussian distribution throughout the optical measurements [114]. Then, this phenomenon is adopted in the following models [33] [112].
- Constant injection rate: injection velocity is constant across the injection process. The 'ramp up' period is removed, and the injection rate reaches the maximum immediately after the fuel ejection.
- No velocity slip between fuel and entrained air: single-phase flow is assumed in this spray model. Thus, there are no droplets in the assumption, hence, the velocity slip can be seen as zero. In addition, it can also help to reduce the complexity of mathematical analysis.
- Quasi-steady flow with a uniform growth rate: constant spray angle ($\alpha/2$ for half spray) is assigned, and there is no difference between near- and far-field. For a constant injection rate, constant spray angle is also evidenced to be effective in the spray penetration [115].

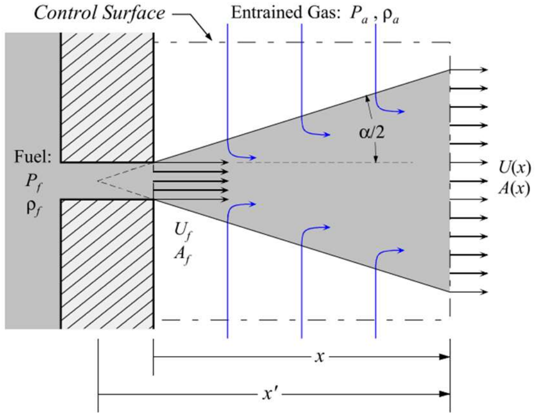

Figure 2.11. Schematic of spray model for penetration correlation in [61]

As mentioned previously, vapor spray is driven by the fuel momentum. In a control volume with starting from the nozzle orifice until an axial distance of x, the conservation of fuel mass and momentum on the control surface can be written as,

$$\rho_f \cdot A_f(0) \cdot u_f = \rho_f \cdot A(x) \cdot u(x)$$

$$\rho_f \cdot A_f(0) \cdot u_f^2 = (\rho_f \cdot A_f(x) + \rho_a \cdot A_a(x)) \cdot u^2(x) \tag{2.15}$$

The nozzle outlet, also seen as the inlet of the control volume, $A_f(0)$ is the cross-sectional area of the fuel at the nozzle outlet, u_f is the fuel velocity. $A(x)$ and $u(x)$ are the corresponding variables at the outlet of the control volume. The constant spray angle amplifies the area with a function of spray penetration, in contrast to the inverse function of velocity with distance. Meanwhile, the entrained air shares the momentum by defining the cross-sectional area of the jet at x occupied by air as,

$$A_a(x) = A(x) - m \cdot A_f(x) \tag{2.16}$$

where m is a parameter with a value from 0 – 1. Thus, the velocity at the outlet $u(x)$ can be written as:

$$u(x) = \frac{u_f}{2} \cdot \frac{A_f(0)}{A(x)} \cdot \left(\frac{\rho_f}{\rho_a} - m\right) \cdot \left(\sqrt{1 + 4 \cdot \frac{\frac{A(x)}{A_f(0)} \cdot \frac{\rho_f}{\rho_a}}{\left(\frac{\rho_f}{\rho_a} - m\right)^2}} - 1\right) \tag{2.17}$$

Assuming that $u(x)$ is equal to the velocity of the spray tip, and integrating the $u(x)$ from nozzle to the distance x, spray penetration can be written as,

$$S = t / \left(1 + t^{\frac{n}{2}}\right)^{1/n} \tag{2.18}$$

Finally, this correlation shows the linear time-dependent function in the near-nozzle region, and a square root time-dependent function for large distance.

Unsteady solution

For a transient injection, the injection velocity varies with time, making it difficult to accurately predict the jet dynamics using an analytical solution [61]. To address this limitation, an approach that discretizes the spray domain into a set of control volumes has been adopted. Musculus and Kattke [33] and Pastor et al. [18] have both utilized this concept, referred to as the SNL model and CMT model, respectively. The prior one primarily focuses on penetration prediction after the end of injection, and the later one is on the penetration during the initial and quasi-steady stages. To be consistent with the description in the steady solution, the discussion in unsteady solution will also start with the model description proposed by Musculus and Kattke. Then, the difference between [33] and [18] will be highlighted. In this thesis, the model development is based on the model established in [18], with further details presented in Chapter 3.

To describe the transient spray behavior, some other hypotheses are proposed apart from the terms mentioned in [61]:

- Non-vaporizing jet theory: single-phase transient gas jet has been evidenced to well predict the penetration of vaporized spray [116] [117], hence, the non-vaporizing jet theory is remained in the transient solution to reduce the model complexity in fuel evaporation process.
- Turbulent/molecular viscous forces in control volumes are neglected.
- The molecular and turbulent diffusion on axial momentum is ignored, only with axial convection is taken into account.
- The net force due to any axial pressure gradient is assumed negligible.

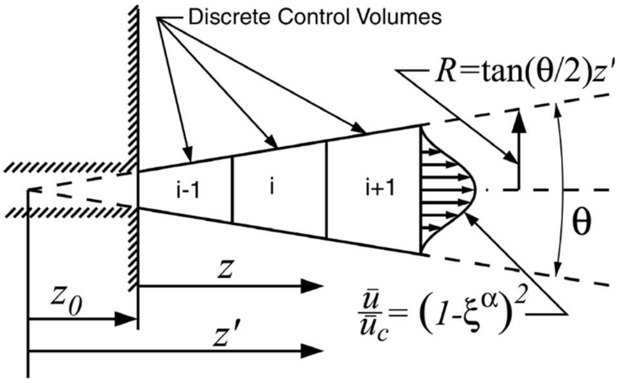

Figure 2.12. Schematic of one-dimensional spray model with discretized control volumes [33]

For a transient injection, the transport equation of fuel mass m_f and axial momentum M will be solved in each individual control volume, as shown in Figure 2.12. The steady equations in Eq. (2.15) can be rewritten for a single cell as:

$$\frac{\Delta}{\Delta t}\left[\int \rho_f u f dA\right] = \dot{m}_{f,in} - \dot{m}_{f,out}$$

$$\frac{\Delta}{\Delta t}\left[\int \rho u^2 dA\right] = \dot{M}_{in} - \dot{M}_{out} \tag{2.19}$$

ρ_f is the liquid fuel density, ρ and u are the turbulent mean density and velocity, respectively. The section of the inlet and outlet is assumed as a round, thus, the area dA is written as $dA = \pi\left(tan\left(\frac{\theta}{2}\right)z'\right)^2$, which is a function of the distance z' from the virtual jet origin. By the way, it brings the question of how to define the spray angle θ. As mentioned in [61], spray angle can be achieved as a function of the ratio of air density to fuel density, or, it is an input assigned by the user [18].

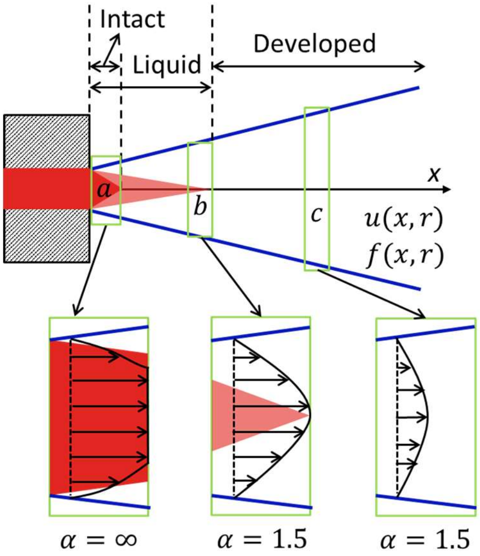

Figure 2.13. Schematic of radial distribution of velocity and mixture fraction in Musculus et al. [33]

In [33], a cross-sectional averaged solution of velocity and mixture fraction are obtained by solving the conservation of fuel mass and momentum. Proposed by Abramovich [118], the radial profile of velocity and mixture fraction can be written as:

$$\frac{u(x,r)}{u_{cl}(x)} = \frac{f(x,r)}{f_{cl}(x)} = \left(1 - \left(\frac{r}{R}\right)^{\alpha}\right)^2 \tag{2.20}$$

where r/R represents the normalized location along the radial direction, and the same profiles are assumed for radial velocity and mixture fraction. As mentioned before, the research on spray penetration focuses on the steady-state region. Displayed in Figure 2.13, as the spray penetrates, the exponent α evolves from a uniform shape ($\alpha = \infty$) in the intact area (~ 1-3 times of the nozzle diameter) to a Gaussian distribution (very similar to a value of $\alpha = 1.5$). In the intact region (a), the on-axis velocity/mixture fraction is assumed to be the same as the value at the exit, and the radial profile is close to a uniform distribution. However, in a liquid-vapor equilibrium region (b), the radial distribution is also assumed to match a Gaussian distribution, although the measurement is limited in this area. In the developed region (c), the vapor spray has been evidenced to fit well with the Gaussian distribution by the measurement [79] [114].

Since the solution of the momentum and mass flow conservation is for cross-sectionally averaged value, denoted as the 'overline' operator $\overline{\quad}$, the relation with the on-axis quantities can be written as:

$$\bar{f} = \frac{\alpha^2}{(\alpha+1)(\alpha+2)} \cdot f_{cl}$$

$$\bar{u} = \frac{\alpha^2}{(\alpha+1)(\alpha+2)} \cdot u_{cl} \tag{2.21}$$

Then, the integral fuel mass flux $\dot{m}_f$ and integral momentum flux $\dot{M}$ in Eq. (2.19) can be rewritten as:

$$\dot{m}_f = \rho_f \int f u \, dA = \rho_f \beta \bar{f} \bar{u} A$$

$$\dot{M} = \int \rho u^2 \, dA = \bar{\rho} \beta \bar{u}^2 A \tag{2.22}$$

and β is written as:

$$\beta = \frac{6(\alpha+1)(\alpha+2)}{(3\alpha+2)(2\alpha+1)} \tag{2.23}$$

and the value ranges from $\beta = 1$ in the near nozzle region (intact core, $\alpha = \infty$) to $\beta = 2$ in the developed region ($\alpha = 1.5$). The cross-sectional averaged density $\bar{\rho}$ in Eq. (2.22) can be simplified to the isothermal mixture of fuel and ambient surroundings:

$$\bar{\rho} = \rho_f \bar{f} + \rho_a (1 - \bar{f}) \tag{2.24}$$

Finally, the cross-sectional averaged velocity and mixture fraction can be obtained by solving the discretized equations using upwind differencing scheme,

$$m_{f,i}^{t+1} = m_{f,i}^{t} + \rho_f \left[\left(\beta \bar{f} \bar{u} A \right)_{i-1}^{t} - \left(\beta \bar{f} \bar{u} A \right)_{i}^{t} \right] \Delta t$$

$$M_{f,i}^{t+1} = M_{f,i}^{t} + \left[\left(\beta \bar{f} \bar{u}^2 A \right)_{i-1}^{t} - \left(\beta \bar{f} \bar{u}^2 A \right)_{i}^{t} \right] \Delta t \tag{2.25}$$

The spray model proposed by Pastor et al [18] aims to obtain the on-axis quantities by solving the conservations along the spray axis, while the radial distribution of velocity and mixture fraction admits another type, written as:

$$\frac{u(x,r)}{u_{cl}(x)} = \left[\frac{f(x,r)}{f_{cl}(x)}\right]^{1/Sc} = exp\left[-k\left(\frac{r}{R}\right)^2\right] \tag{2.26}$$

where k is the constant coefficient equals to $k = \ln{(100)}$ so that the radial limit is set where the local velocity equals to 1% of the value on the axis. Sc is the Schmidt number. The comparison of both normalizing functions for the Abramovich radial profiles used in SNL model [33] and the Gaussian one used in the CMT model [18] is shown in Figure 2.14, with a small discrepancy observed at the range of r/R = 0.2 – 0.8.

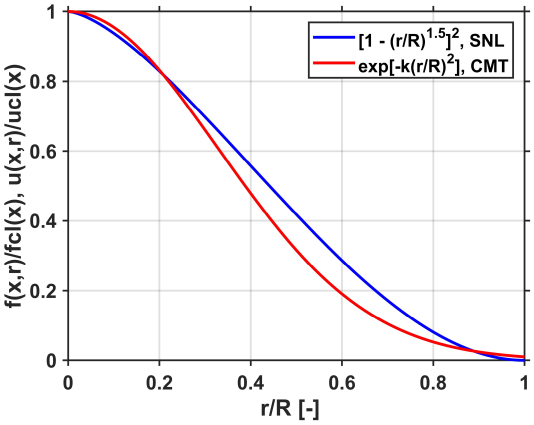

Figure 2.14. Comparison of Gaussion distribution using the normalizing functions in SNL model [33] and CMT model [18]

Mixing-controlled vaporizing spray

With the model description in types of steady and unsteady solution, 1D spray model can predict spray penetration under the conditions of non-vaporizing/vaporizing sprays or play a role of sub-model along injection process in engine cycles [119]. However, the evaporation process can only be characterized by the phase variation, without the details of spray droplets.

In the steady solution, due to the basic assumption of single-phase flow, liquid length was achieved at the axial position where the liquid, vapor, and entrained gas reaching a thermodynamic equilibrium, i.e. same temperature for the three terms. The mixture fraction at this position is also named evaporation mixture fraction. Besides, the following thermodynamic assumptions at the liquid length are added to simplify the heat transfer between the liquid fuel and surrounding air during the vaporization process [56],

- Vapor phase fuel is at a saturated condition
- Idealized phase equilibrium assumptions (i.e., Raoult's and Dalton's rules) is applied
- Ambient gas solubility in liquid phase can be ignored
- The recovery of kinetic energy in the fuel vaporization region of the spray is neglected.

Indicated in Eq. (2.2) – (2.3), an accurate calculation for $Y_{f,evap}$ from enthalpy balance is necessary to obtain a reasonable liquid length. The $Y_{f,evap}$ derivation follows the ideal gas law in SNL model. In addition, the value of β was assessed by Xu et al. [120], a conclusion that $\beta = 1.8$ is the optimal one after the matching on measurements in [53]. In CMT model, non-ideal gas law was adopted to calculate the thermodynamic properties [121].

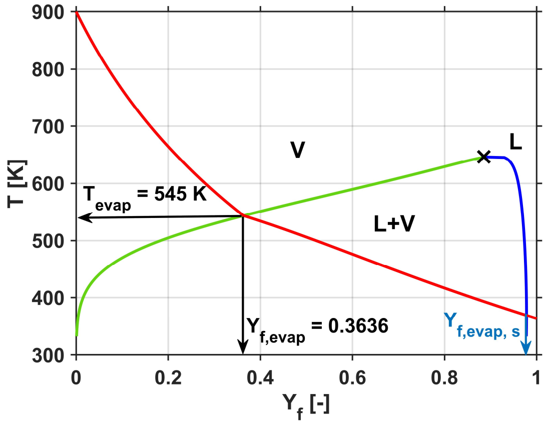

Figure 2.15. Dew (green line) and bubble (blue line) curves along with temperature evolution (red line) for n-dodecane into an ambient of 15%O2 + 85%N2 at $\rho = 22.8\ kg/m3, T_{f,0} = 363\ K\ and T_{a,\infty} = 900\ K$.

Figure 2.15 presents an example of the state relationships for a pure liquid n-dodecane spray injected into an ambient composed of 15%O2 and 85%N2. In the field of temperature T versus fuel mass fraction Y_f, the liquid fuel evaporation can be characterized by two regions. The first region is the liquid-vapor equilibrium. When the fuel ejected into the ambient at 363 K, it can only remain in the liquid state within a limited range where $Y_f > Y_{f,evap,s}$, which lies on the bubble line. As more ambient gas is entrained into the spray, the mixture temperature continues to rise, although it remains below the saturation conditions defined by the dew and bubble lines. The spray maintains its liquid-vapor equilibrium until the mixture temperature reaches T_{evap} and the fuel mass fraction in the mixture increases to $Y_{f,evap}$. Once $Y_f < Y_{f,evap}$, the liquid fuel vaporization was completed, marking the second region where the spray is entirely in the vapor phase. The increase in mixture temperature is also faster due to the disappearance of the latent heat process. Finally, $Y_{f,evap} = 0.3636$ is used to determine the liquid length in spray model under this ambient condition. It should be noted that the calculation to $Y_{f,evap}$ only relies on the inputs of ambient conditions, hence, the value can be obtained prior to solving fuel mass and momentum conservation. Furthermore, Pastor et al [19]. extended this state relationship to multi-component fuels, achieving similar evaporative behavior to experimental measurements. Consequently, the spray model successfully predicted liquid length by tuning the spray angle [79] [122].

2.5 Phenomenological/Low-dimensional models on spray combustion

As previously discussed, phenomenological spray models utilized for inert spray are usually for the prediction of liquid- and vapor- penetration, and the spatial distribution of velocity and mixture fraction. Together with chemical kinetics, it can also be used for reacting spray simulation. In light of various application scenarios, the discussion will be presented in the following sections: parametric scaling under steady engine-like conditions, mixing characteristics under transient engine conditions, non-free spray/wall impingement spray, and the reacting spray as a final section.

2.5.1. Analysis under steady ambient conditions

Spray vapor penetration has been validated to be primarily influenced by the following parameters: injection properties (i.e., nozzle diameter, injection rate), ambient conditions (i.e., pressure, density, temperature), and fuel types (i.e., biodiesel, oxygenated fuels). To gain a deeper understanding of the behavior of spray and the subsequent ignition in the experimental measurement, phenomenological spray model is usually utilized to validate the penetration so as to assess the effects of these parameters on the penetration and mixing field. To eliminate the interference of turbulence, the measurement was usually carried out in a constant volume/pressure combustion vessel.

Good prediction of spray penetration is a prerequisite for obtaining the mixture fraction field. In the context of a transient injection event, it is essential to accurately predict the spray penetration in the initial stage and after EOI, which corresponds to the ramp up and ramp down in the injection rate. Referring to ECN Spray A nozzle, using a simplified 'top hat' rate of injection (ROI) in 1D spray model can yield a good match for the penetration of a fully developed jet by adjusting the spray angle [123]. However, achieving a match during the initial stage requires the use of a variable ROI and variable spray angles, with smaller values in the near field and larger values in the far field [122]. However, the uncertainties in measuring the spray angle in the near field may still lead to discrepancies in the initial spray penetration [124]. Concerning the validation of spray penetration after EOI, several new hypotheses were proposed to describe the spray evolution [33]:

- Spray angle remains constant at the same value as that of the steady jet.
- The radial profile of mean axial velocity remains unchanged.

Following this assumption, a relatively good match in flow velocity after EOI was obtained for ECN Spray A at two ambient densities and injection pressures [124], supported by the ROI by [125]. After EOI, the entrainment rate was observed to increase by a factor of three, and the region of increased entrainment travels downstream through the jet after EOI at twice the initial jet penetration. This enhancement in mixing leads to a more fuel-lean mixture than a steady jet, which accounts for the observed increase in unburned hydrocarbons [126], the enhanced soot oxidation rate after EOI [33] [127], and the improved fuel evaporation [128].

Injection properties

The spray characteristics under various injection conditions have been investigated concerning injector design (i.e., nozzle geometry, inner structure) and injection strategies (i.e., injection pressure, multiple injections).

In comparing ECN Spray C and Spray D, which differ in k-factor and cavitation preference, Zhang et al [129] found that air entrainment in the injected spray is enhanced in Spray C (k-factor = 0) with this difference being more significant at low injection pressures. Westlye et al [130] contributed additional insight on simulated cavitation using LES and stoichiometry surfaces from SNL spray model, concluding that variations in spray angle in the far field affect the liquid penetration and lift-off length. Pastor et al [131] further analyzed the comparison of these two injectors by examining ignition delay and lift-off length across different ambient temperatures, injection pressures and oxygen concentrations. They noted that the similar mixing fields obtained from CMT spray model account for the analogous ignition sequences. Beyond the conditions in Naber-Siebers empirical spray model, Fitzgerald et al [132] extended the injection pressure up to 250 MPa, ambient density up to 52 kg/m^3, and nozzle diameters from 137 to 353 μm, demonstrating that SNL spray model provides accurate predictions for vapor penetration.

Pastor et al. [133] employed CMT spray model to analyze a pilot-main injection event in an optical single-cylinder engine. Their findings indicate that both liquid and vapor penetration can be accurately predicted, as well as the interactions between the injection pulses. Desantes et al. [134] explored the mixing process of a two-pulse injection under non-reacting conditions and found a good correlation between the penetration of the second pulse as predicted by spray model and the experiments. The observed faster penetration of the second pulse is attributed to the ‘slip stream’ effect. With a proper dwell between two successive injections (0.5 ms – 0.5 ms – 0.5 ms), the spray of the second pulse propagates at twice the velocity of the first pulse until the end of injection [115], which is consistent with the entrainment wave theory [33].

To further reduce computational cost, Liu. et al [135] [136] developed a 0D spray model based on the ‘entrainment wave’ theory, wherein only the velocity at the spray tip will be solved by the ratio of momentum flux to fuel mass flux. Moreover, an incremental spray volume is introduced to account for the broader spray after EOI.

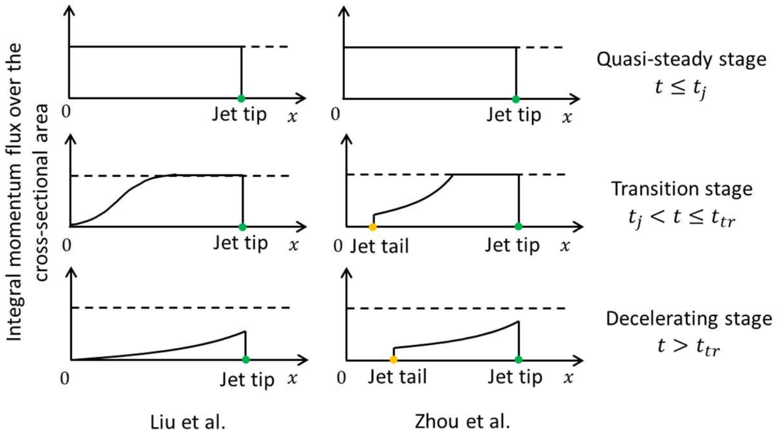

Figure 2.16. Schematic of the integral momentum flux over the cross-sectional area characterized as three stages along the spray evolution process. Left: initially proposed by Liu et al. Right: developed by Zhou et al. t_j: injection duration. t_{tr}: transition time, usually equals to 2 * t_j.

As shown in Figure 2.16, the spray evolution was treated as three stages. A constant injection rate was assumed in the steady jet. In the first stage after EOI, the fuel momentum near the jet tip remains consistent with that of the steady jet, and the flow velocity exhibits similar characteristics as the steady jet, this stage is called transition stage. The duration of this stage typically equals the injection duration. When the entrainment wave front arrives at the jet tip, the reduced fuel momentum in the jet tip starts to decelerate flow propagation. Measurements from water injection [137] and small-quality injection [138] confirm that the spray penetration transitions from a square root time dependence to fourth root time dependence [112]. Consequently, the empirical formula for jet tips can be expressed as follows,

$$S_{tip} = \left(\frac{c_d \beta \rho_f}{\rho_a}\right)^{1/4} \cdot \left(\frac{u_j d_0}{tan\left(\frac{\theta}{2}\right)}\right)^{\frac{1}{2}} \cdot t^{\frac{1}{2}} \qquad 0 \le t < t_{tr}$$

$$S_{tip} = \left(\frac{c_d \beta \rho_f}{\rho_a}\right)^{1/4} \cdot \left(\frac{2u_j d_0}{tan\left(\frac{\theta}{2}\right)}\right)^{\frac{1}{2}} \cdot t^{\frac{1}{4}} \cdot \left(t - t_j\right)^{\frac{1}{4}} \qquad t > t_{tr} \tag{2.27}$$

where c_d is the discharge coefficient, u_j is the effective velocity, defined as the ratio of momentum flux M_j to mass flux $\dot{m}_j$. A strong agreement with the simulated results from Musculus and Kattke's model obtained in [136], then the model validation was extended to the conditions of injection quantity and injection pressure at a triangular injection rate [139]. Building upon Liu's model, Zhou et al. [140] introduced a variable to characterize the space from the nozzle to the jet tail, which was concluded to be square root time dependent. The position of the jet tip remains consistent with Liu's model, while the accuracy of the prediction for the area-averaged equivalence ratio is expected to improve.

Fuel types

Over the past few decades, the performance of numerous types of fuels has been examined in the application of compression ignition engines. The fundamental characteristics of the spray and combustion processes under varied diesel-like conditions also garnered attention. In addition to diesel and gasoline, alternative fuels such as biodiesel, oxygenated fuels, and even zero-carbon fuels have been used. Compared to conventional diesel, the use of pure biodiesel, oxygenated fuels, or blends with diesel in diesel engines has been found to significantly reduce emissions of UHC, CO and particular matter (PM), while an increase in NOx and fuel consumption was observed [28] [141] [142] [143].

In terms of physical fuel properties, the change in fuel density was found to have a minimal effect on vapor penetration for both non-reacting spray and reacting spray prior to ignition, indicating similar air entrainment among the sprays with the various fuels. However, a similar distribution of mixture fraction does not imply a similar distribution of equivalence ratio. For diesel and gasoline, the main components are alkanes, hence, the spatial distribution of equivalence ratio is also comparable among fuels when considering a surrogate fuel in a 1D spray model, where n-Hexadecane represents diesel and n-Heptane represents gasoline [76]. A similar behavior was also observed in the comparison between biodiesel and diesel [144]. When oxygenated fuels are compared with regular hydrocarbons, the increase in fuel oxygen content leads to a decrease in stoichiometric air-fuel ratio, and hence the equivalence ratio field is moved closer to the nozzle outlet [145].

Thanks to the similar equivalence ratio field among alkane fuels, the ignition quality of synthetic fuels can be attributed to differences in their chemical properties, such as cetane number [146]. Meanwhile, the reduced equivalence ratio along the axial direction, resulted from the oxygen content in biodiesel, explains the reduced soot formation downstream when its cetane number is comparable to that of diesel [147]. Furthermore, the spatial distribution of equivalence ratio predicted by spray model has been utilized to understand the subsequent soot formation process of oxygenated fuels [101] [148], including the fuel that blending with diesel [74] [149].

Concerning the effect of fuel properties on liquid length, indicated in Eq. (2.2), the properties like fuel density and boiling point have been verified to be effective on the fuel evaporation [60]. Recently, the inert liquid and vapor penetration of ammonia was effectively captured by SNL and CMT spray model, although some discrepancies remain in the initial penetration [150] [151]. This indicates that the developed jet of ammonia is also subject to mixing control.

2.5.2. Analysis under transient ambient conditions

With transient ambient boundaries (pressure, density/temperature in engine chamber), phenomenological spray model is primarily utilized to provide the mixing characteristics for an understanding of the combustion process and pollutant emission obtained in engine experiments, particularly in for low-temperature combustion modes.

CMT spray model, emphasized on the initial jet penetration and quasi-steady behavior, is usually used to predict the mixing characteristics from SOI to SOC, where the spray penetration remains the same pace as a reacting spray [152]. Consequently, the obtained mixing field aids in comprehending ignition behaviors through accurate predictions of spray penetration. In a High-Speed Direct Injection (HSDI) Diesel engine, Benajes et al. [153] explored the potential of using pure diesel or gasoline in Premixed Charged Compression Ignition (PCCI) combustion mode by adjusting injection timings and oxygen concentrations. The obtained evolution of spatial ϕ at the moment of SOC and after EOI provides an insight into the soot formation. It was observed that gasoline ignites at a leaner mixture compared to diesel, with ϕ_{max} predicted to be lower than 2.0, indicating reduced soot formation during the combustion. Furthermore, the predicted equivalence ratio is also utilized in the condition that gasoline ejected into the port to realize a RCCI mode with the direct-injected diesel [154]. A similar application of CMT spray model in ignition investigations was reported in [155], which examined the differences between pure diesel and gasoline operating in Partially Premixed Combustion (PPC) mode. Recently, this model was also employed in the design of dual-fuel engines, where diesel is injected into the chamber to ignite the fuel ejected into the port [156] [157].

In conditions where ignition occurs after EOI, such as in low-temperature combustion in diesel engines, SNL model is usually preferred to obtain the mixing field. Malbec et al [158] evaluated the impact of injection duration on ignition delay in a 2.34 L optical diesel engine after the observation of a good correlation with the penetration of a transient jet. They found that if the temperature at the top dead center is below 800 K, the ignition delay decreases as the injection duration decreases when it is shorter than 1.3 ms. In addition to its application in understanding combustion characteristics, SNL spray model was also developed to evaluate the accuracy of infrared techniques. Mancaruso et al. [159] [160] found that the emission of infrared radiation at a wavelength of 3900 nm is correlated with the equivalence ratio, thereby, confirming the suitability of this wavelength for detecting the liquid phase.

2.5.3. Non-free spray/wall impingement

In small-bore diesel or direct-injection gasoline engines, the spray/jet impingement on a moving piston has been proven to significantly affect the mixing, combustion and pollutant emissions. When the liquid phase impinges on the piston, the accumulated fuel on the cylinder wall can lead to the formation of a fuel film, which adversely affects combustion and consequently increases the emissions of UHC, CO and soot particles. Moreover, the heat transfer can reduce the spray temperature, thereby extending the ignition delay. Conversely, when the vapor phase impinges on the piston, the interaction between the jet and the wall enhances fuel-air mixing, resulting in a reduction of soot emissions. For a non-reacting spray, the awareness of the mixing field is essential to the understanding of the combustion process and the soot formation. To this end, Ruth et al [161] and Osorio [162] developed the SNL spray model to predict the spray characteristics associated with gas jet impingement.

As shown in Figure 2.17, the spray profile of a liquid-fuel impinging a flat wall can be classified as four regions: liquid phase, free penetration, stagnate and wall spreading. In the first two regions, the spray profiles remain consistent with free penetration. Upon reaching the flat wall, the spray spreads laterally in two directions. In the overlapped region, where the spray begins to penetrate radially, the flow is considered to be in a stagnation state. Subsequently, the surrounding entrainment can be characterized by the spray height H at various radius S_r [163].

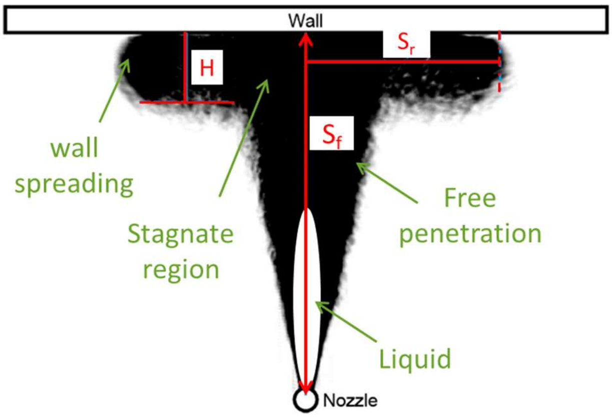

Figure 2.17. Schematic of the spray structure and the characteristics for a perpendicular impingement. Reprint by the ensemble-averaged frame shown in Figure 5 in [161]. S_f: spray penetration in the free penetration region; S_r: spray radius in the wall spreading region; H: spray height in the wall spreading region.

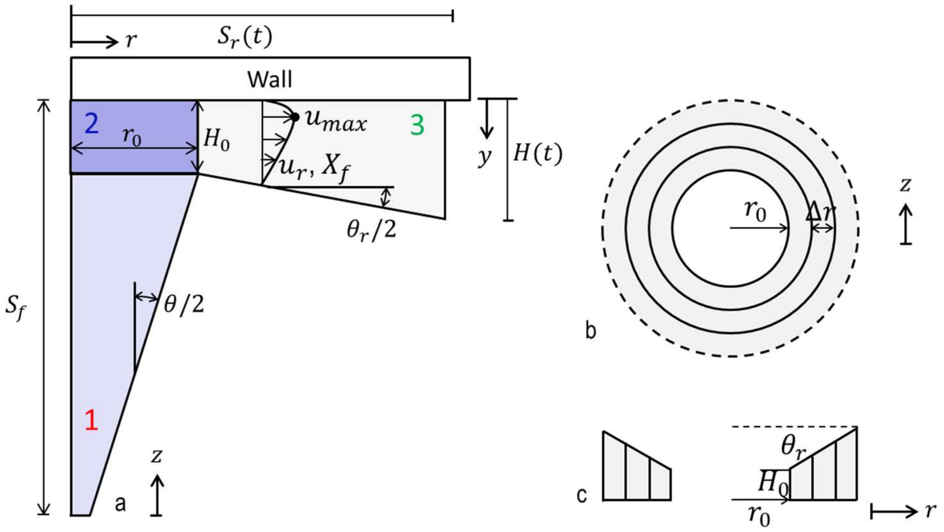

Figure 2.18. Schematic of phenomenological spray impinging model [161].

Consistent with the spray structure obtained by optical techniques, the spray impinging model can also be simplified as three regions, as shown in Figure 2.18. In region 1, spray penetrates along ‘z’ direction. The stagnate region was simplified as a rectangle area ‘2’. Then, a ‘new spray’ leaves from the boundary at the distance of ‘r_0’, and a trapezoid spray profile is also presumed, similar to region 1. Different from the known boundaries for the free penetration region, the boundary for the wall spreading simulation will be derived by the following hypotheses:

- The effect of friction force is neglected in the turning region.
- No entrainment of air into the turning region.
- The normal force does not change the fluid’s kinetic energy.

Similar to Eq. (2.22), the output boundary of the turning region (i.e., H_0, u_{out}) can be obtained by solving the conservation equation of fuel mass,

$$\overline{\overline{X_f}}\bar{\bar{\rho}} \cdot \beta_{in}\bar{\bar{u}}_{in} \cdot A_{in} = \overline{\overline{X_f}}\bar{\bar{\rho}} \cdot \beta_{out}\bar{\bar{u}}_{out} \cdot A_{out}$$

and the conservation of kinetic energy,

$$\bar{\bar{\rho}} \cdot \alpha_{in} \cdot \bar{\bar{u}}_{in}^2 \cdot A_{in}\bar{\bar{u}}_{in} = \bar{\bar{\rho}} \cdot \alpha_{out} \cdot \bar{\bar{u}}_{out}^2 \cdot A_{out}\bar{\bar{u}}_{out} \tag{2.28}$$

Considering the no entrainment in the turning region, the sectional-averaged mixture fraction and mixture density can be seen as constant at the inlet and the outlet. Then, the turning parameters can be written as,

$$\bar{\bar{u}}_{out} = \bar{\bar{u}}_{in}\sqrt{\frac{\alpha_{in}\beta_{out}}{\alpha_{out}\beta_{in}}} \approx 1.03173 \cdot \bar{\bar{u}}_{in}$$

$$H_0 = \frac{r_0}{2}\sqrt{\frac{\alpha_{out}\beta_{in}}{\alpha_{in}\beta_{out}}} \approx 0.48467 \cdot r_0 \tag{2.29}$$

where $\alpha_{in} = 5.0736$, $\alpha_{out} = 4.7658$, $\beta_{in} = \beta_{out} = 2.0195$. Osorio taken the effect of friction in the wall jet into account, the value obtained for β is 2.868 and 3.014 from the fitting data in the measurement of Wood [164] and Alachopoulos [165], respectively.

Along with the direction of spray wall spreading, the conservation of fuel mass and momentum is also applied here. Indicated in Eq. (2.25), the coefficient of β and sectional area A should be known before the calculation. Concluded by empirical formula of radial velocity profile proposed by Wood [164], Ruth et al. obtained the value for $\theta_r = 17.572°$ used in the calculation for sectional area $A = 2\pi r \cdot [H_0 + (r - r_0) \cdot tan\theta_r]$, and the same value for $\beta = 2.0195$ is adopted for both conservation equations. Osorio introduced a similar Gaussian profile to describe the effect of fuel friction distribution along the radial direction, then, the value for $\beta = 2.878$ is used for the fuel mass conservation $\dot{m}_f = \beta\bar{\rho}\overline{X_f}\bar{u}A$, and a different value $\beta = 2.959$ for the momentum conservation $M = \beta\bar{\rho}\bar{u}^2A$. Furthermore, the angle θ_r is obtained as 5.38°, which is much smaller than the value in [161].

Concerning the applications, enhanced air entrainment is observed in the wall spreading region for a non-reacting spray, which explains the less sooting formation in the gas jet impingement conditions. In addition, the influence of injection pressure, injection duration and bowl diameter on the spray penetration and mixing characteristics can be investigated, and a good match with measurement on the trend is found in [161]. Regarding the reacting spray, Osorio et al [166] employed it in a variable volume combustion chamber together with multiple injection strategies. In general, a good agreement in the qualitative trends (i.e. fuel efficiency, heat release rate) can be achieved between the measurement and the developed spray impinging model.

2.5.4. Analysis of reacting spray and combustion process

The spray-related variables under reacting conditions are reported for various spray characteristics, such as spray tip penetration and mixture fraction distribution, as well as the combustion metrics such as ignition delay, lift-off length, temperature and species distribution. To describe the combustion process, researchers often utilized either a single-step reaction or a detailed chemical mechanism.

Reacting spray tip penetration

Compared to the inert spray case, where spray tip penetration is extensively quantified and analyzed with both experimental and numerical approaches, the reacting spray tip evolution has been analyzed only in few studies. To the authors' knowledge, only the CMT model has been validated against experimental results. For the prediction of reacting spray tip penetration, the first immediate effect induced by combustion is the modification in local conditions. Desantes et al. [20] proposed the following assumptions for the reacting flow description:

- The turbulent mixing time is assumed to be much longer than the chemical reaction time thereby, a frozen chemistry is assumed, and the effect of scalar dissipation is also ignored. Hence, a single-step irreversible reaction is assumed.
- The momentum-dominated regime is still effective. The buoyancy effects are not considered.
- Local composition is derived from the mixture fraction following a Buke-Schumann approach, and the temperature calculation uses absolute enthalpy values.
- The heat radiation from the flame is ignored.

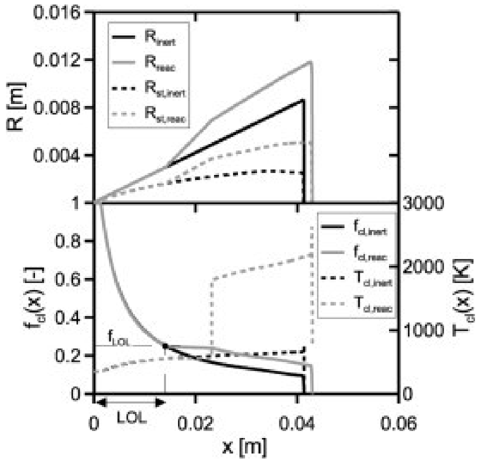

Figure 2.19. Example of simulated diesel flame under inert and reacting conditions. The following characteristics are plotted: Spray radius R, stoichiometric radii R_{st}, on-axis temperature T_{cl}, on-axis mixture fraction f_{cl}. $\tau_{comb} = 1680\ \mu s$

When applied to a diesel-like reacting spray, the reaction is only considered after the lift-off length. The transition from an inert state to a reacting state occurs at a particular time instant, denoted as τ_{comb}. The simulated diesel flame under both inert and reacting conditions is shown in Figure 2.19, with τ_{comb} quantified at $1680\ \mu s$. The spray characteristics of reacting spray until reaching LOL are expected to be the same as under inert case. Then, an increased radial expansion of both spray boundary and stoichiometric radii is observed until the distance where the T_{cl} suddenly increases. Beyond this distance, the composition of the reacting spray is predominantly comprised of products, and the on-axis mixture fraction is also higher than that of the inert one.

To get a better prediction of spray tip penetration, a good match in the penetration in the steady-state spray is observed using a larger spray angle [123]. Subsequently, an analysis of the spray dynamics between inert and reacting sprays indicated that the radial expansion downstream LOL is almost parallel [152], as shown in Figure 2.20. Thus, the inputs of same spray angles for the near- and far-field are followed in CMT spray model, with the calculation of ΔR based on mass conservation downstream LOL [167]. Xuan et al. employed this model to obtain the distribution of equivalence ratios, thereby elucidating the differences in CH_2O and OH formation in quasi-steady spray under various ambient temperatures for n-dodecane and PODE3 [101].

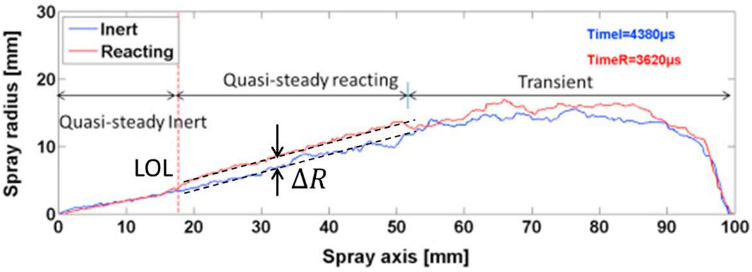

Figure 2.20. Radial width for both inert and reacting spray at quasi-steady state. Condition: ECN Nominal Spray A [152].

Combustion characteristics

To achieve the prediction of numerous combustion characteristics with a low computational cost, combustion model is required and the integration with spray model can be categorized as two types:

- **Direct chemistry integration**: in this approach, the chemical rates in the control volumes are calculated directly using either single-step chemistry or detailed chemistry by the mixing field obtained from empirical formulas or 1D discretized spray model. The control volumes can be defined by spatial coordinates or mixture fractions. To preserve the advantage of low computational cost, the number of control volume is usually limited when using detailed chemistry.
- **Flamelet approaches**: in this method, the chemical process is represented by one or several variables, instead of the Arrhenius-type equation, which are calculated by means of flamelet approaches. The integration of spray

models with these variables could facilitate the predictions of the combustion process with the balance of accuracy and computational cost.

Direct chemistry integration

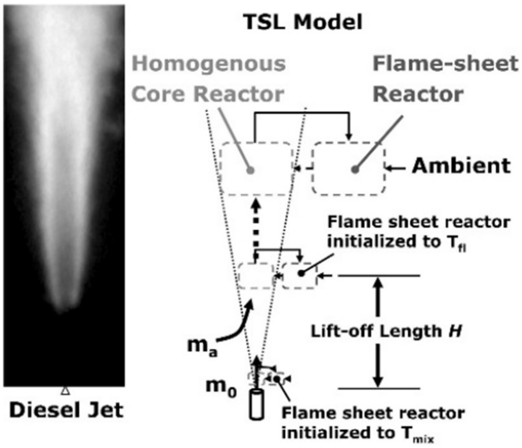

Figure 2.21. Schematic of two-stage Lagrangian model for turbulent spray. The left is an OH chemiluminescence image [168].

To understand the soot formation at engine-like conditions, Pickett et al. [168] employed a two-stage Lagrangian (TSL) model to predict n-heptane oxidation and soot precursor formation using a detailed chemical kinetic, consisting of 696 species and 3224 reactions. Empirical correlations were used to obtain the jet entrainment rate. As initially proposed by Broadwell and Lutz [169], the two-stage Lagrangian model assumes that the fluctuations in scalar mixing can be negligible on the average product concentrations. The reactions take place in flame sheets and well-mixed regions, corresponding to the diffusion-flame reactor where the mixing is at stoichiometry, and fuel-rich homogeneous reactor in the core of the jet. Shown in Figure 2.21, as the progressive entrainment, the surrounding gas is gradually transported into the reactors starting from the nozzle and moving downstream, eventually all the fuel in the homogeneous reactor is consumed, and the simulation at the spray tip is in a diffusion flame [168].

In the simulation using the same fuel, n-heptane, Knox et al [170] also employed the TSL model, while the transient ambient entrainment was simulated using a 1D spray model [33]. As shown in Figure 2.22, the calculation of entrainment rate $\dot{m}_{ent}$ is conducted for all physical control volumes discretized in 1D spray model. To balance the computational cost and the complexity of chemical mechanisms, some simplifications were proposed:

- Radial distributions of quantities (mixture fraction, velocity) are replaced by the cross-sectionally averaged value, which is the more like the TSL model.
- The diffusion-flame reactor is not included in the simulation for n-heptane flame.
- The transient ambient entrainment does not affect combustion since the nearly equivalence measurement of jet penetration under spray-H reacting and non-reacting condition. This point prevents an accurate prediction of reacting tip penetration.

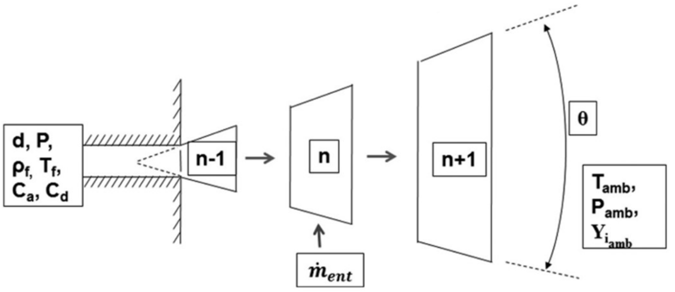

Figure 2.22. The schematic of control volume discretization in 1D spray model and the entrainment process [170].

After the determination of the species composition and enthalpy in the current control volume, the reaction was assumed to take place in a constant-pressure homogeneous batch reactor, lasting for the same duration as the local residence time. It was observed that predicted ignition is in good agreement with the experimental trend as the ambient oxygen content variation using two different chemical mechanisms.

A strong correlation between vapor penetration and axial mixture fraction under non-reacting conditions was observed, alongside a consistent experimental trend in ignition delay as a function of ambient oxygen content, utilizing two distinct chemical mechanisms. Furthermore, this model effectively captured the combustion recession at high ambient temperatures, which can be attributed to its accurate prediction of the entrainment-wave mixing process, as modeled by a 1D spray approach. Subsequently, the model was applied to transient injection strategies, allowing for an analysis of the differences in the evolution of global temperature and heat release rate in response to variations in end-of-injection rate shaping and dwell time during multiple injections.

To evaluate the combustion process and pollutant emission formation in DI diesel engines, Spessa et al. integrated a 1D spray model with a diagnostics multizone thermodynamic model [104] [171] [172]. If the mixing process of each injected fuel parcel is known in terms of spatial distribution and temporal evolution, the chemical process can be calculated following the conceptual scheme of combustion. As shown in Figure 2.23, the spatial control volumes with a constant interval ΔZ are rescaled as several mixture zones. At each time step during the injection event, a fuel parcel (bordered with colored dash lines) is formed by the model, and it penetrates downstream and progressively entrains the surroundings. For example, the first injected fuel parcel is located at the spray tip (red color). Obtained from the 1D spray model, the jet penetration will be known at each instant, then, the mixture zone can be identified by integrating the fuel mass, which would span one or several control volumes. Finally, the equivalence ratio can be estimated, and a time history of the equivalence ratio in all the mixture zones can be obtained.

In the employed pilot-main injection event, the pilot injection is assumed to have a lean/stoichiometric premixed combustion process, while the combustion of the main injection is considered to initiate under fuel-rich conditions, undergoing a two-stage premixed-diffusive combustion scheme. The onset of diffusive combustion depends on the engine load. By applying the principles of energy and mass conservations in all zones, the in-chamber mass and temperature evolutions can be obtained. Subsequently, submodels for evaluating the formation of NOx, CO, soot and UHC can be implemented. In addition, heat exchange with the chamber wall is accounted for through a convective term and a radiative term attributed to the hot soot particles. The cooling effect caused by the surrounding unburned gas is also considered during the post- combustion mixing process. Concerning the interference of turbulence, i.e., air flow motion and swirl ratio, it is assumed to be included in the measured pressure signal.

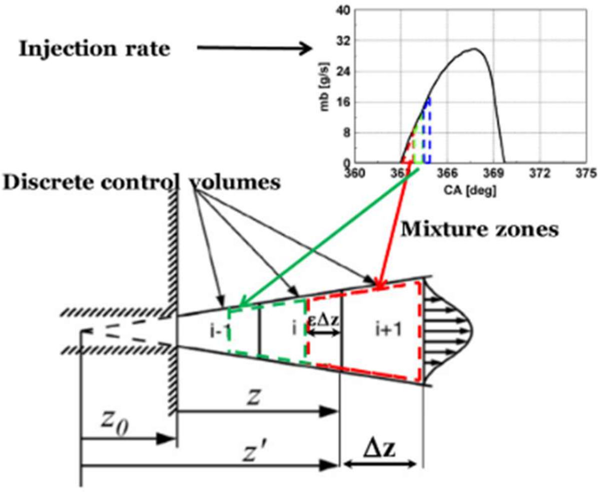

Figure 2.23. Schematic of the multizone combustion model employed in 1D discrete control volume, along with an injection rate example [104].

Using tuning parameters such as spray angle, number of mixture zones, and coefficients in submodels, the multizone combustion model successfully predicted the evolution of CO, NOx, UHC, and soot formation under various engine loads and speeds [171]. This behavior was found to be consistent with that of the Dec combustion model [29]. Then, the application was extended to post combustion by examining the different injection strategies, including injection pressure, the number of injection shots and dwell time between pilot and main injections [172]. Later, a good match is achieved on the spray penetration and soot mass evolution between the measured and modeled results under two different engine loads [104]. This further confirms its applications in engine design and calibration.

In previous approaches that integrating combustion model with 1D spray model, simplifications were done either in the spray model or in the chemical kinetics. Lee et al. [173] proposed a novel multizone model for simulating a direct-injection methane reacting spray. As shown in Figure 2.24, the spray domain is divided into 100 cells in the axial direction and 10 cells in the radial direction, with the radial quantities maintaining the self-similar radial profiles. Unlike a homogeneous reactor, the fuel gradually reacts with the entrained surrounding gas along the axial direction, while the species transfer between cells is only considered in the axial direction. In other words, radial diffusion is neglected. About the combustion process, fuel is initially cracked into CO, H_2, and other small hydrocarbons by high temperature ambient conditions in the first stage, then, the ignition takes place after the fuel is completely mixed and rapidly reacted with sufficient oxygen. Under the different orifice pressure drops, the model exhibits a good match on the spray penetration with the measurements obtained through Schlieren imaging. In addition, the model reasonably predicts the trends of ignition delay and ignition position in response to the variations in injection pressure, ambient pressure and the blending ratio of ethane in methane/ethane mixture.

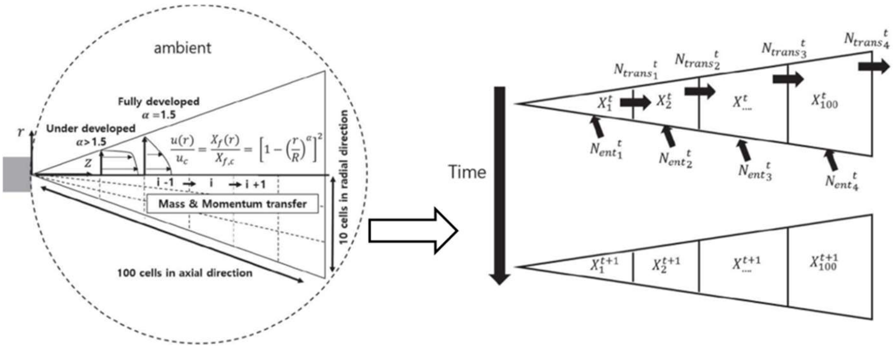

Figure 2.24. Concept of the division of computational domain (left) and the species transfer and the ambient entrainment (right) [173].

Ma et al. [174] developed an integration of a 1D multizone combustion model with a 1D spray model to predict the pressure rise during the combustion process occurring in a constant volume chamber. Meanwhile, detailed chemistry was used to calculate the chemical process. As an extension of SNL spray model, several new hypotheses were proposed:

- The spray was treated as a vaporized spray, and the liquid length is determined by the evaporation rate $\dot{m}_{f,evap}$, which is calculated by

  $$\dot{m}_{f,evap} = R_{evap} \cdot m_{f,liq} \tag{2.30}$$

  where $m_{f,liq}$ is the liquid fuel mass, and the coefficient R_{evap} was set as $1 \times 10^{-6}\, s^{-1}$ after the calibration on the liquid length and the check of sensitivity on the ignition delay.
- Locally homogeneous mixing is assumed in each control volume.
- Unlike the constant spray angle for inert spray simulation, variable spray angles are used for reacting flow.

To describe the combustion process, energy and species conservation equations were incorporated into each control volume. The chemical kinetic model is only applied in fuel gas phase. The consumption of liquid fuel is treated as the evaporation process. In addition, the mass considered for the conservation equations contains the exchange between the zones and the entrainment from the ambient gas, instead of the single fuel component in the original model. Finally, ideal-gas law is used to calculate the pressure after obtaining the local temperature.

For the purpose of reduction in the computational cost, the spray domain was divided into several zones of either constant length or constant volume, with the number of zones limited to no more than 10 for a domain size of 100 mm. About the iteration procedures, the boundary conditions used as inputs for the current zone retrieves from the outputs in the zone upstream. In general, the model is capable of predicting reasonable trends in response to parametric variations, such as ambient temperature and oxygen concentration. However, it still has some discrepancies in quantitative comparison with experiments due to the limitations in the zone number.

With the aim of simultaneously improving the accuracy and maintain the low computational cost, Tauzia et al. [175] tried the method that implying a single-step chemistry kinetic in the control volumes discretized in SNL spray model. The reaction elements involved in the reaction contain liquid and vapor fuel, O_2, N_2, CO_2 and H_2O. In addition to the optimizations presented in [174], the prediction of liquid length was further refined by introducing a characteristic time τ_{vap}, to account for the time required for the entrained air to reach the fuel near the spray centerline. Validated by the ECN database, considering variations in oxygen concentration (XO_2 = 13 – 21%), ambient density ($\rho_a = 7.6 - 22.8\, kg/m^3$) and ambient temperature ($T_a = 750 - 1200\, K$), the model in [175] realized an excellent match on lift-off length with the varied ambient temperature under the standard ambient density ($\rho_a = 22.8\, kg/m^3$). In addition, a reasonable trend in ignition delay was observed with increasing ambient temperature, ambient density and oxygen concentration. However, some discrepancies in vapor penetration predictions were noted, which were attributed to the inaccurate estimations of the injection rates.

In [176], a comparison in the obtained two-dimensional (2D) distribution of quantities was conducted between Lagrangian and Eulerian models. The radial distribution of mixture fraction follows the self-similar profiles in [33]. As shown in Figure 2.25, the 2D image showed that the Eulerian model is more favorable to the spray prediction, due to the similar spray shape with measurement.

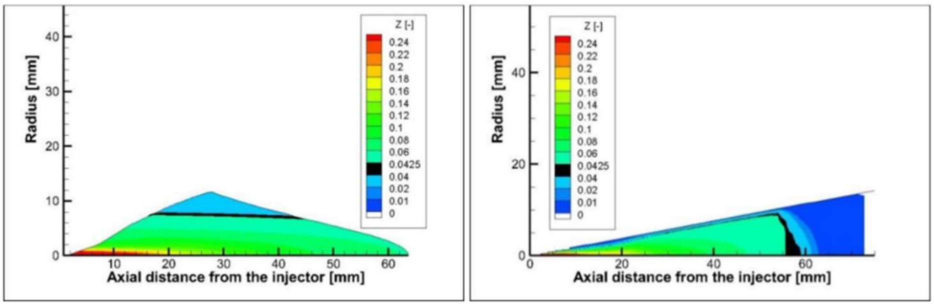

Figure 2.25. Two-dimensional field of mixture fraction of a reacting spray from Lagrangian model (left) and Eulerian model (right). The black line represents the stoichiometric ratio [176].

The dilatation sub-model based on the concept that no negative entrainment in the spray contributes to a more accurate prediction of spray penetration, as shown in Figure 2.26. Radial dilatation takes place in the distance of 20 – 56 mm, spanning from the lift-off length to the onset of the transient region. Thereby, the penetration was reduced, aligning more closely with the measurement.

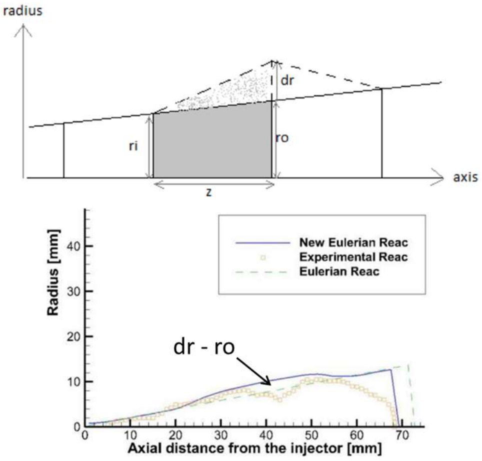

Figure 2.26. Schematic of radial dilatation of one control volume by increasing the outlet radius dr, while remaining the inlet radius ro and axial distance z (upper), and the influence of radial dilatation on the spray sharp for the Eulerian model (bottom).

In the calculation of heat release, only the term of exchange with the chamber wall was considered. The direct implication of single-step chemical kinetics in control volumes resulted in an overprediction of the pressure rise, as indicated by the 'old' label in the legend of Figure 2.27. To improve the accuracy, the new method proposed in [177] integrated 1D spray model with a combustion mapping which tabulates the combustion process in a mixture fraction space. The combustion process was represented by progress variable that illustrating the passage from a mixture regime to a steady rate combustion regime. Besides, no reaction was assumed to be in the liquid fuel. Using this model, the calculation time was found to be about 20 mins for an injection duration of 2.0 ms. Good agreement on the pressure rise/heat release rate was achieved throughout the injection process.

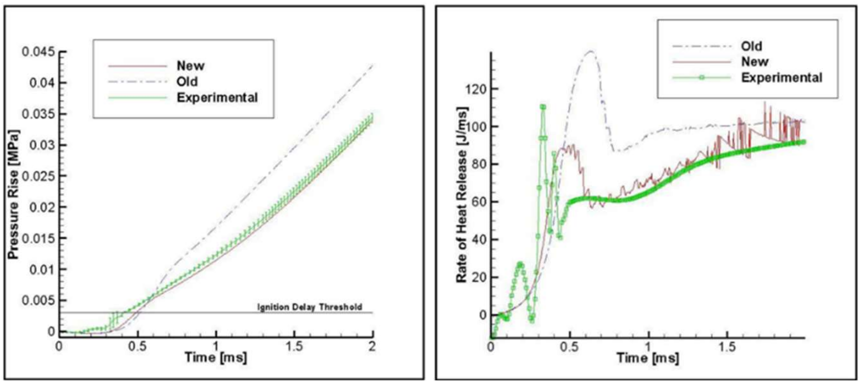

Figure 2.27. The comparison of the integration approach between the direct integration of single-step chemistry kinetics and the integration with a combustion mapping [177].

Flamelet approaches

The discussion above highlights that achieving accurate predictions requires both fine mesh resolution and detailed chemistry. Given the characteristic times of diesel-like combustion, where the chemical timescale is significantly shorter than the physical timescale, the flamelet approach treating turbulent flames as an ensemble of laminar flame sheets has gained widespread acceptance. The combustion process is pre-tabulated into a series of tables by the scalar dissipation rate, with each table describing the combustion process through the following variables: normalized progress variable, mixture fraction, and variance of mixture fraction. Recently, the integration of a 1D spray model or a reduced-order spray model with the flamelet approach has been employed to predict ignition delay, lift-off length, and temperature fields under both steady and transient conditions. Due to space constraints, the integration of the spray model and flamelet will only be briefly discussed here. This chapter focuses on recent advancements in the application of the 1D spray model. Further details on the flamelet concept will be presented in the next chapter.

Garcia-Oliver et al. [21] incorporated an existing 1D spray model with unsteady flamelet progress variable, thereby enabling the prediction of combustion metrics such as ignition delay, lift-off length and spatial distribution of temperature and species. The introduction of mixing trajectories allows for the conceptualization of the spray as a series of reactors along the axial direction, wherein pure fuel is introduced and gradually mixed with ambient air. Using a constant scalar dissipation rate in this model, the trends in ignition delay and lift-off length were reasonably predicted across various ambient temperatures, while the accuracy requires improvement, especially in the low temperature cases. This model is the starting point for the present PhD.

When the 1D spray model was employed in transient cases, the turbulence caused by the intake flow, squish flow and compression cannot be roughly disregarded. For a micro-pilot injection in a rapid compression machine (RCM), Park et al. [25] regarded turbulence as a form of momentum loss, designing the model to exhibit greater loss as turbulence intensifies and the velocity gradient in the radial direction gets higher. Besides the mixture fraction, scalar dissipation rate (SDR) is also required to access the chemical model. The transient values of the area-averaged SDR obtained from the 1D spray model serves as a boundary condition, thereby allowing for the characterization of the interaction between turbulence and chemistry. Using this transient flamelet approach, the prediction of ignition is within an uncertainty of 0.5 ms for the ECN conditions, with only the cases at a low ambient temperature of 750 K being overpredicted.

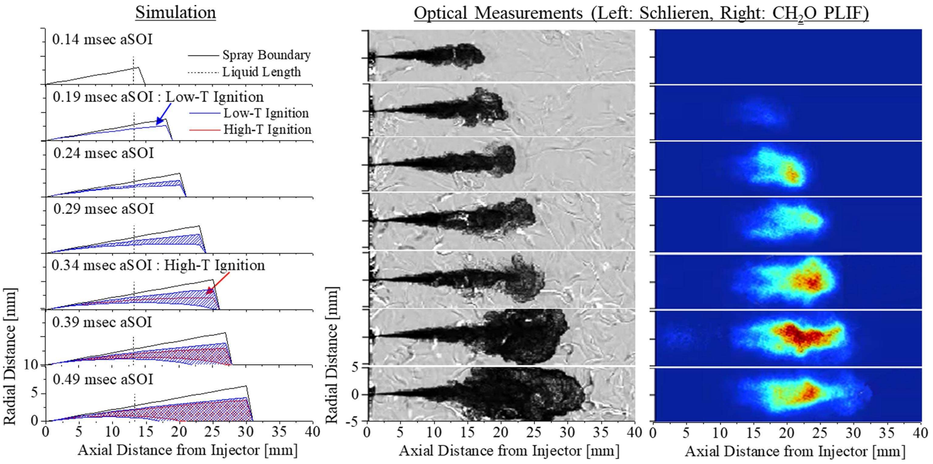

Figure 2.28. Ignition process by the low- and high-temperature region from simulation (left), Schlieren images (middle) and CH_2O PLIF images (right). Condition: Nominal Spray A ($T_a = 900\ K, P_{inj} = 1500\ bar, \rho_a = 22.8\ kg/m^3$) [25]

The comparison of the ignition process shown in Figure 2.28 reveals that the low- and high-temperature ignition delays defined as a temperature increase of 100 K and 500 K at each mixture fraction, are consistent with the experimental results by means of CH_2O PLIF and Schlieren images, respectively. Concerning the ignition position, both low- and high-temperature ignition positions appear from the nozzle outlet to the spray head, which is attributed to the ignorance of liquid length in the simulation. In addition, the low-temperature ignition position was observed near the boundary, and the spray center is too rich to be ignited, which is different from the CH_2O PLIF results that the highest CH_2O concentration generated in the spray centerline. After the appearance of high-temperature ignition, its ignition area expands into the rest of low-temperature ignited spray envelope. However, the regions near the spray boundary are too lean to be ignited, consistent with the weak luminosity of CH_2O signal observed in the measurement.

Following the success of predictions under ECN conditions, the model application was extended to two additional cases. The first case involves a micro-pilot injection event in which n-dodecane was injected into a background of neat air or air/methane mixture in RCM. The second case pertains to a medium-speed dual-fuel engine, where natural gas is ejected into the intake port and a small amount of diesel fuel is directly injected into the cylinder through the micro-pilot injector for ignition. The model demonstrates accuracy in predicting ignition delay, with results consistently within 0.5 ms across various conditions, including ambient temperature, injection duration, air-to-methane ratio in the background, ambient pressure, and compression ratio.

In the aforementioned implementations, turbulence is not considered in the integration of 1D spray model and flamelet, despite the momentum conservation was corrected in [25]. Limited by the assumption of 1D spray model based on Eulerian approach, the variance of mixture fraction is assumed to be zero, thus, the combustion process, which is typically represented in three-dimensional tables, is effectively reduced to two-dimensional tables. In this sense, Deshmukh et al. [178] integrated a cross-sectionally averaged reactive turbulent spray (CARTS) model with a flamelet solver using multiple flamelets and achieved a reasonable prediction to the trends of ignition delay, lift-off length and soot emissions. CARTS model is an extension of the cross-sectionally averaged spray (CAS) model, which was derived from a three-dimensional multiphase model using a top-down approach [179].

Unlike the Eulerian model, the CAS model offers a more comprehensive description of the spray process, encompassing the drag force on droplet movement, droplet breakup, evaporation, and droplet heating. Following the integration of the turbulence model into a steady-state spray, parameters such as turbulent kinetic energy (TKE), turbulence dissipation rate, and the variance of the mixture fraction can be obtained, leading to the calculation of the transient scalar dissipation rate. Under the ECN nominal Spray A condition, a strong agreement was observed between the measurements and simulations regarding the mixture and variance of the mixture fraction in both axial and radial directions. However, the calculated turbulent kinetic energy and turbulent dissipation rate were found to be higher than those from the

URANS (unsteady Reynolds-averaged Navier-Stokes) simulation at distances upstream of the liquid length, which may be attributed to neglecting turbulence in this region.

Before the interaction between spray model and flamelet, the flamelet solver has already solved the species mass fraction and temperature in mixture fraction space, and the solutions were represented in the physical space using a convolution over the local β-PDF. With the obtained scalar dissipation rate, as well as the gas pressure provided by spray model, the solution from the flamelet solver was mapped to the spray model, thereby, the spatial distribution of the gas temperature and species mass fraction can be determined. In addition, the soot modelling requires additional soot model to predict the soot evolution, and density correction along the radial direction is also required due to the phase transition during the soot formation.

Figure 2.29 displays an example of the 2D radial profiles of temperature and species (CH_2O & OH) along the ignition process from CARTS model (top) and URANS results (bottom). The species profiles indicate that CH_2O and OH initially form at the spray head in both methods; however, the CARTS model demonstrates a smaller distribution area and higher concentration. Additionally, the temperature is also observed to be higher in the CARTS results compared to the URANS results, attributed to the constant flamelet along the radial direction in CARTS model.

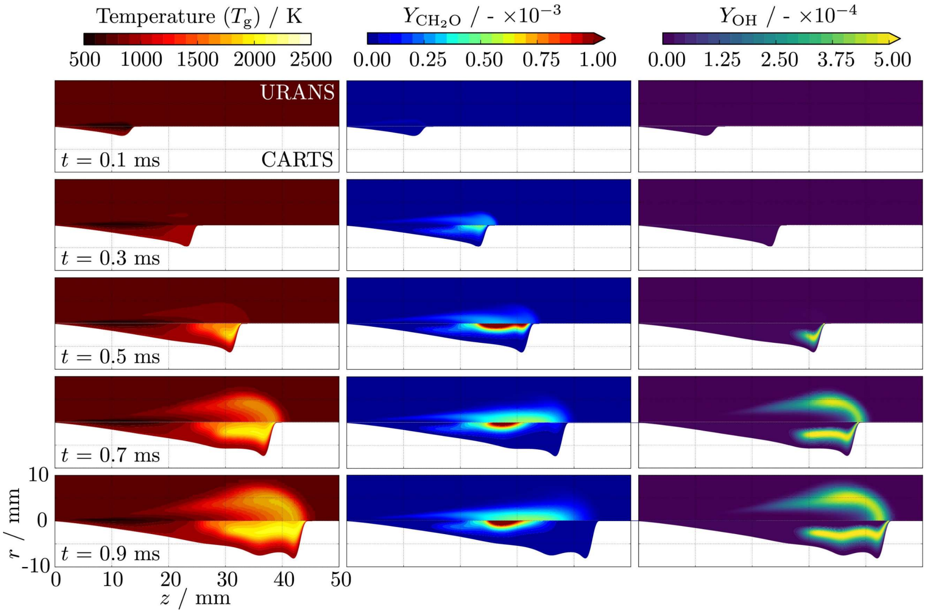

Figure 2.29. Example of the 2D radial profiles of the temperature and species from CARTS model (bottom), and the URANS results are plotted for a comparison (top). Condition: ECN Nominal Spray A. Mechanism: CAI [178].

In terms of predicting ignition delay, both multiple flamelet and single flamelet approaches demonstrated accurate trends relative to measurements across a wide range of ECN conditions and various fuels, reflecting the variation in fuel reactivity. Notably, the use of multiple flamelets yielded slightly more accurate predictions. However, the predicted lift-off length consistently exceeded the measured values across all conditions and fuels. Regarding soot mass modeling, initially explored in the reduced-order spray model, the predicted total soot mass was significantly lower than the measurements under the nominal Spray A condition. This discrepancy could be mitigated by applying a self-similar radial profile to describe radial quantities.

In general, this reduced-order spray offers new insights into the modelling of spray and combustion modelling, with its derivation allowing for further exploration of model applications, such as the recent research on flash-boiling spray [180]. The good prediction in ignition delay and lift-off length indicated that the simplified approach can be a good tool to identify the combustion characteristics of potential fuel candidates.

2.6 Summary

Throughout this chapter, the spray and combustion process under steady engine-like conditions and the phenomenological modelling approaches have been reviewed. When the liquid fuel is ejected into a high-temperature high-pressure reactive environment, it undergoes the atomization, including primary and secondary breakup, evaporation and air entrainment, then, the fuel-oxidizer mixture is ignited at some distance downstream the nozzle after some time. Finally, the reacting spray is characterized by mixing-controlled combustion scheme. To simplify the description of these processes, some parameters are used to quantify that, such as the spray characteristics including liquid length, spray vapor penetration and spray angle, and combustion characteristics including ignition delay and lift-off length. If the prediction is only targeted at these parameters, phenomenological model is a good tool with the advantage of low temperature cost and acceptable accuracy.

Concerning the spray characteristics prediction, empirical formulas concluded from the measurements are firstly given in the description of the corresponding process. Literature review on the phenomenological spray models shows that the widely used models are based on either Lagrangian or an Eulerian model, treating the spray as a one-dimensional flow. The former model considers the spray area as several individual droplets or parcels, traveling in time and space along the specific trajectories. The latter approach treats the spray as a continuous flow, thereby, assuming the turbulent gas jet as a mixing-controlled jet. Conservation of fuel mass and momentum is used to calculate the spray penetration, together with the liquid length determined by the evaporation rate determined by the energy conservation. Both kind of Eulerian spray models proposed by CMT – Clean Mobility Thermofluids and Sandia National Laboratory can realize excellent prediction of spray characteristics. As a consequence, this modelling approach has been widely employed in the analysis of the ignition behavior in engines by means of the mixing state prediction, validation with the parametric variation and an extension to spray impingement.

In terms of the prediction of reacting spray characteristics, a combustion model is required to integrate with the spray model, as well as the chemistry kinetics used to describe the combustion process. The integrations in the literature can be categorized as follows: direct integration of single-step or detailed chemistry in the transient control volumes discretized in spray model, and the integration of flamelet with the control volumes on the axial direction or along the mixing trajectories. In general, the prediction of ignition delay and lift-off length is in agreement with the experimental trend, meanwhile, the accuracy is improved as a finer mesh and/or more detailed chemistry kinetics is used. Furthermore, the low computational cost across a broad range of conditions indicates potential utilization on training artificial neural network-based models.

In the present thesis, the modelling is based on the integration of laminar flamelet with in-house spray model, which has been initially tried. Based upon the literature review, the model development will be performed to improve accuracy and further reduce the computational cost. Additionally, its low computational cost across a broad range of conditions indicates promise for training artificial neural network-based models. The details will be presented in the next Chapter.

Chapter 3

Model development

Content

3.1 Introduction

From the literature review on phenomenological models discussed in Chapter 2, 1D spray model based on mixing-controlled hypotheses can achieve an accurate prediction of the most important spray metrics (liquid and vapor penetration, velocity and mixture fraction distribution) under non-reacting conditions [18] [33]. Starting from the analysis of an iso-thermal spray [181], 1D spray model, DICOM, was also successfully employed in multi-component hydrocarbon fuels for a non-reacting spray [18] [19] [182]. Recently, the analysis was also extended to the near field for non-vaporizing sprays [183]. However, the calculation under reacting conditions has to account for the influence of chemistry mechanism, turbulence and species diffusion. The first trial using DICOM on reacting spray simulation dealt with the reacting flow penetration [20] and local velocity [114] with a simplified 1-step chemistry and feeding the experimental ignition delay and lift-off length as the user inputs. To realize a fully prediction to the combustion process of a diesel-like reacting spray without the need of the experimental database as the user inputs, the incorporation of an unsteady flamelet progress variable (UFPV) approach to 1D spray model is adopted in this thesis.

In this chapter, the description of this incorporation, named as Quasi-1D modelling, is illustrated. First, the background and basic theory of 1D spray model is described in Section 3.2. Second, the concept of UFPV is discussed in Section 3.3. Then, the model configurations and the inert spray validation is given at the starting of Section 3.4, followed by the optimizations of Quasi-1D modelling from the initial version used in [21], including the terms of spray tip reconstruction, mixing trajectory, scalar dissipation rate, chemical rate reconstruction, explicit solution, vaporization correction, Y_C diffusion balance, radial expansion and multiple flamelets employment. Experimental database used for validation has been measured under the Nominal Spray A condition fueled with n-dodecane which is available at the ECN website [22]. LLNL mechamism consisting of 2878 species and 12839 reactions [184] was used to generate the flamelet manifold and incorporated into the Quasi-1D model for the checking of optimizations. The performance of optimized Quasi-1D model using different chemical mechanisms is presented in the next chapter. Finally, the summary is presented in the final Section.

3.2 General description to 1D spray model

In order to simplify the process, swirl or other turbulent flow in the combustion chamber are not considered. In addition, the ambient volume is seen as quiescent and large enough so that there is no wall impingement, and air condition far away from the nozzle will not be changed by the flow evolution.

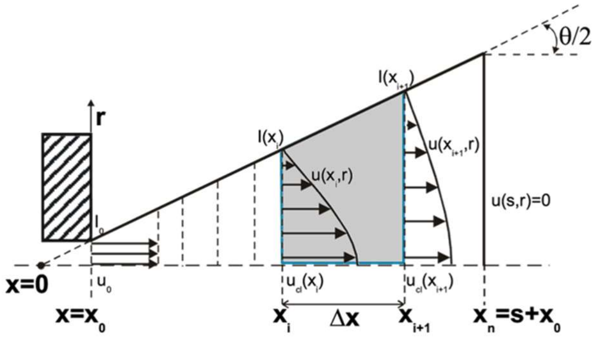

Figure 3.1. Schematic of 1D spray model [18]

Figure 3.1 shows a schematic of the basic configuration of this problem [18]. At the nozzle exit (x = x0), which is the inlet of fuel stream, a radially uniform velocity profile across the radial direction is assumed. The injected flow exchanges momentum with the ambient gas in downstream direction and until the spray tip (x = s), which increases with time. In this way, the flow increases in width with the axial distance. The spray cone half angle $\theta/2$ defines the radial growth of the flow in terms of the radius R, which is also an input to the model. Together with the nozzle diameter d_0, the spray angle defines the virtual origin of the spray by the formula

$$x_0 = \frac{d_0}{2\tan\left(\frac{\theta}{2}\right)} \tag{3.1}$$

Due to the transient nature of the general problem, the spray domain is axially divided into a series of cells with a certain thickness Δx spanning the whole spray cross section. For each cell, two conservation equations of axial momentum ($\dot{M}$) and fuel mass (m_f) are solved for two unknowns, axial velocity (u) and mixture fraction (f),

$$\dot{M}(x_i,t) - \dot{M}(x_{i+1},t) = \frac{d}{dt}\left[\int \rho(x,r,t)\cdot u(x,r,t)\cdot dV\right]$$

$$m_f(x_i,t) - m_f(x_{i+1},t) = \frac{d}{dt}\left[\int \rho(x,r,t)\cdot f(x,r,t)\cdot dV\right] \tag{3.2}$$

where the terms in the left side of the equations correspond to the conserved property fluxes across the cell inlet (x_i) and outlet (x_{i+1}) surfaces. The detailed solution procedure can be found in [18] [20]. Note that, unless otherwise stated, all variables within the model description correspond to Reynolds-averaged formulations.

3.2.1. Starting hypotheses

Since the first version proposed in [75], an amount of work has been done to optimize the model. Until now, the hypotheses for this model can be categorized as follows:

- Symmetry around the axis, i.e., no swirl flow or turbulence inside the chamber.
- The turbulent flow is assumed to be fully developed. In this way, the self-similar radial profiles can be defined for the conserved variables. This is one of the major assumptions in this model, which has been validated in steady gas jet or spray flows under inert and reacting conditions [18] [114]. This hypothesis can be translated into the following equation:

  $$\frac{u(x,r)}{u_{cl}(x)} = \left[\frac{f(x,r)}{f_{cl}(x)}\right]^{1/Sc} = exp\left[-k\left(\frac{r}{R}\right)^2\right] \tag{3.3}$$

  where u_{cl}, f_{cl} are the axial component of velocity, mixture fraction on the spray centreline, r/R is the normalized radial position with the range from 0 to 1, Sc is set as unity [18]. Another parameter, Prandtl number, Pr, is assumed to be consistent with Sc, and, there is no need to solve the enthalpy properties [18]. Under this Gaussian assumption, the calculation has to start after a certain distance to the nozzle exit, denoted as 'intact length'. At any instant time, intact length will be calculated first. In the downstream, f_{cl} will be lower than 1. And Eq. (3.1) will be solved for each cell. As a sequence, the mixing-controlled model always predicts the states for a fully developed flow region while the prediction to the near-nozzle region is not very accurate.
- The spray width R is linearly dependent on the corresponding axial coordinate, and it is defined as the location where axial velocity is equal to $\zeta = 1\%$ of that on the spray centreline. In other words, for the Gaussian profile, the variable k in Eq. (3.3) follows this correlation, $k = \ln(1/\zeta) = 4.6052$.
- The flow is assumed to be locally homogeneous, like that there exists a local equilibrium both in thermal and velocity conditions. In other words, the spray can be considered as a gas jet, which is also reasonable for the prediction of diesel-like spray [116].
- Spray propagation causes no fluctuation to ambient pressure, and the pressure across the whole spray is also constant. Thus, compressibility effects are neglected.
- A non-ideal gas equation of state (Peng-Robinson) is used to calculate the local state for liquid sprays, while an ideal gas one is used for gas jets. The comparison in [19] showed that the discrepancy between ideal and non-ideal gas equation on vaporization fuel mass fraction only occurs at high ambient

pressure conditions. As a consequence, local density can be calculated under an assumption of ideal mixing,

$$\rho(x,r) = \frac{1}{\sum_i \frac{Y_i(x,r)}{\rho_i(x,r)}} \tag{3.4}$$

where Y_i is the mass fraction of mixture component i, ρ_i is the density for component i at the local temperature T and pressure P. For fuel species, $f = Y_f$. Combining Eq. (3.1) – (3.3), conservation equation for each cell can be rewritten as,

$$\frac{\Delta}{\Delta t}\left[\int \rho u dV\right] = \dot{M}(x_i, t) - \dot{M}(x_{i+1}, t)$$

$$\frac{\Delta}{\Delta t}\left[\int \rho f dV\right] = m_f(x_i, t) - m_f(x_{i+1}, t) \tag{3.5}$$

The terms on the right-hand side of the equations correspond to the conserved property fluxes across the cell inlet and outlet surfaces. The fact that both axial velocity and mixture fraction are self-similar enables recasting the previous equations in terms of two unknowns, namely f_{cl} and u_{cl}, which means that the problem becomes 1D. According to the analysis in [185], the conservation equation in Eq. (3.2) can be simplified as,

$$A \cdot u_{cl}^2 + B \cdot u_{cl} + C = 0$$

$$A_f \cdot u_{cl} \cdot f_{cl} + B_f \cdot f_{cl} + C_f = 0 \tag{3.6}$$

Note that all variables shown here are turbulent time-averaged quantities.

3.2.2. State relationship for the 1D spray model

Following the assumptions, the flow can be treated as a gas jet or vaporizing spray. With the target of an accurate prediction to local mixture thermodynamics, several options to state relationships are available for specified demand. The detailed description can be found in [19], only a short discussion will be shown in the section.

- For the isothermal or non-vaporizing spray, the temperature across the spray is the same as the environmental, thus enthalpy conservation equation will not be solved. The only relative variable is the local density, and the local density for each component can be simplified as fuel and air density.

- For the prediction of liquid sprays, the phenomenon becomes complex with the presence of liquid and vapor fuel, and ambient air. In this way, thermal exchange has to be considered. As a result, liquid length can be predicted, and more considerations are made. The solution of enthalpy defined by fuel mass fraction Y_f can be expressed by,

$$Y_f(x,r) = \frac{h(x,r)-h_{a,\infty}}{h_{f,0}-h_{a,\infty}} \tag{3.7}$$

where $h_{f,0}$ and $h_{a,\infty}$ are the enthalpy of pure fuel and pure air, respectively. According to that, the flow can be seen as two streams of fuel and air with an adiabatic mixing, and the local temperature can be interpolated when enthalpy of the local composition for the whole range of fuel mass fraction (0-1) is known. For that, the enthalpy of the different species as a function of temperature or pressure should be known before. After that, local mixture density can be calculated at a given fuel mass fraction, i.e., $T = T(Y_f)$.

- For reacting spray, the dependent variable Y_f is no longer conservative, as fuel disappears due to the chemical reactions. As a substitution, the problem can be solved with the same approach only Y_f switching to mixture fraction f, i.e., $T = T(f)$, $Y_i = Y_i(f)$ and $\rho = \rho(f)$. The hypotheses are also valid under reacting conditions, especially the self-similar Gaussian radial profile for axial velocity, mixture fraction is also effective [167].

The general description of 1D spray model structure is shown in Figure 3.2. The output of this model consists of velocity, mixture fraction, temperature and species at arbitrary position across the spray, and the main results are the on-axis variable u_{cl} and f_{cl} by solving the conservation equations for axial momentum and fuel mass with the inputs of momentum and mass flow in the fuel stream. For that purpose, the radial integral F that defined as the cross-sectional integral of the product of density, the self-similar radial profile and normalized area (Figure 3.2) should be calculated in advance, which is dependent on the axial mixture fraction, Schmidt Number, spray angle, and the self-similar function of the radial profiles and the local density. The latter variable is one of the results from the state relationships, which calculate the local equilibrium from the boundary conditions, i.e., thermodynamic properties. Once obtaining the local mixture fraction, the other properties such as temperature can be calculated from the state relationships.

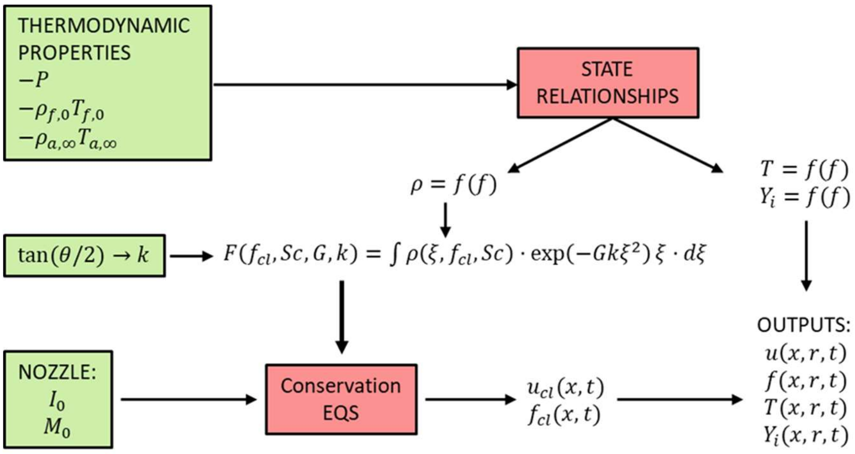

Figure 3.2. General overview of 1D spray model [18]

3.3 Unsteady Flamelet Progress Variable model

Compared to the inert case, the ignition in the reacting flow brings a more complex process, constituting the species recombination, heat release, and, consequently, higher temperature, lower density, which yields a faster velocity. Simplified model based on infinite-rate chemistry (1-step reaction) has been applied in 1D spray model, while the prediction is limited in the reliance of external ID & LOL as the user inputs [20]. For some cases, the accuracy is not good on ID prediction [186]. Thereby, the utilization of detailed chemical mechanism is essential to achieve an acceptable prediction. Referring to the methodology incorporated in [174], the method that directly links detailed chemistry reactions has to restrain the number of control volumes, otherwise, the computational cost will be enlarged. Taking into account the flow property of diesel-like spray (high-DamKöhler number flow) that chemical characteristic time is much shorter than physical characteristic time, the incorporation of tabulated flamelet to account for detailed chemistry effects, making up a flamelet manifold, is frequently applied in spray combustion simulations under diesel-like conditions.

For that purpose, the UFPV combustion model originated by Pitsch [187] and the version developed by CMT [188] is coupled with 1D spray model in this thesis. It is tabulated offline by the assumption that a turbulent flame can be described as a set of strained laminar counterflow flamelets [189]. The evolution of chemical state is tracked by a variable with a monotonic increase, that is progress variable Y_C, defined by a species combination of main products. In the previous study, two different definitions for n-dodecane calculation have been used in CFD-RANS simulation [21] [190], and the definition that $Y_C = 0.75Y_{CO} + Y_{CO_2} + Y_{H_2O}$ is preferred. Moreover, the simulation for OMEx-type fuels also follows this definition and obtains a good prediction in CFD-RANS work [191]. Therefore, this Y_C definition is considered in this thesis.

To obtain the transient species mass fraction Y_k, ZLFLAM [192], a code developed at Centro de Investigaciones Energéticas, Medioambientales y Tecnológicas (CIEMAT) is used to calculate a set of 1D laminar flamelets throughout the Eq. (3.8) in the space of mixture fraction,

$$\frac{\partial Y_k}{\partial t} = \frac{\chi}{2}\frac{\partial^2 Y_k}{\partial f^2} + \dot{\omega}_k \tag{3.8}$$

where the net production rate of species k is $\dot{\omega}_k$ is retrieved from the chemical mechanism. The scalar dissipation rate χ, representing the effects of convection and diffusion into the mixture fraction space diffusion, is defined as,

$$\chi(f) = 2D\left(\frac{\partial f}{\partial x_j}\right)^2 \tag{3.9}$$

where D is laminar diffusivity, f is mixture fraction. The model is derived from the steady laminar counterflow diffusion flame with constant density and diffusion coefficients by Peters [193],

$$\chi(SR, f) = \frac{SR}{\pi}\exp\left(-2\left(erfc^{-1}(2f)\right)^2\right) \tag{3.10}$$

where $erfc^{-1}$ is the inverse complementary error function. SR is the strain rate, defined by the velocity gradient at the oxidizer side of the counterflow flamelet [191]. As a user input to the manifold tabulation, a vector of SR sweeps from an extremely low value to auto-ignition limitation, which is highly dependent on the chemical mechanism. More points are assigned in the range of small values. The prescribed χ profile expression can be normalized by the scalar dissipation rate at stoichiometric conditions χ_{st} so that it can be independent on SR, as shown in Eq. (3.11), which shows that SR and χ_{st} are equivalent variables for flamelet tabulation.

$$\chi(\chi_{st}, f) = \chi_{st}\frac{F(f)}{F(f_{st})} \tag{3.11}$$

A normalized progress variable C ranging from 0 (inert state) to 1 (fully burned state) reparametrizes the chemical evolution. This is defined as

$$C = \frac{Y_c - Y_c^{inert}}{Y_c^{steady} - Y_c^{inert}} \tag{3.12}$$

where Y_c^{inert} and Y_c^{steady} are the inert and steady values for progress variable.

To incorporate the combustion evolution into the 1D spray model, the laminar flamelet is tabulated for every strain rate value as a two-dimensional manifold composing 201 points in f vector and 501 points in C vector. It is worth noting that the turbulence-chemistry interaction is neglected in 1D spray model, the flamelet information is only used in laminar terms. Hence, the model mixture fraction (which can be considered as a time-average value) is the only parameter that bridges the connection to the flamelet, and the absence of variance prevents from following a similar path to that in [178], which reconstructs the manifold by probability density function (PDF).

3.4 Integration of the UFPV approach into the Quasi-1D model, Mixing Trajectory

Note that according to the 1D model hypothesis, the species mass transport is described in terms of axial convection, which is quantified by the axial convective velocity u , and radial convection plus diffusion, which are described by the corresponding radial convective velocity v and radial diffusion velocity v_{diff} so that $v_{tot} = v + v_{diff}$, the detailed derivation of these terms is given in Appendix. A. As for progress variable Y_c, it doesn't follow the self-similar profile along radial direction, thus, a similar streamline derived in CFD for the mixture fraction [194], was adopted to deliver a 2D distribution of progress variable, known as mixing trajectory. Indicated in Eq. (3.13), it only needs inlet and outlet terms for the surface. As shown in Figure 3.3.a, a control volume is defined across a given mixing trajectory, where the only unknown in Eq. (3.13) is the point at the right upper side. In the initial model version, the surfaces limiting the control volume were perpendicular to the mixing trajectory in the upwind side k. Information is only transported between neighbour trajectories due to the fact that the source term includes the flamelet diffusion along the gradient of mixture fraction. To reduce the model complexity, the surface has been changed to be perpendicular to the coordinate axis (Figure 3.3.b), thereby, the flow balance at the inlet and outlet will only account for the axial component velocity. Along the radial direction, the size of control volume is rearranged by a uniform mixture fraction distribution starting from f_{cl} (spray centreline value) to the position of 1% times of f_{cl} near the spray boundary.

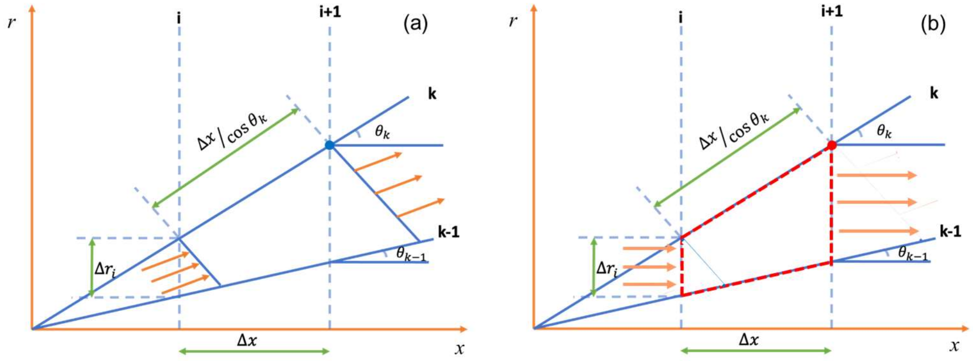

Figure 3.3. Definition of mixing trajectories. The control volume is designed with the axial inlet side i and outlet side i+1, the radial inlet at the bottom side k-1 and outlet at the upper side k. The only unknown in the control volume is the values of the point (i+1, k). The left sketch (a) shows the version proposed in [21], the right one is the optimized one in this thesis.

The convection conservation equation for Y_c along every mixing trajectory can be written as:

$$\frac{\Delta \int \rho Y_c dV}{\Delta t} = (\rho u Y_c \, \Delta A)_i - (\rho u Y_c \, \Delta A)_{i+1} + \dot{w}_c \Delta V \tag{3.13}$$

where the term on the left-hand side defines the transient accumulation/deaccumulation of progress variable, the first two terms on the right-hand side correspond to the balance of convective transport of progress variable, and the last one $\dot{w}_c$ is the source term, which is obtained from the tabulation in terms of mixture fraction, progress variable and strain rate. $\dot{w}_c$ is the term of $\dot{Y}_c \cdot \rho$, including both the flamelet local chemical rate and diffusion. Similar to Eq. (3.6), the conservation of progress variable can be rewritten as,

$$A_C \cdot u \cdot \rho \cdot Y_c + Bc \cdot \rho \cdot Y_c + C_C = 0 \tag{3.14}$$

However, this is only used for single cell, rather than the cross-section parameter u, f in Eq. (3.6). Therefore, the solution of progress variable is a 2D problem.

The flow chart of the Quasi-1D model is shown in Figure 3.4. Compared to the structure displayed in Figure 3.2, another user input, SR, is required to access the specified flamelet before the procedure of radial integrals. It is necessary to explain that the call-up tables here do not consider the effect of turbulence, i.e. only laminar flamelet information is stored, which is much different from the original UFPV model adopted in the CFD framework [190] [194] [195]. By solving the conservation equations of axial momentum and fuel mass fraction (substituting by mixture fraction under reacting spray), the 1D distribution of axial velocity $u_{cl}(x)$ and mixture fraction $f_{cl}(x)$ are obtained, and the self-similar profiles are also considered. With the chemical source term $\dot{w}_c$, the 2D distribution of local progress variable $Y_c(x,r)$ is obtained after the iteration on the local density, instead of the state relationships. Finally, the parameters of temperature, density and species mass fraction is achieved at each cell.

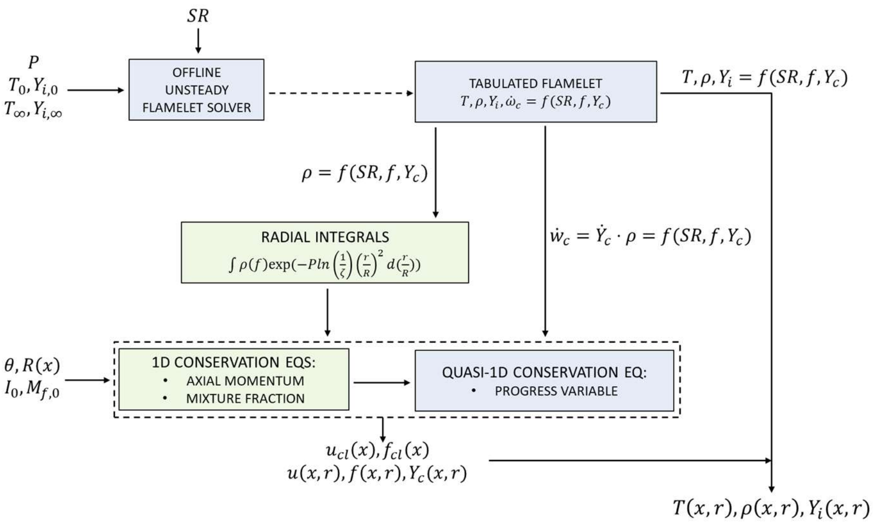

Figure 3.4. General structure of Quasi-1D modelling

3.5 Derivation of scalar dissipation rate estimation from self-similar mixture fraction and velocity fields

As mentioned in the previous section, the concept of flamelet is to describe a turbulent flame as an ensemble of laminar diffusion flamelets by scalar dissipation rate which has an effect on chemistry in terms of species along the mixture fraction gradient. For the implementation of single-step irreversible reaction on the reacting spray simulation using 1D spray model, the effect of scalar dissipation rate is ignored [20].

As the evolution with a flamelet is characterized by the scalar dissipation rate or strain rate, an estimation of this quantity is necessary. This section will develop a theoretical equation for this parameter that can be later used within the Quasi-1D model. Following the analogy to laminar flow, this parameter will be calculated from the 1D model using the laminar diffusivity and the time-average mixture fraction according to the following equation:

$$\chi = 2 \cdot D_l \cdot grad^2(f) = 2 \cdot D_l \cdot [\left(\frac{\partial f}{\partial x}\right)^2 + \left(\frac{\partial f}{\partial r}\right)^2] \tag{3.15}$$

where $grad^2(f)$ is the square of the gradient of the time-averaged mixture fraction. D_l is the laminar diffusivity, which will be calculated as,

$$D_l = -f \cdot \frac{v_{diff}}{\partial f/\partial r} \tag{3.16}$$

where v_{diff} is the diffusive velocity in radial direction. The gradient of mixture fraction along radial direction $\partial f/\partial r$ can be written as,

$$\frac{\partial f}{\partial r} = f_{cl}(x)\frac{-k_f 2r}{R(x)^2} exp\left[-k\left(\frac{r}{R(x)}\right)^2\right] \tag{3.17}$$

Considering the formula of v_{diff}, D_l can be written as

$$D_l = \frac{1}{4k_f k_u} u_{cl}(x) R(x) \tan(\theta/2) \frac{1-\exp\left[-k\left(\frac{r}{R}\right)^2\right]}{\left(\frac{r}{R}\right)^2} \tag{3.18}$$

where k, k_f, k_u are all equal to $\ln(100)$ at the condition of unity of Schmidt number, $u_{cl}(x)$ is the on-axis velocity at position x, and $R(x)$ is the spray radius at the position x. Furthermore, the term $\left(\frac{\partial f}{\partial x}\right)^2 + \left(\frac{\partial f}{\partial r}\right)^2$ can be written as,

$$\left(\frac{\partial f}{\partial x}\right)^2 + \left(\frac{\partial f}{\partial r}\right)^2 = \left[\frac{\partial f_{cl}}{\partial x}\right]^2 \exp\left[-2k_f\left(\frac{r}{R}\right)^2\right]\left\{1 + 4k_f^2\left(\frac{r}{R}\right)^2\left\{\left[\frac{\frac{f_{cl}}{R(x)}}{\frac{\partial f_{cl}}{\partial x}}\right]^2\left[\left[\frac{\partial R}{\partial x}\right]^2\left(\frac{r}{R}\right)^2 + 1\right] + \frac{1}{k_f}\frac{\frac{f_{cl}}{R(x)}}{\frac{\partial f_{cl}}{\partial x}}\frac{\partial R}{\partial x}\right\}\right\} \tag{3.19}$$

Substituting Eq. (3.17) – (3.18) into Eq. (3.14), the calculation of scalar dissipation rate will be finished. The important point about this analytical derivation lies upon the fact that χ is found to depend only on on-axis values $\left(f_{cl}, \frac{\partial f_{cl}}{\partial x}\right)$, the spray radius R and self-similar functions.

After this derivation, the calculated spatial scalar dissipation rate is validated against DNS calculations of a steady-state turbulent round jet of air discharging into quiescent air, as shown in Figure 3.5, i.e. a constant-density jet. The calculation results will be compared to the numerical analysis of Vlad Aparece-Scutariu [196] [197], who performed the modelling of spatial characteristics and scalar dissipation rate within DNS framework based on the experimental measurement studied by Panchapakesan and Lumley [198]. The gas flow was ejected into the windowless room from the outlet surface with diameter of $D = 10\ cm$. A top-hat injection rate is assumed at a constant velocity, fixed at M = 0.35 (120.05 m/s). As a user input to 1D spray model, spray angles should be provided, and the value can be obtained from the position of spray radial boundary. For a constant density steady-state jet, a single spray angle value is enough for the simulation.

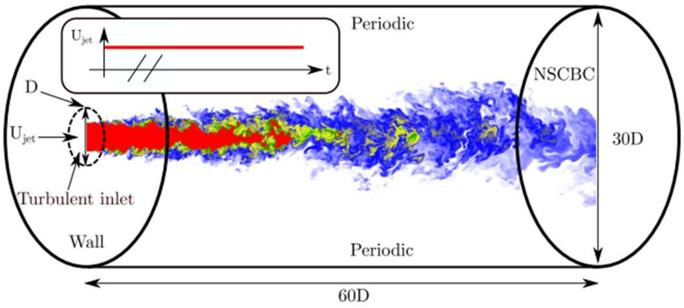

Figure 3.5. The flow configuration for the steady-state air-to-air jet [196]

To start the comparison, axial velocity and mixture fraction fields will be validated. As depicted in [196], DNS data also suggests a self-similarity in the steady-state jet, written as,

$$\frac{\bar{u}}{\bar{u_c}} = \exp(-\gamma_t \eta^2)$$

$$\frac{\bar{f}}{\bar{f_c}} = \exp(-\gamma_t Sc_t \eta^2) \tag{3.20}$$

where $\eta = r/x$, the radial profiles after $x/D = 10$ indicates a match value of γ_t = 90, $Sc_t = 0.72$. γ_t is similar to k in Eq. (3.*1*). For the 1D spray model, the self-similar profiles have been defined in Eq. (3.3) with a similar formula,

$$\frac{u}{u_{cl}} = \exp[-k_u \left(\frac{r}{x \cdot \tan{(\theta/2)}}\right)^2]$$

$$\frac{f}{f_{cl}} = \exp[-k_f \cdot Sc \left(\frac{r}{x \cdot \tan{(\theta/2)}}\right)^2] \tag{3.21}$$

Thereby, the spray angle can be obtained as 25.5° under the same criteria of spray radius that defined as the radial index where the local velocity equals to 1% of the axial value.

On the other hand, results of axial velocity and mixture fraction have been fitted by the authors to DNS data [196],

$$\frac{u_{cl}}{u0} = B \cdot \frac{d_0}{x}$$

$$f_{cl} = C \cdot \frac{d_0}{x} \tag{3.22}$$

where B, C represent the constant of velocity decay and mixture fraction, and they are fitted as B = 6.7, C = 5.6 respectively.

For a steady constant-density jet with self-similar radial profiles, the solution of Eq. (3.2) in u_{cl} and f_{cl} can be derived analytically to obtain an inverse function of axial distance [18],

$$u_{cl} = \sqrt{\frac{\ln(1/\zeta)}{2}} \cdot \frac{d_{eq}u_0}{\tan\left(\frac{\theta}{2}\right)} \cdot \frac{1}{x}$$

$$f_{cl} = \sqrt{\frac{\ln(1/\zeta)}{2}} \cdot \frac{1+Sc}{2} \cdot \frac{d_{eq}}{\tan\left(\frac{\theta}{2}\right)} \cdot \frac{1}{x} \tag{3.23}$$

where d_{eq} currently equals to d_0 for constant-density flow, ζ equals to 1%. Substituting the previously derived value of $Sc = 0.72$ and the derived spray angle $\theta = 25.5°$ from the radial profiles into Eq. (3.23), the term $\sqrt{\frac{\ln(1/\zeta)}{2}} \cdot \frac{1}{\tan\left(\frac{\theta}{2}\right)} = 6.78$, and the term $\sqrt{\frac{\ln(1/\zeta)}{2}} \cdot \frac{1+Sc}{2} \cdot \frac{1}{\tan\left(\frac{\theta}{2}\right)} = 5.82$, which are highly similar to the B,C values fitted to the DNS (Eq. (3.22)).

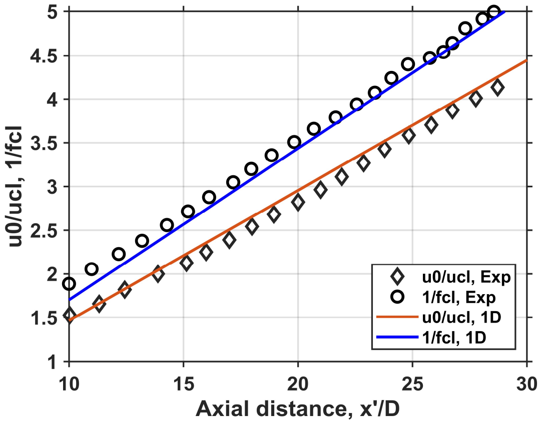

Figure 3.6. Axial profiles of velocity and mixture fraction. Markers: Measurement data [198]; lines (1D): 1D spray model

To compare the accuracy of this approach, good agreement on the axial velocity and mixture fraction is achieved in Figure 3.6 in terms of a linear relationship of $\frac{u_0}{u_{cl}}$ and $\frac{1}{f_{cl}}$ versus $\frac{x'}{D}$ by comparing the results from measurement and 1D spray model. It is necessary to point out x' is the distance counting from the virtual original $x = 0$, as displayed in Figure 3.1.

The 3D field of mean scalar dissipation rate of steady-state jet composes of the components $2D_t\left(\frac{\partial f}{\partial x}\right)^2$, $2D_t\left(\frac{\partial f}{\partial r}\right)^2$ and $2D_t\left(\frac{1}{r}\frac{\partial f}{\partial \theta}\right)^2$, corresponding to the terms in the axial, radial and azimuthal direction. For the first term, the on-axis mixture fraction decays with x^{-1} over this range, and turbulent diffusivity D_t remains constant. Thereby, the centreline scalar dissipation rate follows a relationship of negative fourth power of distance $\chi_{cl}{\sim}x^{-4}$. The derivation process to this relationship is given in Appendix. B. As indicated in DNS data, this fitting in the range of x/D from 14 to 29 is plotted in Figure 3.7 by characterizing the χ_{cl} according to the equation:

$$\chi_{cl}\cdot\tau = C_\chi/x^4 \tag{3.24}$$

where x in Eq. (3.24) actually represents x/D, $\tau = D/U_0$, and the fitting constant $C_\chi = 56$ is obtained for this jet.

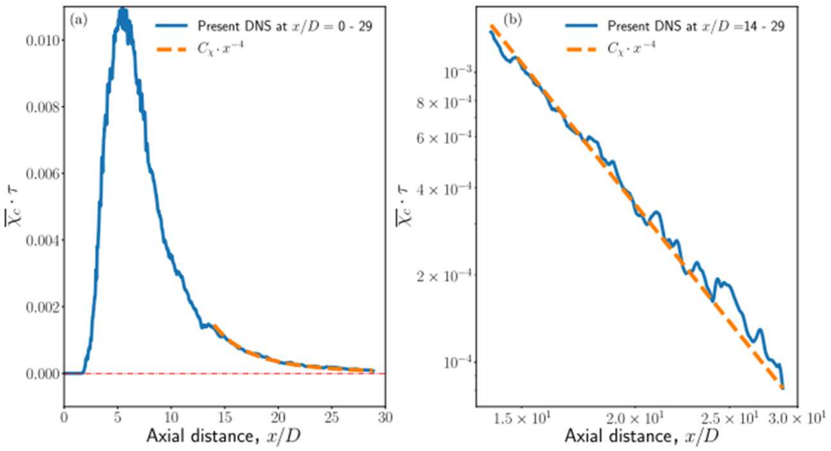

Figure 3.7. Evolution of normalised centreline scalar dissipation rate over the axial distance (a) in the linear scale and (b) in the log scale [196].

Following this idea, a similar plotting is presented in Figure 3.8 for the 1D model results, the dashed line represents the fitting over the range x/D = 15 – 28, and the coefficient is close to the theoretical value of 1.7447, as derived in Appendix B. The fitting coefficient from DNS data is much higher than the value derived from 1D spray model, approximately 30 times to the latter one. For the averaged scalar dissipation rate, the contribution of gradient of scalar fluctuations are much larger than gradients of the mean, that's to say, the mean scalar dissipation rate is approximately the turbulent dissipation rate [199]. Therefore, the absence of turbulence in 1D spray model results in the reduced magnitude of the on-axis scalar dissipation rate.

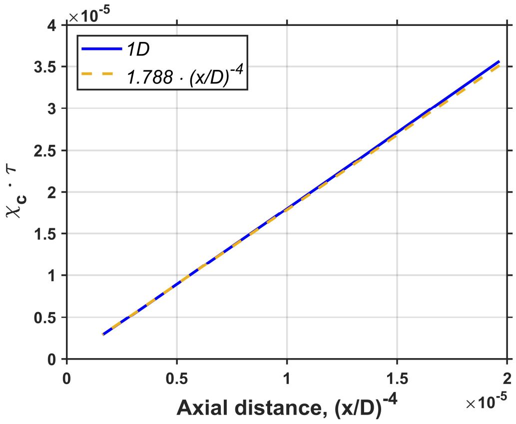

Figure 3.8. Evolution of characteristics of centreline scalar dissipation rate

The radial distribution of scalar dissipation rate is displayed in Figure 3.9 when divided by the maximum value. On the left, the average of DNS radial profiles for 14 < x/D < 29 are shown, along with experimental measurements of [200], and the models of Libby & bray [201] and Peters & Williams [202]. On the right, the curves derived in 1D spray model are similar at four different axial indexes (x/D = 15, 17.5, 20, 25). Similar to the results of Peters & Williams (orange curve in the left image), the peak locates around r/x = 0.076, then decays until the boundary. The value at the peak is approximately 100 times higher than that on the centerline. In DNS results [197], the term of $2D_t\left(\frac{\partial f}{\partial x}\right)^2$ is about 1/3 of the sum of the three terms. This means that the failure of the prediction of the simplified model for the scalar dissipation rate on the centreline is caused by the absence of fluctuation of mixture fraction in 1D spray model and Peters & Williams model.

To compensate for the disagreement on the centreline, we assume a plateau from the centreline to the peak (red line in the right image). To further qualify the feasibility of this assumption, the comparison of $\chi \cdot \tau$ in the centerline from DNS data and the maximum across the radial section in 1D spray model is presented in Figure 3.10. The value from both simulations is observed to be nearly the same after x/D = 20, where the jet is fully steady state, and the highest discrepancy at x/D = 14 is no more than 20% compared to DNS data. As a conclusion, the method using mean mixture fraction together with the assumption of constant value from the centerline to the peak is feasible to predict the scalar dissipation rate, and this is also the basics for the following optimizations of the implementation of multiple flamelets.

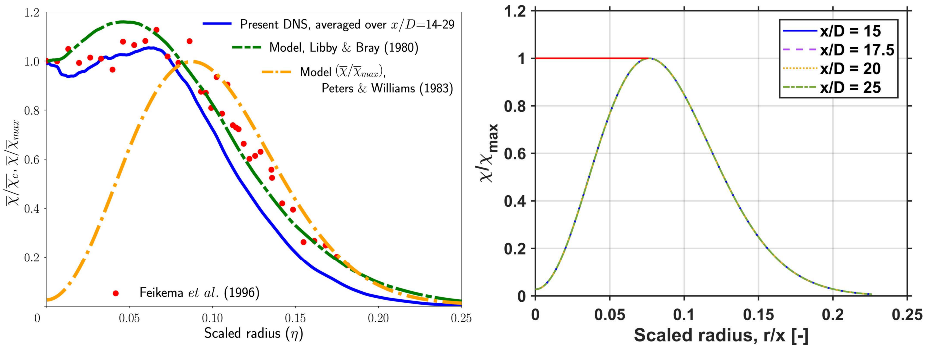

Figure 3.9. Radial profiles of scalar dissipation rate normalized by the centreline or the maximum. Left: the average over x/D = 14 – 29 in DNS data (blue line) [196], Experimental measurement in points from [200], and modelling of Libby & Bray [201] and Peters & Williams [202], right: normalized scalar dissipation rate by the maximum at four axial index of 1D spray model.

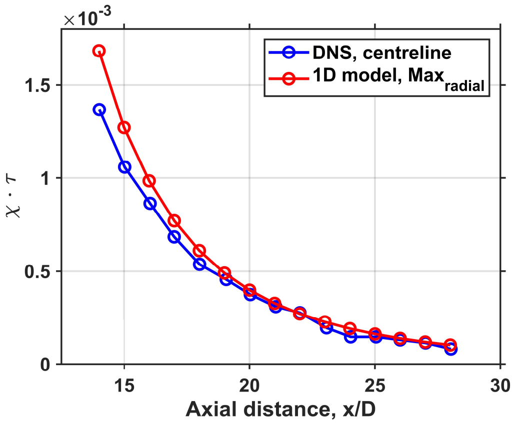

Figure 3.10. Comparison of characteristic scalar dissipation rate along the radial direction between DNS and 1D spray model.

3.6 Numerical details of the implementation

3.6.1. Spray tip reconstruction

Spray tip penetration can be obtained directly from the model by finding out the furthest cell starting from the nozzle where mixture fraction exceeding 0.001. This cell is found out after the solution of u_{cl} and f_{cl} from conservation equations of momentum and mixture fraction [18]. Furthermore, the convergence criteria on the progress variable calculation is also based on the comparison of on-axis mixture fraction between two successive iterations. As seen in Figure 3.11, there is a steep drop at the spray tip (shown in blue line). Indeed, from a purely theoretical point of view, the spray tip in 1D models is a discontinuity in on-axis variables. Such a strong gradient near the tip causes more iteration times, even leading to the failure of convergence. Therefore, a procedure to find a quasi-analytical prediction of tip penetration at every timestep has been developed, so that progress variable equation is only solved from the end of the intact length until this tip penetration value. In that sense, tip penetration can be obtained from a cross-sectional average velocity evolution [181] defined as:

$$\frac{dS}{dt} = \bar{u}(x = s) = \frac{I(x=s)}{M(x=s)} = \frac{\int \rho u^2 2\pi r dr}{\int \rho u 2\pi r} \tag{3.25}$$

Starting from that, the reconstruction of the tip penetration can be written as:

$$s_{tip}^{j} = s_{tip}^{j-1} + \bar{u}_{tip}^{j-1} \cdot \Delta t \tag{3.26}$$

where subscript tip is the section of spray tip, superscript j is current time index. $\bar{u}_{tip}^{j-1}$ is the cross-sectional average velocity at the spray tip at the previous instant $j-1$, which is the ratio of momentum to fuel mass rate, Δt is the timestep. Once $\bar{u}_{tip}^{j-1}$ is obtained, the corresponding s_{tip}^{j} will be derived by linear relationship. The reconstructed spray tip displayed in Figure 3.11 (red line) is only slightly shorter than the distance defined by the velocity. A comparison of the spray tip with two definitions under the inert nominal Spray A condition is shown in Figure 3.12, results agree quite accurately for both methods.

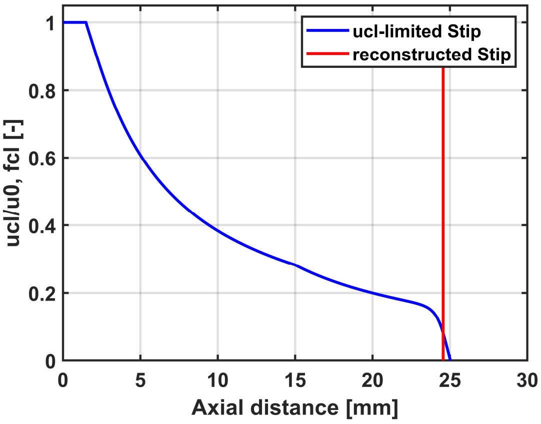

Figure 3.11. Normalize centreline velocity, mixture fraction along spray axial distance at 0.2 ms ASOI. The position of reconstructed spray tip was shown as red line.

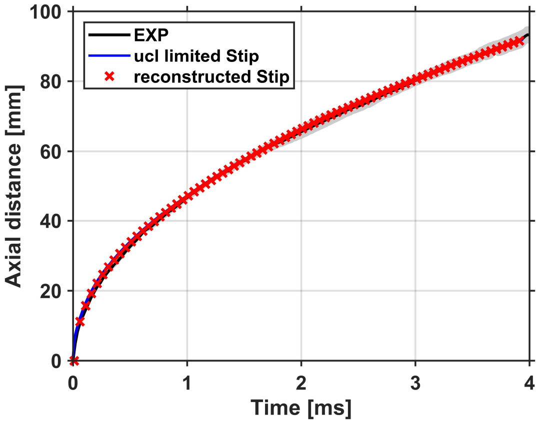

Figure 3.12. The comparison of spray penetration among the experiment data, limitation by velocity and the reconstructed data

3.6.2. Time discretization

As proposed in [21], the solution of progress variable adopts the chemical source term at the current timing j, then Eq. (3.13) can be written as,

$$\frac{(\rho Y_c \Delta V)^j-(\rho Y_c \Delta V)^{j-1}}{\Delta t} = (\rho u Y_c\, \Delta A)_i^j - (\rho u Y_c\, \Delta A)_{i+1}^j + (\dot{w}_c \Delta V)^j \tag{3.27}$$

According to this formulation, iterations are needed to obtain the chemical source term, which costs more computational cost and even causes convergence failure in some cases.

To further reduce the cost, an explicit method formulation is considered that uses the chemical source term at the previous timing $j-1$, hence, the procedure in Eq. (3.27) is not needed any more. Eq. (3.13) can be written as,

$$\frac{(\rho Y_c \Delta V)^j-(\rho Y_c \Delta V)^{j-1}}{\Delta t} = (\rho u Y_c\, \Delta A)_i^j - (\rho u Y_c\, \Delta A)_{i+1}^j + (\dot{w}_c \Delta V)^{j-1} \tag{3.28}$$

In this way, the chemical rate is assumed to be constant within an extremely short timestep (~1.5 μs) and the unknown $Y_c|_i^j$ can be solved immediately. Computational time shows that explicit method only takes 56 mins for the case of Nominal Spray A with an injection duration of 2 ms, while the original method in [21] takes 156 mins. This comparison was performed in a PC with Intel i5-9400F CPU at 2.9 GHz with 6 cores and 16 GB RAM memory [115].

3.6.3. Numerical reconstruction of the tabulated source term at the initial inert state

As discussed before, the solution of the conservation equation for progress variable (Eq.(3.28)) incorporates both the source term $\dot{w}_C$ and the density ρ by interpolation of the corresponding transient term in the flamelet manifold time evolution of Yc is very stiff, i.e. very small changes occur during a long time, and transition from the almost inert case (C=0) to the fully reacting one (C=1) is indeed very fast. Therefore, discretization in a finite number of C values around the inert state is very critical, i.e. a small error of the initial chemical reaction rate will cause amplified deviations of the solution against the flamelet one.

In the initial approach in [21], the source term value at inert state was simply equated to the second value in the tabulated time vector. Following the experience in [203], interpolation by means of piecewise linear interpolations is preferred so that the continuity in the time/progress variable relationship in the original flamelet simulation can be retained in the tabulated version. However, close to the initial values this procedure has to be improved. The idea is to find a corrected initial value $\dot{Y}_{C,0} = \dot{Y}_C(C = 0, inert\ state)$ that makes it possible to reach a given value C_1 in a time t_1 when integrating $\dot{Y}_C$ with a linear interpolation in the interval [0, C_1]. In general, C_1 corresponds to the first non-null tabulated value of the vector C used for the chemical database. In some cases, specified t_1 is used, i.e., 5.0e-4 s [191], then, C_1 was linear interpolated by the adjacent values.

From the concept of piecewise linear interpolation, a linear relationship of the corresponding source term

$$\dot{Y}_C = m \cdot c + \dot{Y}_{C,0} \tag{3.29}$$

is built in the region $c \in [0, c_1]$ with a slope $m = (\dot{Y}_{C,1} - \dot{Y}_{C,0})/c_1$. Referring to the definition of $\dot{\omega}_c$ and the integrating in the interval $[0, c_1]$,

$$\dot{\omega}_c = \frac{\dot{Y}_C}{Y_C^{equil} - Y_C^{inert}} = \frac{dc}{dt} -> \int_0^{t_1} \frac{dt}{Y_C^{equil} - Y_C^{inert}} = \int_0^{c_1} \frac{dc}{\dot{Y}_C} = \int_0^{c_1} \frac{dc}{mc + \dot{Y}_{C,0}} \tag{3.30}$$

Solving

$$\frac{t_1}{Y_C^{equil} - Y_C^{inert}} = \frac{1}{m} \ln\left(\frac{mc_1 + \dot{Y}_{C,0}}{\dot{Y}_{C,0}}\right) = \frac{c_1}{\dot{Y}_{C,1} - \dot{Y}_{C,0}} \ln\left(\frac{\dot{Y}_{C,1}}{\dot{Y}_{C,0}}\right) \tag{3.31}$$

Assuming $t_1' = \frac{t_1}{Y_C^{equil} - Y_C^{inert}}$, the above expression can be written as,

$$\frac{\exp\left(\frac{t_1'}{c_1} Y_{C,1}\right)}{\frac{t_1'}{c_1} \dot{Y}_{C,1}} = \frac{\exp\left(\frac{t_1'}{c_1} \dot{Y}_{C,1}\right)}{\frac{t_1'}{c_1} \dot{Y}_{C,1}} \tag{3.32}$$

With the notation $A = \frac{\exp\left(\frac{t_1'}{c_1} Y_{C,1}\right)}{\dot{Y}_{C,1}}$, $B = \frac{t_1'}{c_1}$, the expression can be rewritten as,

$$-\frac{B}{A} = -B\dot{Y}_{C,0}\exp\left(-B\dot{Y}_{C,0}\right) \tag{3.33}$$

This is similar to lambert W function $f(x) = x \cdot \exp(x)$, and the real value of $\dot{\omega}_{Yc,0}$ will be,

$$\dot{Y}_{C,0} = \begin{cases} -\frac{W_0\left(-\frac{B}{A}\right)}{B}, -B\dot{Y}_{C,1} < -1 \\ -\frac{W_{-1}\left(-\frac{B}{A}\right)}{B}, -B\dot{Y}_{C,1} \geq -1 \end{cases} \tag{3.34}$$

Figure 3.13 displays an example of the accuracy of the previously derived procedure, which has been validated against a flamelet case. The figure shows a comparison of solution $C = C(t)$ provided by the tabulated flamelet manifold and the reconstructed profiles with the reconstructed initial value,

$$Y_c^j = Y_c^{j-1} + \dot{Y}_c^{\,j-1} \cdot \Delta t \tag{3.35}$$

In the left image, good reconstructions to normalized progress variable are observed at the timestep ($\Delta t = 0.2$ & $1.0\ \mu s$) under the stoichiometry, indicating that $\dot{Y}_c$ can be seen as the same between the adjacent frames. Enlarging the timestep, the time shift in the curves of normalized progress variable is still within the range of 5 μs when the timestep is shorter than $2.0\ \mu s$, while the shifting becomes significant when the timestep increases to 4.0 μs. In the right image, the comparison under different mixture fractions is presented at the timestep of $0.2\ \mu s$. The reconstructed normalized progress variable matches well with the tabulated in lean and stoichiometric mixtures, only with a slightly earlier shift in rich mixtures. To balance the computational cost, $\Delta t = 1.0 - 2.0\ \mu s$ is a good time interval that will be noticed in 1D model.

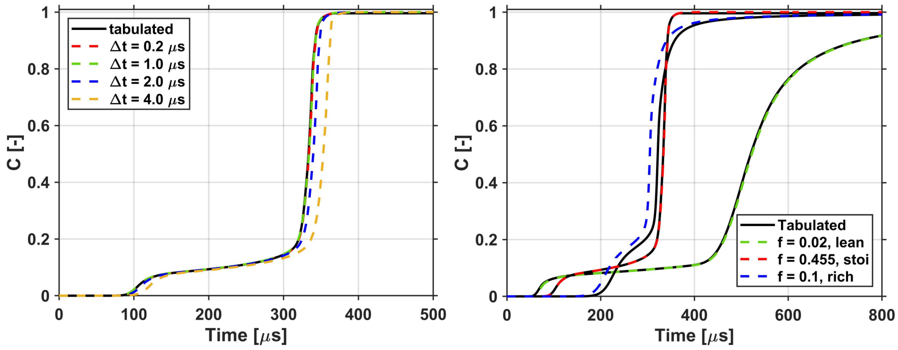

Figure 3.13. Comparison between the tabulated and reconstructed profiles C = C(t). The sensitivity of timestep (Δt) on the stoichiometric mixture fraction is shown in the left image; the performance in different mixtures is shown in right image. Mechanism: LLNL; Condition: Nominal Spray A; Strain rate: 50 1/s.

3.7 Liquid spray effects

The initial assumption of gas jet theory still can deliver a good prediction to reacting spray tip penetration. Observations from gas jet are relevant because many aspects of the mixing and transient development of diesel jets are analogous to single-phase transient gas jet [116]. However, the calculated mixture fraction in gas phase is higher than the real one in the dense spray region, which is calculated as a diffuse interphase, i.e. the local density is calculated from that of a local mixture including both liquid and gas phases. This overprediction in mixture fraction results in faster ignition behavior, especially for low injection pressure and large orifice diameter. In addition, to compensate for the enthalpy loss during the vaporization cooling process, the fuel initial temperature in the flamelet manifold was set as 185 K to match the maintained fuel temperature at 363 K in the measurement.

Under the mixing-controlled spray hypotheses, LL is defined as the location where the mixture fraction on the axis starts to be lower than a characteristic value, corresponding to a mixing-controlled spray evaporation f_{evap} (Table 4.1 in Chapter 4). Near the nozzle, the mixture temperature is close to fuel temperature, and the reactions are also weak. Thus, to balance the computational cost, no reactions are assumed to occur upstream of LL, as displayed in Figure 3.14. It is important to point out that this assumption would not be much feasible under the condition of high-reactive environment and low injection pressures, due to the observed CH_2O formation at LL [204] [205], and the LOL is even shorter than LL [206].

3.8 Further considerations at ignition timing

Ignition propagation

According to the previous description, interaction between adjacent trajectories is not considered in terms of progress variable transport [21]. This results in a development of ignition along a particular trajectory, which extends radially as far as each trajectory ignites on its own (more details will be found in the next chapter). In the end, trajectories at high radial locations and/or those very close to the axis ignite much more slowly, as shown previously [115], which is far from a more physical ignition of a Diesel-like spray, starting at particular locations and later transiting to a fully reacted spray over the spray cross-section.

To compensate for such unphysical ignition, the transition to fully reacted state ($C = 1$) at ignition timing is imposed in the present study for all the spray region downstream of the lift-off length until the spray tip, irrespective of the trajectory state. Figure 3.14 shows this igniting region as a trapezoidal zone with a red boundary. This transition extends from a characteristic axial position $x_{LOL,c}$. In this sense, $x_{LOL,c}$ is defined at the closest position to the orifice where the radially integrated mass at ignited state $(mass^{i}_{ignited})$ represents more than the fraction $\alpha_{LOL,c}$ of the total mass within the spray cross-section ($mass^{i}_{tot}$).

Hence, two parameters will affect the $xLOL_C$, namely $\alpha_{LOL,c}$ and the criteria of C value defining the ignition. As depicted in Figure 3.15, the sensitivity of this constant ($\alpha_{LOL,c}$ =10%, 15%, 20% and 25%) is presented in the left image, and the effect of different C value for ignition (C = 0.80 – 0.95) is given in the right one. The results of lift-off length from OH mass fraction $xLOL_{OH}$ is also plotted as a comparison. At first glance, changing on the two parameters shows little effect on $xLOL_{OH}$. The situation where $xLOL_C$ slightly longer than $xLOL_{OH}$ is the most practical solution to this combustion state transition, which only modifies the downstream distribution of temperature and species, rather than the ignition delay timing and/or lift-off length location. By comparing experimental values at the nominal Spray A condition, the combination of $\alpha_{LOL,c}$ = 20% at C = 0.95 is selected for the subsequent calculations.

Ignition-induced radial Expansion

Finally, previous studies have shown the importance of including a radial expansion ΔR term of the spray at the ignition timing to enable adequate predictions of local mixing and velocity distributions [152] [167], as well as tip penetration in agreement with experimental observations. In particular, the absence of ΔR results in faster penetration and slower mixing. This precedent work has shown that the radial expansion can be calculated by a mass balance between inert and reacting states downstream of the ignition location, written as Eq. (3.36).

$$\int_{LO\ C}^{S}\int_{0}^{R}\rho_{inert}\cdot 2\pi r\cdot dr\cdot dx = \int_{LO\ C}^{S}\int_{0}^{R+\Delta R}\rho_{react}\cdot 2\pi r\cdot dr\cdot dx \tag{3.36}$$

The same integral function appears on both sides of the equation, with the left-hand side term being integrated under inert condition (C = 0), and right-hand side one under reacting ones, just after start of combustion. The same approach has been followed here with the Quasi-1D spray model.

It must be noted that ΔR is calculated once at the start of combustion, and it remains constant in the following timings. An example of such radial expansion is presented in Figure 3.16, where a single flamelet with strain rate at 50 1/s is incorporated to Quasi-1D model. As observed from the temperature contour at steady state (2.0 ms ASOI), the forced transition of combustion state is only affecting the part of the spray downstream of $xLOL_C$ that temperature distribution is only dependent on the local mixture fraction and the combustion state reaching the steady state (C = 1). Compared to the results of trajectory ignition in the first row, this transition is more effective in the fuel-rich region, especially in the area where equivalence ratio larger 2.0. To make a difference in ignition behavior, the ignition with the transition is named as intertrajectory ignition. Furthermore, this transition also results in a shift of the equivalence ratios surface towards spray boundary, which is more significant in the radial expansion condition $\Delta R > 0$.

In general, this forcing transition is a balanced choice to compensate for the absence of Y_C diffusion, and it mainly influence the contours distribution of temperature and species, while shows little effect on ID & LOL prediction, the most important combustion metrics in Quasi-1D modelling.

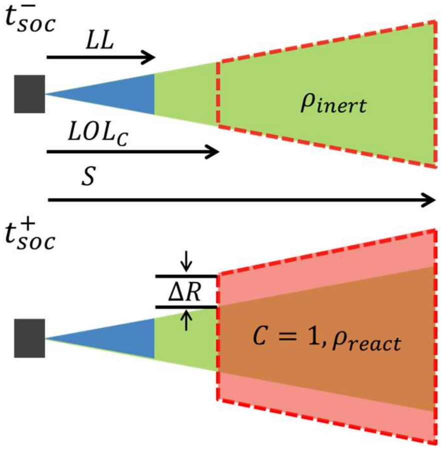

Figure 3.14. Schematic of mixing-controlled evaporation assumption, transition of combustion state and radial expansion in Quasi-1D model

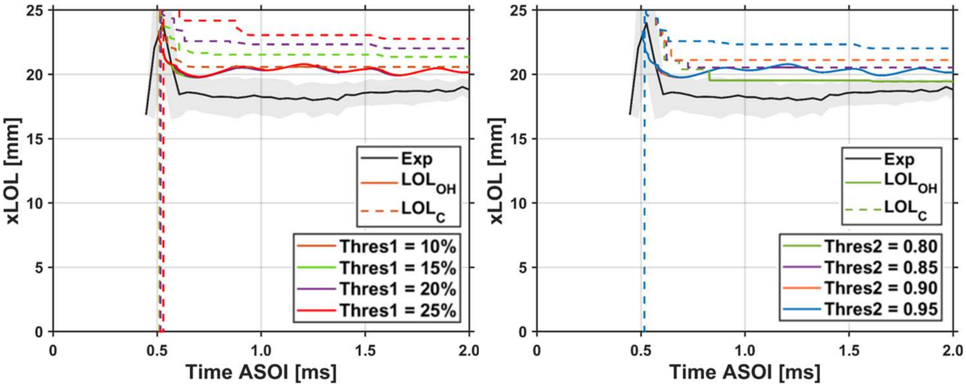

Figure 3.15. Sensitivity of lift-off length defined by OH mass fraction and C to $\alpha_{LOL,c}$ (Thres1); and to the criteria to define the ignition state by C value (Thres2).

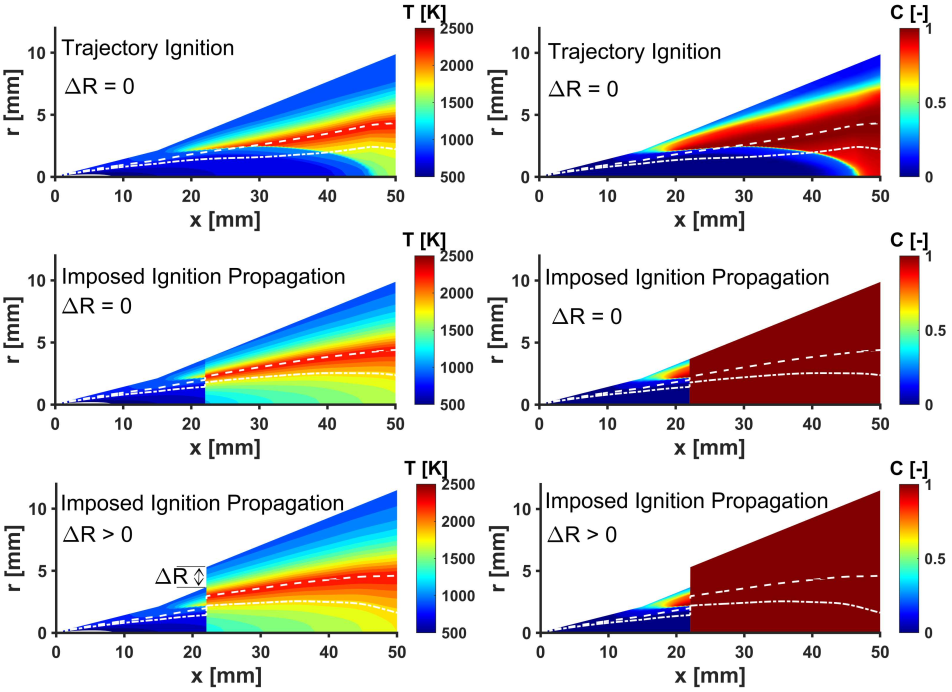

Figure 3.16. The comparison of temperature (T) contours and normalized progress variable (C) contours at steady state (2.0 ms ASOI) with the discussed optimizations. Mechanism: LLNL; Strain rate: single@50 1/s. Upper: results with trajectory ignition (original version); middle: results with imposed ignition trajectory without radial expansion; bottom: results with imposed ignition propagation with radial expansion. The dash line: stoichiometric ratio surface. The dotted line: the surface of $\phi = 2.0$

3.9 Summary and Conclusions

This chapter presents the development of the 1D spray model and highlights the optimizations for the reacting turbulent spray simulation coupling to laminar flamelet, finally named as Quasi-1D model. Thereby, this developed model can realize a full prediction of important combustion metrics, namely ignition delay, lift-off length and contours of temperature and species concentration. The details of the optimizations of the Quasi-1D model since its initial proposal in [21] are summarized as follows:

- In pursuit of model simplification, modifications have been made by adjusting the control volume to be defined perpendicular to the axial coordinate. Furthermore, spray tip was reconstructed using a cross-sectional average velocity to effectively prevent the iteration failure when updating local density and progress variable. An explicit time formulation for the progress variable, incorporating a transient term at the previous timing, was also implemented to further reduce the computational cost.

- To enhance the accuracy of ID & LOL prediction, the first optimization is to reconstruct the chemical reaction rate at the initially inert state by means of a numerical procedure that has already been used in the past at CMT. Good agreement with the tabulated evolution of normalized progress variable is achieved by this reconstruction at a short time interval. Additionally, the assumption of no reactions upstream of liquid length is adopted, which weakens the effect of long local residence time in the extremely lean mixture and prolongs the ignition delay and lift-off length.
- As a balanced choice of progress variable diffusion among the trajectories at ignition timing, a so-called 'Imposed ignition spread' is implemented, which enforces the chemical state downstream of the lift-off length to be steady. This adjustment improves the reactivity in the spray centreline and near the boundary, which only influences the distribution of temperature and species, without affecting the ID & LOL prediction. The steep drop in density causes an acceleration of penetration, which is then slowed down by the expansion in the radial direction.
- The key procedure in flamelet incorporation is to find the reasonable strain rate, especially in the radial direction. Initially, the calculation of local strain rate is validated using experimental results of an air-to-air flow. In addition, a further comparison with a DNS result indicates a good match for r/x > 0.07 in the developed region, while the calculated results in the inner regions are much underestimated. Lastly, the assumption of constant value from the centreline to the peak is adopted to predict the scalar dissipation rate.

3.10 Appendix. A. Calculation of flow velocities in the radial direction

In Eq. (3.16), turbulent diffusivity is a function of radial diffusive velocity v_{diff}, defined as the difference of radial velocity v_{tot} to mean radial velocity v. The derivation of these two terms will be presented in the following:

Radial mean velocity v

In a control volume, the continuity equation states the rate at outlet is equal to the rate at inlet plus the accumulation within the volume. The differential form of it for a constant density can be written as,

$$\frac{\partial(\rho u r)}{\partial x}+\frac{\partial(\rho v r)}{\partial r}=0 \tag{3.37}$$

Along the radial direction, the velocity follows Gaussian profile,

$$u = u_{cl}(x)\, exp\left[-k_u \left(\frac{r}{R(x)}\right)^2\right] \tag{3.38}$$

and the first derivative to x can be written as,

$$\frac{\partial u}{\partial x} = exp\left[-k_u \left(\frac{r}{R(x)}\right)^2\right]\left\{\frac{\partial u_{cl}}{\partial x} + u_{cl}(x)\frac{\partial R}{\partial x}\frac{2k_u r^2}{R^3}\right\} \tag{3.39}$$

substituting Eq.(3.39) into Eq.(3.*37*),

$$v = -\frac{1}{r}\frac{\partial u_{cl}}{\partial x}\int_0^r exp\left[-k_u \left(\frac{r}{R(x)}\right)^2\right] r\, dr - \frac{1}{r} u_{cl}(x)\frac{\partial R}{\partial x}\frac{2k}{R^3}\int_0^r exp\left[-k_u \left(\frac{r}{R(x)}\right)^2\right] r^3 dr \tag{3.40}$$

The integral $\int_0^r \exp\left[-k_u \left(\frac{r}{R(x)}\right)^2\right] r\, dr$ can be written as,

$$\int_0^r \exp\left[-k_u \left(\frac{r}{R(x)}\right)^2\right] rdr = -\frac{R}{2k}\int_0^\zeta \exp[\zeta]\, d\zeta = \frac{R^2}{2k}(1 - \exp[\zeta])$$

$$\zeta = -k_u \left(\frac{r}{R(x)}\right)^2 \rightarrow d\zeta = -\frac{k_u}{R^2} 2rdr \tag{3.41}$$

The integral $\int_0^r \exp\left[-k_u \left(\frac{r}{R(x)}\right)^2\right] r^3 dr$ can be written as,

$$\int_0^r \exp\left[-k_u \left(\frac{r}{R(x)}\right)^2\right] r^3 dr = \frac{R^4}{2k^2}\int_0^\zeta \exp[\,\zeta]\,\zeta d\zeta = \frac{R^4}{2k^2}(\exp[\,\zeta]\,(\zeta - 1) + 1)$$

$$\zeta = -k_u \left(\frac{r}{R(x)}\right)^2 \rightarrow \zeta^2 = k_u^2 \left(\frac{r}{R(x)}\right)^4 \rightarrow 2\zeta d\zeta = \frac{k_u^2}{R^4} 4r^3 dr \rightarrow r^3 dr = \frac{2\zeta d\zeta}{\frac{k^2}{R^4}4} = \frac{R^4}{2k_u^2}\zeta d\zeta$$

$$\int_0^\zeta \exp[\,\zeta]\,\zeta d\zeta = \exp[\,\zeta]\,(\zeta + 1) \tag{3.42}$$

Thus, Eq. (3.*40*) can be written as,

$$v = u\frac{R^2}{rx}\frac{1}{k_u}\left(\frac{(-1\, exp[-\zeta] + 1)}{2} - \zeta\right) = u\frac{R^2}{rx}\frac{1}{k_u}\left(\frac{1 - exp[-\zeta]}{2} - \zeta\right) \tag{3.43}$$

Finally, radial mean velocity at each cell will be written as,

$$v(x,r) = u(x,r)\frac{R}{x}\left(\frac{r}{R} + \frac{1 - exp\left[k_u\left(\frac{r}{R}\right)^2\right]}{2k_u\frac{r}{R}}\right) = u(x,r)\, tan(\theta/2)\left(\frac{r}{R} + \frac{1 - exp\left[k_u\left(\frac{r}{R}\right)^2\right]}{2k_u\frac{r}{R}}\right) \tag{3.44}$$

Radial velocity, v_{tot}

Under the assumption of equal diffusivity, the radial velocity can be derived from mixture fraction transport equation:

$$\frac{\partial(\rho f u r)}{\partial x}+\frac{\partial(\rho f v_{tot} r)}{\partial r}=0 \tag{3.45}$$

where v_{tot} is the sum of mean radial velocity v_{tot} and diffusive velocity v_{diff}. Mixture fraction along the radial direction also follows the Gaussian distribution,

$$f=f_{cl}(x)\exp\left[-k_f\left(\frac{r}{R(x)}\right)^2\right]$$

$$fu=f_{cl}u_{cl}\exp\left[-k_{tot}\left(\frac{r}{R}\right)^2\right] \tag{3.46}$$

where $k_{tot}=k_u+f_f$, the first derivative to x can be written as,

$$\frac{\partial fu}{\partial x}=\exp\left[-k_{tot}\left(\frac{r}{R(x)}\right)^2\right]\left\{\frac{\partial f_{cl}u_{cl}}{\partial x}+f_{cl}(x)u_{cl}(x)\frac{\partial R}{\partial x}\frac{2k_{tot}r^2}{R^3}\right\} \tag{3.47}$$

Thus, v_{tot} can be written as,

$$v_{tot}=$$
$$-\frac{1}{rf}\frac{\partial f_{cl}u_{cl}}{\partial x}\int_0^r exp\left[-k_{tot}\left(\frac{r}{R(x)}\right)^2\right]r\,dr\,\frac{1}{rf}f_{cl}u_{cl}\frac{\partial R}{\partial x}\frac{2k_{tot}}{R^3}\int_0^r exp\left[-k_{tot}\left(\frac{r}{R(x)}\right)^2\right]r^3dr \tag{3.48}$$

Similar to the conversion of integrals in Eq.(3.42), Eq.(3.*48*) can be forward derived as,

$$v_{tot}=-\frac{1}{rf}\frac{\partial f_{cl}u_{cl}}{\partial x}\frac{R^2}{2k_{tot}}(1-exp[\zeta])-\frac{1}{rf}f_{cl}u_{cl}\frac{\partial R}{\partial x}\frac{2k_{tot}}{R^3}\frac{R^4}{2k_{tot}^2}(exp[\,\zeta]\,(\zeta-1)+1) \tag{3.49}$$

$$f_{cl}u_{cl}=\frac{k^{**}}{x^2}\rightarrow\frac{\partial f_{cl}u_{cl}}{\partial x}=-2\frac{f_{cl}u_{cl}}{x}$$

$$\frac{\partial R}{\partial x}=\frac{R}{x}=\tan(\theta/2)$$

Then, it can be simplified as,

$$v_{tot}(x,r)=u(x,r)\,tan(\theta/2)\frac{r}{R} \tag{3.50}$$

Finally, the radial diffusive velocity will be derived as,

$$v_{diff}(x,r)=v_{tot}(x,r)-v(x,r) \tag{3.51}$$

In a steady-state jet, the example of calculated v_{tot}, v, and v_{diff} is presented in Figure 3.17, normalized by the axial velocity u_{cl}. From the centreline to the half radius, all the three terms are positive, and v_{tot} reaches the maximum at the position of r/R =

0.3, consistent with the position where the peak scalar dissipation rate locates. Towards the spray boundary, mean radial velocity tends to be negative, and the total radial velocity approaches zero, resulted from a high diffusive velocity near the spray boundary.

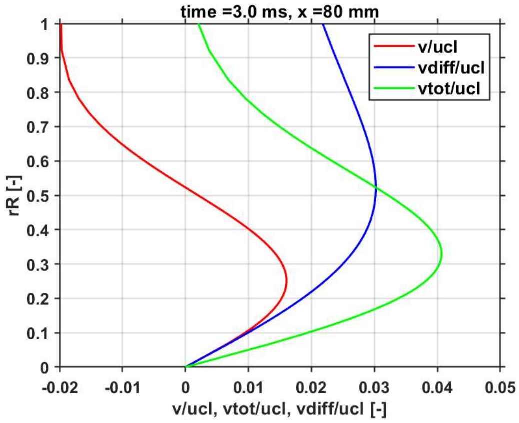

Figure 3.17. Radial mean velocity, radial total velocity, and radial diffusive velocity normalized to local centreline velocity along axial direction

3.11 Appendix. B. Characteristics of on-axis scalar dissipation rate

The calculation to scalar dissipation rate χ concludes the parameters of turbulent diffusivity D_t and the square of the gradient of mixture fraction $\left(\frac{\partial f}{\partial x}\right)^2 + \left(\frac{\partial f}{\partial r}\right)^2$, as written in Eq. (3.15). Along the centreline, the scalar dissipation rate was observed to follow a relationship of negative fourth power of distance $\chi_{cl} \sim x^{-4}$, and this trend is also found when it extends to other trajectories. Described in 1D spray model, the mixture fraction along the centreline drops downstream with the typical x^{-1} law in the developed region, thereby, the square of the gradient of mixture fraction also follows the x^{-4} law. In other words, turbulent diffusivity should be constant along the centreline, the theoretical analysis is presented in the following.

Firstly, the formula of laminar diffusivity D_l is written as

$$D_l = \frac{1}{4k_u k_f} u_{cl}(x) R(x)\, tan(\theta/2) \frac{1-exp\left[-k\left(\frac{r}{R}\right)^2\right]}{\left(\frac{r}{R}\right)^2} \tag{3.52}$$

and the velocity also follows the x^{-1} law,

$$u_{cl} = \sqrt{\frac{\ln(100)}{2} \cdot \frac{d_{eq} u_0}{\tan\left(\frac{\theta}{2}\right)}} \cdot \frac{1}{x} \tag{3.53}$$

and therefore

$$D_l = \sqrt{\frac{log(100)}{2}} \frac{u_o d_{eq}}{2k_f} tan(\theta/2) \frac{1-exp\left[-k\left(\frac{r}{R}\right)^2\right]}{2k\left(\frac{r}{R}\right)^2} = \frac{1}{4} \frac{tan(\theta/2)}{\sqrt{log(100)/2}} \frac{u_o d_{eq}}{Sc} \frac{1-exp\left[-k\left(\frac{r}{R}\right)^2\right]}{2k\left(\frac{r}{R}\right)^2} \tag{3.54}$$

For the trajectory of the spray centreline,

$$\frac{r}{R} = 0$$

Then,

$$D_{l,cl} = \frac{1}{4} \frac{\tan(\theta/2)}{\sqrt{\log(100)/2}} \frac{u_o d_{eq}}{Sc} \frac{1}{2} = \frac{1}{8} \frac{\tan(\theta/2)}{\sqrt{\log(100)/2}} \frac{u_o d_{eq}}{Sc} = constant \tag{3.55}$$

Secondly, moving towards to the calculation of scalar dissipation rate, on-axis mixture fraction fits the law of x^{-1}, written as,

$$f_{cl} = \frac{(Sc+1)}{2} \sqrt{\frac{\log(100)}{2} \frac{d_{eq}}{\tan\left(\frac{\theta}{2}\right)}} \cdot \frac{1}{x} = \frac{(Sc+1)}{2} k_{cl,u} \cdot d_{eq} \frac{1}{x} \tag{3.56}$$

Next, on-axis scalar dissipation rate can be derived as,

$$\chi_{cl} = 2 \frac{tan\,(\theta/2)}{8\sqrt{\log(100)/2}} \frac{u_o d_{eq}}{Sc} \left[\frac{f_{cl}}{x}\right]^2 = 2 \frac{1}{8k_{cl,u}} \left[\frac{(Sc+1)}{2} k_{cl,u}\right]^2 \frac{u_o d_{eq}}{Sc} \frac{d_{eq}^2}{x^4} \tag{3.57}$$

Divided by the term $\frac{u_0}{d_{eq}}$,

$$\frac{\chi_{cl} d_{eq}}{u_0} = 2 \frac{1}{8k_{cl,u}} \left[\frac{(Sc+1)}{2} k_{cl,u}\right]^2 \frac{1}{Sc} \left(\frac{d_{eq}}{x}\right)^4 = 2 \frac{1}{8} \left[\frac{(Sc+1)}{2}\right]^2 \frac{k_{cl,u}}{Sc} \left(\frac{d_{eq}}{x}\right)^4 \tag{3.58}$$

Finally, the coefficient $2 \frac{1}{8} \left[\frac{(Sc+1)}{2}\right]^2 \frac{k_{cl,u}}{Sc}$ equals to 1.7447, as shown in Figure 3.8. Although it also fits the law x^{-4}, the coefficient is much smaller than the value 56 derived in [197].

Chapter 4

The effects of chemical mechanism and mixing characteristics on n-Dodecane reacting sprays

Content

4.1 Introduction

Building upon the concepts outlined in Chapter 3, a Quasi-1D model was developed by integrating a spray model with a single flamelet manifold. This manifold is pre-tabulated offline and takes into account variations in ambient components, thermophysical properties, and fuel reactivity. The present chapter applies the model to discuss the impact of spray mixing characteristics, namely injection pressure and nozzle diameter, on the prediction of combustion metrics in conjunction with various chemical mechanisms. The simulation utilizes the same flamelet manifold across different mixing conditions. Experimental data suggests that higher injection pressure enhances fuel evaporation and mixing, resulting in a shorter ID, while the increase in momentum leads to a longer LOL. Conversely, reducing the nozzle orifice diameter boosts the air entrainment rate, leading to a consistent decrease in ID and LOL [194].

Besides the assumptions describing the physical spray flow in 1D spray model, the choice of chemical mechanism and definition of progress variable (Y_c) in the UFPV model, are also considered crucial factors influencing predictions. Using this combustion model and the progress variable definition $Y_c = Y_{CO} + Y_{CO_2}$, Payri et al. [195] conducted simulations of ECN Spray A using RANS-CFD framework with chemical mechanisms proposed by Narayanaswamy (abbreviated as Nara) [207], Yao [208], Wang [209], and Cai [210]. Results indicated that Yao mechanism is more accurate for predicting ID under varying ambient temperatures, while Cai mechanism performs better for ID predictions under the conditions varying oxygen concentration. On the other hand, Nara and Wang mechanisms are more effective for LOL predictions. Pachano [211] modified the definition of progress variable to $Y_c = 0.75Y_{CO} + Y_{CO_2} + Y_{H_2O}$ to ensure monotonic time evolution of Y_c, and achieved accurate prediction to both ID & LOL using Yao mechanism. The inclusion of more components in this definition, theoretically leads to a more accurate description of the chemical state [212]. Despite this, predicting under low temperature conditions remains challenging. The present work will make use of the same Y_c definition as in [211], which has been used in Chapter 3.

Quasi-1D modelling in this chapter was arranged as follows: in section 4.3, the influence of chemical mechanisms was studied by comparing the performance of Quasi-1D modelling on combustion metrics (ID & LOL) and contours (Temperature, CH_2O) using Yao, LLNL [184] and Nara [207] mechanism. Next, the effect of mixing will be conducted in section 4.4 with the variation of injection pressures and nozzle diameters under Nominal conditions. Finally, in section 4.5, the model extension was performed under the ECN recommended conditions [213], consisting of the variation of ambient temperature, oxygen concentration, nozzle diameter and injection pressure. But prior to these sections, in section 4.2, an overview of the operating conditions used for the forthcoming study will be presented

4.2 Overview of operating conditions

The boundary conditions of the parametric study correspond to those experimentally measured in the constant pressure flow facility available at CMT [22], where the ambient gas thermochemical conditions are controlled by supplying an oxygen and nitrogen mixture compressed and pre-heated before entering the open combustion chamber in which the fuel is injected. Table 4.1 shows the configurations of the investigated conditions, which are defined in terms of nozzle diameter and injection pressure, and ambient air density, temperature and oxygen content. The nominal case (marked as bold) is defined by setting the ambient conditions at $T_a = 900\ K, X_{O_2} = 15\%, P_{inj} = 1500\ bar, \rho_a = 22.8\ kg/m^3$ [214], and three parametric studies are considered:

- The first study varied the temperature from $T_a = 800\ K$ to $T_a = 1000\ K$ while maintaining the oxygen concentration at the nominal level.
- The second study focused on the effects of dilution levels, with the oxygen concentration modified to that of ambient air (21% in mole fraction) and temperature at the nominal level.
- The third study involved varying the nozzle diameter using Spray A (D_0 = 89.4 μm, no. 210675) and Spray D (D_0 = 190.3 μm, no. 209135).

All studies were conducted with injection pressure P_{inj} ranging from 500 bar to 1500 bar, while ambient density remains constant for all operating conditions.

Table 4.1. Parameters defining operating conditions. Nominal conditions are denoted in bold.

Nozzle/Diameter[μm]	P_{inj} [bar]	ρ_a[kg/m^3]	T_a [K]	X_{O2} [%]	fevap [-]
Spray A / 89.4	500/1000/1500	22.8	800	15	0.3115
Spray A / 89.4	500/1000/**1500**	22.8	**900**	**15**	0.3636
Spray A / 89.4	500/1000/1500	22.8	1000	15	0.4085
Spray A / 89.4	500/1000/1500	22.8	900	21	0.3629
Spray D / 190.3	500/1000/1500	22.8	900	15	0.3636

The evaporation mixture fraction, f_{evap}, is provided in the final column of Table 4.1. This parameter defines the limit of the liquid spray from a mixing-controlled point of view and is only dependent on ambient air conditions (pressure and temperature) as well as fuel temperature. The ambient density ρ_a remains constant at 22.8 kg/m^3, and the fuel temperature of the liquid spray is held at 363 K. This parameter has been calculated using the liquid spray state relationships previously developed for the 1D model in [19].

In addition to the thermodynamic conditions (shown in Table 4.1), the time evolution of injection profiles are also essential inputs to 1D model. For Spray A, Figure 4.1 shows the mass flow rate $m_f(t)$, which is obtained from a virtual injection rate generator [125], and the injection duration is long enough to ensure a steady-state combustion. Then, the profile of fuel momentum $\dot{M}(t)$ can be derived by

$$\dot{M}(t) = m_f(t) \cdot u = m_f(t) \cdot \frac{m_f(t)}{Ca \cdot \rho_f \cdot \frac{\pi}{4} d_0^2} \tag{4.1}$$

where Ca is area coefficient, set as 0.98, ρ_f is the fuel density, and d_0 is the nozzle diameter. As for the Spray D, the mass flow rate is obtained from an 'educated' profile, which has been accepted in the ECN community [122]. They are generated with a model that accounts for expected hydraulic fluctuations in pressure, injector opening times, nozzle minimum diameter and discharge coefficient.

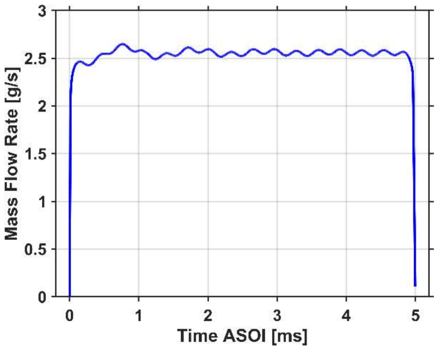

Figure 4.1. Mass flow rate at ECN Spray A condition fuelled with n-dodecane.

Table 4.2. Configurations of Quasi-1D model of Spray

Items	Spray A	Spray D
Nozzle diameter [μm]	89.4	190.3
Spray angle, θ_1 [°]	15.75	15.75
Spray angle, θ_2 [°]	25	25
Intact length, IL [mm]	15	33 [131]
Area coefficient, Ca [-]	0.98	0.98
Discharge coefficient, Cd [-]	0.9	0.9
Injection rate type	VIG	educated

To ensure a free-spray situation, the calculation domain is set as 150 mm length with the mesh grid of 1.37 mm. 52 trajectories are considered along the radial direction, and higher resolution is embedded in the spray centreline. As confirmed in [152], the input of the two spray angles for near-θ_1 and far-field θ_2 with a transition occurring at an intact length distance IL from the orifice is calibrated for the inert spray tip penetration of nominal Spray A. The details of the inputs to the 1D model can be found in Table 4.2.

4.3 Nominal Spray A condition

In this section, the influence of chemical mechanisms under nominal Spray A condition is discussed in terms of chemical source term from the flamelet, ID and LOL against strain rate obtained from flamelet and Quasi-1D modelling. The analysis in this section will not use the radial expansion nor the imposed ignition propagation (Section 3.8), mainly to have a better feeling of the actual model performance during ignition sequence. Note that this does not have an effect on ID & LOL, which is the focus of the present section. The analysis will start with the inert spray evolution, followed by the performance of flamelet ignition as the strain rate variation, then the comparison of single and multiple flamelets will be discussed, finally, the comparison of calculated ID & LOL and ignition sequence among the different chemical mechanisms will be presented.

4.3.1. Inert spray analysis

The analysis starts with the evolution of the inert spray, which builds up the mixing field upon which ignition and subsequent flame development will later occur. The time evolution of the vaporizing spray is usually characterized by the liquid length and tip penetration. The vapor tip penetration is defined as the axial distance to the furthest location where the axial velocity reaches a value of 0.1% of the one at the orifice outlet, and the liquid length is defined as the axial distance to the shortest location where the axial mixture fraction firstly reaches the value of evaporation mixture fraction. Figure 4.2 shows a comparison between experimental data [152] and 1D spray model results, demonstrating excellent agreement for both spray tip penetration and liquid length. Input settings for the model have been summarized in Table 4.2.

For a further comparison, spatial axial profiles of velocity and mixture fractions are compared in axial direction (Figure 4.3) and radial direction (Figure 4.4) between the 1D modelling results and experimental database from [79] [114]. The ensemble-averaged experimental results are shown in black lines, and the uncertainty 95% confidence intervals of the average are shown as gray fill. To enable comparison of different ECN nozzle units used for the experiments, the spatial coordinates are normalized by the nozzle equivalence diameter defined as $d_{eq} = d_0(\rho_f/\rho_a)^{0.5}$, where d_0 is nozzle diameter, ρ_f is the fuel density, ρ_a is the ambient density. The radial profiles at axial distances of 25, 40 and 55 mm, corresponding to the normalized coordinates at 50, 80 and 110, respectively.

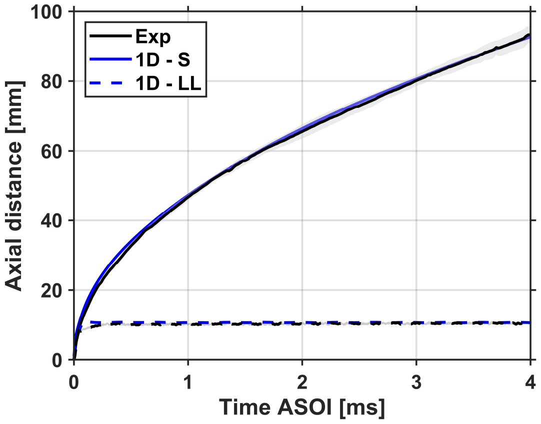

Figure 4.2. The validation of spray tip penetration (Solid) and liquid length (Dashed) for inert spray A. The uncertainty of experiments is delimited with shadows.

Figure 4.3 demonstrates a strong agreement between the measurement and Quasi-1D modelling in terms of axial velocity (left hand) and mixture fraction (right hand) at 1.5 ms ASOI. The left side of the figure shows some overprediction to axial velocity for x/deq < 60, attributed to measurement limitations in the dense spray region [114]. In the right image, following the setup of Sc = 0.72 used in air-to-air jet (Chapter 3), the on-axis mixture fraction is slightly underestimated from the distance at x/deq = 80 to the spray head. The setup of Sc = 0.72 slightly underestimates the on-axis mixture fraction in the distance from x/deq = 80 to the spray head. To get a better prediction, the setup of unity Schmidt Number is used in 1D spray model (Table 4.2), and the prediction in the distance 50 < x/deq < 80 is also within the measurement uncertainty.

The validation of radial velocity and mixture fraction at different axial distances is presented in Figure 4.4. Gaussian profiles are adopted to characterize the radial properties (u, f). The images in the upper reveal a slightly wider velocity distribution compared to the experimental data [114], whereas the mixture fraction in the bottom is a little bit narrower, and an excellent agreement was observed at the distance of x/deq = 50 [79]. In general, the prediction to both velocity and mixture fraction is deemed acceptable, supporting the use of the 1D model setup in the following calculations for reacting spray.

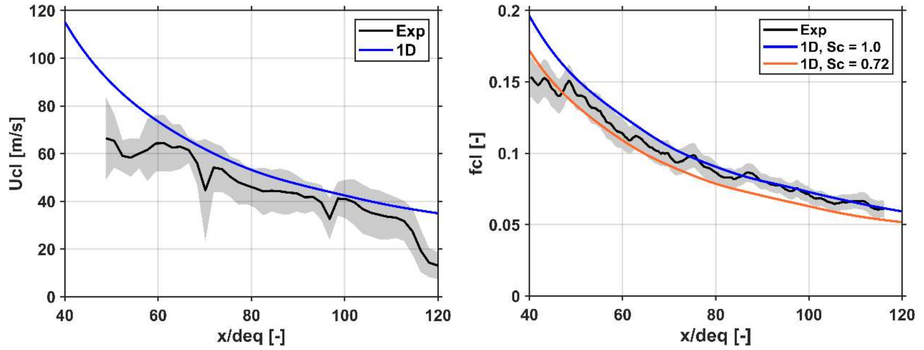

Figure 4.3. The validation of axial velocity (left) and mixture fraction (right) under inert Nominal spray A condition. Experimental database: black; 1D modelling result: blue. The uncertainty of experiments is delimited with shadows.

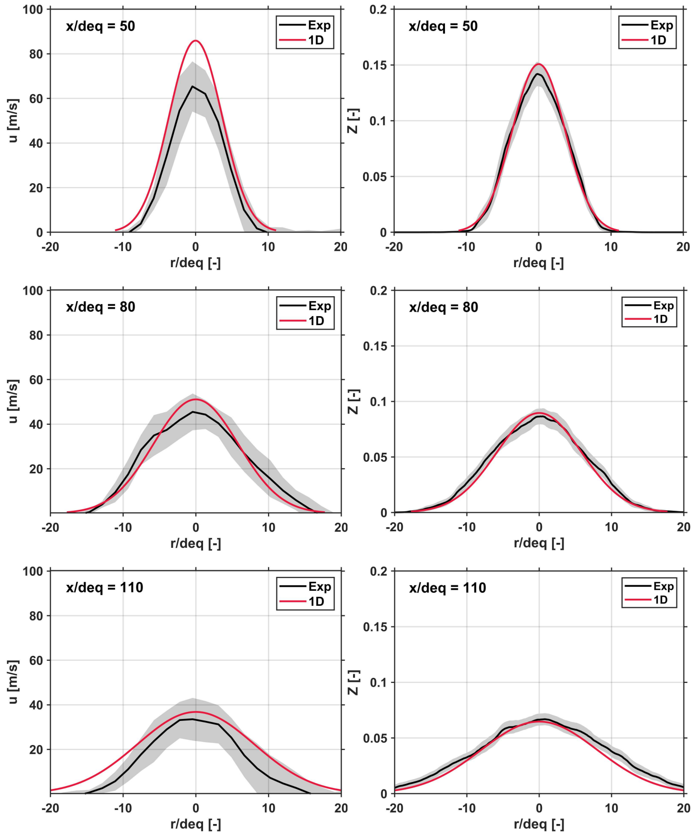

Figure 4.4. The validation of radial profiles of axial velocity (left) and mixture fraction (right) at three axial distances (x/deq = 50, 80, 110). Experimental database: black; 1D modelling result: blue. The 95% uncertainty interval of the average is delimited with shadows.

4.3.2. Effect of strain rate on flamelet ignition in mixture fraction space

In this study, the Quasi-1D model calls up the laminar flamelet database directly and employs a single flamelet configuration, i.e. a single strain rate value. Therefore, examining flamelet ignition across a broad range of strain rates is a fundamental starting point for understanding the spray ignition process throughout Quasi-1D modelling. Figure 4.5 shows the temporal evolution of profiles of temperature in mixture fraction space with a timestep of 10 μs. The black solid lines in the upper and bottom part represent the temperature at steady state (C = 1) and inert state (C = 0), respectively. Ignition starts in the lean mixtures (t = 110 μs), then the maximum temperature increases to 1100 K after 200 μs, and the maximum temperature location also shifts towards the richer side. After the steep increase within 40 μs in the rich mixture, the position moves back to the stoichiometry. Finally, it reaches the steady state at 380 μs. The profile that includes all the maximum temperature at different timings is shown as the dash-dotted black line.

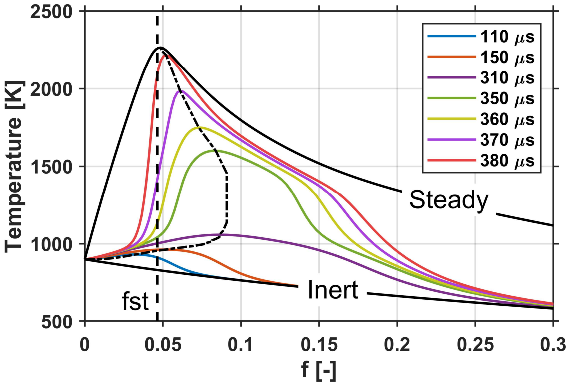

Figure 4.5. Temperature evolution along ignition process in flamelet under Nominal Spray A condition. Mechanism: LLNL; Strain rate: 300 1/s. The vertical line is the stoichiometric mixture fraction.

The chemical source term is illustrated in Figure 4.6, showing maps of T – *f* (Figure 4.6 a) and C – *f* (Figure 4.6 b) for strain rates of 10, 300 and 1000 1/s among the three selected mechanisms at nominal Spray A condition. Here, the chemical source term is the transient flamelet term for Y_c equation, which is directly extracted from flamelet data. A logarithmic colour scale is used for better visualization. Besides the vertical dashed-dotted line (equivalence ratio, *f*st = 0.04605), a number of solid black lines imposed on contour represent the instantaneous flamelet temperature with a constant timestep of 10 μs between two adjacent lines. The dashed line extending from T = 900 K to the maximum or from C = 0 (inert) to the steady state (C = 1) highlights the maximum value at each instantaneous phase during the combustion process [191].

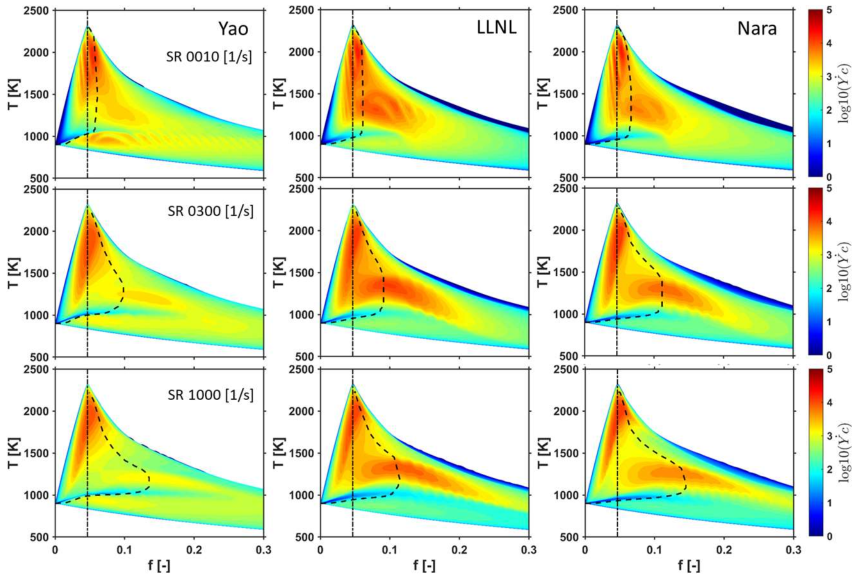

a) *T - f*

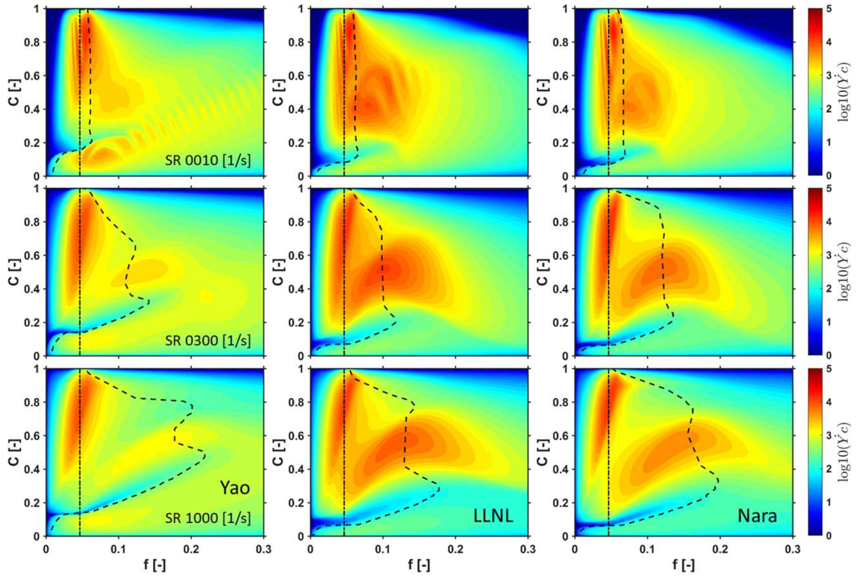

b) *C - f*

Figure 4.6. Contours of $\dot{Y}_c = \frac{\partial Y_c}{\partial t}$ in terms of mixture fraction and temperature (a), mixture fraction and normalized progress variable (b). Dashed line superimposed on the contour is the evolution of (a) maximum temperature and (b) maximum progress variable at every 10 μs timestep. The vertical line is the stoichiometric mixture fraction. From left to right, corresponding to the mechanism of Yao, LLNL and Nara. From top to bottom, corresponding to strain rates at 10, 300 and 1000 1/s

The flamelet ignition process predominantly takes place in the region where the mixture fraction is below 0.2. Within this range, as the system moves towards higher temperature or the steady state (C = 1.0), chemical reactivity can be divided into three regions, corresponding to a two-stage ignition process that is consistent across different strain rates and chemical mechanisms.

- Starting from an ambient temperature (Ta = 900 K) in the oxidizer stream, the temperature rises to approximately 1000 K near the stoichiometric ratio (cool flame phase), before reaching a plateau until a final increase at the end of the curve, known as first-stage ignition. Across the three strain rates, a consistent morphology is observed, with high intensity expected under lower strain rates. Among the three mechanisms, Yao scheme exhibits the strongest chemical activity at a constant strain rate, particularly in the $0.05 < f < 0.1$ range. Qualitatively similar trends are seen in the LLNL and Nara schemes, with slightly weaker activity in the latter mechanism. Despite starting at Ta = 900 K, all three mechanisms reach T = 1000 K near stoichiometry, but the Yao scheme achieves a higher C level due to its enhanced chemical source term. While increasing strain rate does not impact the initial temperature rise, it prolongs the first-stage ignition stage, characterized by a steady temperature and gradual chemical evolution in C curves. Notably, the LLNL scheme shows minimal strain rate influence on this behavior.
- A significant rise in temperature at a constant mixture fraction in the rich region was observed at the end of the initial stage, demoted as the second-stage ignition, typically occurring within the temperature range of 1000 K < T < 1500 K. The evolution of the normalized progress variable illustrates that a higher strain rate leads to a prolonged period of the first-stage ignition, resulting in increased levels of C during the second-stage ignition. Additionally, a decrease in chemical reactivity is anticipated, as well as a narrower distribution of the chemical source term across the temperature and a wider distribution across mixture fraction. Consequently, the magnitude of the steep increase diminishes at higher strain rates. Furthermore, the narrower contours contribute to the displacement away from stoichiometry. Unlike the behavior exhibited in the initial region, Yao solution attains the lowest chemical activity, resulting in the highest C values at the second-stage ignition.
- Afterwards, the flame was fully ignited, leading to an increase in temperature and normalized progress variable towards the steady state. The reactivity shifts back towards stoichiometry at SR=300, 1000 1/s, but this effect is less apparent at low strain rate (SR = 10 1/s), where high temperature ignition takes place almost at a stoichiometric condition for all three mechanisms.

To further elucidate on the flamelet ignition process, the evolution of ignition delay in relation to mixture fraction is compared across different mechanisms and strain rates, as illustrated in Figure 4.7. First-stage ignition (referred to 1st-ID) is the instant when each mixture reaches its chemical state at C = 0.1 first, while the second-stage ignition (referred to 2nd-ID) is the moment when its chemical state C > 0.9.

At the lowest strain rate, the curves of both first- and second-stage ignition for the three mechanisms exhibit a V-shape over the range of mixture fractions considered ($0 < f < 0.2$), with the sensitivity of ignition delay to mixture fraction being more pronounced on the fuel-lean side. The position of the minimal value across the mixture fractions is also known as the most reactive mixture fraction. For the first-stage ID of Yao solution, this position locates at the fuel-lean side ($f = 0.015$), whereas for the other mechanisms, it is observed on the fuel-rich side. Furthermore, both first- and second-stage ID reach their minimum values at similar mixture fractions (0.06 for LLNL, 0.065 for Nara). Consistent with the lower intensity of chemical activity, Nara mechanism exhibits the longest ignition delay for both first- and second-stage ignition. When comparing Yao and LLNL, a highly similar second-stage ignition delay is found between the two mechanisms. For the first-stage ignition delay, similar results are LLNL shows a longer value when the mixture fraction is smaller than 0.07, aligning with the lower reactivity in this region.

Profiles of ID versus mixture fraction are observed to increase in width with increasing strain rate for both the first- and second-stage ID, i.e. diffusion accelerates ignition on both the fuel-rich and lean cases. In terms of the first-stage ID, the minimum value remains relatively constant across three mechanisms, with only a longer ID for the LLNL and Nara schemes near the stoichiometric ratio. This also indicates that reactivity is further reduced in the fuel-lean side at the low-temperature region. As expected, a longer second-stage ID is found with an increasing strain rate independent of the mechanisms. At the highest strain rate, LLNL solution is close to the extinction limit (SR = 1250 1/s), thereby, a longer ID was found than Yao in this scenario.

In summary, Figure 4.6 and Figure 4.7 gather and condensate the process of how ignition develops for laminar flames which is similar to the assumption in Quasi-1D modelling. If turbulence-chemistry interaction is neglected, the general trends of flamelet using different mechanisms should align with the corresponding performance of the Quasi-1D model, as will be discussed in the following section.

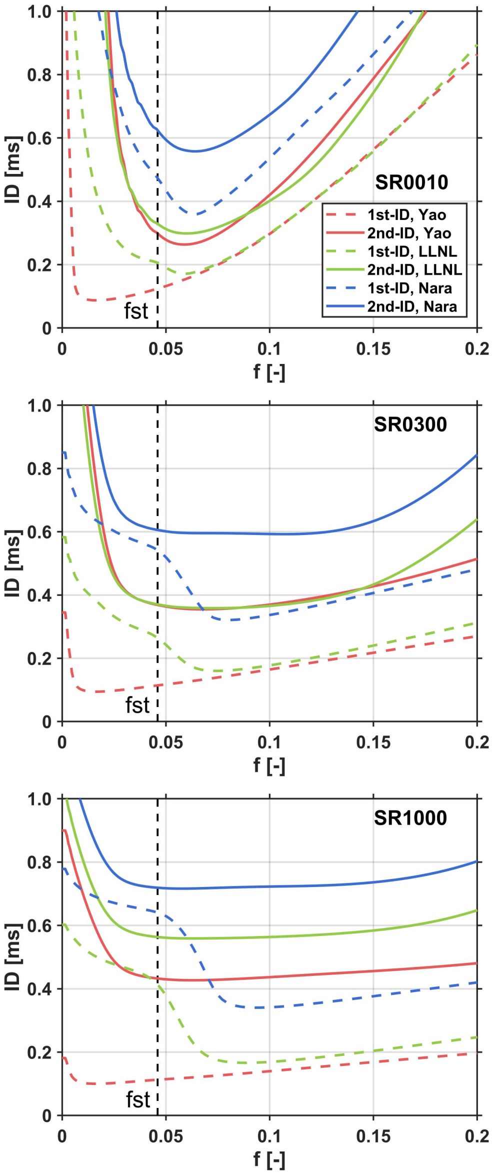

Figure 4.7. Ignition delay against mixture fraction for low-temperature (dash) and high-temperature (solid) ignition. The mechanism of Yao, LLNL and NARA are compared. The vertical dash line is stoichiometric. The upper to bottom, corresponding to strain rate at 10, 300 and 1000 1/s.

4.3.3. Effect of strain rate on Quasi-1D spray ignition

This section will focus on the effect of strain rate on the Quasi-1D spray ignition process, as well as the difference among the commonly used chemical mechanisms for n-dodecane, named as Yao, LLNL and Nara. The calculation will be carried out under Nominal Spray A condition.

To give a first description of the spray ignition process as obtained from the Quasi-1D model, an example case will be used based upon the result of a SR = 10 1/s using LLNL mechanism. First, the time-evolution of maximum temperature across the spray is shown in Figure 4.8, where a typical two-stage ignition process is shown, the cool-flame ignition starting at ~160 μs and the hot-flame starting at ~500 μs.

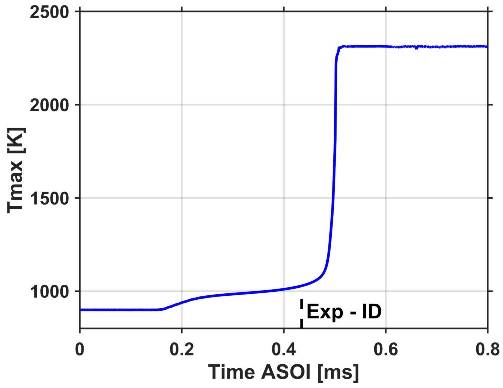

Figure 4.8. Time evolution of maximum temperature across the spray domain along the injection process. Condition: Nominal Spray A; Mechanism: LLNL; Strain rate: 10 1/s.

As the next step, the temporal evolution of the temperature as a function of mixture fraction along three trajectories are presented in Figure 4.9 under the starting assumption that no interaction among trajectories exists. Note that the mixture fraction axis shows information in the inverse direction compared to the spray axis, i.e., trajectories mainly extend along a decreasing mixture fraction. Taking the evolution in the middle trajectory (r/R = 0.55) as an example, the ignition process can be categorized as three stages. The first stage corresponds to the cool flame period in Figure 4.8, where the Tmax remains constant in ~1000 K after the initial rise at 0.16 ms ASOI. After the initial temperature rise in the rich mixture at 0.35 ms, the conservation of progress variable enhances the reactions of the control volumes downstream of the first ignition site, while the maximum temperature of these control volumes maintains at around 1000 K. Next, the rapid increase in temperature appears in the stoichiometric mixture, while position further downstream is still not ready to be ignited. This is called as the second stage, corresponding to the hot-temperature ignition in Figure 4.8. After that, the Tmax reached the highest value of 2313 K. However, the mixture with a high temperature (T > 1000 K) switches to a lean side. After the high temperature ignition at 0.55 ms, the reacting zone slightly shifted towards leaner mixture (0.75 ms), this is the third stage. Due to the transport of progress variable along the trajectory, as well as the chemical activity, reaction eventually propagates towards lean regions (3.50 ms), while the richest location remains relatively steady. This rich limit will make up the location marking the most upstream transition from inert to reacting state, i.e. the lift-off location.

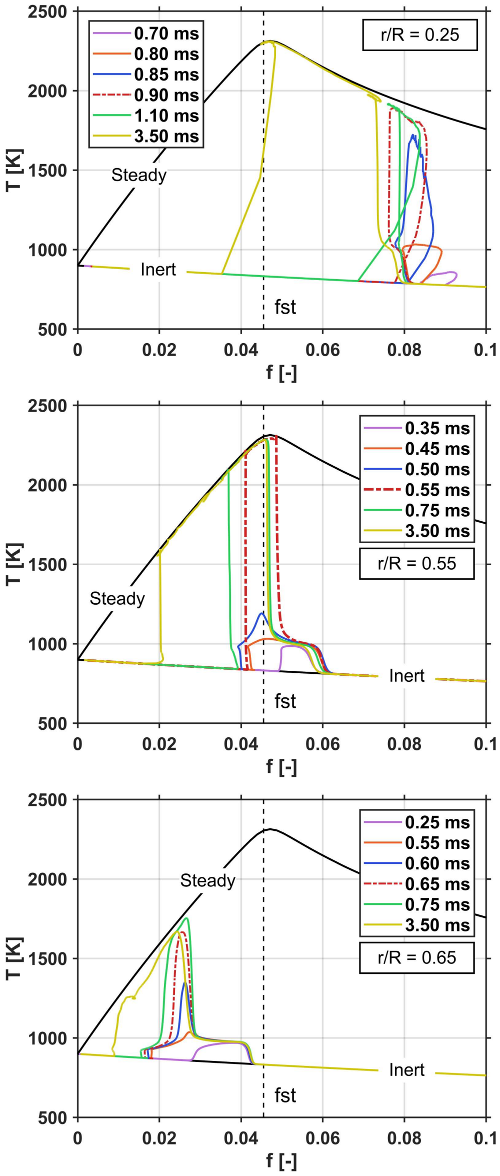

Figure 4.9. Time evolution of temperature against mixture happening at the trajectories where the radial position at r/R = 0.25 (top), 0.55 (middle) & 0.65 (bottom). Condition: Nominal Spray A; Mechanism: LLNL; Strain rate: 10 1/s. The dashed line represents the shortest time when the temperature in this trajectory reaches steady state.

Similar three-stage ignition behavior is also observed in the inner trajectory (r/R = 0.25) and outer trajectory (r/R = 0.65). However, the instant when the temperature starts to rise is both later than the middle trajectory. As for the inner trajectory, the ignition takes place at a rich mixture where *f* = 0.08 and finally reaches the steady state at the first instant of 0.90 ms ASOI. At the steady state (3.5 ms ASOI), the reaction in the initial control volume with *f* = 0.08 has ended, and the trajectory has also been ignited across a wider range of mixture fractions, compared to the other two cases. As for the outer trajectory, the ignition occurs at a lean mixture where *f* = 0.25, and the longest cool flame period (0.25 ms – 0.60 ms) allows to spread into a leaner mixture in the first-stage ignition. The analysis of trajectory ignition shows that, even at steady state, reaction only extends up to a minimum mixture fraction value that is above zero, which corresponds to the corresponding value at the spray tip. As a short conclusion obtained from the three trajectories, the appearance of the cool flame or the CH_2O formation was dominated by the trajectories in the outer region (r/R> 0.5), and the hot-temperature ignition delay is determined by the middle trajectory.

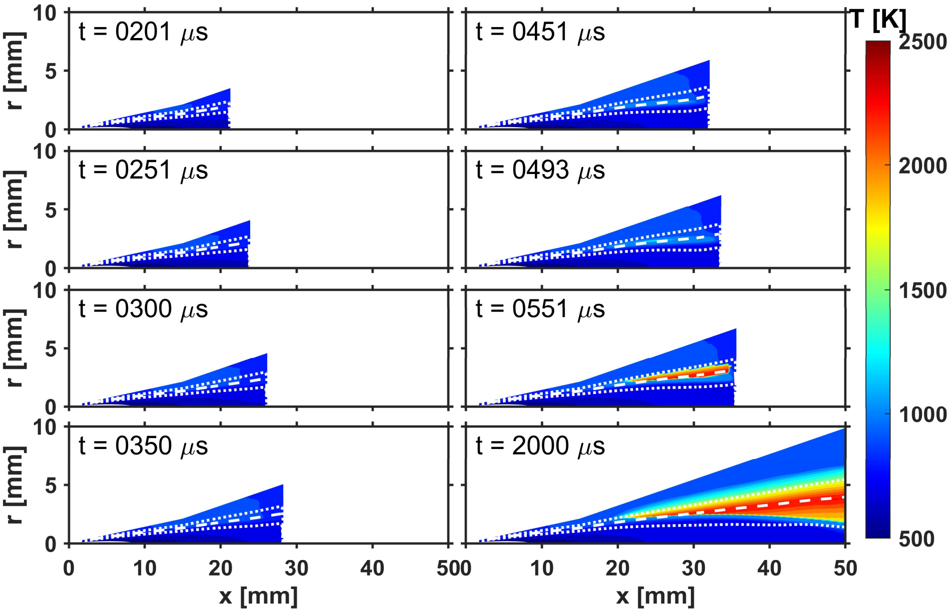

Figure 4.10. Sequence of 2D contours of temperature along the ignition process. Condition: Nominal Spray A; Mechanism: LLNL; Strain rate: 10 1/s.

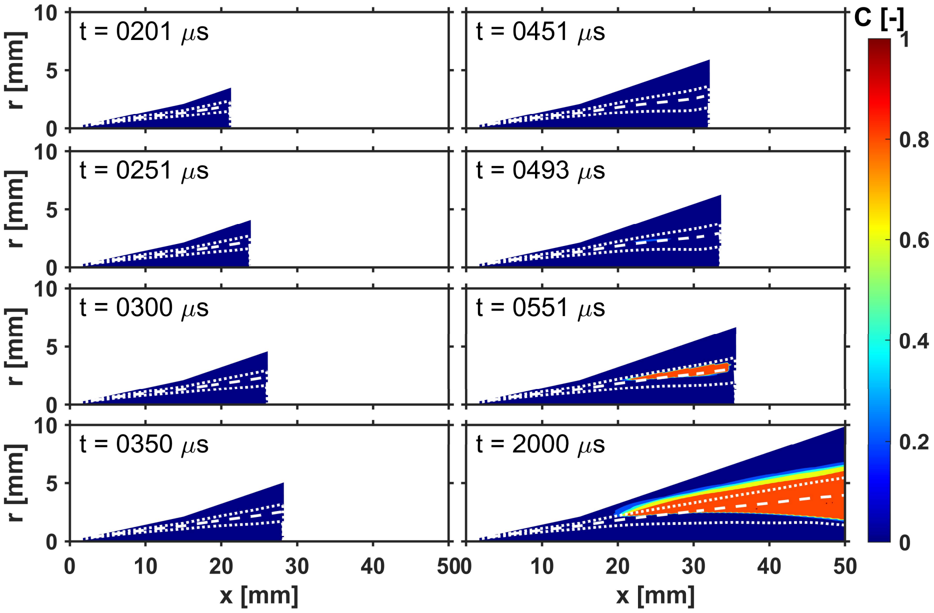

Figure 4.11. Sequence of 2D contours of normalized progress variable C along the ignition process. Condition: Nominal Spray A; Mechanism: LLNL; Strain rate: 10 1/s.

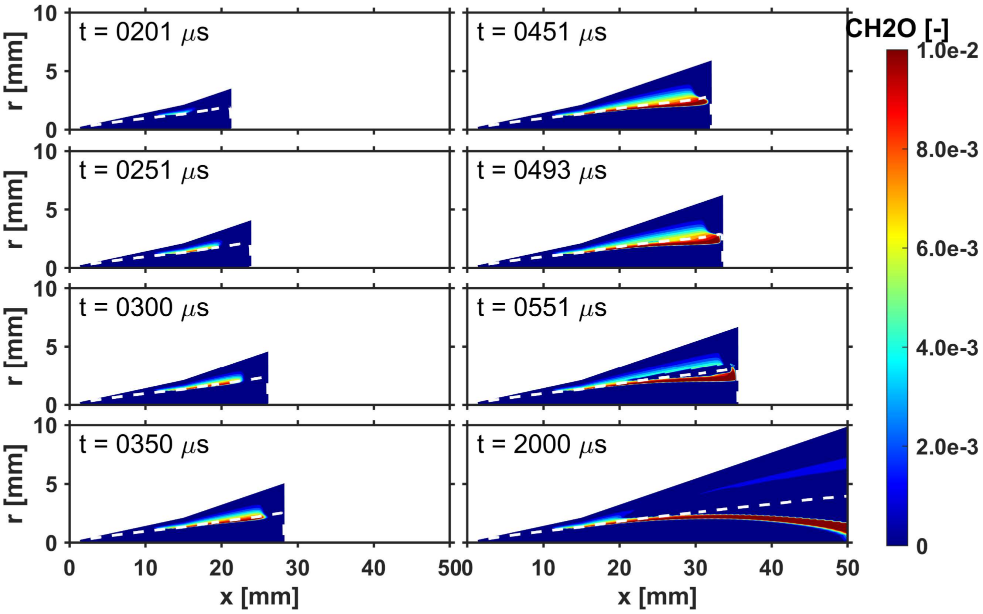

Figure 4.12. Sequence of 2D contours of formaldehyde CH_2O along the ignition process. Condition: Nominal Spray A; Mechanism: LLNL; Strain rate: 10 1/s.

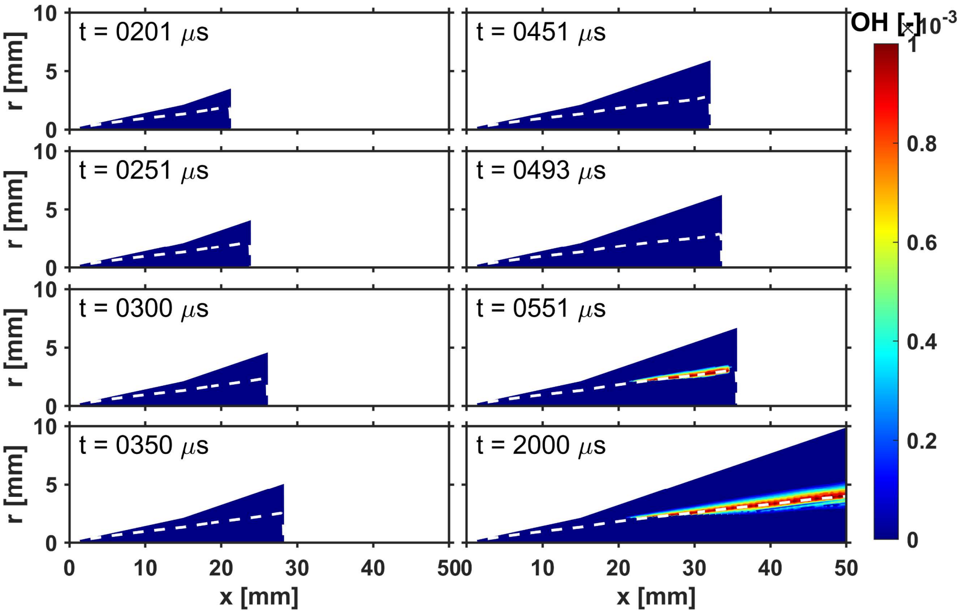

Figure 4.13. Sequence of 2D contours of hydroxy OH along the ignition process. Condition: Nominal Spray A; Mechanism: LLNL; Strain rate: 10 1/s.

Figure 4.10 shows a time sequence of 2D contours of temperature along the ignition process, normalized progress variable is shown in Figure 4.11, mass fraction of formaldehyde (CH_2O) is shown in Figure 4.12 and hydroxyl (OH) radical is shown in Figure 4.13. Such 2D contours are essentially an aggregation of the ignition of all the radially distributed trajectories. Three white lines are plotted to represent the surfaces of equivalence ratio at stoichiometry (solid line) and 0.5 and 2.0 (corresponding to the outer and inner dashed lines, respectively). At 200 μs ASOI, formaldehyde was firstly observed in the region, extending from 11 to 15 mm from the nozzle and radially displaced in the lean reacting mixtures, which is consistent with the earliest rise in temperature in r/R = 0.65 shown in Figure 4.9. As reaction progresses, the temperature in the lean mixture exhibits a moderate range, in agreement with the observed formaldehyde between the surface of $\phi = 0.5$ and $\phi = 1.0$. However, the reactivity is still low, corresponding to the maximum temperature lower than 1000 K and an extremely low value in the field of C and OH mass fraction. At 493 μs ASOI, when the maximum temperature firstly exceeds a threshold value of the ambient temperature plus 400 K, an increase in temperature can be found near the surface of stoichiometric. Soon after that, the lean mixture is ignited, as well as a nearly steady state is achieved. The high temperature consumes CH_2O, and OH is formed. At the quasi-steady-state combustion, 2000 μs ASOI, the reaction is seen to have fully extended downstream until the spray tip for those trajectories that have ignited. A lifted flame structure is observed in terms of temperature field, which was one of the goals of the present modelling approach. However, the temperature at around ~30 mm along the trajectory near the centreline is lower than 1000 K due to the weak diffusion among trajectories, which is also much lower than the simulated results (~1600 K) in CFD work [215]. In addition, the distribution of formaldehyde demonstrates a maximum concentration in rich zones, while it remains a structure of thin layer compared to the broader cool flame observed in the experiment [99]. During the ignition process, its appearance in the lean side ($\phi < 0.5$) tends to be oxidized in the high temperature fields. The missing reactivity in the spray centerline downstream of the lift-off length region, as well as in the largest radial trajectories, is the main motivation for the correction in the C field at ignition timing that has been described in Section 3.8. However, it will not be used in the present section because it is only focused on ignition timing and behavior upstream LOL.

Figure 4.14 displays the ignition delay derived from flamelet manifold as a function of strain rates, extending from 1 1/s to the extinction limit. Ignition delay is defined as the instant when the maximum C (Cmax) exceeds 0.9 over all the mixture fraction space, i.e. it represents the shortest value, corresponding to the most reactive mixture fraction, as already explained in Figure 4.7. Ignition delay and lift-off length from the Quasi-1D spray model is plotted in Figure 4.15, as well as the experimental database shown as black lines with the grey shadow as uncertainty. The ignition delay follows the same criteria as the plots in Figure 4.14, and the lift-off length is defined as the minimum axial distance from the nozzle to the closest location where 14% of the maximum value of the mass fraction of OH in the domain is reached. Then, the consistency of ID & LOL as the variation of strain rate is shown in Figure 4.16. Finally in Figure 4.17 the spray ignition process is analysed in terms of profiles of Tmax (maximum temperature across the spray domain) against mixture fraction, similar to the flamelet ignition evolution shown in Figure 4.6. The comparison of flamelet-derived and Quasi-1D ignition delays will provide some interesting feedback on the effect of residence time on the spray ignition, compared to a diffusion flamelet configuration.

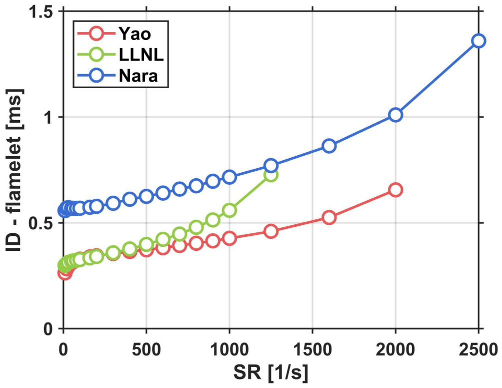

Figure 4.14. Ignition delay from flamelet manifold as a function of strain rate for the investigated chemical mechanisms

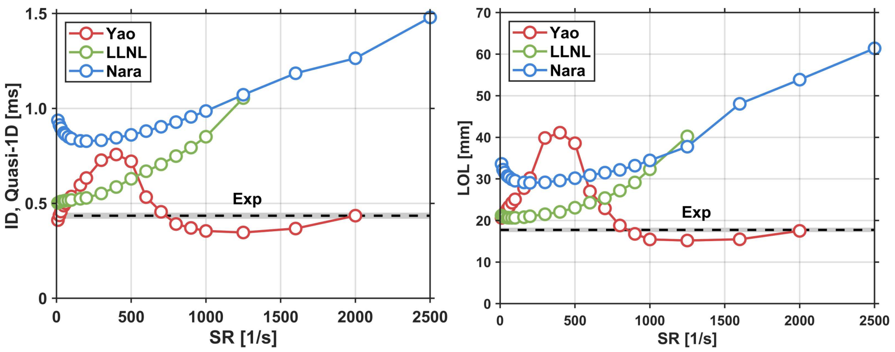

Figure 4.15. Ignition delay (left) and lift-off length (right) calculated by Quasi-1D model as a function of strain rate for the investigated chemical mechanisms.

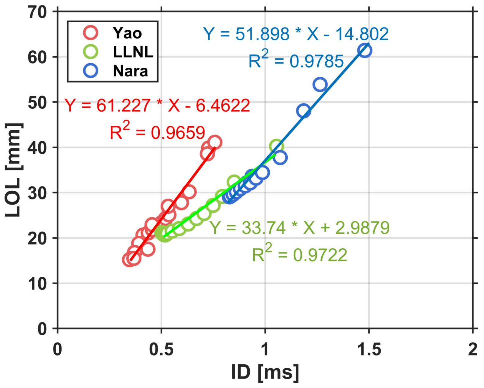

Figure 4.16. Relationship of lift-off length as ignition delay across the entire strain rates using the investigated chemical mechanisms.

Consistently with the previous analysis of flamelet results, the globally weaker reactivity at a higher strain rate contributes to a longer ID for the spray cases, with strong sensitivity at a large strain rate value. Quasi-1D ignition delay is longer than the flamelet-derived one, consistently with the need to create the mixture in the spray cases, which is already available from the start of the calculation for the flamelet case. Nara solution exhibits the longest ID among all three mechanisms, while in the low strain rate range (SR < 400 1/s), the solutions from LLNL and Yao are similar.

A remarkable result is obtained for Yao scheme, which shows a non-monotonic trend in both ID and LOL with strain rate. Initially, there is an increase in values up to a maximum at a strain rate of 400 1/s, followed by a decrease over a wide range of strain rates. The analysis of temperature evolution in Figure 4.17 shows that this increasing trend occurs when ignition happens in stoichiometry or slightly rich mixtures. This is consistent with the trend of flamelet ID (Figure 4.7), which is a result of the retarded reactivity at high strain rates. As the strain rate further increases, ignition shifts to fuel-lean regions rather than fuel areas in the flamelet, leading to a decrease in ID until SR

= 1250 1/s, followed by a slight increase up to the extinction limit at SR = 2000 1/s. The lean ignition locations can be explained by the longer local residence time in the peripheral trajectories, where lean conditions are dominant. As the strain rate increases, ignition delay decreases for lean conditions (Figure 4.7), ultimately influencing spray ignition. The role of 1st stage ignition, which is much faster for Yao compared to the other two mechanisms, is most probably the governing factor leading to this difference in sensitivity of the Quasi-1D spray ignition to strain rate.

For LLNL scheme, the temperature evolution against mixture fraction in the low-temperature range (1000 K < Tmax < 1300 K) resembles the Yao scheme, with near-stoichiometric ratio for SR = 10 1/s, fuel-rich side for SR = 300 1/s, and fuel-lean-side for SR = 1000 1/s. Regarding high-temperature ignition, the ignition position is typically around stoichiometry. In the Nara scheme, V-sharp profiles are found for both ID versus strain rate, with the minimum at SR = 200 1/s. Throughout the range of strain rates, ignition consistently occurs on the fuel-lean side, with leaner ignition for higher strain rates.

On the other hand, lift-off length sensitivity versus strain rate as derived from the Quasi-1D model is similar to that of ignition delay for all three mechanisms. Figure 4.16 proves that a nearly linear relationship exists between ID and LOL for the chemical mechanisms investigated, which is a confirmation that has been extensively observed experimentally in the literature [94].

When comparing Quasi-1D spray model predictions against the experimental results, Nara solution is always overpredicted, then it will only be considered within the present section, and it will be discarded for the analysis in Section 4.4 dealing with different conditions. The predicted ID using Yao mechanism matches the measurement at SR = 20, 700 and 2000 1/s with a very similar result for LOL, except for the slight underprediction at 20 1/s. Similarly, LLNL results are slightly overpredicted for both combustion metrics, but it is still close to the measurement at low strain rates.

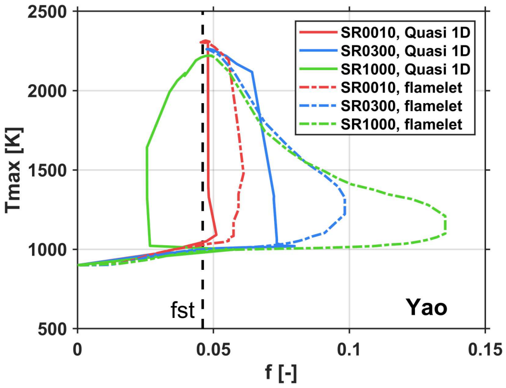

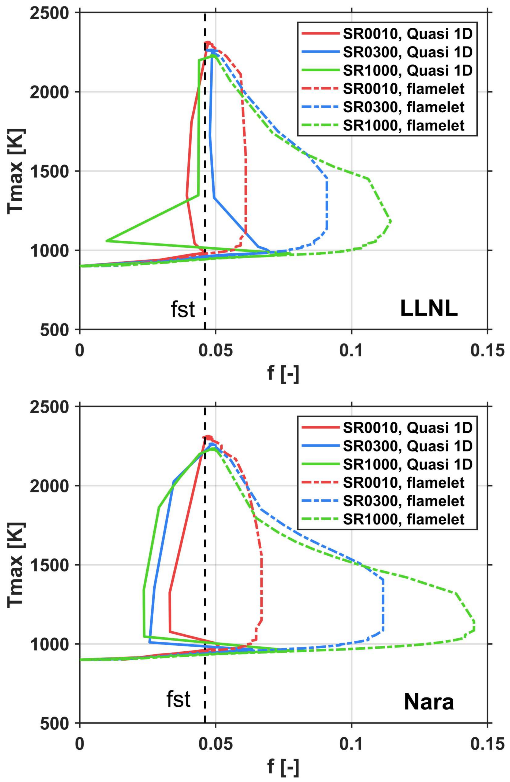

Figure 4.17. Maximum temperature as mixture fraction from flamelet (dash-dotted) and Quasi-1D model (solid) at three strain rates (10, 300, 1000 1/s) for mechanism Yao (upper), LLNL (middle) and Nara (bottom)

As a further analysis, the ignition process in terms of the maximum C (Cmax) evolution within the spray, is illustrated in Figure 4.18. Across all cases, a two-stage ignition pattern is evident. Following the start of injection, Cmax shows a tendency to increase and remains stable (low temperature phase) until a sudden rise, followed by a high-temperature flame.

Consistent with the similar first-stage ID among strain rates shown in Figure 4.7, there is also little impact on the beginning of first-stage ignition and the chemical state of first-stage combustion in Quasi-1D modelling, regardless of the mechanism. However, the high-temperature ignition delay is primarily influenced by the duration of the first-stage ignition, which is very sensitive to strain rate.

When comparing different mechanisms, the Yao mechanism demonstrates the highest level of the first-stage ignition. Similarly, the Yao and LLNL mechanisms exhibit a similar onset of first-stage ignition, suggesting a resemblance in the distribution of chemical source terms in the low-temperature range between these two mechanisms, albeit with lower reactivity in the LLNL solution. Furthermore, the Nara solution displays the lowest combustion state and the longest duration for the first-stage ignition.

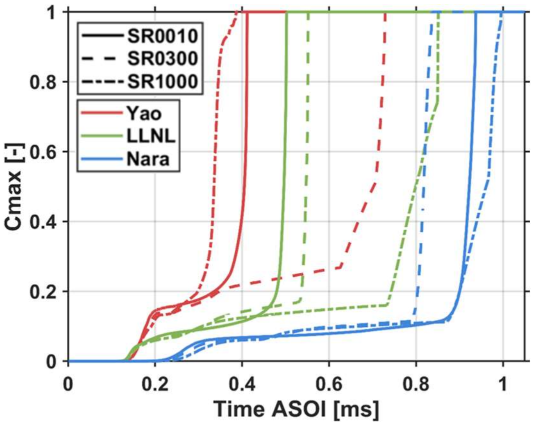

Figure 4.18. Quasi-1D model evolution of Cmax at three strain rates (10, 300, 1000 1/s) for different mechanisms (Yao, LLNL, Nara)

A time evolution of 2D contours displaying temperature (Figure 4.19) and formaldehyde mass fraction (Figure 4.20) provide insights into the ignition process predicted by Quasi-1D model. The performance of using different chemical mechanisms (Yao, LLNL and Nara) as well as the strain rates (10, 300, 1000 1/s) is analyzed. Four typical instants are included:

- First appearance of CH_2O
- Maximum temperature exceeding 1300 K (Ta + 400 K)
- 200 μs after the previous instant
- Steady combustion (2000 μs)

At the lowest strain rate at 10 1/s, the earliest appearance of CH_2O was observed with the LLNL scheme, while the earliest hot-flame ignition occurs with the Yao scheme. This observation is consistent with the broader gap of low chemical activity in the intermediate temperature region of LLNL scheme, as shown in Figure 4.6. After the ignition instant, Quasi-1D model exhibits similar temperature contours between Yao and LLNL schemes that the ignition position takes place between 20 to 30 mm along the stoichiometric surface. Subsequently, the local temperature rises to ~2300 K and the ignition spot spreads towards the lean and rich sides. Finally, the high temperature zone is around the stoichiometry downstream 20 mm from the orifice. Nara mechanism, characterized by weak reactivity, prolongs the ignition, and results in a contour located further away from the nozzle (~30 mm). Moreover, the longer residence time on the lean side enhances the local ignition.

For the intermediate strain rate at 300 1/s, the behavior that chemical reactivity being weaker in the rich side and stronger in the extremely lean side leads to a longer ignition delay and a new ignition position in the fuel-lean zone at the distance of 20 – 30 mm in Yao scheme. Additionally, the longer local residence time in the fuel-lean side of the spray further enhances fuel-lean ignition.

At the highest strain rate at 1000 1/s, temperature distribution primarily stays in the fuel-lean zones. Conversely, the layer of formaldehyde tends to be thicker, as well as a higher CH_2O concentration. However, as the strain rate increases, the highest CH_2O concentration, which occurs at the highest strain rates in Yao and LLNL schemes, appears at the intermediate strain rate in the Nara scheme. Among the chemical mechanisms, the highest CH_2O concentration is found in LLNL solution, in agreement with the long cool flame period and highest chemical reactivity in the rich mixture. In addition, when considering the profiles of ID & LOL versus strain rate, lower values of strain rate are typically preferred. Overall, the Yao and LLNL mechanisms are suitable for n-dodecane calculations, provided that an appropriate strain rate is selected.

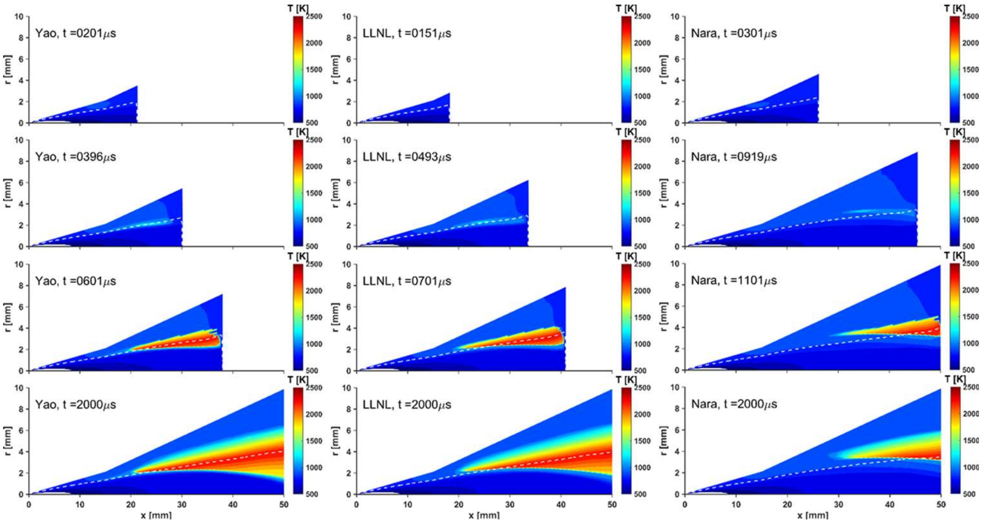

a. SR = 10 1/s

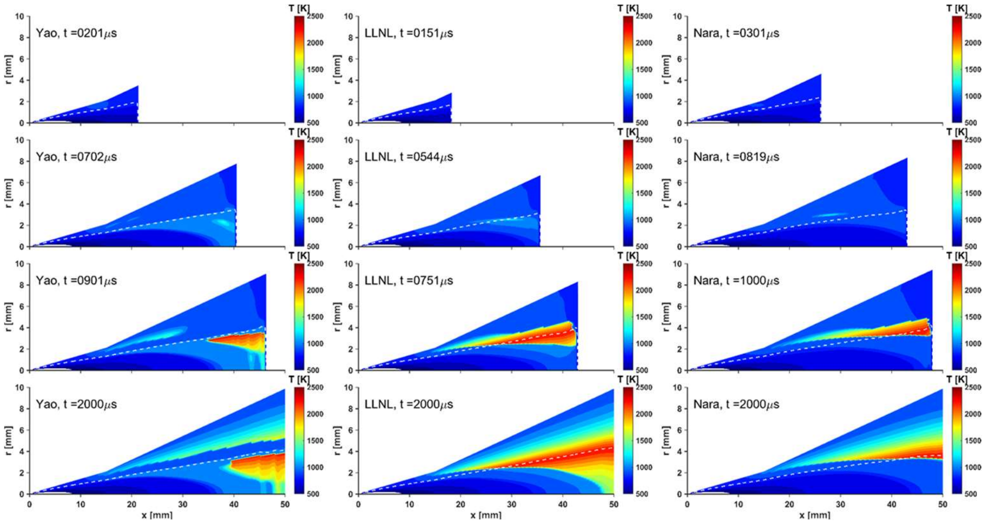

b. SR = 300 1/s

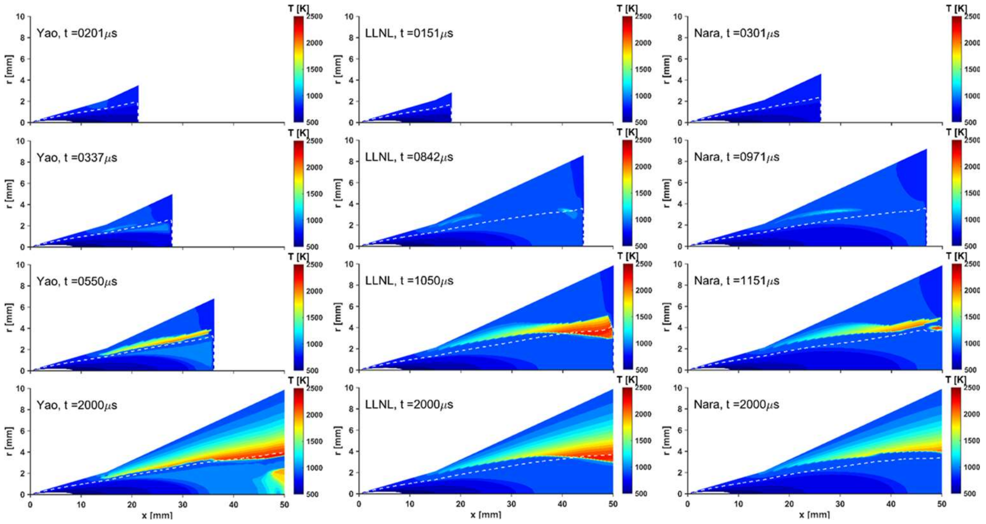

c. SR = 1000 1/s

Figure 4.19. A time-sequence of 2D maps of temperature along ignition process under nominal Spray A condition. Strain rates: 10, 300, 1000 1/s. Mechanism: Yao, LLNL, Nara.

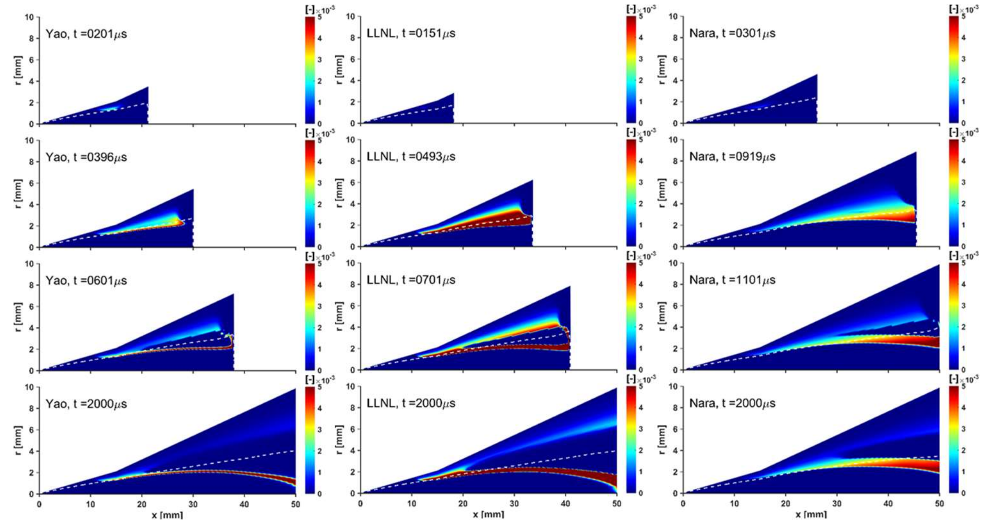

a. SR = 10 1/s

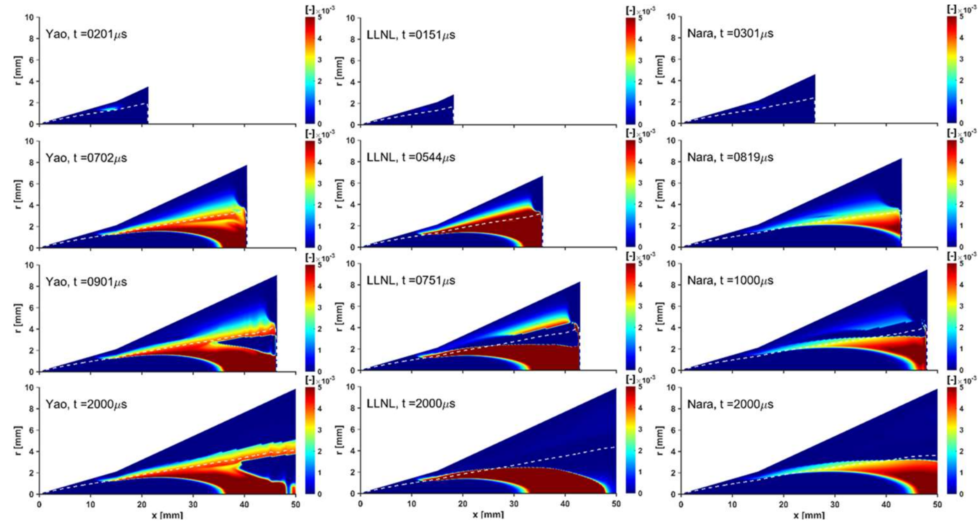

b. SR = 300 1/s

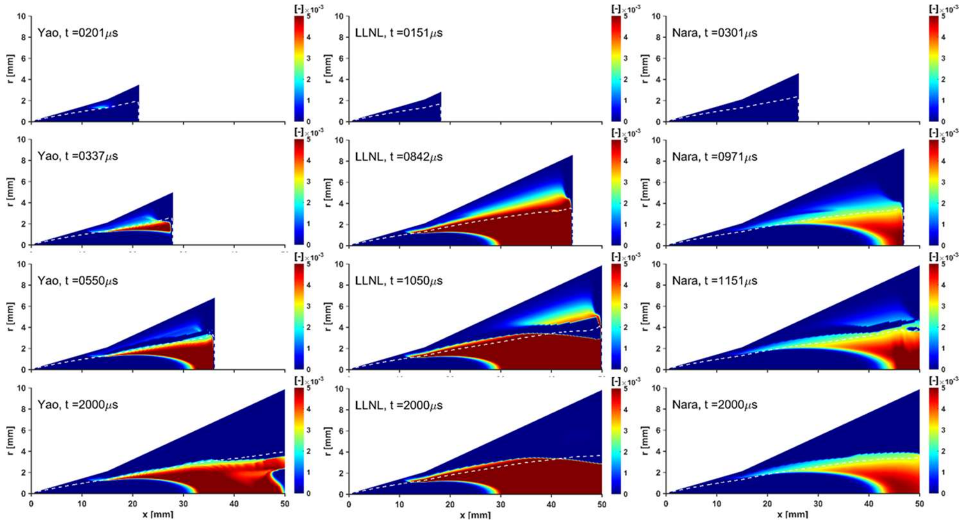

c. SR = 1000 1/s

Figure 4.20. A time-sequence of 2D maps of formaldehyde along ignition process under nominal Spray A condition. Strain rates: 10, 300, 1000 1/s. Mechanism: Yao, LLNL, Nara.

4.3.4. Multiple flamelet approach

For the simulation of nominal reacting Spray A with n-dodecane, the auto-ignition range of strain rate in the typical S curve in flamelet manifold usually spans from 100 1/s to 103 or 104 1/s, depending on the selected chemical mechanism. For the sake of simplicity, the simulation using a constant strain rate could also obtain a good prediction, where the choice of strain rate comes from the area-averaged value across the spray [25], or a representative one in the auto-ignition range along the S curve, i.e., SR = 500 1/s in the research [216] [217]. Thereby, it is worth discussing the difference of single or multi flamelet in the predictions using Quasi-1D model. For the implementation of multiple flamelets, the individual flamelet manifolds were read into the memory, then, the source term ($\dot{Y}_c \cdot \rho$) is obtained by linear interpolation after the calculation of local strain rate, which has been explained in Chapter 3.

Figure 4.21 shows the effect of strain rate on ID & LOL using LLNL mechanism. As shown before, ignition delay from flamelet increases as the strain rate increases and finally approaches the extinction limitation. The result is insensitive to the strain rate when it is smaller than 200 1/s. This value is strongly dependent on the chemical mechanism, i.e., this insensitivity is found until 1000 1/s for Yao [218] and Nara mechanism [216]. The calculated ignition delay from Quasi-1D modelling also shows a consistent monotonic increase, remaining insensitive to strain rates below 400 1/s. Similar trends are observed for the lift-off length. On the other hand, results from the multiple flamelet approach produce an ID & LOL prediction that are within the range of those obtained with a single-flamelet. The ignition delay calculated by multiple flamelets matches the data of a single flamelet at a strain rate ~ 300 1/s, while the lift-off length shows the match at a higher value of ~800 1/s. Both approaches, single or multiple flamelets show the ID & LOL predictions higher than the corresponding experimental data, possibly due to the absence of components like CH_2O in the progress variable definition.

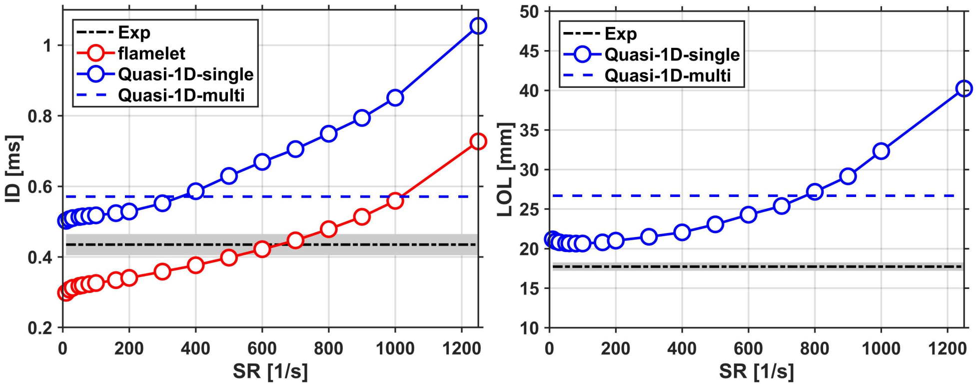

Figure 4.21. Effect of strain rate on the ignition delay and lift-off length using LLNL mechanism. Red line is the data from flamelet manifold, blue line is the calculated results from Quasi-1D modelling using constant strain rate. Experimental data is provided as dashed black line, the uncertainty is given as the grey shadow. The dashed blue line is the result of Quasi-1D modelling using multiple flamelets.

The evolution of Cmax across the spray is presented in Figure 4.22 for both constant and multiple strain rates, where a typical strain rate 50 1/s in the range of insensitivity is selected. Additionally, time-resolved two-dimensional contours of temperature (T), formaldehyde (CH_2O) and normalized progress variable (C) during the ignition process are presented in Figure 4.23 - Figure 4.25.

Compared to the results of constant strain rate, the initial increase in Cmax using multiple flamelet approach also takes place at 0.13 ms ASOI, in agreement with the insensitivity of initial phase of Cmax appearance observed in Figure 4.18. Further, Cmax shows a similar increase until 0.25 ms ASOI. After that, Cmax using multiple flamelet approach exhibits a slightly higher value along the cool flame period, consistent with the behavior of high Cmax value in high strain rates shown in Figure 4.18, eventually showing a faster high temperature ignition compared to the 50 1/s case. As the multiple flamelet approach integrates results from individual flamelets at different strain rates, the prediction is some sort of an average over the whole flamelet manifold.

Considering the 2D contours in Figure 4.23 - Figure 4.25, the difference of ignition process between constant and multiple flamelet approach can be briefly described as two aspects:

- Cool-flame period: formaldehyde firstly appears in the distance of 12 – 16 mm along the stoichiometric surface at 0.2 ms ASOI for both approaches. Then, a larger CH_2O distribution in the fuel-rich side is observed using multiple flamelet approach, which can be explained by the higher local strain rate than the constant case (SR = 50 1/s). A similar observation that larger CH_2O distribution in rich side detected in Figure 4.18 also supports it.

- Hot-flame period: At the end of cool flame stage, the ignition using constant strain rate (SR = 50 1/s) takes place earlier (0.5 ms ASOI) at the high-temperature regions around the stoichiometry surface. In contrast, it was found in the slightly fuel-rich side at the spray head under the multiple strain rate approach (0.55 ms ASOI), which has been verified in CFD-LES work [205]. After the ignition, the mixtures in both radial sides are gradually ignited. At the steady state (2.0 ms ASOI), temperature distribution ($T > 1500$ K) is similar for both methods, while the level of low temperature in the fuel-rich side is slightly higher using multiple strain rate approach. In addition, two distinct regions with highest value can also be found, where the first region is along the stoichiometry, similarly to a constant flamelet approach. The second region is found at the spray boundary in the distance of 12 – 30 mm, caused by the higher intensity of chemical reactivity in the extremely lean mixture at a higher strain rate.

In general, the implementation of multiple flamelet approach in Quasi-1D model considers the effect of local flow straining on the flamelet and it is conceptually more consistent with the precondition of describing the turbulent flame as an ensemble of strained laminar flames. As described in Chapter 3, the calculated local strain rate is only dependent on the local mixture fraction, while the implementation of multiple flamelet is strongly limited by the chemical mechanisms, i.e., the ignition limiting strain rate is at 1250 1/s for LLNL mechanism, but it is at 2500 1/s for Nara mechanism. Furthermore, in the lean mixture, the longer residence time causes a faster reach to the steady state. Meanwhile, the absence of turbulence-chemistry interaction (e.g. by means of a presumed PDF) probably also limits the accuracy of the predictions. Therefore, the current implementation of multiple laminar flamelet cannot realize a reasonable ID & LOL prediction using arbitrary mechanism. Considering the computational accuracy, the employment of a constant strain rate at low ranges could achieve a more accurate ID & LOL, and it also simplifies the calculation. In view of the additional degree of freedom that the selection of a single strain rate offers, the latter approach has been selected for the calculations.

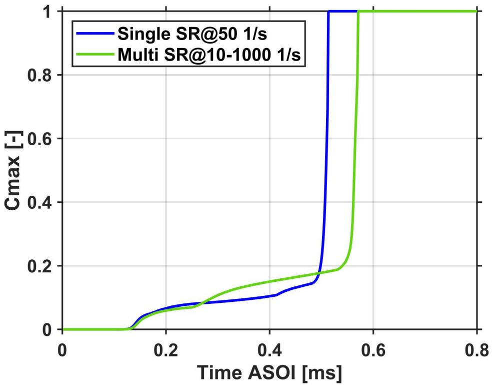

Figure 4.22. The time evolution of Cmax across the spray from the constant flamelet and multiple flamelets approach

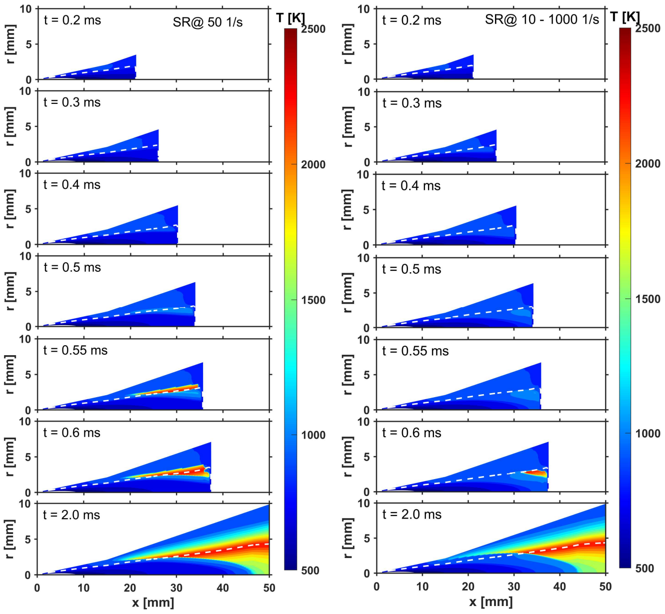

Figure 4.23. Time-sequence 2D contours of temperature (T) along the ignition process and the steady state. Left: constant strain rate @ 50 1/s; Right: multiple strain rates @ 10 – 1000 1/s. The white dash line represents the surface of the stoichiometric ratio.

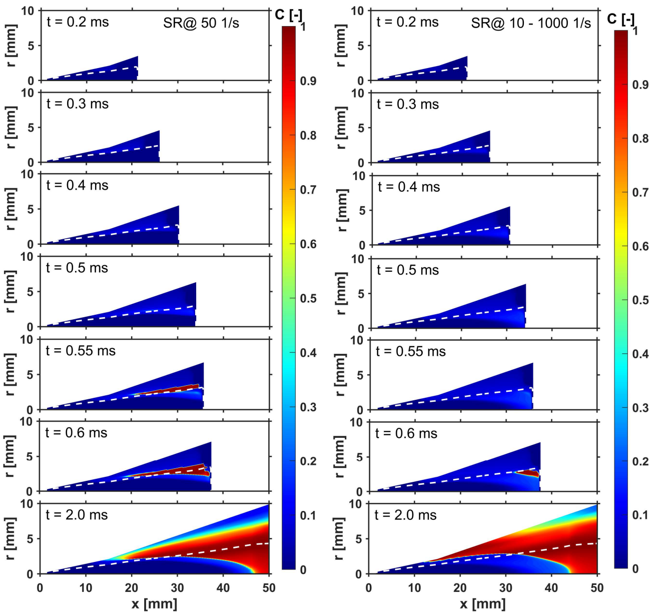

Figure 4.24. Time-sequence 2D contours of normalized progress variable (C) along the ignition process and the steady state. Left: constant strain rate @ 50 1/s; Right: multiple strain rates @ 10 – 1000 1/s. The white dash line represents the surface of the stoichiometric ratio.

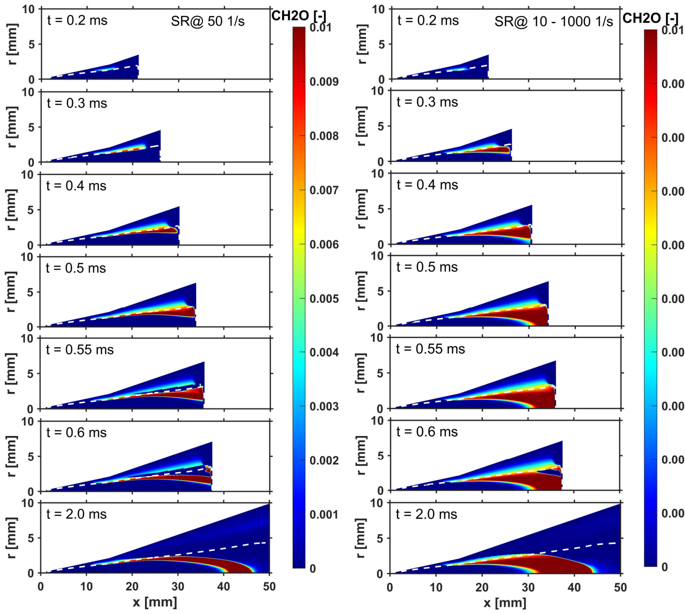

Figure 4.25. Time-sequence 2D contours of formaldehyde (CH_2O) along the ignition process and the steady state. Left: constant strain rate @ 50 1/s; Right: multiple strain rates @ 10 – 1000 1/s. The white dash line represents the surface of the stoichiometric ratio.

4.4 Variation of mixing characteristics

Starting from Quasi-1D modelling results, the study in this section examines the impact of varying injection pressure and nozzle diameter on the spray and combustion process. According to experimental results, ID is weakly inversely proportional to injection pressure, while the relation to LOL is proportional [22]. Furthermore, the injector with a large-diameter nozzle, typically found in heavy-duty engines, results in longer ID and LOL, as well as increased soot formation [219]. The present section will show a discussion on the performance of Quasi-1D modelling to the varied injection pressure/nozzle diameter.

To achieve this target, the validation of inert spray tip penetration for liquid and vapor phases is presented firstly, followed by an analysis of mixture fraction and local residence time. Subsequently, the prediction of ID & LOL versus strain rate using Quasi-1D modelling is discussed by making the comparison between injection pressures and nozzle diameters. The ignition process is then depicted through T- f spaces and CH_2O – T spaces. Next, validation on reacting spray tip penetration, ID & LOL are provided for a variation of injection pressure ($P_{inj} = 500/1500\ bar$) and nozzle diameter (Spray A/D) around the nominal condition ($T_a = 900\ K, XO_2 = 15\%, \rho_a = 22.8\ kg/m^3$). Finally, the validation is extended to different ambient conditions ($T_a = (800/900/1000)\ K, XO_2 = 15/21\%$) together with the three injection pressures ($P_{inj} = 500/1000/1500\ bar$), and statistical analysis is conducted to assess the accuracy across all investigated conditions. Previous section has shown that Nara mechanism is much less reactive than Yao and LLNL, resulting in an overly delayed ignition at the nominal Spray A condition. Therefore, the present section only considers Yao and LLNL mechanisms.

4.4.1. Inert spray analysis

Following the configuration outlined in Table 4.2, the model validation for the liquid and vapor penetration is presented in Figure 4.26, where liquid length is defined as the axial distance to the shortest location where the axial mixture fraction firstly reaches the value of evaporation mixture fraction f_{evap}, and the vapor penetration is defined as the axial distance to the furthest location where the axial velocity reaches a value of 0.1% of the one at the orifice outlet. The results show good agreement between the measurements and the 1D modelling, although there is a slight overprediction of LL for Spray D. Additionally, the profiles of axial mixture fraction at 3.5 ms ASOI are displayed in Figure 4.27. The graph illustrates an overlap in mixture fraction with the variation of injection pressure, as the entrainment rate is not affected by this parameter, i.e. a higher injection rate results in a higher air entrainment. On the other hand, a larger nozzle diameter causes a higher mixture fraction, due to reduced entrainment rate.

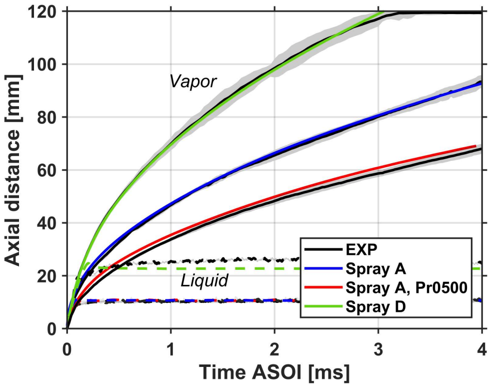

Figure 4.26. The validation of spray tip penetration of inert n-dodecane spray under the conditions of Spray A (SA), injection pressure 500 bar of Spray A (SA), and Spray D (SD)

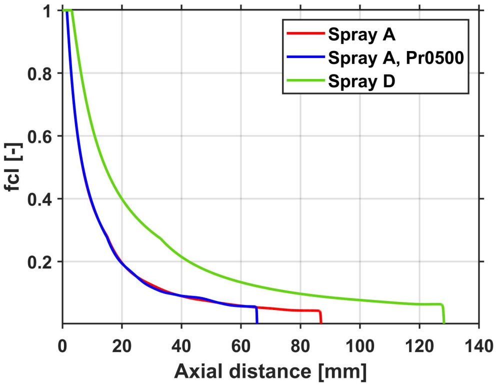

Figure 4.27. Axial mixture fraction of inert spray under the condition of Spray A (red), injection pressure 500 bar at Spray A (blue) and Spray D (green)

In addition to the local mixture fraction, which is directly related to the chemical source term, another parameter that affects the chemical state along mixing trajectories is the local residence time. Following Pachano [194], a local residence time (dt/df) that represents the time spent at a specific mixture fraction f (or equivalence ratio ϕ) is defined based on mixing trajectories as the time spent per unit of mixture fraction f according to

$$\frac{dt}{df} = -\frac{dt}{dx}\frac{dx}{df} = -\frac{1}{u}\frac{dx}{df} \tag{2}$$

where dx/df is the gradient of mixture fraction as projected along the horizontal direction defined by the axial velocity field (u) [194]. Figure 4.28 presents the contours of local residence time for Spray A at nominal case and injection pressure 500 bar, as well as for Spray D under inert conditions. A logarithmic scale in the colormap has been adjusted for better visualization. Three white lines are plotted to represent the surfaces of equivalence ratio at 1.0 (solid line) and 0.5 and 2.0 (corresponding to the outer and inner dashed lines, respectively). Generally, local residence time increases as it transitions to a lower mixture fraction, both axially and radially, which results in largest values on the fuel-lean side ($\phi < 1.0$). The contours show that residence time at a given equivalence ratio value tends to increase when shifting from nominal to low injection pressure or larger orifice cases.

For a more comprehensive comparison of the mixing conditions, the values of residence time along the surface of $\phi = 1.0$ & 2.0 is shown in Figure 4.29 (bottom), as well as the profiles of these two surfaces with spatial coordinates normalized by deq. The use of a normalized spatial coordinate results in identical iso-lines location for all three investigated cases, which shows that the mixing field scales essentially with this parameter, i.e. with nozzle diameter, and is independent of injection pressure. In comparison to the nominal condition, a lower fuel injection velocity at low injection pressure leads to a longer local residence time, which is approximately the square root of injection pressure ratios ($1500bar/500bar$). Meanwhile, the low injection pressure also results in a slower mixing. In the case of Spray D, the time spent at given equivalence ratios ($\phi = 1.0$ & 2.0) is approximately twice as long as in Spray A, which corresponds to the ratio of nozzle diameter ($d_{SprayD}/d_{SprayA} = 191\mu m/89.4\mu m$).

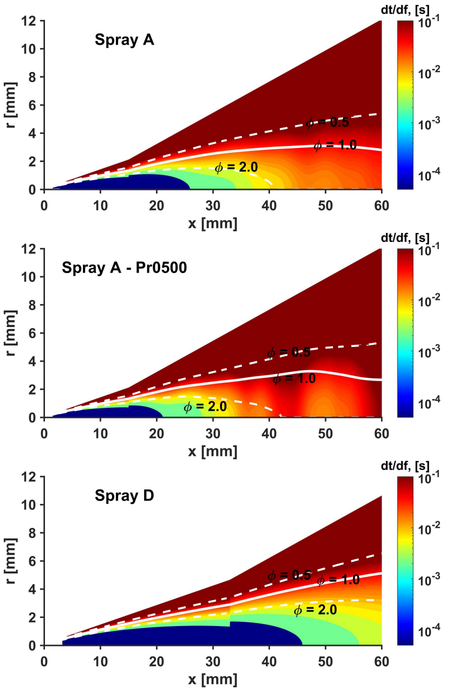

Figure 4.28. The contours of local residence time for the inert condition of Spray A, injection pressure 500 bar, and Spray D. the lines of equivalence ratio at ϕ = 0.5, 1.0, 2.0 from the upper to the bottom.

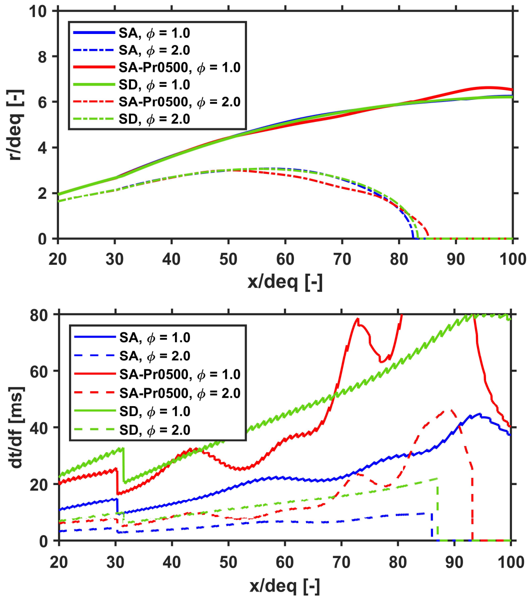

Figure 4.29. Iso-contours of $\phi = 1.0$, 2.0 (upper) and the corresponding local residence time along iso-contours of $\phi = 1.0$ and $\phi = 2.0$ (bottom) for inert Spray A, injection pressure 500 bar and Spray D.

In summary, a decrease in injection pressure results in a spray developing at a lower speed over a similar mixing field, while the increase in nozzle diameter results in a faster development of the spray over a richer mixing field. On the other hand, the time spent at a given mixture fraction increases with both a decrease in injection pressure and an increase in nozzle diameter. This makes up the mixing conditions where subsequent combustion will develop.

4.4.2. Mixing effects on combustion development at nominal ambient conditions

Ignition and lift-off length

The profiles of ID & LOL against strain rate under the conditions of nominal Spray A are presented in Figure 4.30 and Figure 4.31, respectively. The comparison is carried out in terms of different injection pressures (1500/500 bar), nozzle diameters (Spray A/D) and chemical mechanisms (Yao & LLNL). Additionally, the corresponding ignition delay from the flamelet tabulation is also included in red color for reference. For each case, the experimental result is plotted by a dashed line with shadow to denote measurement uncertainty.

According to the results of the Yao scheme (Figure 4.30.a), at low injection pressure, the predicted ID values align closely with those under Nominal Spray A within a strain rate range of [1 – 80 1/s], with ignition occurring near stoichiometry, similar to the analysis in Figure 4.14. As the strain rate increases up to 700 1/s, a shorter ID is observed at the lower injection pressure. As previously discussed for the nominal condition, this corresponds to the fact that the ignition position shifts towards the fuel-rich side. Figure 4.28 shows that residence time values overall increase with decreasing injection pressure. With further increase in strain rate, the ignition position shifts towards the fuel-lean side (as indicated in Figure 4.17), and the local residence time between injection pressures becomes less sensitive in this area. For the case of LLNL mechanism, the trend of ID versus SR shows a monotonic increase for both cases at injection pressure 500 and 1500 bar, which is similar to the data originating from flamelet (red symbol). Meanwhile, the predicted ID at low injection pressure is slightly longer, except for the conditions within the strain rate range of [400 – 900 1/s], but differences are certainly small.

For the effect of nozzle diameter on the ignition delay, shown in Figure 4.30.b, the sensitivity of the model is certainly similar to the one previously observed for injection pressure for both mechanisms, with Yao solution being more sensitive than LLNL. The latter one shows a slight increase in ID with nozzle diameter at low SR values that is not observed for the low injection pressure.

As the strain rate increases towards the extinction limit, the profiles of LOL as a function of strain rate are consistent with the corresponding profiles of ID. However, compared to the Nominal Spray A condition, LOL is more sensitive to the varied mixing conditions, which differs from the overlapped ID at small strain rates in Yao scheme and close ID across the entire strain rate in LLNL scheme. Across the entire strain rates, the sensitivity of LOL at both lower injection pressure and larger nozzle diameter are observed to be weaker than that at Nominal Spray A condition, while this weaker sensitivity is observed at smaller strain rate in Yao scheme and at large strain rate in LLNL scheme. In addition, LOL at lower injection pressure is expected to be shorter along the whole strain rates, regardless of Yao or LLNL mechanisms. For the Spray D conditions in Yao scheme, LOL is predicted to be shorter than that of Spray A in the strain rates of 300 – 600 1/s.

Summarizing, the sensitivity of numerical ID predictions to both operating variables is quite different depending on the chemical mechanism. While Yao shows a similar sensitivity of ID to both variables, with a trend that depends on the SR range, LLNL mechanism is essentially insensitive to injection pressure and only slightly dependent on orifice diameter. The latter mechanism captures better experimental ID sensitivity, which is much lower in injection pressure compared to that of nozzle diameter. As for LOL, both chemical mechanisms capture very nicely the experimental variation with injection pressure and nozzle diameter.

In the comparison of experimental database and simulation, it has been discussed that the choice of SR = 20 1/s is the feasible one from the results under nominal Spray A condition with Yao mechanism, and SR = 50 1/s is the one for LLNL mechanism. When extended to low injection pressure at Yao mechanism, the predicted ID matches the measurement at SR = 40 1/s while the predicted LOL is closer to the experiment at SR = 20 1/s. At LLNL mechanism, the curve of LOL as SR is nearly flat in the range of SR < 300 1/s, and predicted ID also shows a good agreement in a small range SR < 100 1/s. For the case of Spray D, with Yao mechanism, it is expected to match the measurement at a higher strain rate of 100 1/s based on ID, but it is overpredicted for LOL at this case. With the LLNL scheme, a good prediction to ID can be found near SR = 50 1/s, and the curves of LOL against SR are also nearly constant under the SR lower 50 1/s. This suggests that the difference on the mixing state has little effect on the ID with Yao mechanism in the range of stoichiometric ignition and LLNL mechanism. Finally, the initial selection at nominal condition of a constant value of strain rate equal to 20 1/s for Yao mechanism and 50 1/s for LLNL mechanism can be kept here for the parametric variations in injection pressure and orifice diameter.

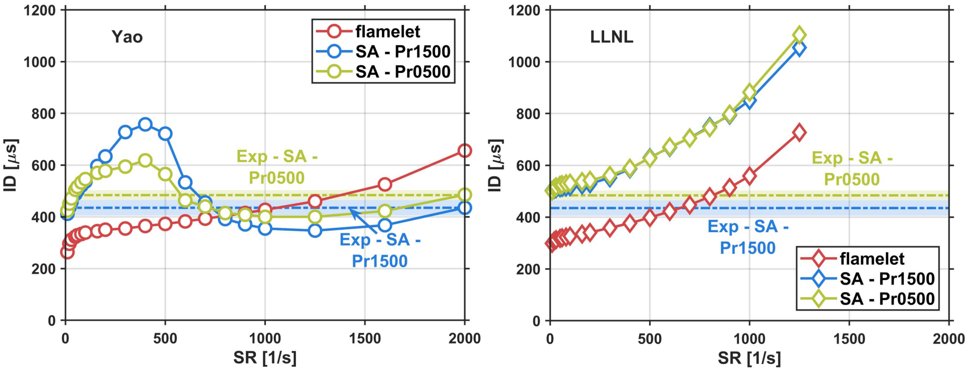

a. Injection pressure 500 bar and 1500 bar

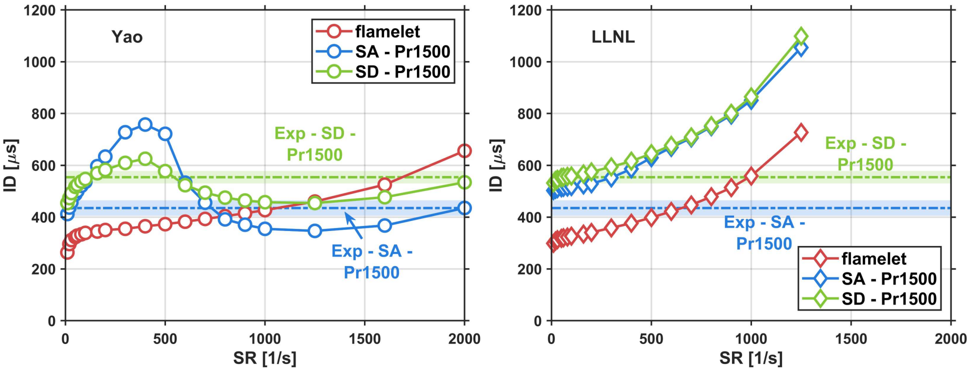

b. Spray A and Spray D

Figure 4.30. Quasi-1D model results for ignition delay against strain rate shown as the comparison between injection pressure at 1500 bar and 500bar (a), Spray A and Spray D (b). Left images: Yao mechanism; Right image: LLNL mechanism

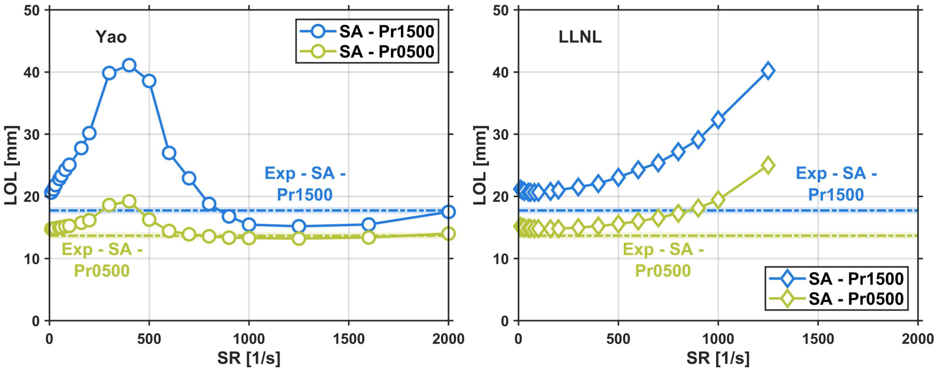

a. Injection pressure 500 bar and 1500 bar

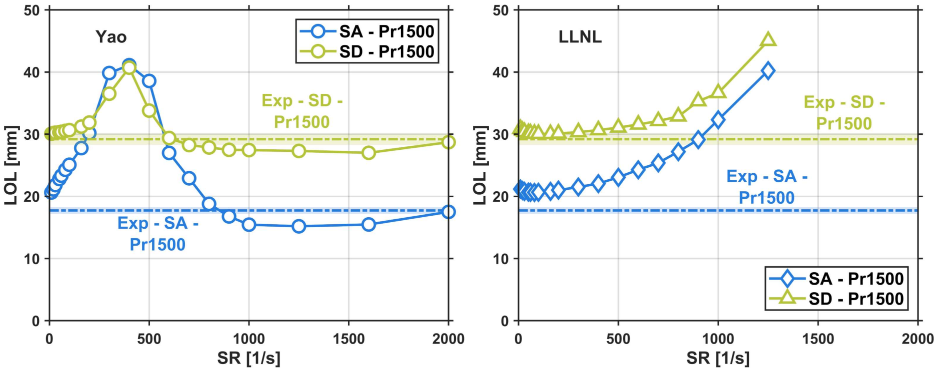

b. Spray A and Spray D

Figure 4.31. Quasi-1D model results for lift-off length against strain rate shown as the comparison between injection pressure at 1500 bar and 500bar (a), Spray A and Spray D (b). Left images: Yao mechanism; Right images: LLNL mechanism

Figure 4.32 shows the ignition process by instantaneous Cmax across the spray for three different mixing conditions using Yao (left) and LLNL mechanisms under a constant strain rate (SR = 50 1/s). After the fuel ejection, Nominal Spray A first travels to the liquid length, where the reaction is assumed to begin. Then, a similar time period (~50 μs) is observed from the point of reaching the first maximum liquid length to the onset of chemical reaction (first-stage ID). However, there is little impact on the chemical state level (Cmax value reached) during the first-stage ignition process, regardless of the Yao and LLNL mechanisms. Moreover, the longest residence time leads to the shortest duration of the second-stage ID under the low injection pressure and Spray D conditions. However, the final ignition point eventually occurs earlier for the nominal condition compared to the lower injection pressure or larger nozzle orifice. As previously discussed, sensitivity is very similar for both injection pressure and nozzle diameter for Yao, while the effect of injection pressure is less noticeable for LLNL. Corresponding to the experimental results, the difference in ignition delay is larger in the comparison of Spray D and low injection pressure, compared to the comparison of different injection pressures, and this trend is only captured in LLNL scheme.

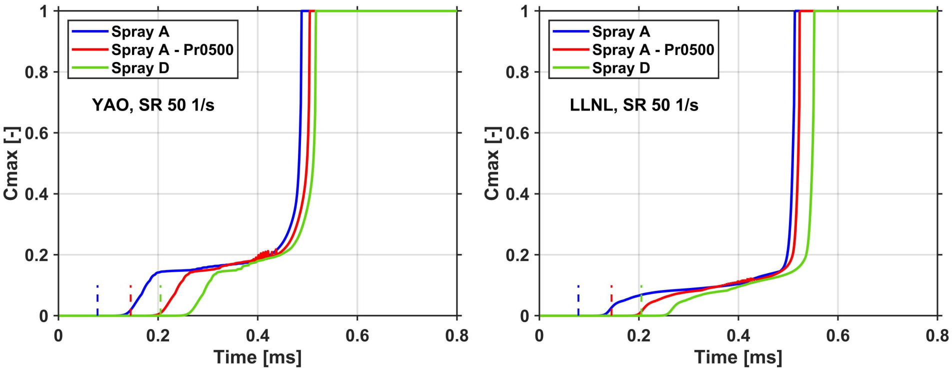

Figure 4.32. The evolution of Cmax rate for nominal Spray A, injection pressure 500 bar and Spray D with mechanism Yao (left) and LLNL (right). The vertical dashed lines represent the instant when the spray tip first reaches its maximum liquid length. The dotted lines in the right side of the dashed lines represent the measured ignition delay.

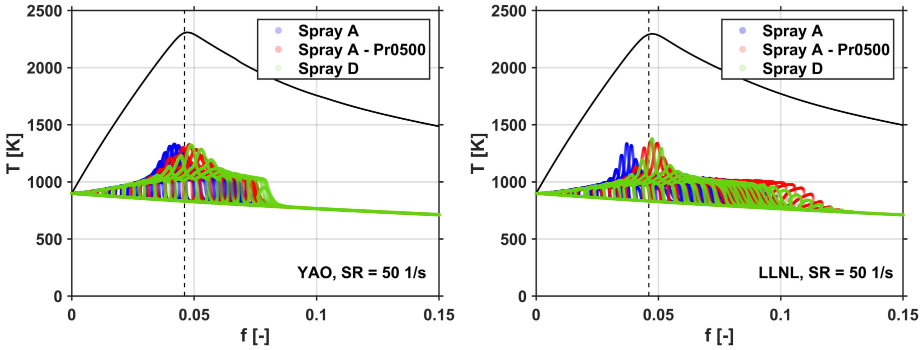

Figure 4.33. Scatters in T- f space at the instant of Tmax ≥ 1300 K for the case of Nominal Spray A, injection pressure 500 bar and Spray D using mechanism Yao (left) and LLNL (right). Dashed line: stoichiometric ratio; solid lines: steady-state solution.

To further analyze mixture formation during ignition, Figure 4.33 illustrates the thermochemical state of the spray (temperature vs mixture fraction) in the mixture fraction space of at ignition timing (defined as the timing to reach a maximum temperature of 1300 K, also adopted as the ID definition in [21] [190]). The strain rate is at 50 1/s for both mechanisms. The scatterplot includes all the trajectories. Compared to nominal Spray A, the mixture fraction ignition site slightly shifts to the fuel-rich side as the decrease in injection pressure as well as larger nozzle diameter, which is also consistent with the results reported in [220]. This shift is more pronounced in LLNL scheme. Moreover, ignition also takes place near the stoichiometry. As a result of the longer residence time in the fuel-rich side for both lower injection pressure and larger diameter, a wider range of mixture fraction is observed, especially in the LLNL results, as opposed to Spray A.

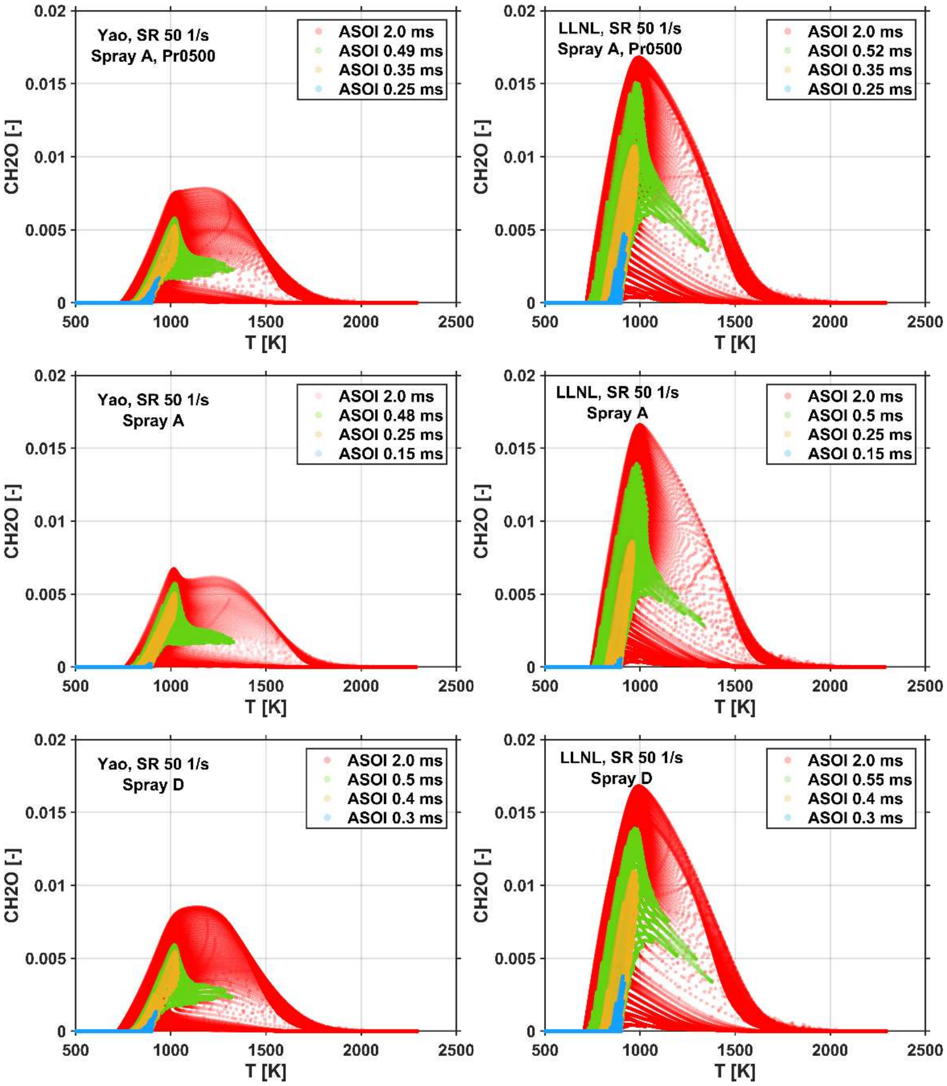

Figure 4.34. The integration of CH_2O mass fraction as temperature along ignition process for the different mixing conditions (upper: Injection pressure 500 bar, Spray A; middle: nominal Spray A; bottom: Spray D)

Figure 4.34 presents the evolution of CH_2O formation in CH_2O – T spaces at four specific time points:

- the onset of CH_2O formation,
- 100 μs after CH_2O initiation,
- the moment when the maximum temperature exceeds 1300 K,
- the steady state at 2.0 ms ASOI.

Acting as an indicator for cool-flame ignition, CH_2O is produced shortly after the onset of chemical reactions (Cmax > 0) in the mixture at temperatures around 900 K. As the reaction progresses, more CH_2O is generated in the low temperature range (700 – 1000 K), then it is consumed as an intermediate species during subsequent high-temperature combustion. Ultimately, at steady state, CH_2O is observed across a temperature range of 750 K – 1800 K, with a peak at around 1000 K under nominal Spray A condition.

As for the difference on injection pressure, the appearance of CH_2O happens earliest at the nominal Spray A condition for both Yao and LLNL mechanisms, which is against with the discussion in [205]. In Quasi-1D model, the vaporization correction is based on the mixture fraction in the axial centreline, and the chemical activity in the upstream of liquid length is ignored. However, CH_2O formation near the spray periphery is still observed. At low injection pressure, the later appearance of CH_2O is attributed to the longer time required to reach the maximum liquid length (Figure 4.32). At steady state (2.0 ms ASOI), a higher CH_2O mass fraction is observed in the temperature range of 1000 – 1300 K in Yao scheme. However, the highest CH2O mass fraction is almost the same for both injection pressures, and more CH_2O formation is only found at a lower CH_2O mass fraction in the oxidation region where temperature exceeding 1300 K, which is also shown in Yao scheme. Lastly, higher CH_2O formation is observed in the LLNL scheme compared to Yao due to its increased reactivity.

Following a similar argument, the appearance of CH_2O in Spray D is also compared to Spray A at a later stage, as a result of the time needed for vaporization. In addition, the higher mixture fraction all over the spray due to slower mixing contributes to more CH_2O formation, as evidenced by the higher concentrations in the high temperature range (1000 K – 1500 K) at steady state. The highest level in the contour is larger than Spray A using Yao mechanism, while it is nearly constant under LLNL scheme. Summary, the trend of CH_2O formation among the different mixing conditions is reasonable at the steady state, even though the instant when the CH_2O appearance is not fully consistent with CFD work.

Penetration and velocity field

To finalize the discussion on mixing effects, the analysis of tip penetration and velocity field will be carried out. In this case, the approach of imposed ignition spread is adopted that includes radial expansion in the downstream of lift-off length.

Firstly, the effect of radial expansion on the spray penetration and axial velocity for the nominal Spray A condition is shown in Figure 4.35 and Figure 4.36, respectively. When including radial expansion, spray penetration was slightly deaccelerated after 1.5 ms ASOI and consequently it matches better with the measurement at a large distance. Meanwhile, no significant difference was observed between Yao and LLNL mechanism.

As for on-axis velocity, Figure 4.36 shows that at the distance of x/deq ~43, the ignition-induced radial expansion causes the steep increase in axial velocity, hence, the predicted axial velocity is more accurate in the normalized axial distance from x/deq = 50 – 100. Due to the difference in the predicted ignition delay using Yao and LLNL mechanism, the LLNL scheme shows a slightly higher value in the interval of x/deq = 60 – 100, while both schemes are within the measurement uncertainty.

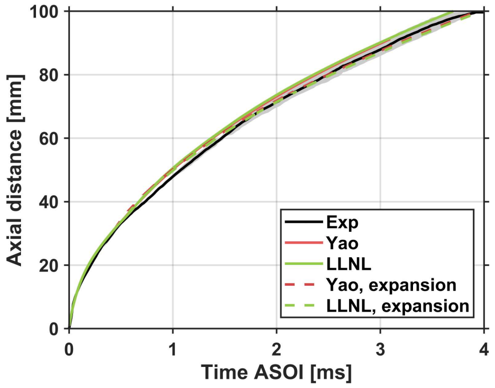

Figure 4.35. The comparison of penetration between experiments and Quasi-1D model. Yao mechanism: SR = 20 1/s; LLNL mechanism: 50 1/s. Solid lines: Quasi-1D modelling without the expansion; Dashed lines: Quasi-1D modelling with expansion.

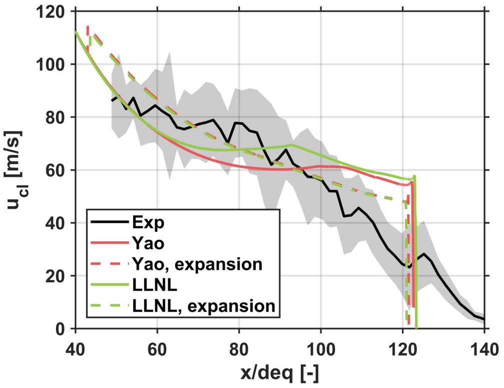

Figure 4.36. The comparison of axial velocity of reacting spray at 1.5 ms ASOI between experiments and Quasi-1D model. Yao mechanism: SR = 20 1/s; LLNL mechanism: 50 1/s. Solid lines: Quasi-1D modelling without the expansion; Dashed lines: Quasi-1D modelling with expansion.

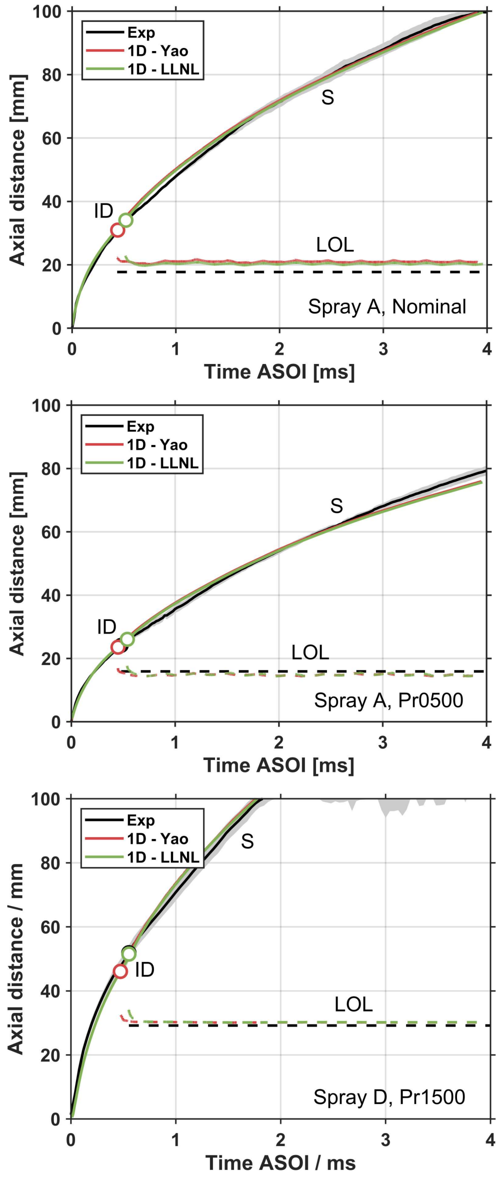

Figure 4.37. The validation on reacting spray tip penetration, ignition delay and timed lift-off length under the conditions of Spray A (upper), injection pressure 500 bar (middle) and Spray D (bottom) using mechanism Yao (SR = 20 1/s) and LLNL (SR = 50 1/s)

Figure 4.37 illustrates the comparison of results for spray tip penetration (solid lines), ignition delay (round markers) and lift-off length (dash lines) for the nominal, low injection pressure and Spray D calculations with both Yao and LLNL mechanisms. Corresponding strain rates are 20 1/s (Yao) and 50 1/s (LLNL). The experimental data for each variable is plotted in black, with the grey shadow indicating the measurement uncertainty [22] [131] [152]. Good agreement on spray tip penetration is observed for both mechanisms at all three conditions, with a slight overprediction during the transient phase immediately after ignition. It is noted that penetration is slightly underestimated after ASOI 3.0 ms at low injection pressure, possibly due to inaccuracies in ΔR calculation.

The evolution of temperature contours during the ignition process are presented in Figure 4.38, with the top halfplane displaying results calculated using Yao mechanism and the bottom halfplane showing results from the LLNL scheme. The white dashed line is the stoichiometric ratio. The black dashed lines correspond to the instantaneous lift-off length. Five instants are selected for each condition: the first line is at the instant when Tmax > 1300 K, the second, third and fourth show subsequent instants, and the final one is obtained at 2.0 ms ASOI.

For the nominal Spray A condition, at the first instant, the ignition takes place in the distance of 20 – 30 mm along the stoichiometric surface. Soon, the maximum temperature rises to the value at equilibrium state, and the radial expansion can be observed that starting at the distance of ~25 mm. Under the assumption of imposing ignition propagation downstream of the C-defined lift-off length, the spatial spread of progress variable along the radial direction is neglected, and the temperature is only dependent on the local mixture fraction. As a sequence, a strong reactivity near the spray center and periphery is formed, different from the little reactivity shown in Figure 4.19, where ignition only happens along preferential trajectories. As combustion proceeds, a slight recession in lift-off can be observed until it eventually stabilizes at $x = 22$ mm.

Under lower injection pressure and Spray D, the ignition process exhibits similar behaviors to nominal Spray A. However, the ignition position is closer to the nozzle for lower injection pressure and farther for Spray D, in agreement with lift-off length predictions. Additionally, the temperature at the spray centerline is lower, particularly for Spray D, as mixing proceeds slower and the stoichiometric reacting surface will be stabilized further away from the nozzle. When comparing mechanisms, minimal differences were observed in terms of temperature contours.

During the ignition process, the position of LOL is always at the upstream of the position where radial expansion begins. Meanwhile, the discrepancy between them is larger at the bottom halfplane. This confirms that forcing the transient to flamelet steady state does not affect the prediction to lift-off length.

For the comparison between Yao and LLNL schemes, earlier instants at the maximum temperature exceeding 1300 K and the radial expansion appearance are observed in Yao scheme for the three conditions. However, the ignition position is similar using these two mechanisms, i.e., spray ignited at the distance of ~35 mm near the stoichiometry at 457 μs ASOI using Yao mechanism, and a similar ignition is found at 546 μs ASOI using LLNL mechanism. At steady state, the temperature contour is almost the same between Yao and LLNL scheme, with only a longer distance in radial expansion appearance in LLNL scheme.

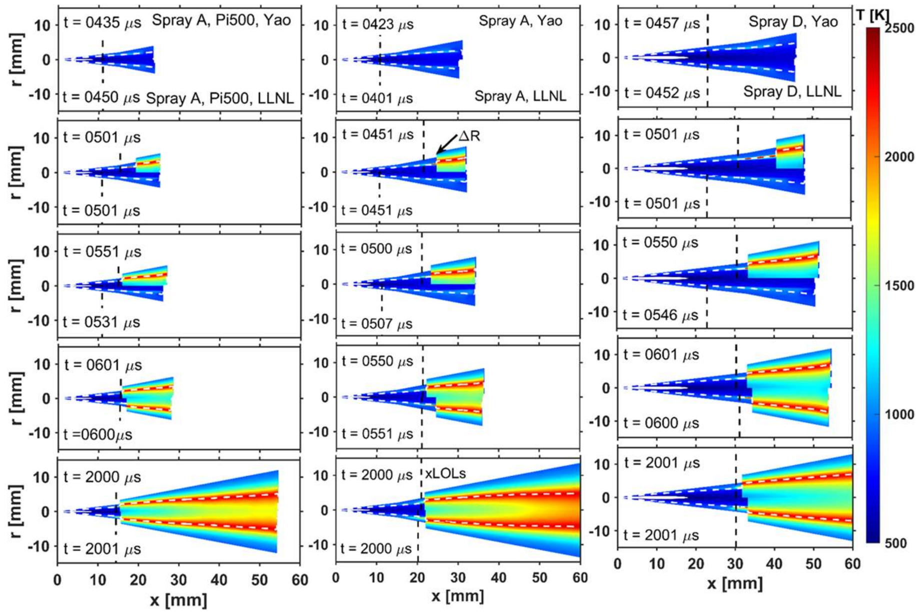

Figure 4.38. The comparison of temperature contours along ignition process between mechanism Yao and LLNL under the conditions of Nominal Spray A (middle), injection pressure 500 bar (left) and Spray D (right)

4.5 Further parametric variations

As previously discussed, the main advantage of the Quasi-1D model is the accurate calculation with low computational cost. The present section explores the accuracy of this approach over a wide range of ECN experimental conditions to evaluate its predictive capabilities.

The calculation of radial expansion ($\Delta R = R_{reac} - R_{inert}$), which has been introduced in the final version of Quasi-1D modelling, directly impacts spray penetration, velocity field and mixing after the ignition delay. Comparison between predicted and measured ΔR values are shown in Figure 4.39 over a wider set of experimental conditions. Even though experimental results only include three injections pressure values at nominal ambient conditions, plus one higher oxygen concentration and one low ambient temperature at nominal injection pressure, the simulated cases include all conditions in Table 4.1. Consistently with previous observations [152] [167], lower injection pressure results in smaller ΔR, particularly noticeable at low ambient temperature and with a large nozzle (Spray D). Additionally, overprediction occurs at low injection pressure, contributing to the underestimation of penetration at greater distances. Furthermore, the level of ΔR is proportional to ignition delay, with longer ID leading to greater radial expansion distances and consequently larger R values. Note that the chemical mechanism has little influence on radial expansion, except at lower temperature.

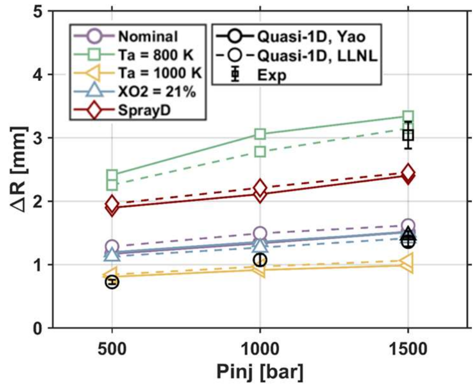

Figure 4.39. ΔR for parametric variation of injection pressure together ambient conditions and Spray D using mechanism Yao and LLNL. The black points are the data from experiment [152] [167].

The Quasi-1D model leverages the prediction to ID & LOL, which are two key parameters of key importance for describing the characteristics of transient mixing-controlled reacting sprays in a cost-effective manner. In Figure 4.40, the comparison of ID & LOL is presented between measurements and Quasi-1D modelling using Yao and LLNL mechanisms. This comparison was conducted for cases involving varying injection pressures, ambient temperatures (800 K and 1000 K), oxygen concentration (XO2 = 21%), and nozzle diameter (Spray D). The analysis is complemented here by the information in Appendix A and B, including the sensitivity to SR of ID and LOL, as well as sample temperature contours to understand ignition.

Nominal Spray A condition

Under the nominal 900 K Spray A conditions with the difference on injection pressure, which has been described extensively in previous sections, good agreement is observed at three cases, only with a slight deviation for the predicted ID using LLNL mechanism. Besides, the resolutions at two mechanisms show the same results on LOL.

Ambient temperature

For the validation under higher ambient temperature (Ta = 1000 K, the third row), both mechanisms present underestimated ID for the three cases, with the discrepancy being less pronounced in the LLNL scheme. The ignition position shifted towards the fuel-rich side ($1.0 < \phi < 2.0$), and the predicted ID matched the measurements within the range of SR 200 – 300 1/s, as shown in Appendix A. This suggests that a single strain rate for all conditions limits the diffusion in the modelling. Similarly, there was little difference in the prediction to LOL between the two mechanisms.

At low temperature 800 K, significant overprediction of ID and LOL is observed for both mechanisms, particularly at an injection pressure 1500 bar. As shown in the appendix. A, the 800 K case exhibits longer overpredicted values for ID & LOL across all strain rates. This discrepancy may be attributed to different causes. One of them can be the limitations in the chemical mechanisms, which may not be as accurate in such low temperature conditions. Another point could be the limited species (CO, CO_2, H_2O) considered in the current Y_c definition, which does not adequately capture combustion process at low temperature. Including additional species such as HO_2 and CH_2O could improve ignition predictions [216] [221]. Previous numerical results have demonstrated accurate ID predictions but underestimated LOL when using the Y_c definition $(Y_C = Y_{CO} + Y_{CO_2})$ with a CFD framework [195]. Another factor could be the lack of consideration for turbulence-chemistry interactions and radial species diffusion in Quasi-1D modelling, which is also highlighted in [222]. Another noticeable effect that shows the challenge in predicting spray behavior under such conditions is the fact that sensitivity of ID to injection pressure changes. Experiments show that increasing injection pressure delays ID, while the opposite trend is observed for the other operating conditions. This trend is not captured by the Quasi-1D model, for which predictions deviate from experimental measurements, whereas the trend of LOL with Pinj aligns with experimental data [22]. It must be noted that the ignition under low temperature conditions occurs at a significant distance in the downstream of liquid length, where the mixture phase resembles a gas, supporting the gas jet theory assumption in Quasi-1D modelling. Inert simulations have shown higher local residence time at lower injection pressures and in lean mixtures, resulting in shorter ID. LOL predictions are more influenced by fuel injection velocity, with shorter LOL values at lower injection pressures in line with experimental findings.

Oxygen concentration

At high oxygen concentration (XO2 = 21%), higher chemical reactivity is achieved in the flamelet database, while the liquid length is similar to the non-reacting case, indicating similar fluid dynamical characteristics prior to ignition. Consequently, the curves of ID/LOL against SR closely resembled those of the nominal Spray A case, as illustrated in Appendix A. Both mechanisms yielded nearly identical predictions, with accurate results for ID but slight overprediction for LOL. This discrepancy may be attributed to neglecting reactions in the upstream of the liquid length in the nominal case, as observed experimentally, as well as differences in the definition of lift-off length based on chemiluminescence of the excited-state hydroxyl radical in measurement versus ground state OH in simulation. Nonetheless, the trend of ID/LOL with Pinj aligns well with experimental findings.

Nozzle diameter

Finally, the validations are performed with the variable of injection pressure accompanied with Spray D. An excellent agreement on the ID prediction is found using LLNL mechanism, and it is underestimated with Yao mechanism. Meanwhile, the discrepancy on the predicted ID between both mechanisms is nearly constant as the injection pressure decreases. A larger deviation in LOL prediction is observed at lower injection pressure. All in all, the prediction is still acceptable.

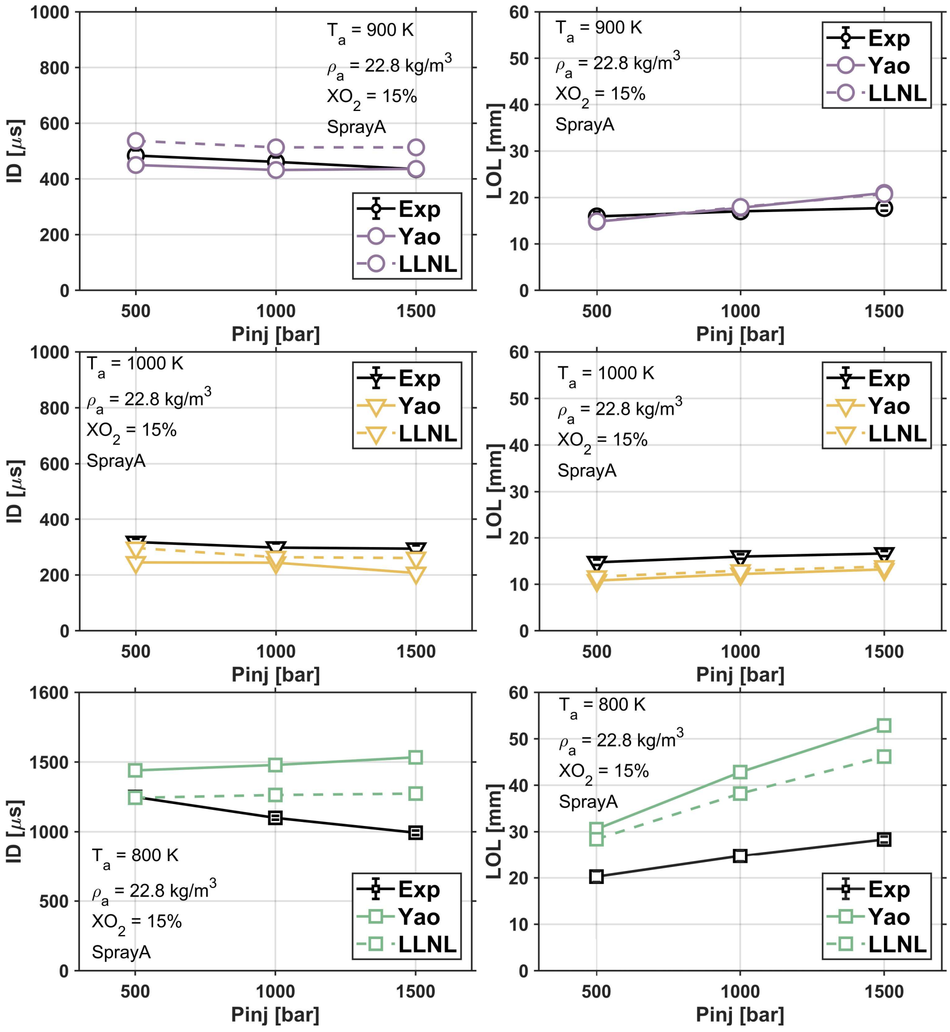

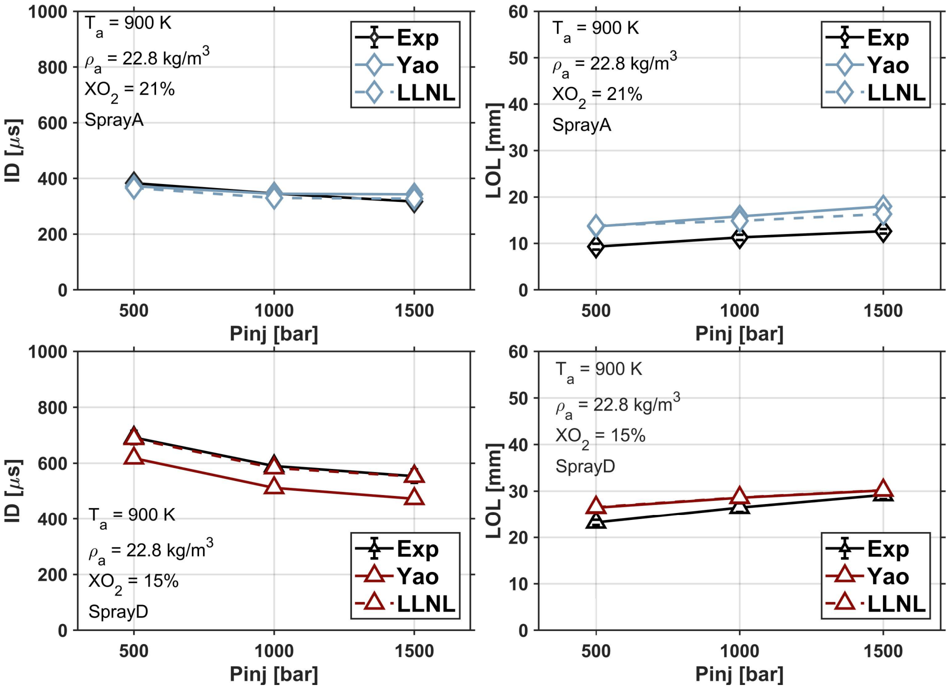

Figure 4.40. Comparison of calculated ignition delay (left) and lift-off length (right) using Quasi-1D model with Yao and LLNL mechanisms under the parametric variation.

For a global overview of the prediction accuracy with two mechanisms, the comparison of ID & LOL between the experiment and Quasi-1D modelling is shown in Figure 4.41 encompassing all investigated cases. Overall, this model delivers reasonable predictions within a deviation of 0.1 ms from the experimental ID and 5 mm from the experimental LOL for most of the conditions, also within a discrepancy of 20%. Notably, there is a minimal variance in LOL prediction between the two mechanisms, except for cases at low temperatures.

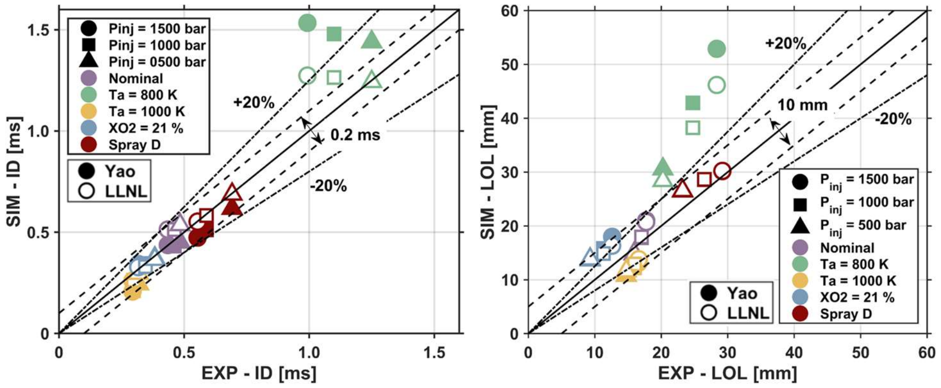

Figure 4.41. The comparison of experimental data and Quasi-1D model under all conditions. Solid markers are used for Yao mechanism, and the empty markers for LLNL mechanism. Markers with the same colour correspond to a variation of injection pressures. Dashed diagonals correspond to a ±20% and ±0.1 ms/5 mm for ID and LOL respectively.

4.6 Summary

In this chapter, the optimized Quasi-1D model has been validated by the conditions fueled with n-dodecane. Under ECN Nominal Spray A condition, the model validation was initially conducted with the inert spray characteristics, followed by the effect of strain rate on ignition process obtained from flamelet and Quasi-1D model. The integration of Quasi-1D model is evaluated between the single and multiple flamelets. Then, the effect of chemical mechanisms together with the variation of strain rate is analyzed. Finally, the model validation was performed under recommended ECN conditions using the approach of imposed ignition spread. The results obtained can be summarized as follows:

- The study establishes good agreement between the measurement and 1D modelling on the liquid length and vapor penetration for inert Spray A, as well as the good match on the quantities (velocity and mixture fraction) along axial direction and radial direction at three points.
- Flamelet ignition from all three chemical mechanisms reveals a two-stage process derived from the contours of transient term. Yao mechanism is more reactive in the first stage, while LLNL mechanism is more reactive in the moderate temperature within rich mixture. Nara mechanism performs like a reduced-intensity LLNL mechanism. Similar first-stage ID is observed between Yao and LLNL solutions, while the discrepancies in the lean side was found to be larger as strain rate increases. The second-stage ID is similar for both Yao and LLNL schemes in a low and middle strain rate across the entire mixture fraction. As for Nara, the longest ID for both first- and second-stage ignition is obtained.
- Regarding the ignition process from Quasi-1D model, as the strain rate increases, the results using Yao mechanism show a transition in ignition position from stoichiometric mixture to fuel-rich mixture, eventually progressing to lean mixture. This accompanies with the trends of both ID and LOL versus strain rates exhibiting an increase in the low SR, then decreases, and finally slightly increases again until the extinction limit. The results with LLNL mechanism display a transition beginning in lean mixture, then moves to rich side, and finally switches to lean mixture again. However, all the ignition is around the stoichiometry. Thus, both ID & LOL shows a consistently monotonic increase as strain rate. As for Nara, the ignition occurs at a leaner

mixture as the strain rate increases. Among the three mechanisms, the Nara solutions exhibit the longest ID and LOL.

- The first-stage ignition delay is not sensitive with the variation of strain rate. As for the temperature and species distribution, a thinner layer was found at a lower strain rate. Among the three mechanisms, the earliest first-stage is found with LLNL mechanism, while it lasts a longer time in the first-stage ignition period compared to Yao solution. At steady state, similar distribution of temperature is observed between Yao and LLNL solution, while LLNL solution shows a larger layer of CH_2O formation. The solution of Nara mechanism shows the distribution with the smallest area and lowest intensity.
- As a comparison of the prediction between the results obtained from individual flamelets and a global integration with multiple flamelets, the utilization of multiple flamelet doesn't affect the appearance of cool flame, but it prolongs the cool-flame period. The predicted ID matches the data from a single flamelet at strain rate ~300 1/s, while the predicted LOL shows the match at a higher value of ~800 1/s. It also results in a larger layer of CH_2O distribution and unexpected reactions occurring near the spray boundary in the middle distance. The predicted ID & LOL is further away from the measurement compared to the single flamelet at a low range of strain rate. In addition, the direct integration with multiple laminar flamelets will be limited by the different extinction limit of the used chemical mechanisms. Consequently, constant strain rate is more favorable in the calculations in this thesis.
- The discussion on the effect of mixing controlling operating variables introduces the performance of Quasi-1D model on the variation of injection pressure and nozzle diameter. The use of a normalized spatial coordinate results in identical iso-lines location for all three investigated cases, which shows that the mixing field scales essentially with this parameter. A lower fuel injection velocity at low injection pressure leads to a longer local residence time, which is approximately the square root of injection pressure ratios. The time of Spray D spent at given equivalence ratios is approximately twice as long as in Spray A, which corresponds to the ratio of nozzle diameter.
- The sensitivity of numerical ID predictions to both operating variables (injection pressure and nozzle diameter) is quite different depending on the chemical mechanism. While Yao shows a similar sensitivity of ID to both variables, with a trend that depends on the SR range, LLNL mechanism is essentially insensitive to injection pressure and only slightly dependent on orifice diameter. The latter mechanism captures better experimental ID sensitivity, which is much lower in injection pressure compared to that of nozzle diameter. As for LOL, both chemical mechanisms capture very nicely the experimental variation with injection pressure and nozzle diameter.

- Using the approach of imposed ignition spread with constant strain rate, good prediction on reacting spray penetration and on-axis mixture fraction have been achieved with both mechanisms, and there are little discrepancies between them. The consideration of liquid effect helps to achieve a consistent trend with measurement in ignition delay as the variations of injection pressure and orifice diameter.
- With the choice of SR = 20 1/s with Yao mechanism and 50 1/s with LLNL mechanism, Quasi-1D modelling demonstrates good predictions to ID and LOL within a 20% deviation from the measured values. However, it tends to overpredict cases at 800 K and slightly underestimates for cases at 1000 K. In general, LLNL is more favorable to the ID & LOL predictio. Therefore, LLNL mechanism is recommended in the calculation for n-dodecane when adopting Quasi-1D model, and the results using LLNL mechanism will be used in the following chapters.

4.7 Appendix A. Sensitivity to strain rate of ignition delay and lift-off length over parametric conditions

The selection of strain rate for the calculation using Quasi-1D model is from the plots of ID & LOL as strain rate under the Nominal Spray A condition. The profiles are known to be little influenced by the variation of oxygen concentration. Furthermore, the significant difference on the chemical reactivity caused by the variation of ambient temperature will lead to the difference on the matching on experimental ID & LOL among the strain rates, so we include the results of ID & LOL as a function of strain rate in Figure 4.42 – Figure 4.44. This also helps to explain the discrepancy on the ID & LOL predictions shown in Figure 4.40.

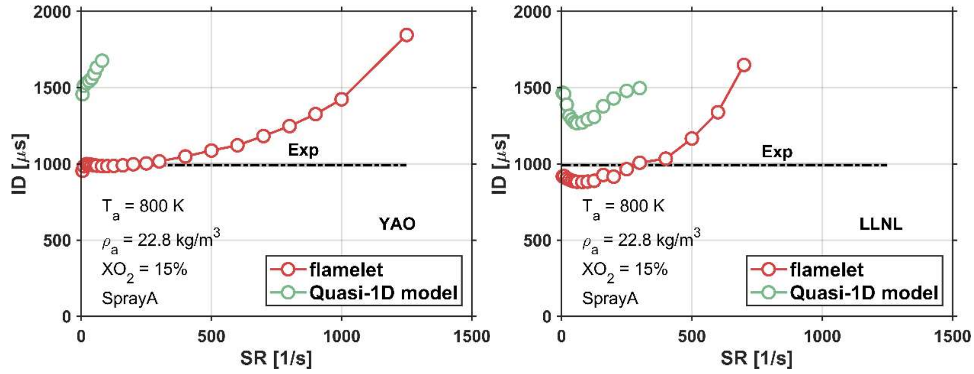

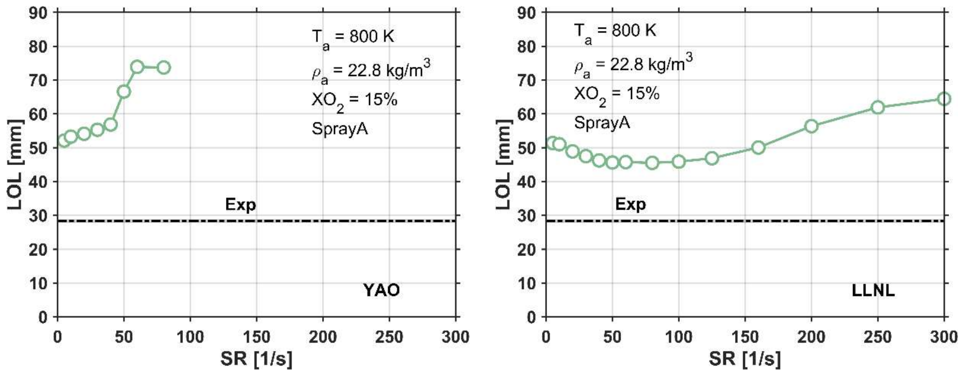

Figure 4.42. Ignition delay (top) and lift-off length (bottom) against strain rate for T800K at Spray A using mechanism Yao (left) and LLNL (right)

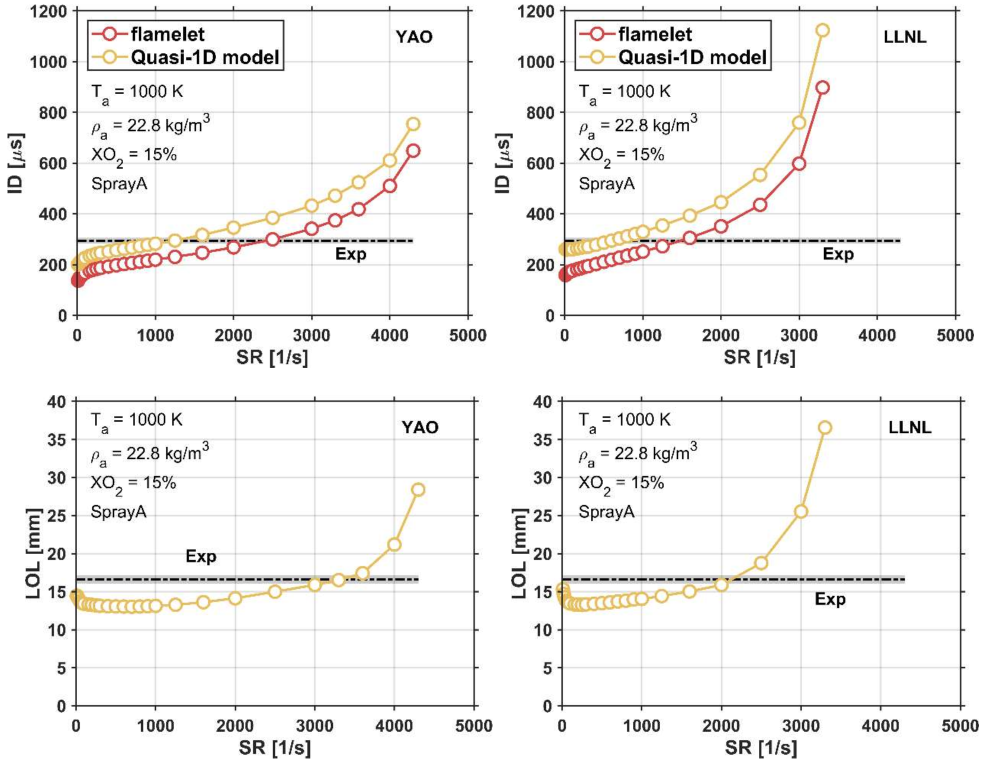

Figure 4.43. Ignition delay (top) and lift-off length (bottom) against strain rate for T1000K at Spray A using mechanism Yao (left) and LLNL (right)

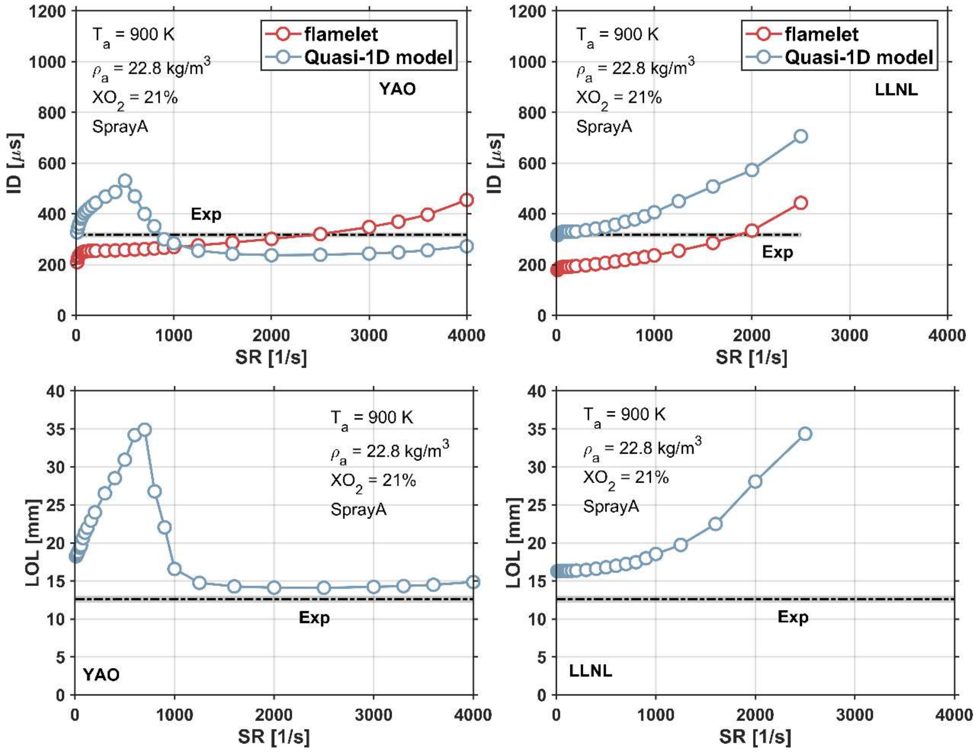

Figure 4.44. Ignition delay (top) and lift-off length (bottom) against strain rate for 21O2 at Spray A using mechanism Yao (left) and LLNL (right)

4.8 Appendix B. Ignition process for all the investigated cases using final version with radial expansion.

This appendix shows temperature contours around ignition delay time. Due to the simplified single strain rate approach employed on the calculation to all conditions, the stoichiometric ignition observed in the nominal Spray A will not be found under the lower or higher temperature conditions. As a next step of the analysis to the ID & LOL prediction, the ignition process under all conditions provided here also helps to assist a further evaluation of Quasi-1D model on the variation of ambient conditions.

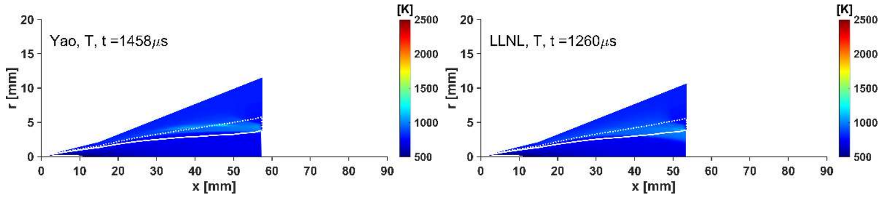

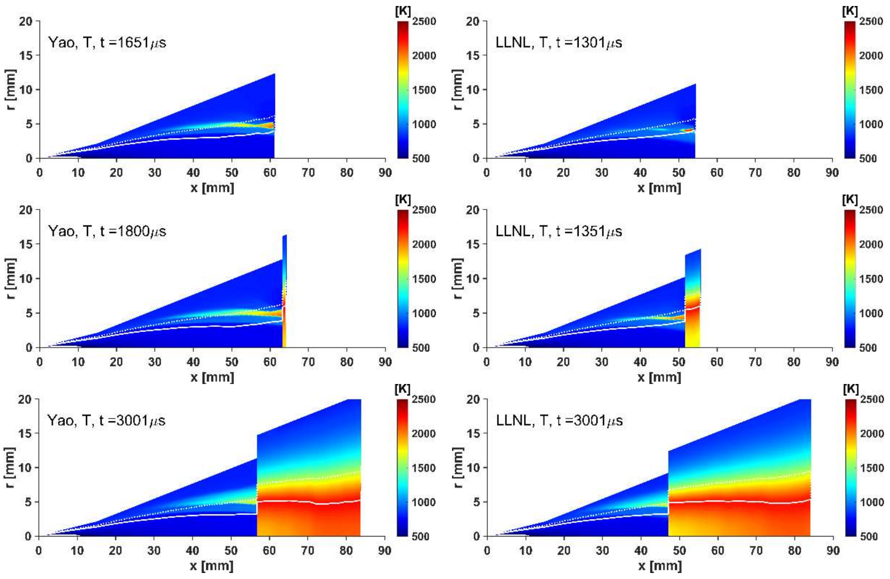

a. $T_a = 800\ K, XO_2 = 15\%, Pr = 1500\ bar$

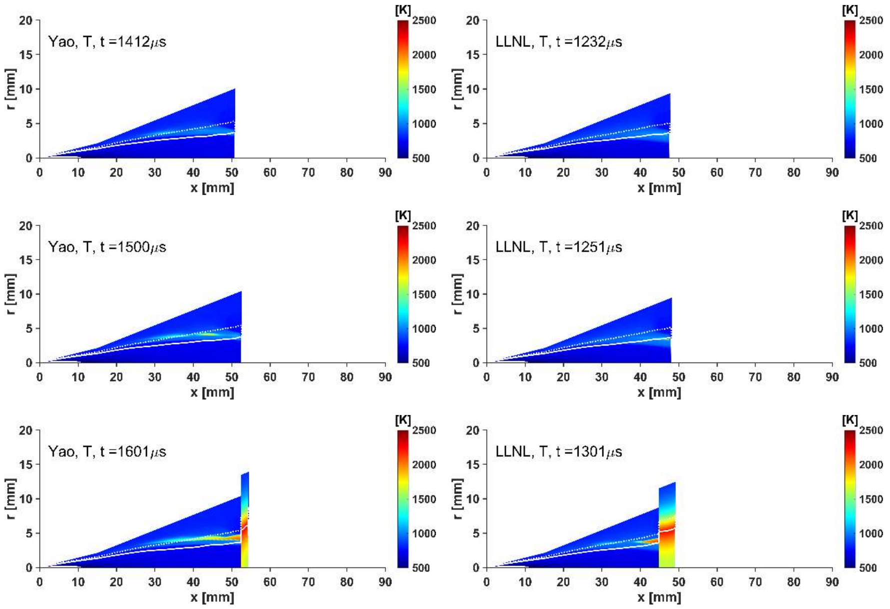

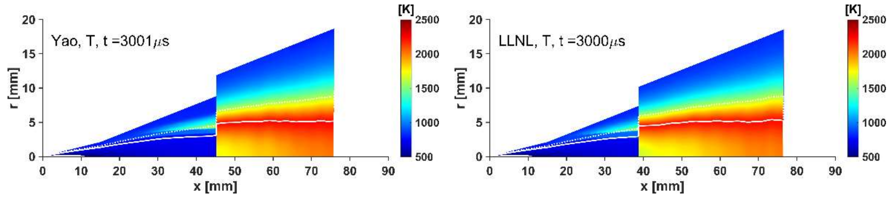

b. $T_a = 800\ K, XO_2 = 15\%, Pr = 1000\ bar$

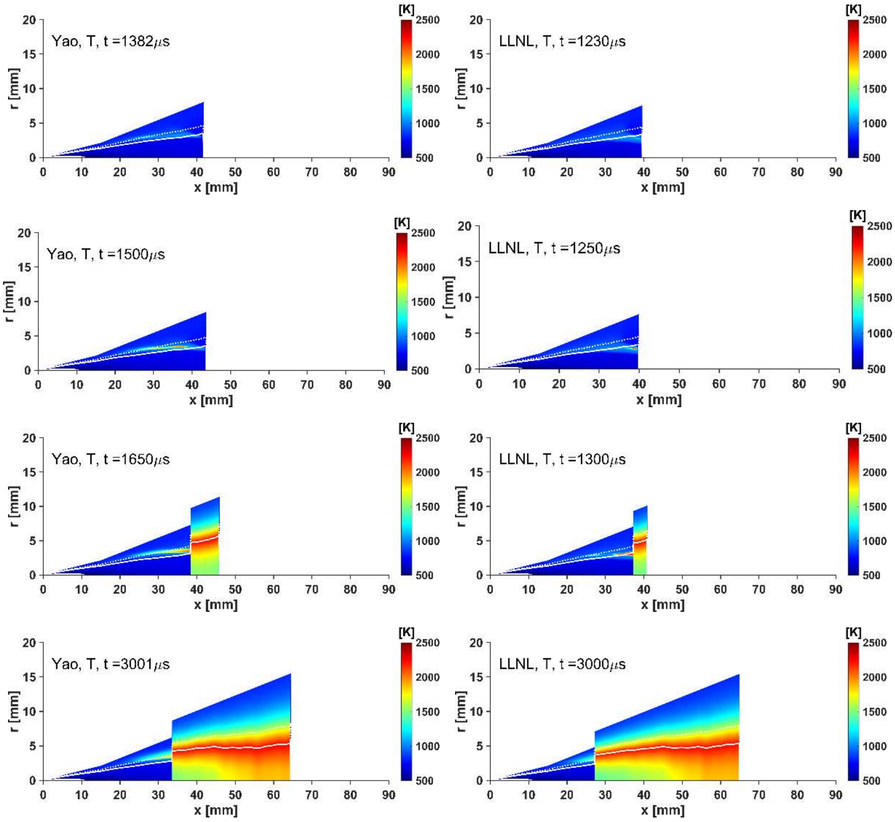

c. $T_a = 800\ K, XO_2 = 15\%, Pr = 500\ bar$

Figure 4.45. Temperature contours along ignition process for the variation of injection pressures at the condition of low ambient temperature Ta = 800 K using Yao (left) and LLNL (right) mechanism. White dash line: surface of stoichiometric ratio; white dash-dotted lines: surface of ϕ = 0.5 (outer) and ϕ = 2.0 (inner)

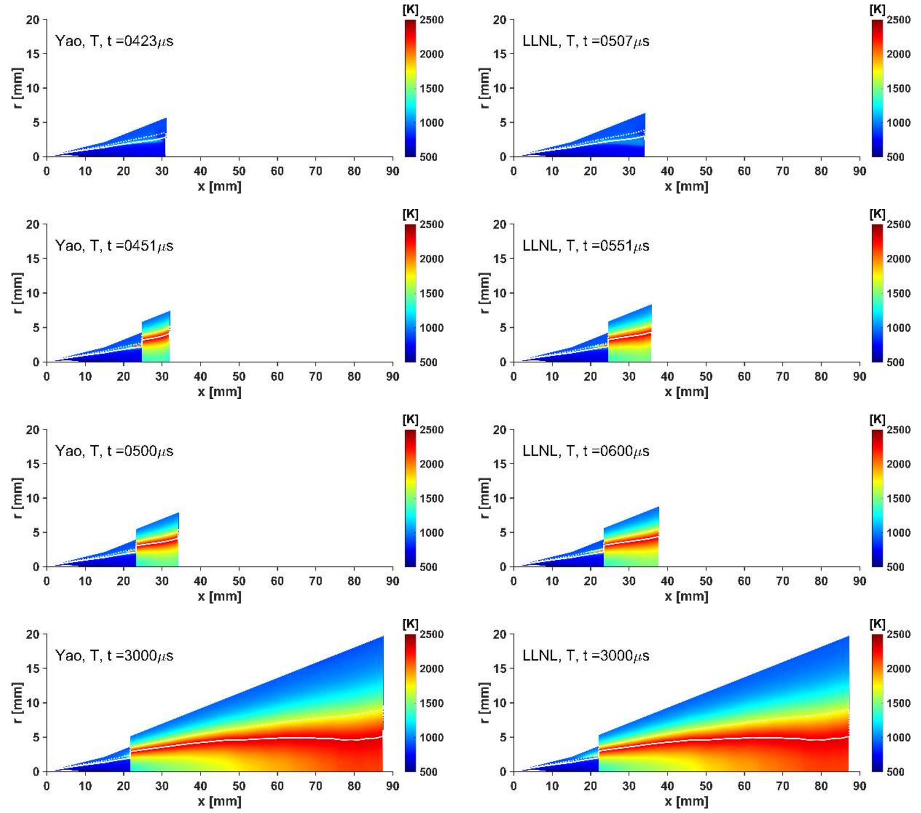

a. $T_a = 900\ K, XO_2 = 15\%, Pr = 1500\ bar$

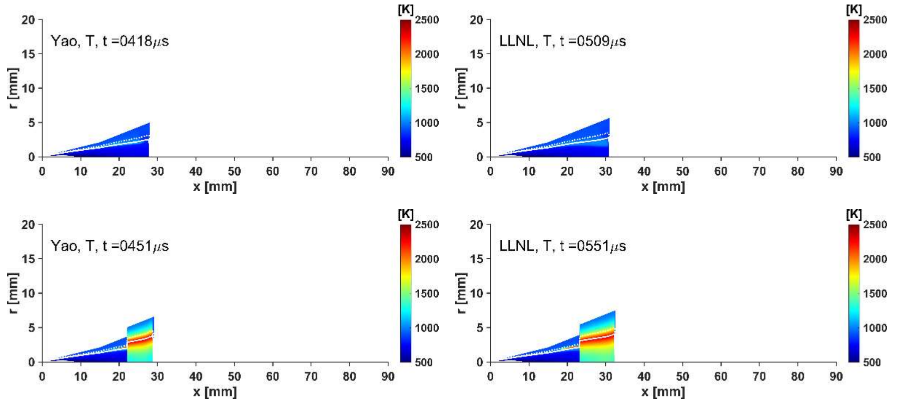

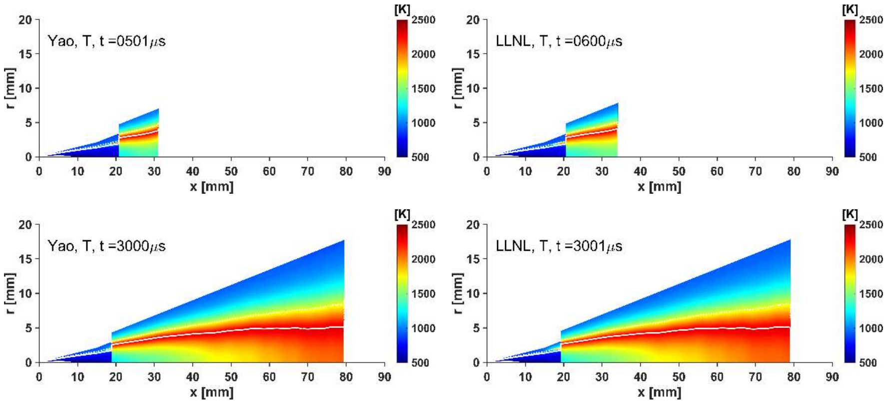

b. $T_a = 900\ K, XO_2 = 15\%, Pr = 1000\ bar$

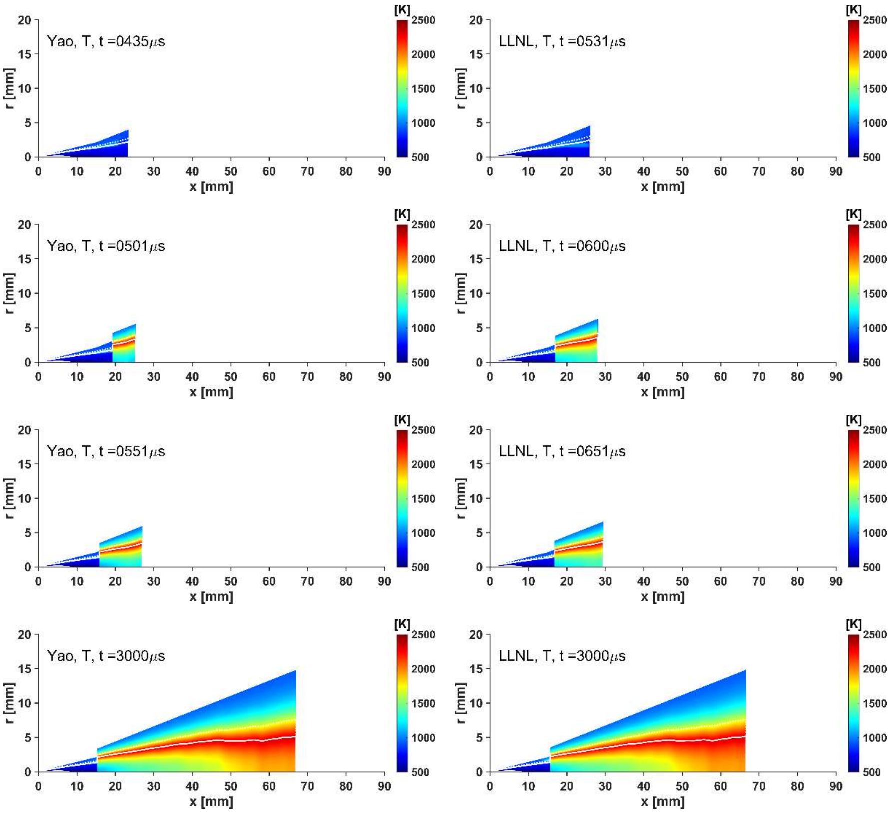

c. $T_a = 900\ K, XO_2 = 15\%, Pr = 500\ bar$

Figure 4.46. Temperature contours along ignition process for the variation of injection pressures at the condition of Spray A using Yao (left) and LLNL (right) mechanism. White dash line: surface of stoichiometric ratio; white dash-dotted lines: surface of $\phi = 0.5$ (outer) and $\phi = 2.0$ (inner)

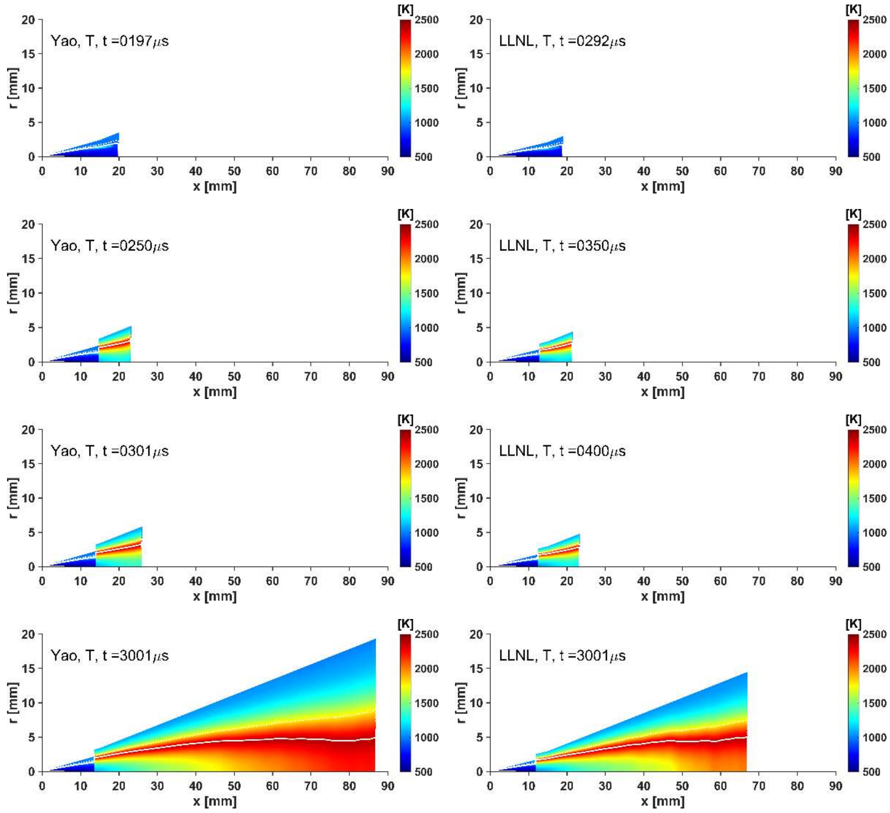

a. $T_a = 1000\ K, XO_2 = 15\%, Pr = 1500\ bar$

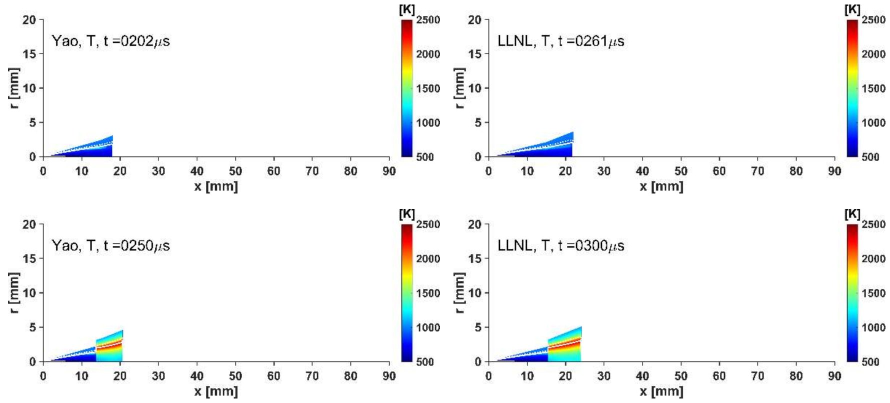

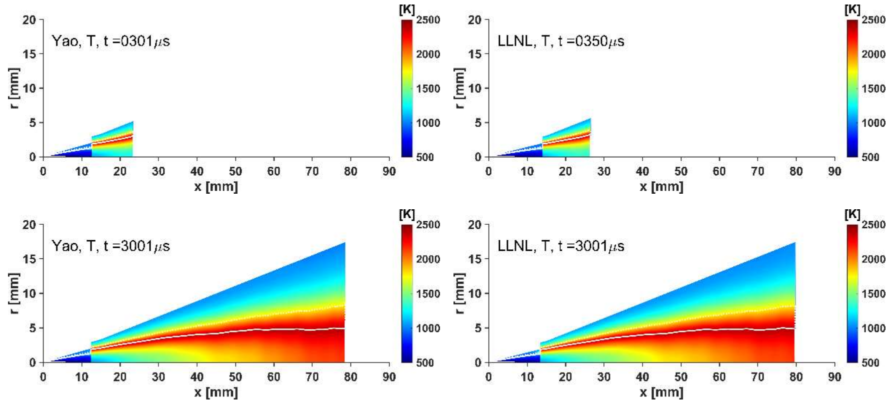

b. $T_a = 1000\ K, XO_2 = 15\%, Pr = 1000\ bar$

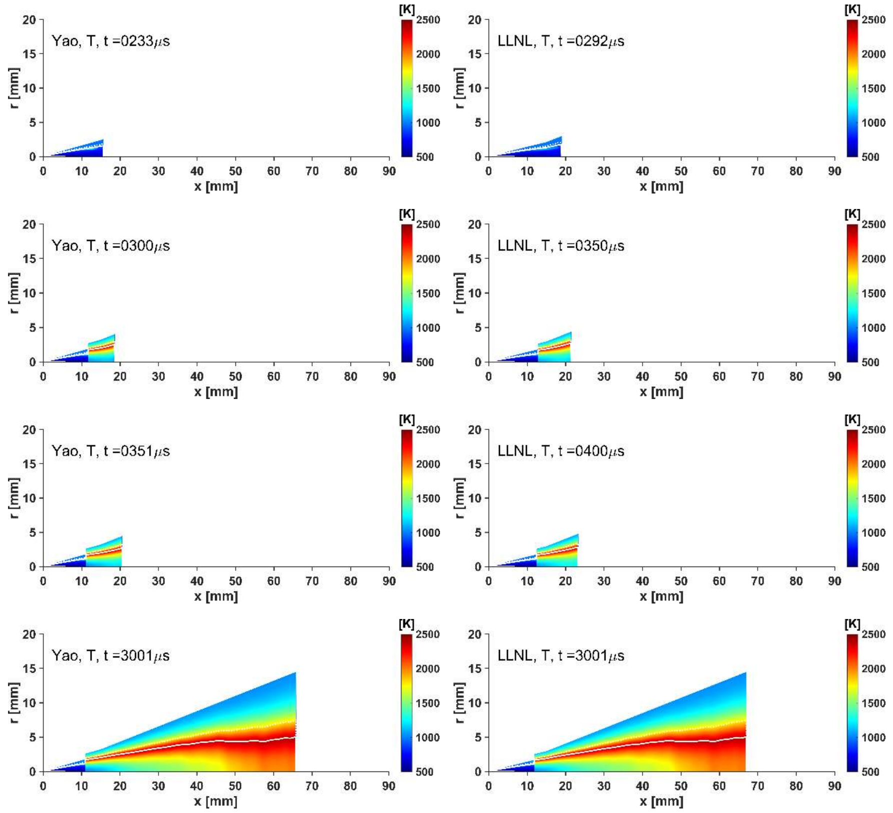

c. $T_a = 1000\ K, XO_2 = 15\%, Pr = 500\ bar$

Figure 4.47. Temperature contours along ignition process for the variation of injection pressures at the condition of high ambient temperature Ta = 1000 K using Yao (left) and LLNL (right) mechanism.

White dash line: surface of stoichiometric ratio; white dash-dotted lines: surface of ϕ = 0.5 (outer) and ϕ = 2.0 (inner)

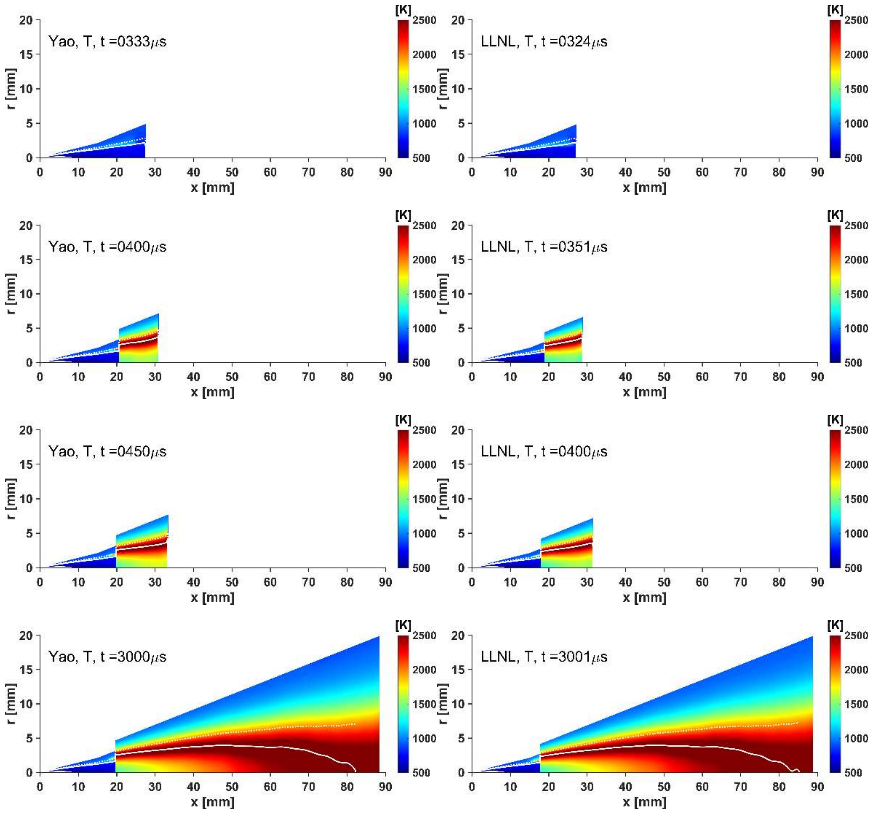

a. $T_a = 900\ K, XO_2 = 21\%, Pr = 1500\ bar$

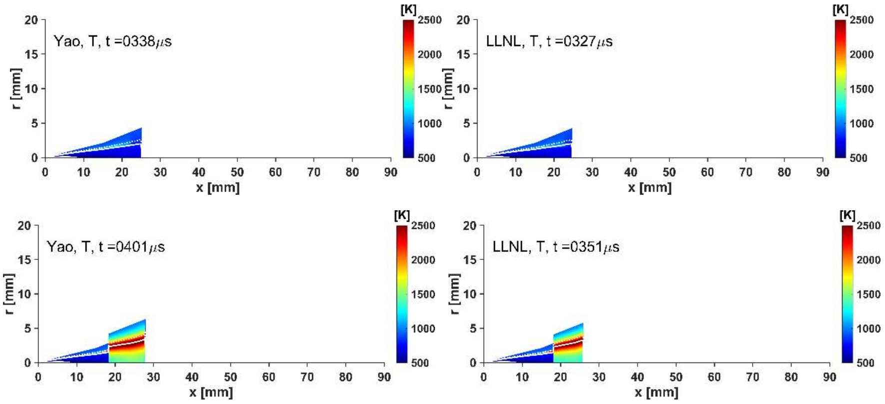

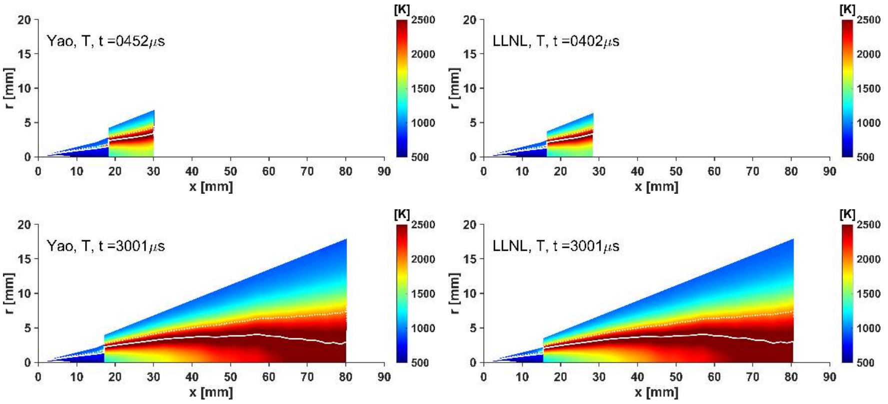

b. $T_a = 900\ K, XO_2 = 21\%, Pr = 1000\ bar$

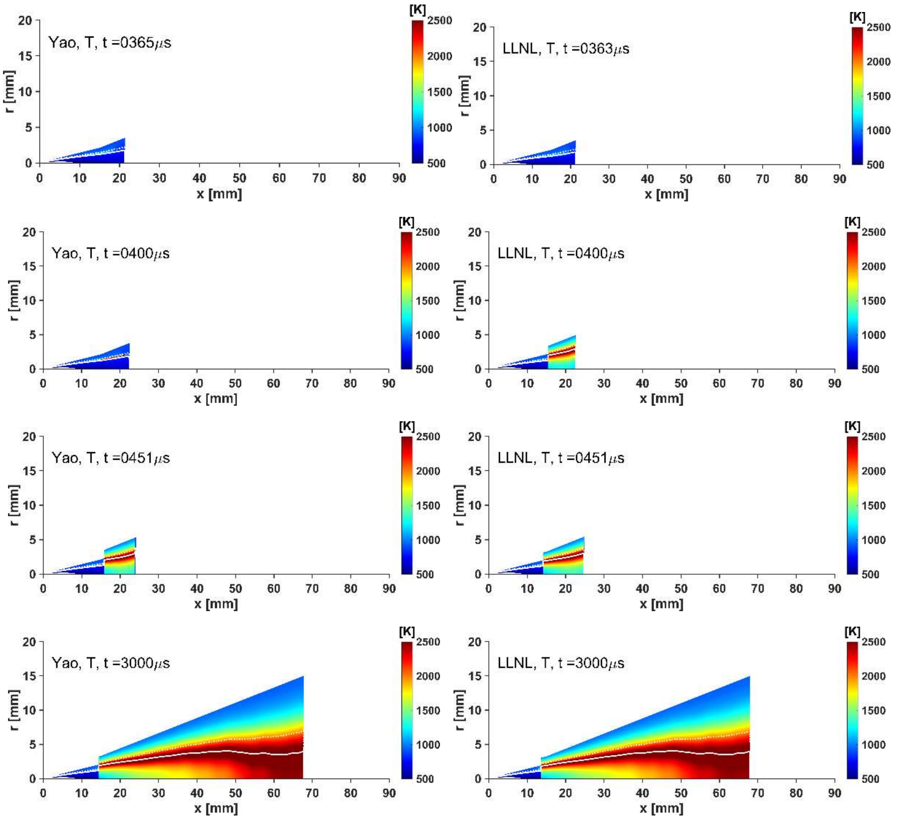

c. $T_a = 900\ K, XO_2 = 21\%, Pr = 500\ bar$

Figure 4.48. Temperature contours along ignition process for the variation of injection pressures at the condition of high oxygen concentration XO2 = 21% using Yao (left) and LLNL (right) mechanism.

White dash line: surface of stoichiometric ratio; white dash-dotted lines: surface of ϕ = 0.5 (outer) and ϕ = 2.0 (inner)

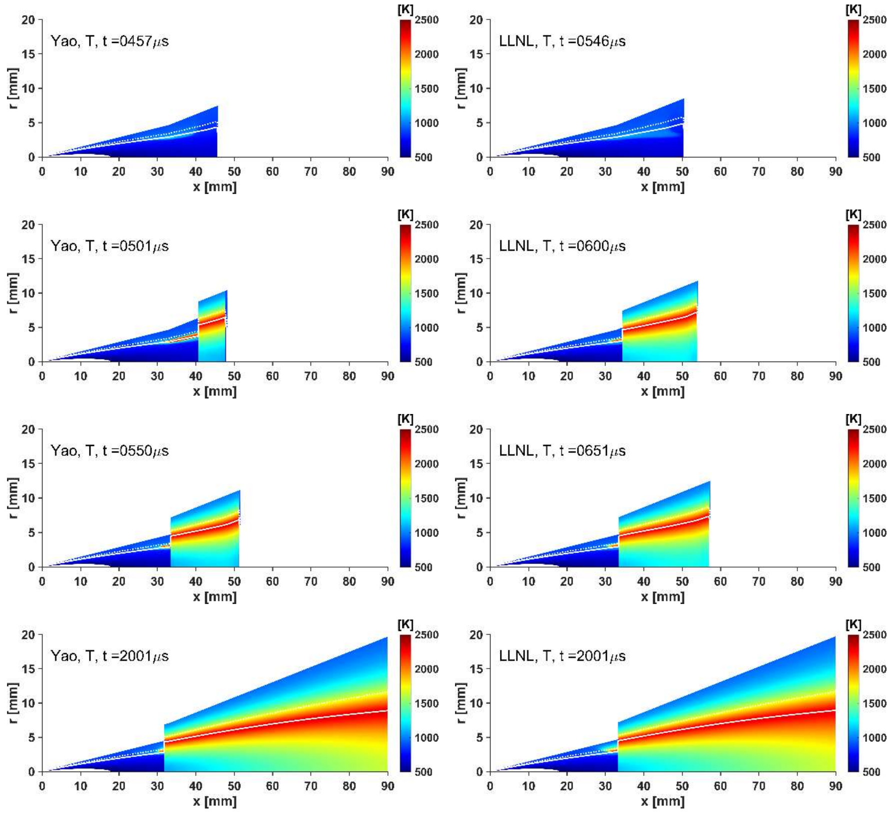

a. $T_a = 900\ K, XO_2 = 15\%, Pr = 1500\ bar$

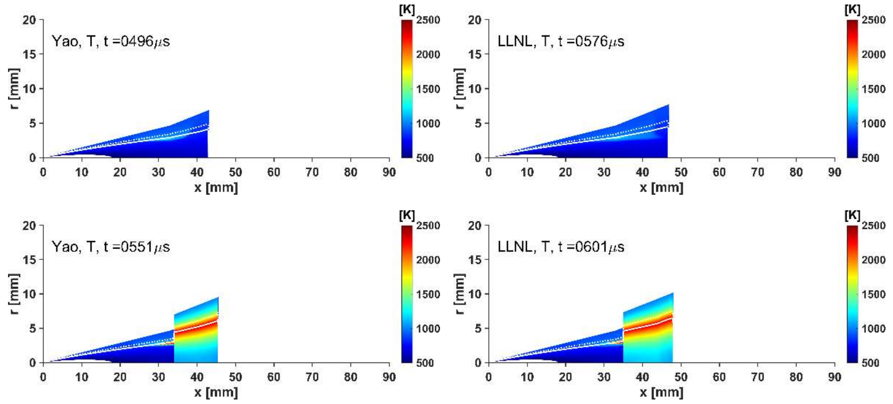

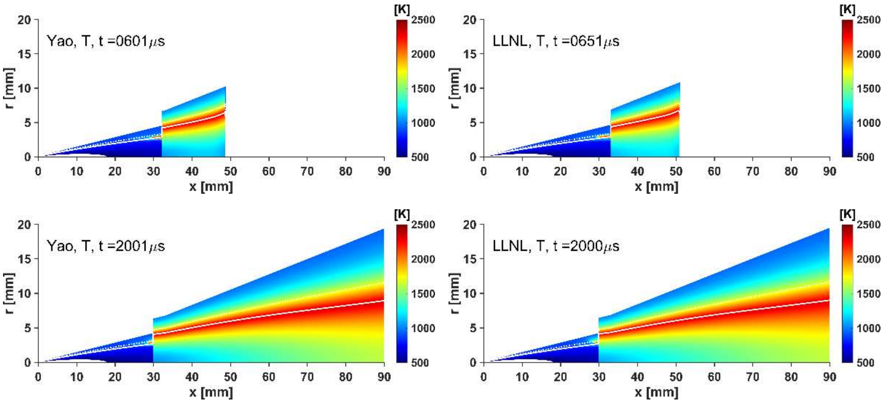

$b.\ T_a = 900\ K, XO_2 = 15\%, Pr = 1000\ bar$

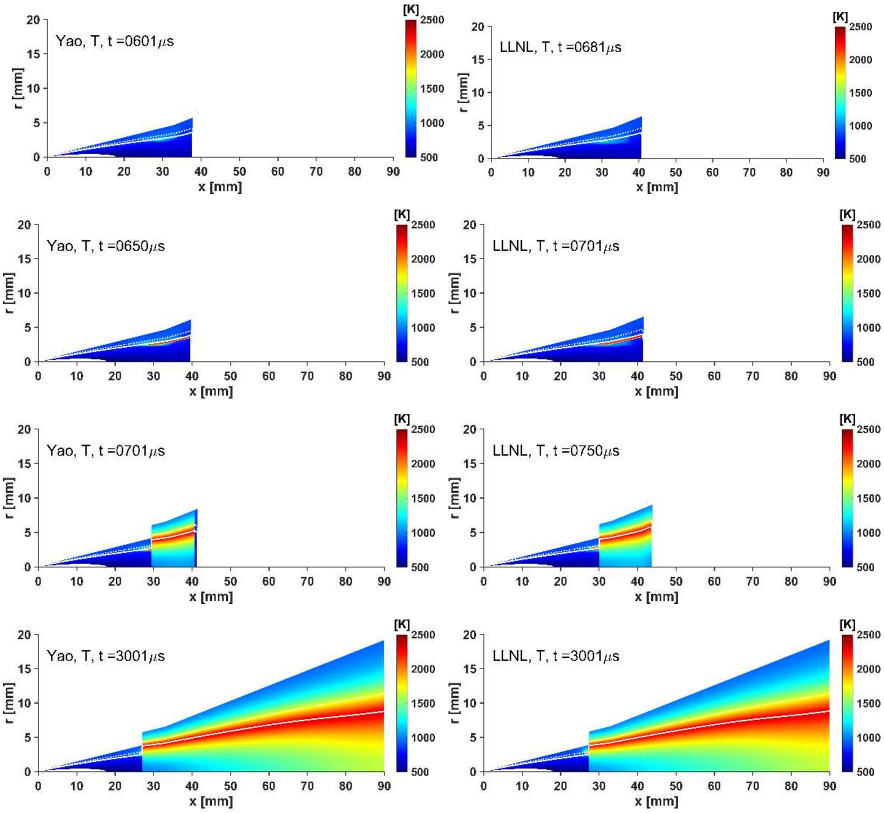

$c.\ T_a = 900\ K, XO_2 = 15\%, Pr = 500\ bar$

Figure 4.49. Temperature contours along ignition process for the variation of injection pressures at the condition of Spray D using Yao (left) and LLNL (right) mechanism. White dash line: surface of stoichiometric ratio; white dash-dotted lines: surface of $\phi = 0.5$ (outer) and $\phi = 2.0$ (inner)

Chapter 5

Model validation on Primary Reference Fuels

Content

5.1 Introduction/Objective

The so-called low-temperature combustion strategy provides a promising solution for reducing emissions, mainly from heavy-duty CI engines, while delivering higher engine efficiency. Following this idea, many approaches have been explored, such as altering the fuel stratification and combustion phasing by adjusting the ambient environment reactivity, injection timing, or dual injection [29]. Gasoline compression ignition (GCI), utilizing low-reactivity gasoline-like fuels in CI engines, has been commonly realized with no significant modifications to the injection system [223]. The longer ignition delay in GCI mode operated in conventional diesel engines results in increased fuel-air premixing in the chamber and effective control of the combustion phase, reducing the NOx and soot emissions simultaneously. Concerning the research on the effects of fuel reactivity, the optimum range of octane number (ON) for GCI was suggested in the range of ON = 75 – 85 for a light-duty engine [224] and a lower value ON = 70 for a heavy-duty engine [225].

Primary reference fuels (PRF), which consist of a binary blend of n-heptane (ON = 0) and iso-octane (ON = 100), are primarily used to evaluate the effect on the combustion and emission properties of CI engines with the range of ON from Diesel-like fuels to gasoline-like fuels [226] [227] [228]. Compared to diesel or gasoline, the binary components in PRFs reduce the complexity of chemical mechanisms, simplifying the numerical investigations [229] [230]. To further explore the effect of fuel octane number on the ignition and combustion characteristics under engine-like conditions, some fundamental research focused on the spray penetration, ignition delay, and lift-off length have been performed in an optically accessible constant volume/pressure facility under ECN conditions [23] [231]. ID & LOL are expected to be reduced as the fuel reactivity increases. In addition, the studies revealed a possible engine calibration based on a similar ignition delay between PRF00 at 15% oxygen concentration and PRF40 at 21% oxygen concentration, which is also adopted in [232] for further investigation of the flame structure.

In low-power applications, liquid hydrocarbon fuels are being gradually substituted by electrical motors. However, it is still used in high-power applications, and the high-octane fuel is still promising. Validating the Quasi-1D model for PRFs with different blend ratios under various ambient conditions is meaningful, especially as a fast engine calibration with varying operation loads. In the present chapter, the performance of the Quasi-1D model for the binary blends of n-heptane (PRF00) and iso-octane (PRF100) was evaluated under the same operating conditions as measured experimentally in [23]. Similar to the analysis for n-dodecane described in Chapter 4, the evaluation starts with the inert spray validation on the liquid and vapor penetration, followed by the study of the chemical reactivity and the combustion metric (ID & LOL) derived from flamelet manifold, then, the performance of Quasi-1D model on the variation of strain rate is presented. A suitable strain rate is selected, and the model validation is extended to the conditions of sweeping oxygen concentration, ambient temperature, nozzle diameter, and injection pressure. Finally, the analysis ends with statistics on the relationship of LOL as ID among all the conditions.

5.2 Test conditions and fuel properties

In this paper, PRFs are blended of n-heptane and iso-octane in steps of 20% of iso-octane in mass. The fuel properties of these blends and n-dodecane are detailed in Table 5.1. By definition, ON=0 for n-heptane is 0 and ON=100 for iso-octane. To simplify the description, the blends are denoted as PRF#, where # represents the PRF number, corresponding to the octane number or the mass fraction of iso-octane. The experimental data for validation and assessment of the Quasi-1D model was conducted at a constant pressure facility in CMT – Clean Mobility Thermofluids, including the liquid length under inert conditions for PRF00 and PRF100 throughout Mie scattering [19], ignition delay by high-speed Schlieren and lift-off length by means of OH* chemiluminescence [23] [167].

Table 5.1. Fuel properties. Source of PRF#: NIST Chemistry WebBook [233]

Properties [unit]	**n-Dodecane**	**n-heptane**	**Iso-octane**
Density [kg/m^3] (T = 15°C)	751.2	680	690
Viscosity [mm^2/s] (T = 40°C)	1.44	0.559	0.559
Cetane Number [-]	74	53	14
Octane Number [-]	-40	0	100
Lubricity [μm]	563		
Flash point [°C]	83	-1	-12
Lower heating value [MJ/kg]	44.20	44.9	44.3
Carbon content [% m/m]	84.7	84	84.2
Hydrogen content [% m/m]	15.3	16	15.8
Oxygen content [% m/m]	-	-	-

As illustrated in Table 5.2, the experimental conditions were standardized using the ECN Spray A injector (no.209135), which has a single hole with a diameter of 89.4 μm. The tests were conducted under a constant ambient density of 22.8 kg/m3 and a fuel temperature of 363 K. Nominal Spray A condition highlighted by bold involves an injection pressure of 150 MPa, an ambient temperature of 900 K, and an oxygen mole fraction of 15%. Variations were then explored, including oxygen mole fraction of 15/18/21% at 900 K and 150 MPa and ambient temperatures ranging from 800 K to 1000 K at 15% O2 and 150 MPa. Three injection pressures (50/100/150 MPa) were conducted under every ambient condition. It should be noted that the ambient temperature can only reach 950 K for PRF20 – 80 due to the facility limitation and was also considered part of the higher ambient temperature group. The injection duration is maintained at 3.5 ms to ensure a steady-state jet. The injection rate was obtained by a virtual injection rate generator [125] with the area coefficient (Ca = 0.98) and discharge coefficient (Cd = 0.9), consistent with Chapter 4.

Table 5.2. Test conditions

Ta [K]	Pinj [MPa]	XO2 [%]	Fuel
800	150	15	PRF00, 20, 40, 60, 80
900	50/100/**150**	**15**	PRF00, 20, 40, 60, 80
900	50/100/**150**	18	PRF00, 20, 40, 60, 80
900	50/100/**150**	21	PRF00, 20, 40, 60, 80
950	50/100/150	15	PRF20, 40, 60
1000	50/100/150	15	PRF00

5.3 Nominal Spray A condition

5.3.1. Inert spray analysis

A simulation was conducted under the Nominal Spray A condition for PRF00 to evaluate the configurations of the Quasi-1D model. Two spray angles for near-θ_1 and far-field θ_2 is used with a transition occurring at an intact length distance IL from the orifice. The main validation metrics are tip penetration and liquid length. As shown in Figure 5.1, the input of $\theta_1 = 18°$ matches well with the measured liquid length, and the same setup of $\theta_2 = 25°$ and $IL = 15\ mm$ as C12 also achieves the good agreement on the vapor tip penetration. As shown in Figure 4.2, the input of near-θ_1 = 15.75° achieves an excellent prediction of liquid length in the 1D spray model for n-dodecane. However, this value in near-θ_1 is not feasible for all fuels. The measured liquid length of PRF# is observed to be shorter than C12 under the Nominal Spray A condition. Apart from the shorter distance caused by the smaller evaporation mixture fraction ($f_{evap,C12} = 0.3636, f_{evap,PRF00} = 0.4282$) shown in Figure 5.2, the value of near-θ_1 is also enlarged to reduce the predicted liquid length.

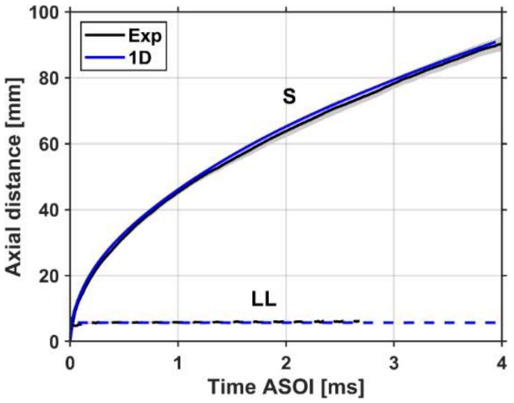

Figure 5.1. Model validation on spray tip penetration (S) and liquid length (LL) of PRF00 under inert nominal Spray A condition

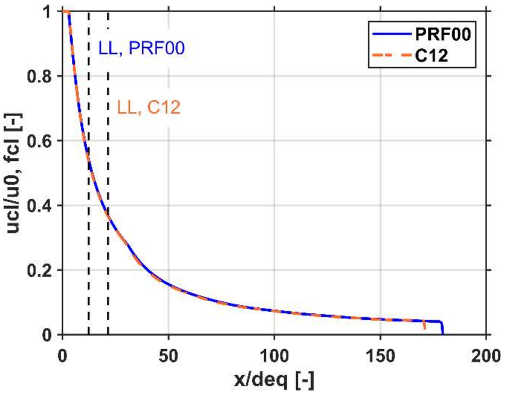

Figure 5.2. Axial profiles of mixture fraction and normalized velocity at 3.5 ms ASOI of inert nominal Spray A for PRF00 and C12. The vertical dash lines represent the position of liquid length.

Note that due to the small density difference between n-heptane and iso-octane, the injection mass and momentum flux are almost identical, irrespective of PRF#, resulting in a similar spray penetration. Therefore, the calculation for the PRF# shares the same injection rate under the cases of different blends. In addition, the very short liquid length of PRF makes it more suitable for gas jet assumption in the Quasi-1D model.

Table 5.3. Liquid length under the injection pressures at ambient temperature of 800 K and 900 K for the fuels of PRF00 and PRF100

Fuel	Ta [K]	Pinj [MPa]	EXP – LL [mm] [182]	1D – LL [mm]
PRF00	800	50	7.9	7.028
	800	100	7.5	7.279
	800	150	7.4	7.348
	900	50	6.1	5.978
	900	100	5.9	5.929
	900	150	5.9	5.832
PRF100	800	50	7.4	6.326
	800	100	6.7	6.322
	800	150	6.4	6.322
	900	50	5.9	5.418
	900	100	5.6	5.418
	900	150	5.5	5.416

Table 5.3 compares measured and simulated LL under ambient temperatures of 800 & 900 K at three injection pressures, where pure nitrogen is used as ambient gas in the chamber. Measurements in [19] show minimal differences on liquid length when

adjusting the percentage of iso-octane in PRF#, as n-heptane and iso-octane have similar volatility characteristics. This indicates that mixing characteristics for PRF# are not highly influenced by the blending ratio, at least prior to the ignition delay. LL has been studied to be little influenced by the injection pressure [56], and it has a significantly higher value at low injection pressure. Among all the conditions, good prediction is achieved, with an inverse trend of LL observed with injection pressure at low temperatures for PRF00. The model configuration effectively captures the spray characteristics, paving the way for subsequent calculations on reacting sprays.

5.3.2. Flamelet ignition for PRF

As discussed previously, the absence of a turbulence-chemistry interaction term (i.e., presumed PDF approach), a direct link can be established between the laminar flamelet manifold, and the spray ignition as derived from the Quasi-1D model. Therefore, analyzing the progress variable source term for the flamelet manifold generated at different strain rates is necessary for the subsequent discussion of Quasi-1D model performance. The manifold was tabulated with a reduced chemical mechanism (248 species, 1428 reactions) [234] originating from a detailed LLNL mechanism (3701 species, 16048 reactions) [235] by using the method of Direct Relation Graph and Error Propagation coupling with sensitivity analysis [236].

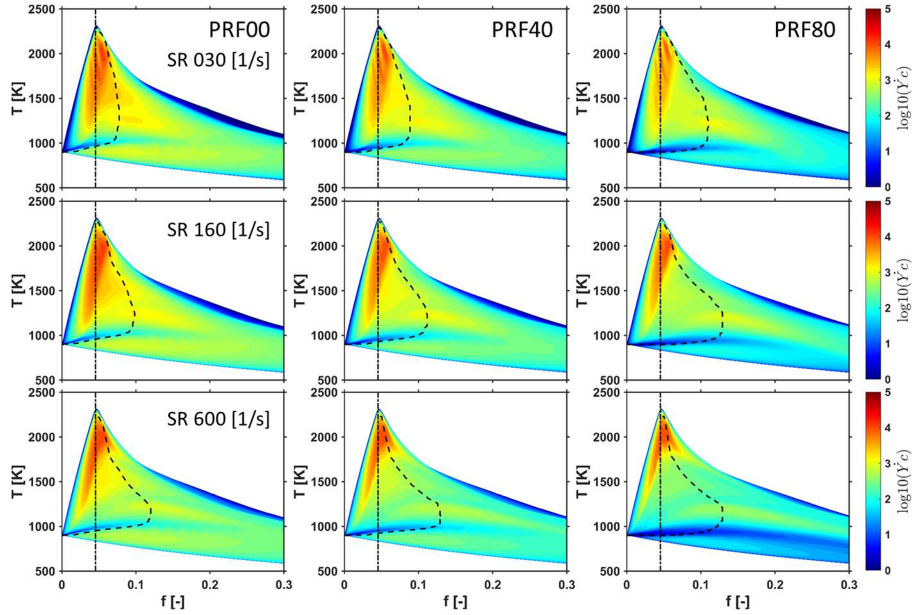

a. T – f

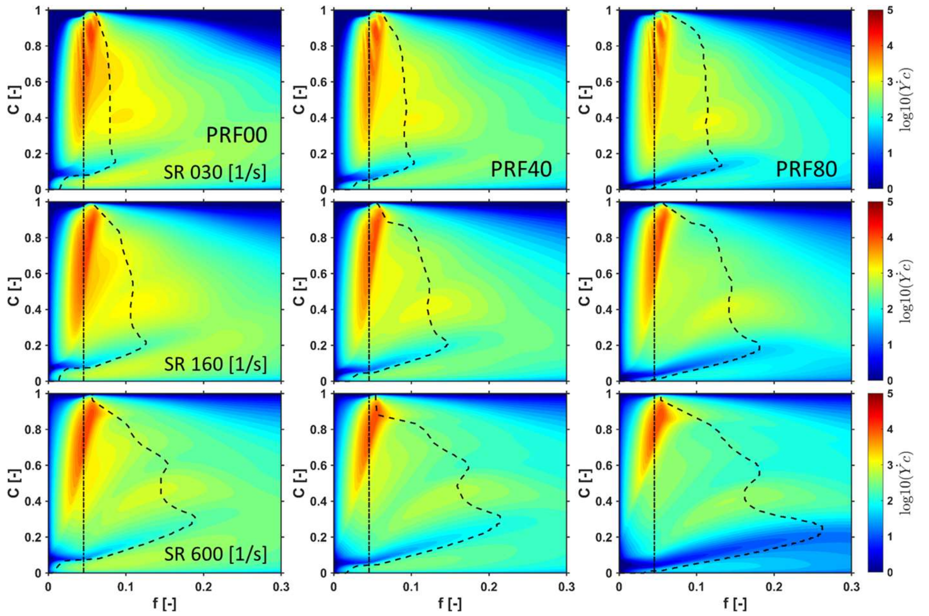

b. C – f

Figure 5.3. Contours of flamelet transient term $\dot{Y}_c = \partial Y_c/\partial t$ displayed in temperature versus mixture fraction (a), normalized progress variable versus mixture fraction (b). The dashed line superimposed on the contour is the time evolution of the maximum temperature / maximum normalized progress variable at every 10 μs timestep. The vertical line is stoichiometric mixture fraction. Different rows from top to bottom correspond to strain rates at 30, 160, and 600 1/s. Different columns from left to right correspond to PRF00, PRF40, and PRF80.

Figure 5.3 presents the contours of transient term $\dot{Y}_C$ in the maps of T – *f* (Figure 5.3.a) and C – *f* (Figure 5.3.b). The analysis will be done by comparing the difference among the PRF00, PRF40, and PRF80 blends at the strain rates of 30, 160, and 600 1/s. Similar to the analysis in Chapter 4, a dashed line highlights the maximum (Tmax or Cmax) at every instant during the combustion process with a constant timestep of 10 μs.

Similar to the ignition process of n-dodecane, the contours of PRF00 also illustrate a typical two-stage ignition characterized by a plateau near the cool flame temperature (~1000 K) where Cmax remains nearly constant. A comparison with n-dodecane (Figure 4.6) reveals that the contour distribution for PRF00 is narrower in the moderate fuel-rich area (*f* ~ 0.01) with reduced intensity due to lower fuel reactivity (lower cetane number). When examining blends of PRF# and different strain rates, the difference in chemical reactivity and the ignition process can be explained as follows:

- As the strain rate increases, the chemical reactivity will be reduced as a result of the intensified diffusion in the mixture fraction space. Near the stoichiometry, the distribution and intensity remain constant in the regions where the temperature exceeds ~1800 K. In the moderate temperature (1000 – 1800 K), the distribution shows a narrower range in mixture fraction. In addition, the distribution near the temperature of ~1000 K shifts towards a leaner mixture, thereby, the reactivity near the line of steady state is also enhanced, which is also found in C12 in Chapter 4. In the rich mixture, the separated spots in the moderate temperature on the slightly rich side, which govern the trace of Tmax, shift towards the richer side, and, of course, the intensity is also drastically reduced.

- As for the effect of blending of iso-octane in PRF#, increasing the blending ratio (higher ON number) plays a role in controlling ignition by reducing chemical reactivity across the entire map, particularly in the low-temperature zone and the moderate-temperature zone in a slightly rich mixture. Therefore, the value of Cmax in the plateau during the first-stage ignition decreases. For PRF80, the reaction in the lean mixture is very weak across the three strain rates, shown as the near-zero Cmax evolution. What's more, the bigger gap of transient term between the low- and high-temperature region leads to a continuous increase in Cmax to a richer mixture, which indicates a single-stage ignition for PRF80, especially at high strain rates.

In Figure 5.4, the calculated ignition delay in the first- and second-stage ignition is plotted as a function of mixture fraction for the fuels PRF00, PRF40, and PRF80 at Strain rates of 30, 160, and 600 1/s. According to the criteria utilized in Chapter 4, the first and second-stage ignition delay are defined as the time when Cmax exceeds 0.1 and 0.9, respectively.

In terms of the 2nd-stage ignition (also known as high-temperature ignition), compared to the observations of n-dodecane in Chapter 4, a similar V-shape is also observed for PRF#. Still, it is more sensitive to the mixture fraction around the minimum value (most reactive mixture fraction), typically located in a slightly fuel-rich area. Moreover, this position shifts towards the richer side with higher blends of iso-octane in PRF#. However, this trend is less pronounced at higher strain rates. The 2nd-stage ignition delay remains relatively constant in the $0.04 < f < 0.08$ range.

As expected, PRF# with a higher-octane number presents a longer 2nd-stage ignition delay, with a more noticeable increase at higher octane numbers. The curves of 2nd-stage ignition delay as a function of mixture fraction are nearly parallel across the entire mixture fraction for all the PRF# fuels. There is slight variation among PRF# fuels on the extremely lean side, with discrepancies becoming more apparent at higher strain rates.

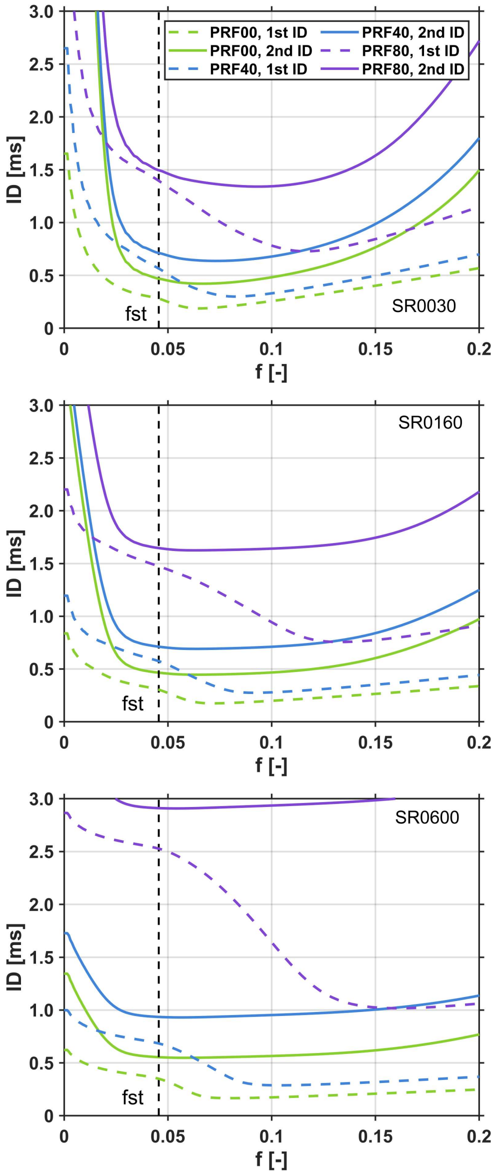

Figure 5.4. Ignition delay against mixture fraction for first- and second-stage ignition for PRF00, PRF40, and PRF80. The vertical line is stoichiometric. The images from top to bottom correspond to the strain rate at 30, 160, and 600 1/s.

Regarding the 1st-stage ignition, a similar trend to the 2nd-stage ignition was found with increased strain rate and iso-octane blending in PRF#. For the shortest 1st-stage ignition delay across the mixture fraction, the strain rate variation exhibits minimal effect for PRF00 and PRF40, but the value of PRF80 increases at a higher strain rate.

Compared to 2nd-stage ignition, 1st-stage ignition delay also shows parallel profiles among PRFs. However, the difference in 1st-stage ignition delay between the adjacent fuel blends differs across the entire mixture fraction. The enlarged difference caused by the increased strain rate is also observed, similar to the 2nd-stage ignition delay. Moreover, referring to the most reactive mixture fraction of 1st-stage ignition, the difference on the leaner side is more significant than that on the rich side. As shown in Figure 5.3, with the decrease in fuel reactivity, PRF00 towards PRF80, the reduced reactivity is more pronounced in the lean mixture (f < fst). Concerning the gap between 1st-stage ignition delay and 2nd-stage ignition delay, the smallest value occurs at a slightly lean mixture (f~0.04).

As a summary, Figure 5.5 displays the flamelet ignition delay as a function of strain rate for PRFs, which will be later compared to the Quasi-1D model results. Here, the flamelet ID is the shortest 2nd-stage ID shown in Figure 5.4. As expected, a continuous increase in ignition delay is observed as the strain rate increases until the extinction limit, and the trend is more obvious when strain rate is above 200 1/s. Meanwhile, a longer ignition delay is also achieved as the fuel reactivity decreases (from PRF00 to PRF80), and the auto-ignition limitation also decreases from SR = 1000 1/s (PRF00/20) to 800 1/s (PRF80). The difference in ignition delay among PRF# is more pronounced at a higher strain rate.

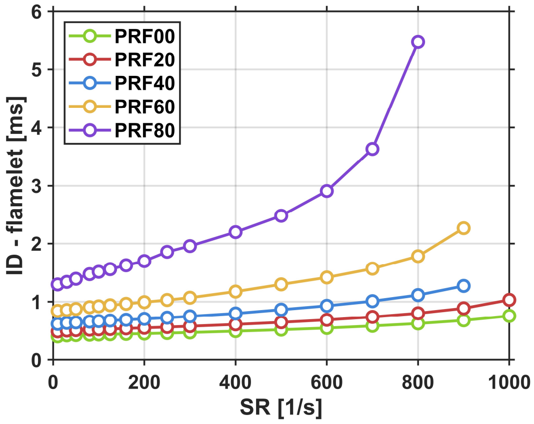

Figure 5.5. Profiles of flamelet 2nd-stage ignition delay versus strain rate for PRF00 – 80.

5.3.3. Effect of strain rate on Quasi-1D spray ignition

Figure 5.6 shows the calculated ID (left) and LOL (right) as a function of strain rate using the Quasi-1D model. Similar to the flamelet ignition delay, ID is also defined as the instant when Cmax exceeds 0.9, and lift-off length is defined as the position where 14% of its maximum of the OH mass fraction.

Quasi-1D ignition delay also shows constant differences among PRF00, PRF20 and PRF40 along the variation of strain rates. The sensitivity of Quasi-1D ignition delay as strain rate is also more significant for low-reactivity fuels (PRF60 & PRF80) at a large strain rate. Different from the monotonic increase in flamelet ID as the strain rate increases, a slightly V-shaped pattern is found for the profiles of both ID & LOL as strain rate for all PRFs. In practical terms, ID remains nearly constant in the strain rate range of 50 – 200 1/s for PRF00 – PRF60. Above SR = 200 1/s, Quasi-1D ignition is more influenced by the fuel-air mixing. Thus, the magnitude of the increased ID at a higher strain rate is more significant than that in flamelet ID.

As for lift-off length (LOL), the overall behavior is similar to ignition delay, i.e., increased ID & LOL with increased iso-octane in blends and V shape in strain rate variation. However, for PRF60 and PRF80, the increase in the LOL caused by increased strain rate slows down, especially at large strain rates. For example, the LOL of PRF80 tends to be constant when the strain rate exceeds 400 1/s, and finally, there is no high-temperature ignition as the strain rate is larger than 600 1/s.

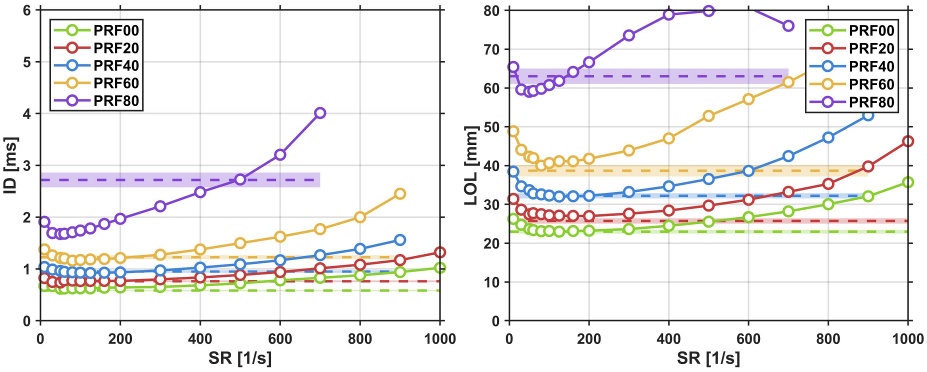

Figure 5.6. The profiles of ID (left) and LOL (right) against strain rate using Quasi-1D model for PRF00 – 80. The dashed line with the shadow graph represents the measurement data, which shares the same color as the symbols at each PRF blend.

In terms of Quasi-1D spray ignition process, different behaviors are observed for different PRF under variations of strain rate. Note that for a single injection event, spray evolution includes reactivity from all the range of mixture fractions simultaneously igniting. To further explain the effect of strain rate and PRF#, the ignition process of PRF00 by means of the evolution of Tmax and Cmax is first analyzed. Figure 5.7 compares the Tmax evolution against mixture fraction under different strain rates which are obtained from Quasi-1D model (solid lines) and flamelet (dash-dotted lines). For a better understanding, the time evolution of Tmax (left) and Cmax (right) has also been plotted in Figure 5.8. At a higher strain rate, the flamelet-derived ignition process exhibits a longer stage of low-temperature ignition, concurrent with a shift of the phase of steep increase in Tmax towards richer mixtures and a reduction in the magnitude of such temperature increase, transitioning from 1100 – 1400 K to 1100 – 1200 K. The

Tmax evolution from Quasi-1D model shows an initially similar trace as the flamelet-derived results, but it returns to the leaner mixture after reaching a so-called 'turning point'. Before the first turning point at 0.4 ms, the temperature rise in the low-temperature combustion stage is the same among the three strain rates, while the similar pace in Cmax stops at 0.23 ms, then a slightly higher value is observed at a higher strain rate.

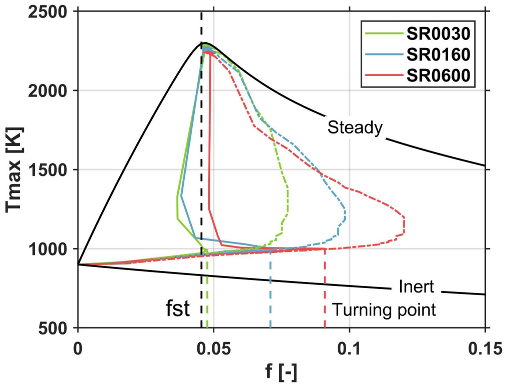

Figure 5.7. Maximum temperature evolution against mixture fraction from flamelet (dash-dotted) and Quasi-1D model (solid) for PRF00 at three strain rates. The black solid lines represent the inert and steady state. The black dash line represents the stoichiometric ratio. The coloured dash line represents the turning point where the ignition returns to a leaner side.

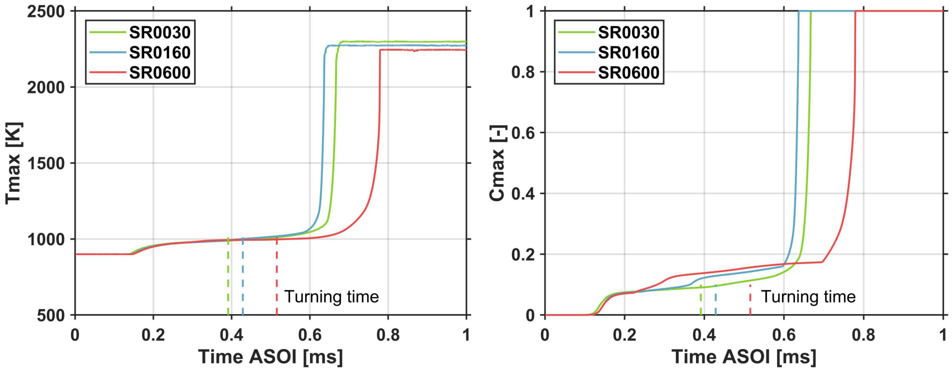

Figure 5.8. The time evolution of Tmax (left) and Cmax (right)obtained from Quasi-1D model for PRF00 at three strain rates. The coloured dash line represents the turning point where the ignition returns to a leaner side.

For all the three strain rates, the turning points along the Quasi-1D ignition is located in the rich mixtures, with a richer value as the strain rate increases, corresponding to a later turning time. In this period, the chemical intensity is the governing factor. Consistent with the observation in Figure 5.3, the reactivity in the low-temperature region tends to be lower as the strain rate increases, this is why the turning point occurring at a richer side/longer timing under higher strain rate. As the injection progresses, more mixture accumulates in the lean zones, which can be ignited due to the longer residence time. This explains the slight shift towards the richer side during the hot-temperature ignition when strain rate increases from 30 to 160 1/s. However, the high-temperature ignition occurs at a slightly rich mixture at the highest strain rate, which can be attributed to both factors. The weak intensity in the lean side shown in Figure 5.3 makes it more difficult for the lean mixture to ignite, and the longer low-temperature combustion allows more time to react near the surface of stoichiometry.

In the second step, analogous way is used to explore the effect of blending of iso-octane number in PRF#. Figure 5.9 gives the profiles of Tmax against mixture fraction along the combustion process for PRF00 – 80, which are plotted in one image at a constant strain rate. Meanwhile, the evolution of Tmax (left) and Cmax (right) for all the fuels are also given in Figure 5.10 as three images, corresponding to three strain rates. Similarly, time evolutions of Tmax and Cmax are shown in in Figure 5.10.

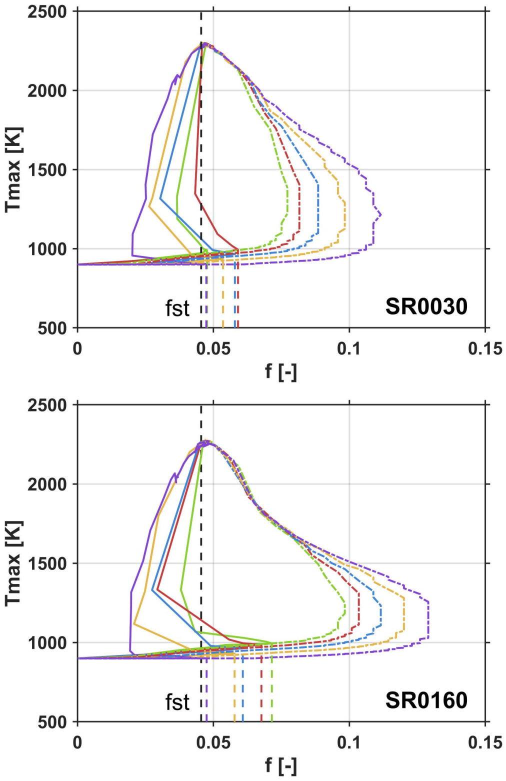

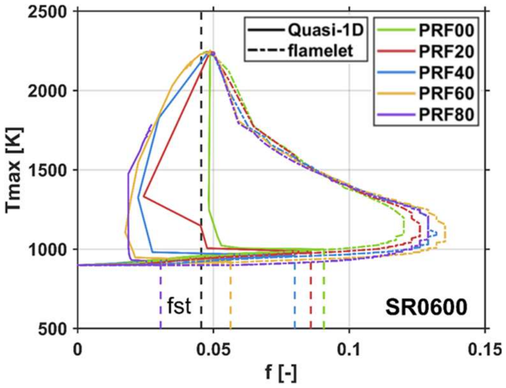

Figure 5.9. Maximum temperature evolution against mixture fraction from flamelet (dash-dotted) and Quasi-1D model (solid) for PRF00 – 80 at three strain rates: 30 1/s (upper), 160 1/s (middle) and 600 1/s (bottom). The colorful dash lines are the turning points for each fuel.

With the higher blending of iso-octane number in PRF#, the temperature rise is reduced in the low-temperature combustion period from the flamelet-derived ignition. Meanwhile, the scale of the temperature increment between the low-temperature and high-temperature ignition is similar for all the fuels, while the position shifts towards richer mixtures. Consistent with the flamelet-derived ignition, in the low-temperature combustion stage, the maximum temperature of the quasi-1D model rises up to a value when it reaches the turning point. Except for PRF00 at the lowest strain rate, the turning point tends to happen at rich conditions. However, it happens at at a leaner mixture as the fuel reactivity decreases (i.e. increasing PRF#). From Figure 5.10, the instant of the turning point, marked as turning time, is also seen to become longer at a low-reactivity fuel, which is in agreement with the chemical intensity indicated in Figure 5.3.

Then, the hot-temperature ignition was observed to move towards a leaner mixture for PRF20 – 80 at the lowest strain rates and for PRF00 – 80 at the larger strain rates. In addition, the monotonic shift towards leaner mixture is also found at a higher strain rate for PRF20 – 80, and this shifting is the most significant for PRF20. For PRF40 – 80, this effect is mainly on the low-temperature ignition process (Tmax < 1300 K).

For all fuels, after the turning point, the position of the maximum temperature returns to the lean side, then it reaches the leanest mixture, finally, the hot-temperature ignition diffuses to the stoichiometry and the temperature arrives the maximum. During this period until the leanest side, the magnitude of the temperature increase is obviously influenced by the strain rate. For example, at the lowest strain rate of 30 1/s, the maximum temperature of PRF60 increases to ~1300 K as the transition of the corresponding mixture fraction from the rich side to the lean side, however, the temperature remains nearly constant when the ignition position transfers to the lean side at the highest strain rate. For PRF80, due to the low chemical reactivity in the low-temperature region indicated in Figure 5.3, the temperature rise is not sensitive in this region, and the maximum temperature is still below 1800 K at the end of the injection under the highest strain rate.

In terms of the low-temperature period, the Tmax and Cmax were expected to be lower for a low-reactivity fuel, and the variation in the ignition period shows the shortest at SR = 160 1/s, resulting in the earliest second-stage ignition across the strain rates. Furthermore, PRF80 undergoes a single-stage, high-temperature ignition in lean mixture, in agreement with the observation in [232].

One important point from this analysis is the selection of a single strain rate value for the calculations under other operation conditions. As shown in Figure 5.6, good matching on Quasi-1D ignition delay occurs in the SR range from 50 1/s to 200 1/s for PRF00 – PRF60, while the agreement in LOL takes place in the same SR range is only for PRF00 – PRF40. The consistency of ID and LOL concerning the strain rate for high-reactivity fuels suggests that using a single flamelet may yield accurate predictions. Considering the fact that excellent prediction to LOL for PRF80 is achieved at the strain rates of 160 1/s and the calculated LOL at the same strain rate is still within the measurement uncertainty for PRF60, a strain rate of 160 1/s is finally chosen for all PRF# for the calculations in the following sections.

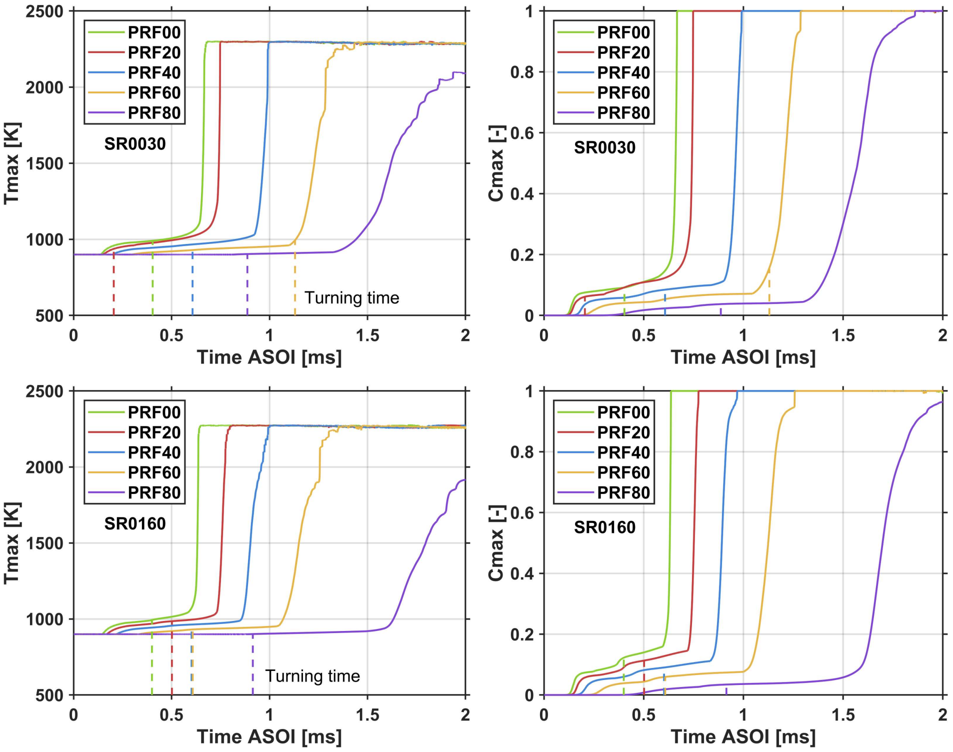

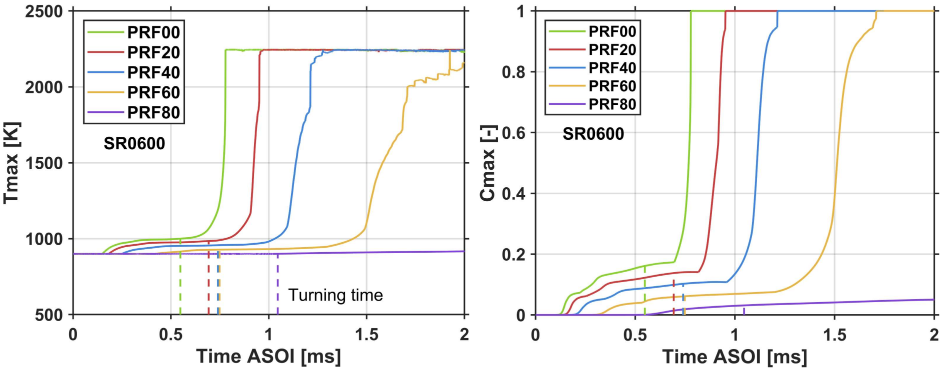

Figure 5.10. The evolution of Tmax (left) and Cmax (right) for PRF00 – 80 under nominal Spray A condition at strain rates of 30 1/s (upper), 160 1/s (middle), and 600 1/s (right). The colorful dashed lines represent the turning time, corresponding to the dash lines in the previous image.

5.3.4. Imposed ignition propagation

Figure 5.11 shows a time sequence of two-dimensional temperature fields around the ignition timing for PRF00 (left), PRF40 (middle), and PRF80 (right) under the nominal Spray A condition. The first-row image corresponds to the instant when the maximum temperature exceeds ambient temperature plus 400 K, a criterion also known as the ignition delay definition as mentioned in [21]. The subsequent images represent the instants during the hot-temperature ignition process (Tmax > 1300 K), with the final one displaying the instant at the end of injection where the combustion has been stabilized.

For PRF00, ignition occurs at 629 μs ASOI, and the highest temperature takes place at an axial distance of ~30 mm from the nozzle along the surface of stoichiometric ratio. It was also observed in rich mixture ($\phi = 1.2$) in [232]. In contrast, PRF40 and PRF80 ignite later and distance farther from the nozzle. As a sequence, ignition occurs near a lean surface, i.e., $\phi \sim 0.5$. The ignition of PRF80 occurs at an almost lean mixture [232]. Compared to PRF0, calculations show a wider radial expansion happening at ~40 mm for PRF40 and ~70 mm for PRF80.

Finally, Figure 5.12 shows the validation of the reacting tip penetration, ignition delay, and temporal evolution of lift-off length for PRF00, PRF40, and PRF80 using an imposed ignition propagation described in Chapter 3. The experimental data comes from [182]. This type of validation is not typically found in other studies utilizing reduced-order models, where local density is not coupled with flow dynamics and the subsequent penetration evolution. For PRF00, the predicted reacting tip penetration matches well with experimental values, albeit with a slight overprediction during the transient phase immediately after ignition. This discrepancy is more pronounced for PRF40 and PRF80, where overprediction holds for most of the reacting penetration period. The discrepancy around ignition timing stems from the fact that a sharp transition is considered in the ignition mixture from inert to a fully reacted state, which induces a stronger density drop and, hence, a faster acceleration compared to the experiments. Similar observations detected in [152] [167] also exhibit a slower spray acceleration under low-reactivity situations (i.e., low temperature or low reacting fuels), which is also evidenced by the comparable penetration between the inert case in Figure 5.2 and the reacting case for PRF40 and PRF80 [182].

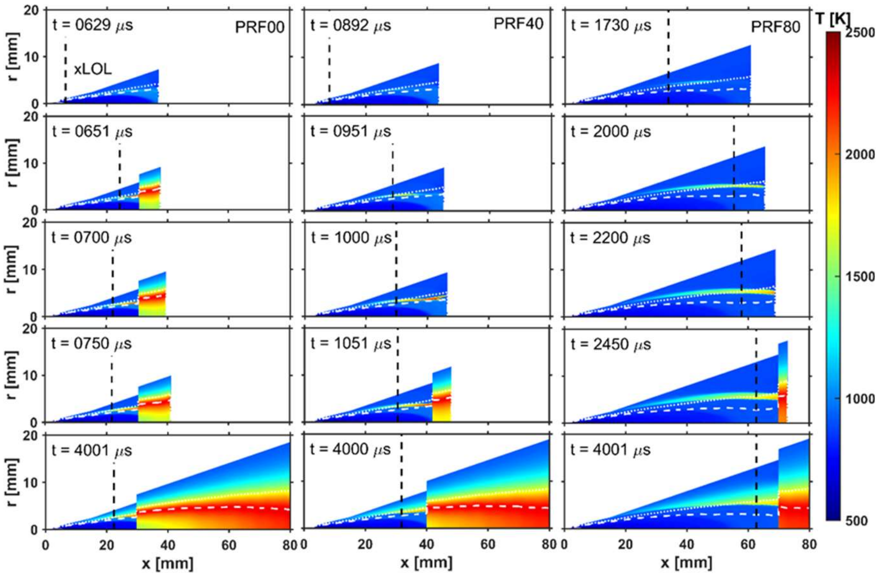

Figure 5.11. Comparison of temperature contours along ignition process among PRF00 (left), PRF40 (middle) and PRF80 (right) under nominal Spray A condition. The white dashed line represents the surface of stoichiometric equivalence ratio, and the white dash-dotted line represents the surface of equivalence ratio of 0.5. The vertical black dashed line represents the temporal lift-off length.

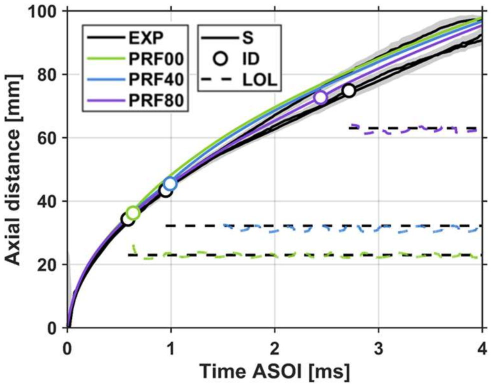

Figure 5.12. The validation on reacting spray tip penetration, ignition delay and temporal lift-off length for PRF00, PRF40 and PEF80 under nominal Spray A condition.

5.4 Parametric variations

In this section, the validation of the Quasi-1D model on ID & LOL prediction is conducted for cases involving injection pressures (50/100/150 MPa), oxygen mole fraction (15/18/21%), and ambient temperatures (800/900/950 & 1000 K). Apart from the ID definition by Cmax > 0.9, the data defined by the time from the start of injection at which dTmax/dt is maximum (Tmax being the maximum temperature across the spray) is also given in red lines.

Nominal Spray A condition

Figure 5.13 compares ID and LOL as a function of PRF number at nominal Spray A condition between the measurements [167] and the Quasi-1D model. n-dodecane results have also been included with the LLNL mechanism. In general, the Quasi-1D model accurately predicts the trend of ID and LOL against PRF, namely a gradual increase of ID & LOL with the rise in ON from -40 to 60 (C12 – PRF60), followed by a significant increase in slope when transitioning from PRF60 to PRF80. Current study demonstrates more accurate predictions than previous numerical work [237], possibly due to differences in the adopted chemical mechanism. Furthermore, when using the same mechanism as in [234], the predicted ID remains consistent between these two criteria (Cmax and dTmax/dt) for high-reactive fuels (C12 – PRF40), while the numerical value aligns more closely with measurements for PRF80 under the criteria based on dTmax/dt, and the prediction for LOL matches well across the entire range of PRF#. Meanwhile, the prediction in [234] and [237] within the CFD-RANS framework both obtained an underestimated LOL, especially for low-reactivity PRF# (i.e., PRF80), while in the present approach the agreement is overall very good.

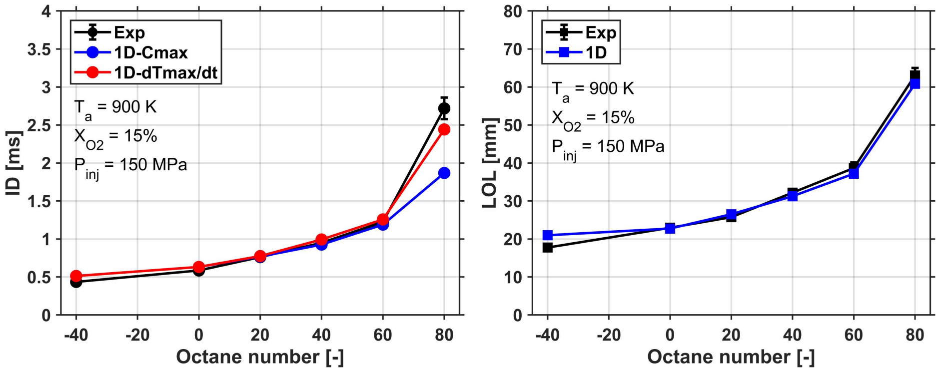

Figure 5.13. The ignition delay (left) and lift-off length (right) against fuel octane number under nominal Spray A condition.

Injection pressure

In further analyzing the model validation under the effect of injection pressure (Pinj = 50/100 MPa), Figure 5.14 presents the relationship between numerical and experimental ID & LOL with respect to ON number under the same ambient conditions as Nominal Spray A. It is necessary to note that experimental ID data for PRF60 were not available on the experimental database. Across all PRF#, the Quasi-1D model effectively captures the trend of ID & LOL corresponding to the decrease in fuel reactivity from C12 to PRF80, irrespective of the injection pressure. Similarly, a consistent observation of longer ID based on the dTmax/dt criteria for low reactive fuels (PRF60, PRF80) can be made for the remaining scenarios. Notably, as injection pressure decreases, the predicted ID & LOL tends to be slightly lower than the measurement, a finding also supported by previous research [234]. It is worth highlighting that the liquid length of PRF# (~6 mm) is shorter compared to C12 (~11 mm) for Nominal Spray A, i.e., the scenario of PRF# calculation is closer to the gas-jet theory in Quasi-1D model. As mentioned in Chapter 4, ID prediction is significantly influenced by longer residence time at low injection pressure, resulting in a shorter ID compared to nominal condition. In terms of LOL prediction, the predicted values are slightly shorter than those of the measurement, with discrepancies falling within 2 mm range for all PRF#.

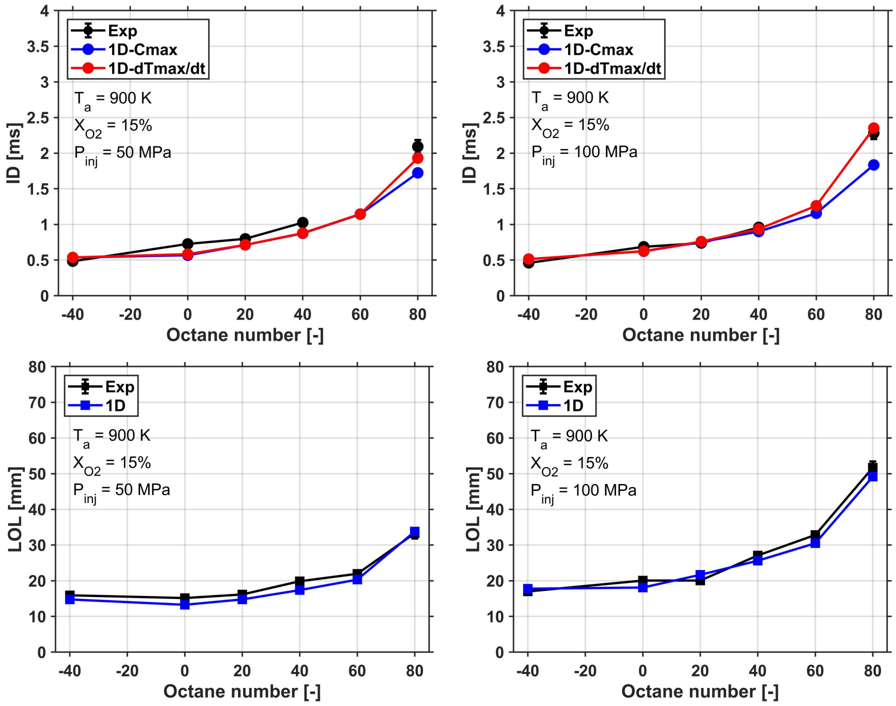

Figure 5.14. The validation of ignition delay (upper) and lift-off length (bottom) against fuel Octane number under lower injection pressure. (Pinj = 50 MPa, left; Pinj = 100 MPa, right)

Ambient temperature

Figure 5.15 illustrates the relationship between predicted and measured ID & LOL at varying ON numbers under different ambient temperatures (800 K and 950/1000 K). It is noted that no ignition takes place for PRF80 at low temperatures, resulting in a lack of measurement data. Additionally, data for LOL at high temperatures is also missing. As previously noted, high ambient temperature tests for C12 and PRF00 were conducted at 1000 K, while PRF20 – PRF80 tests were carried out at 950 K due to facility limitations. The trend of ID & LOL increasing with the ON number is accurately predicted. At low ambient temperatures, an accurate calculation is more challenging. The predicted ID & LOL values are significantly longer than the measured values. Zhou et al. also observed overpredicted ID and underestimated LOL for PRF#, attributing this to simplified mixing and chemistry descriptions rather than the combustion model [237]. At high ambient temperatures, accuracy improves, although the Quasi-1D model predicts lower ID & LOL values compared to measurements for PRF#, with a less pronounced discrepancy in ID prediction. Regardless of ambient temperature, the disparity between the Quasi-1D model and measurements in ID or LOL remains consistent across different PRF#. In contrast to the more accurate predictions for high-reactive fuels (PRF00 and PRF20) in [234], the constant flamelet approach may contribute to inaccuracies at higher ambient temperatures.

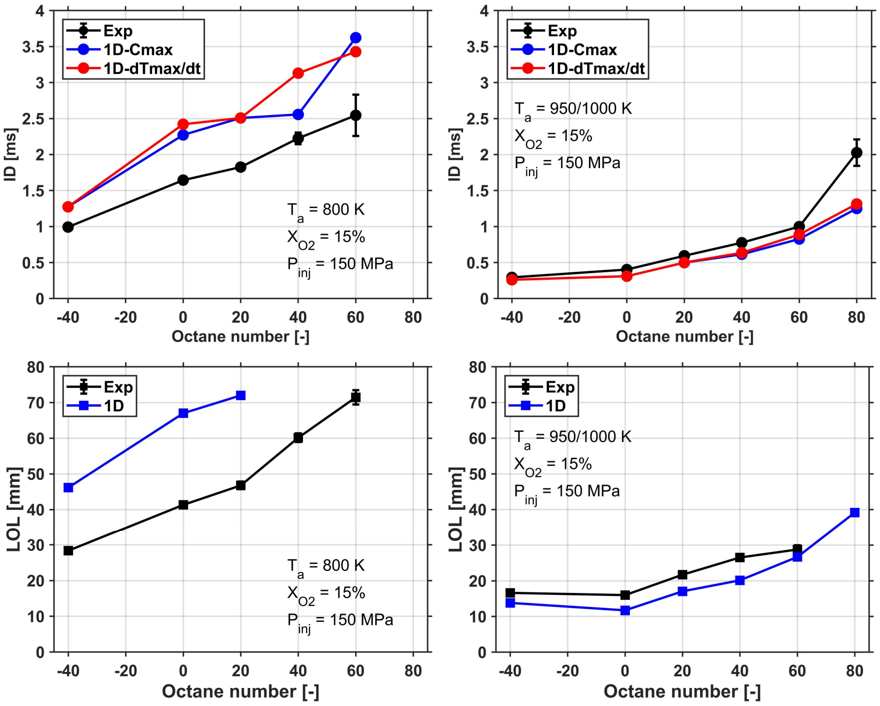

Figure 5.15. The validation of ignition delay (upper) and lift-off length (bottom) against fuel Octane number under lower injection pressure. (Ta = 800 K, left; Ta = 1000/950 K, right)

Oxygen concentration

Figure 5.16 illustrates the relationship between predicted and measured ID & LOL based on the ON number for XO2 = 18% (left) and XO2 = 21% (right). Consistent with previous findings, accurate predictions of ID are achieved from C12 to PRF60, with an underestimation observed for PRF80. Moreover, this underestimation is less pronounced at higher oxygen levels. Regarding LOL predictions, the Quasi-1D model demonstrates sensitivity to ON variations in PRF#, yielding accurate predictions for PRF80 across all oxygen conditions, including the reference setting. However, the accuracy of LOL predictions is less satisfactory at the highest oxygen concentration, particularly for PRF60.

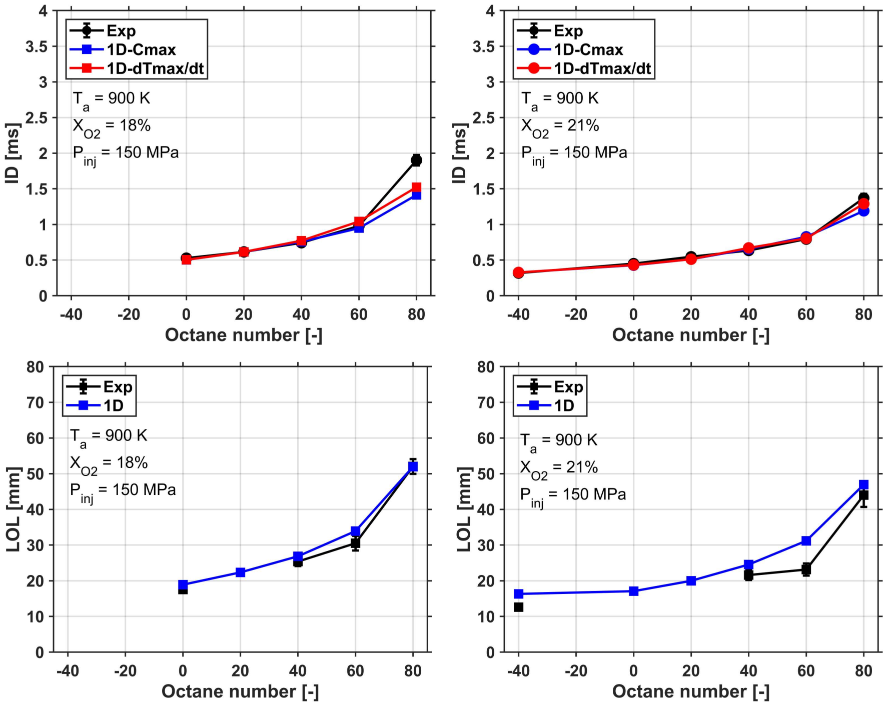

Figure 5.16. The validation of ignition delay (upper) and lift-off length (bottom) against fuel Octane number under higher oxygen concentration. (XO2 = 18%, left; XO2 = 21%, right)

Overall comparison

Figure 5.17 shows the validation of Quasi-1D model for the prediction of ignition delay and lift-off length for the fuels with ON variation at all the ambient conditions. Overall, this model delivers reasonable predictions within a deviation of +-0.1 ms from the experimental ID and 5 mm from the experimental LOL for most of the conditions.

A very consistent stratification in terms of ignition delay is observed depending on fuel reactivity, increasing from C12 to PRF80.

For all cases, ignition delay and lift-off length are both overpredicted for the low 800 K cases, but the discrepancy is less important at lower injection pressure. If the sensitivity of ignition delay to strain rate is calculated similarly to the plots in Figure 5.6, results show that experimental values are far below those from the Quasi-1D model. Another observation is the underprediction under most conditions for PRF80. In addition, Figure 5.6 also shows that the sensitivity of PRF80 ignition delay is much higher than that of the other fuels. Above all, the implementation of constant flamelet approach is limited at the conditions where a long fuel/oxidizer mixing process is needed, thus, multiple flamelets would be more effective in the following prediction in ID and LOL.

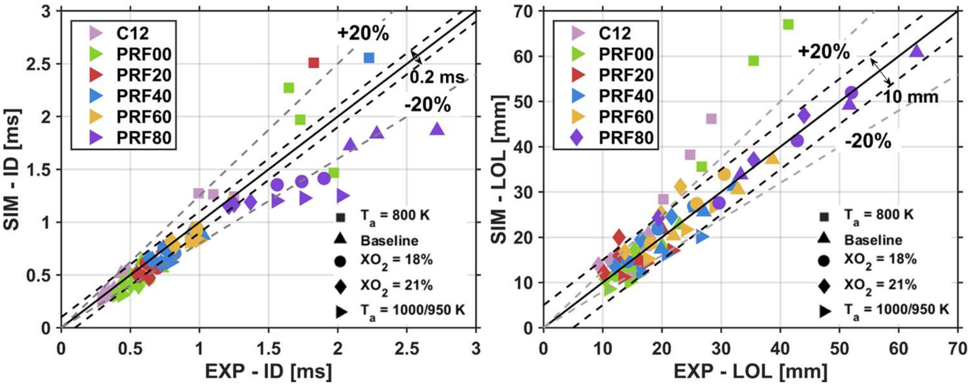

Figure 5.17. Validation of Quasi-1D model predictions of ignition delay (left) and lift-off length (right) for the investigated fuels and operating conditions. Markers with the same shape and colour correspond to a variation of injection pressure for the corresponding ambient conditions. Dashed diagonals correspond to a ±20% and ±0.1 ms/5 mm for ID and LOL, respectively

Due to the wide range of reactivities in the present study, it provides a nice range where the relationship between ID and LOL can be evaluated. This is observed both from the experiments and the Quasi-1D model in Figure 5.18. It can be noted that data have been grouped in terms of injection pressure, which strongly affects the lift-off length but not ignition delay [97] [123]. To make a consistent comparison, a correlation of lift-off length as a function of the injection pressure and ignition delay is also adopted here [238], written as

$$LOL = k_{LOL} \cdot P_{inj}^{a} \cdot \tau^{b} \tag{5.1}$$

where k_{LOL} is the correlation constant, P_{inj} is the injection pressure, τ is ignition delay, and a and b are the exponents of each parameter. The parameters are presented in Table 5.4. Besides the coefficient k_{LOL}, the other parameters used for Quasi-1D model are the same as the experiment. The discrepancies in the fitted k_{LOL} with the measured value indicates the inconsistency between ignition delay and lift-off length with an inaccurate estimation, where lift-off length is more influenced. The value of k_{LOL} is fitted as larger than the measured one, while similar analysis given in [237] exhibited a lower k_{LOL} concluded from CFD-RANS work.

Table 5.4. Exponents for the lift-off length correction according to Eq. ((5.1)

Parameter	k_{LOL}	P_{inj}	τ	R^2
Units	[a.u.]	[MPa]	[μs]	–
Exponent	–	a	b	–
Exp	0.0137	0.432	0.804	98.64%
Quasi-1D	0.0165	0.432	0.804	98.73%

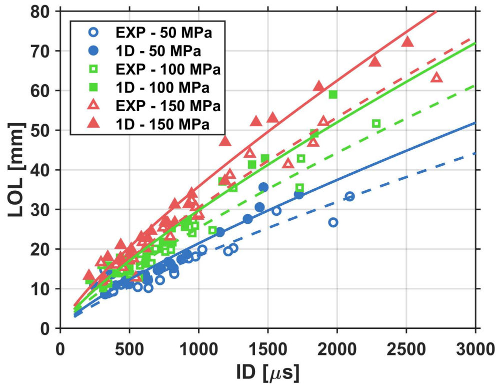

Figure 5.18. Ignition delay and lift-off length relationship for all fuels under all conditions grouped by injection pressure. Empty Marker: Quasi-1D model; Solid marker: Experimental database. Solid Lines: correlation by experiment. Dashed lines: correlation by Quasi-1D model.

5.5 Summary and Conclusions

In this section, the effect of fuel reactivity on Quasi-1D model was evaluated by combustion metrics, mainly ID and LOL. The validation was performed with n-dodecane and Primary Reference Fuels under ECN conditions, including variations in ambient temperatures, oxygen concentrations and injection pressures. The findings and conclusions can be summarized as follows:

- Good match on inert spray penetration and liquid length is obtained by 1D spray model for PRFs with a larger near-field spray angle as the input parameter compared to n-dodecane.
- As for PRF00, an increase in strain rate leads to a reduction in chemical reactivity, particularly in the moderate-temperature region of the fuel-rich

mixture and high-temperature region of the near stoichiometric mixture. Within the specified mixture fractions, spanned profiles of ignition delay as mixture fraction are observed for both first-stage and second-stage ignition, and the shortest first-stage ignition delay remains nearly constant as the strain rate increases. Additionally, the flamelet-derived ignition process exhibits a shift towards richer mixtures during the phase of steep temperature increase, coupled with a reduction in the magnitude of this temperature rise. Quasi-1D model produces a V-shaped profile of ignition delay and lift-off length as a function of strain rate, with a well matching on measurements at low strain rates. As the strain rate increases, first-stage ignition takes place in a richer mixture over a longer duration, resulting in the hot-temperature ignition also occurring in a richer mixture.

- A lower fuel reactivity results in a longer flamelet ignition delay, particularly in the first-stage ignition delay, which is consistent with significantly reduced chemical reactivity in the low-temperature region. The profiles of flamelet ignition delay as a function of mixture fraction are similar across different PRF#. Furthermore, the Quasi-1D ignition delay and lift-off length show a consistent trend as the strain rate increases for all PRF#, and the relationship between both variables and strain rate is comparable across the various PRFs. Hence, a constant strain rate can be chosen for the calculations involving all PRF#.
- Utilizing the same constant strain rate for all PRF#, ignition occurs at a leaner mixture as fuel reactivity decreases, accompanied by longer first-stage ignition duration. By employing the imposed ignition spread approach, accurate predictions of spray penetration were achieved, although a slight overprediction was noted after the ignition delay, especially for low-reactivity fuels. This is attributed to the minimal acceleration in penetration observed after ignition delay observed in the measurements.
- Under a variety of ambient and injection conditions, Quasi-1D model delivers an excellent agreement with measurements of ignition delay and lift-off length for PRF#, with the best matching at varying oxygen concentrations and injection pressures. However, some discrepancies remain in cases of low ambient temperature and in the ignition delay predictions for PRF80. Overall, Quasi-1D model proves to be more feasible for the calculation of the fuels that exhibit good vaporization.

Chapter 6

Model validation on polyoxymethylene dimethyl ethers

Content

6.1 Introduction/Objective

As mentioned in Chapter 1, the use of oxygenated fuels is a good solution to achieve carbon neutrality in the energy and transport sectors. With the high oxygen content, oxygenated fuels also show great potential in simultaneous reduction in NOx and soot emission. Among various oxygenated fuels, ethers, with a broader range of cetane number and the advantage of running in CI engines with modifications, appear to be a more favorable solution compared to alcohols [239].

In the family of ethers, polyoxymethylene dimethyl ethers (OMEx) are presented by the general formula CH3O-(CH2O)x-CH3, where x represents the degree of polymerization degree, usually ranging from 1 to 7. Compared to dimethyl ether (DME) with the simpler molecular structure CH3OCH3, the liquid fuel properties of OMEx make it a more promising candidate for blending with diesel or other hydrocarbon fuels at low temperatures. In addition, the lower production cost of OMEx in comparison to hydrocarbon fuels indicates a wider market potential, especially in the field of marine transportation [240].

Recent experimental investigations performed at CMT have mainly focused on two types of fuel: OME1, a short chain single component fuel, known for good fuel vaporization but difficulty in ignition; OMEx, a long chain multi component fuel mainly composed of OME3 and OME4, which has lower volatility but is outstanding in ignition performance. Previous studies have explored the use of these fuels by means of neat fuel or fuel additive in engines and some of them is performed in constant volume/pressure vessel for fundamental data [101] [241] [242] [243] [244]. Under the Spray A condition proposed in Engine Combustion Network [245], OMEx exhibits different ignition characteristic compared to n-dodecane, with a shorter ID and longer LOL [24] [246]. Meanwhile, the flame structure of OMEx presents no existing of OH downstream of LOL [247] [248], consistent with the observation of reduced soot formation in the spray head [24]. The oxygen component in OMEx is found to play the roles of shifting the equivalence ratio distribution, resulting in a leaner ignition of OMEx [191] and enhancing the soot oxidation, particularly in the spray head. In addition, the absence of C-C bond in OMEx molecular structure also helps to reduce soot precursor formation.

The aim of this chapter is to assess the performance of Quasi-1D model on the OMEx-type fuels previously studied in [191]. The simulations in this chapter contain various ECN conditions, including different ambient temperatures, oxygen concentrations, injection pressures, and nozzle diameters. Furthermore, the comparison between hydrocarbon and oxygenated fuels are performed in terms of two pairs: high-reactivity fuels (C12 vs OMEx) and low-reactivity fuels (PRF60 and OME1). The selection of C12 and PRF60 for comparison against the counterpart oxygenated fuel has been based upon the fact that they should have similar ignition delay. This analysis can help elucidate the independent influence of chemical characteristics (high- vs low-reactivity) as well as that of oxygenated molecule vs regular hydrocarbons. Similarly to Chapter 5, the first discussion will be given in Nominal Spray A condition, including the inert spray characteristics, effect of strain rate on the flamelet ignition and predicted ID & LOL, as well as the validation on reacting spray penetration and temperature contours. Finally, the model validation is extended to parametric variation and concludes with final remarks of the prediction accuracy of ID & LOL between hydrocarbon and oxygenated fuels.

6.2 Test conditions and fuel properties

The validation of Quasi-1D model on the OMEx-type fuels was assessed with the measurements conducted in a high-pressure high-temperature facility in CMT Institute [249]. The investigated fuels contain a single component one OME1, and a multi component one OMEx, consisting of 57.90% OME3, 28.87% OME4, 10.08% OME5, 1.91% OME6, and negligible OME1 and OME2 in the experimental study [24]. In accordance with the components considered in the chemical mechanism (OMEn, n = 2-4) [250], the fuel mixture used in the simulation consists of 59.14% OME3 and 40.96% OME4 by weight. As previously proposed, n-dodecane and PRF60 were selected for comparison of regular hydrocarbons with OMEx and OME1, respectively. The details of the fuel properties are given in Table 6.1.

Table 6.1. Fuel properties [243]

Properties [unit]	**n-Dodecane**	**PRF60**	**OME1**	**OMEx**
Density [kg/m^3] (T = 15°C)	751.2	684	866.7	1057.1
Viscosity [mm^2/s] (T = 40°C)	1.44	0.559	0.36	1.08
Cetane Number [-]	74	37.4	28	68.6
Lubricity [µm]	563		747	320
Flash point [°C]	83	-5.4	<40	65
Lower heating value [MJ/kg]	44.20	44.66	19.25	19.21
Carbon content [% m/m]	84.7	84.08	48.4	44.2
Hydrogen content [% m/m]	15.3	15.92	10.4	8.8
Oxygen content [% m/m]	0	0	42.1	45

The testing conditions are summarized in Table 6.2, where the conditions for each fuel are shown in an individual table. The nominal Spray A condition (highlighted in bold) is defined as the condition at $T_a = 900\ K, X_{O_2} = 15\%, P_{inj} = 1500\ bar$. The fuel temperature was maintained at 363 K, with an ambient density of 22.8 kg/m3. The study explored variations in ambient temperature (800/900/1000 K), injection pressure (500/1000/1500 bar), and oxygen concentration (15/21%). The evaporation mixture fraction is also given in the final column. Except for PRF60, measurements are performed using two injectors: a single-hole nozzle with diameters of 89.4 μm (Spray A: no.210675) and 190.3 μm (Spray D: no.209135). A long injection duration (~4 ms) was employed to ensure a steady spray. The injection rate for Spray A was obtained from a virtual injection rate generator [125], and the injection rate for Spray D is from an 'educated' profile [251].

Table 6.2. Test conditions

a. n-Dodecane

Spray	**Ta / K**	**Pinj / bar**	**XO2 / %**	**fevap [-]**
SA	800	500/1000/1500	15	0.3115
SA	**900**	500/1000/**1500**	**15**	0.3636
SA	900	500/1000/1500	21	0.3629
SA	1000	500/1000/1500	15	0.4085
SD	900	500/1000/1500	15	0.3636

b. OMEx

Spray	**Ta / K**	**Pinj / bar**	**XO2 / %**	**fevap [-]**
SA	800	500/1000/1500	15	0.3744
SA	800	500/1000/1500	21	0.3737
SA	**900**	500/1000/**1500**	**15**	**0.4282**
SA	900	500/1000/1500	21	0.4274
SA	1000	500/1000/1500	15	0.4738
SD	900	1000/1500	15	0.4282
SD	900	1000/1500	21	0.4274

c. PRF60

Spray	**Ta / K**	**Pinj / bar**	**XO2 / %**	**fevap [-]**
SA	800	1500	15	0.4678
SA	**900**	500/1000/**1500**	**15**	**0.5149**
SA	900	500/1000/1500	18	0.5145
SA	900	500/1000/1500	21	0.5141
SA	950	500/1000/1500	15	0.5357

d. OME1

Spray	**Ta / K**	**Pinj / bar**	**XO2 / %**	**fevap [-]**
SA	**900**	500/1000/**1500**	**15**	**0.5999**
SA	900	500/1000/1500	21	0.5981
SA	1000	500/1000/1500	15	0.6378
SD	900	1000/1500	15	0.5999
SD	900	1000/1500	21	0.5981
SD	1000	1000/1500	15	0.6378

6.3 Nominal Spray A condition

In this section, the evaluation of the performance of Quasi-1D model on oxygenated fuels and the comparison with hydrogenated fuels is performed under nominal Spray A condition. Firstly, the analysis of inert spray was presented, including the comparison of liquid and vapor spray penetration, and the 2D maps of residence time. Then, the effect of strain rate on the flamelet ignition and predicted ID & LOL is discussed. Next, the validation on reacting spray penetration will be shown using the radial expansion and the imposed ignition propagation. Finally, the comparison of ignition process between hydrocarbon and oxygenated fuels is presented in terms of 2D maps of temperature.

6.3.1. Inert spray analysis

In Quasi-1D model, two spray angles are specified for the calculation. In Chapter 4, the configurations of near-θ_1 = 15.75° and far-field θ_2 = 25° with a transition occurring at an intact length distance IL = 15 mm from the orifice is utilized for the calculation of n-dodecane under Spray A conditions. Meanwhile, the input of near-θ_1 = 18° was given in Chapter 5 for PRF#. Figure 6.1 presents the calculated liquid length (LL) and vapor tip penetration (S) for the investigated four fuels using the same spray angles as n-dodecane. As expected, fuel type has a minimal impact on vapor penetration, which is mainly dependent on nozzle momentum flux, spray angle and ambient density. Experimental verification has shown that momentum flux is not significantly affected by the fuel density [60] [252]. Using the same injector (Spray A, no.210675) as adopted in [24], there is no experimental data available for OME1 and OMEx under inert conditions. To describe the differences in LL among these fuels, experimental data from [241] [246] [253] was used for comparison with the calculated LL. Notably, LL for OMEx (~11.11 mm) is slightly longer compared to n-dodecane's (~9.7 mm) when using Spray A-3 injector. However, the predicted LL shows an inverse trend, suggesting that LL for OMEx is shorter, which may be caused by the inaccuracies in the fuel properties in 1D model.

In the 1D spray model, the adjustment of near-θ_1 will influence the predicted liquid length. A larger θ_1 results in a shorter LL, but it also leads to reduced vapor penetration. To achieve a good match with the measured spray penetration, the spray angles for OMEx and OME1 calculation are set as follows: near-θ_1 = 18° and far-field θ_2 = 25° with IL = 15 mm for Spray A; near-θ_1 = 16° and far-field θ_2 = 25° with IL = 33 mm for Spray D.

As shown in Figure 6.2, the highest value of on-axis mixture fraction is observed for OMEx, as well as the value of OME1 is slightly higher than n-dodecane, which is consistent with the CFD results reported in [191] [246]. Due to the measurement uncertainty, it didn't show an obvious difference in on-axis mixture fraction between n-dodecane and OMEx [246]. Additionally, the value of PRF60 is nearly close to n-dodecane. Normalized by $d_{eq} = d_0\sqrt{\rho_f/\rho_a}$, the profiles of n-dodecane, OMEx and OME1 are nearly overlapped in the field before the distance of IL/deq and in the far field near the spray head, while the highest value occurring in PRF60, caused by the lowest fuel density among the fuels.

As highlighted by previous studies [191] [248], the ignition of OMEx-type fuels is more likely to occur on the lean side due to the presence of oxygen content and its impact on the distribution of equivalence ratio. The 2D maps of residence time are illustrated in Figure 6.3, superimposed by the lines of equivalence ratios of 0.5, 1.0 and 2.0. Briefly, similar values of mixture fraction and local velocity result in similar residence time. However, the oxygen content in OME1 and OMEx leads to a large value of stoichiometric mixture fraction, i.e., fst(OMEx) = 0.1083, fst(C12) = 0.0465, hence, a longer residence time is achieved at the same surface of equivalence ratio. This phenomenon indicates that shorter time is spent in ignition-relevant equivalence ratio zones (around stoichiometry) and therefore OMEx-type fuels tend to ignite on the leaner side.

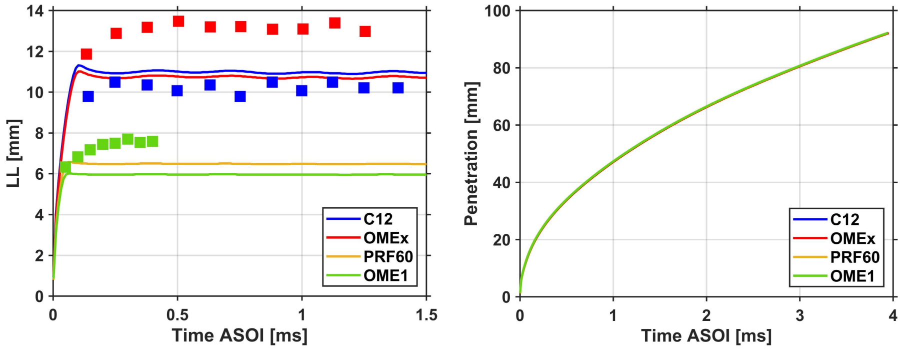

Figure 6.1. Model validation of liquid length (left) and spray tip penetration (right) of inert spray for C12, OMEx, PRF60 and OME1 under nominal Spray A condition with the same spray angles in Quasi-1D model. The symbols represent the experiments using the injector of Spray A - 3 [241] [246].

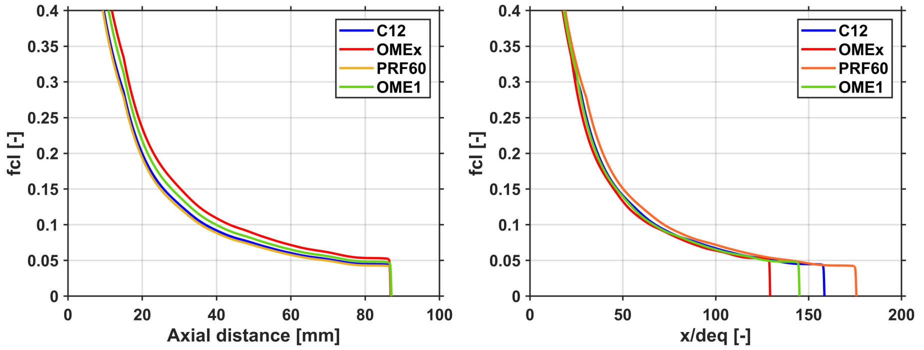

Figure 6.2. Predicted profiles of on-axis mixture fraction as the penetration in unit of mm (left) and normalized distance (x/deq, right) at 3.5 ms ASOI at inert nominal Spray A condition for the investigated fuels

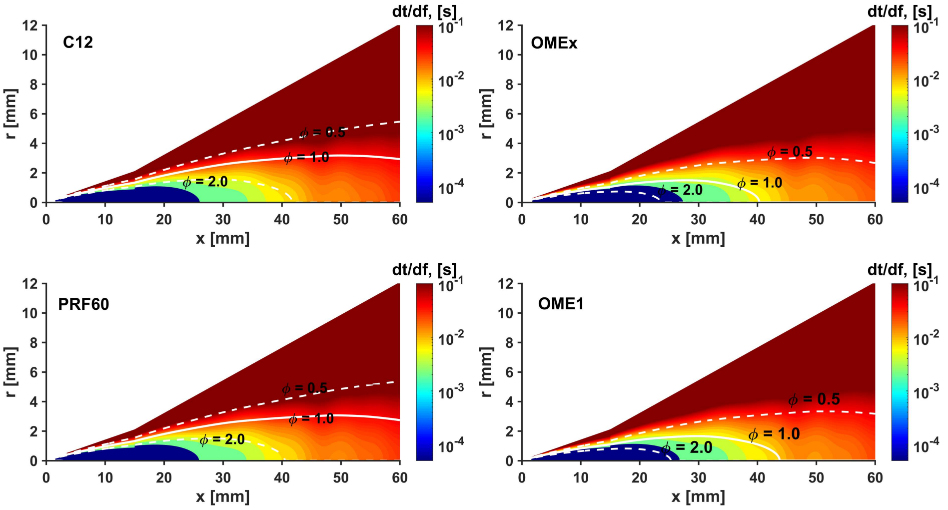

Figure 6.3. 2D contours of local residence time for inert Spray A of investigated fuels at 3.5 ms ASOI. The dashed lines represent the equivalence ratio of 0.5 (upper) and 2.0 (bottom), the solid line is the surface of stoichiometric equivalence ratio (middle).

6.3.2. Effect of strain rate on flamelet ignition in equivalence ratio space

Following the same methodology as in previous chapters, the analysis of flamelet ignition is performed as a reference of the spray ignition sequence. To highlight the effect of equivalence ratio, the contour maps of chemical source term $\dot{Y}_c(T,\phi)$ for the investigated fuels are illustrated in Figure 6.4, showing the difference between hydrogenated and oxygenated fuels under different strain rates. The progress variables are defined consistently across the four fuels as $Y_C = 0.75Y_{CO} + Y_{CO2} + Y_{H2O}$. The chemical mechanism developed by Jacobs et al. with 530 species and 2889 reactions is utilized for OME1 calculation [254], while the chemical mechanism used for OMEx calculation is from Cai et al. with 322 species and 1611 reactions [250]. Based on the discussion in Chapter 4, the LLNL mechanism is recommended for C12 calculations. Additionally, a reduced mechanism for PRF60 calculations was also referenced in the previous chapter.

The effect of strain rate on the distribution of contours for n-dodecane and PRF60 has been examined in previous studies. Additionally, the process of manifold generation for OMEx and OME1 has been extensively discussed in [191]. In this brief discussion, it is noted that a higher strain rate results in a higher intensity of the chemical reactivity in the intermediate-high temperature region and a shift towards rich mixtures.

Meanwhile, the reactivity in the high temperature region near the stoichiometry experiences an increase first, then monotonically decreases until the extinction limit.

In alignment with a similar analysis reported in [191], the contours are classified into three distinct regions for both n-dodecane and OMEx. A comparison between n-dodecane and OMEx reveals several common observations across the three strain rates. In Region 1, which represents the low temperature range, OMEx demonstrates a narrower temperature distribution compared to C12, while the intensity remains relatively consistent with C12, especially in the lean mixture. In Region 2, mainly within moderate temperature (1000 K < T < 1600 K) in the rich mixture, OMEx shows a significantly higher intensity and a broader distribution in both scales of temperature and equivalence ratio. Compared to n-dodecane, the highest intensity in this area of OMEx is located at a leaner mixture, resulting in the steep increase in temperature in the imposed flamelet ignition process (dashed black line) happening at a leaner mixture. In Region 3, which pertains to the high-temperature area near stoichiometry, OMEx also shows a higher reactivity.

For the comparison between PRF60 and OME1, the extinction limit for OME1 is much reduced than OMEx, thus, the selection of strain rate is at a half value that SR = 160 1/s and 500 1/s, representing the middle and high strain rates.

Referring to contours at SR = 50 1/s, the difference between PRF60 and OME1 resemble the comparison of high-reactivity fuels (C12 & OMEx), where OME1 exhibits lower intensity in region 1 and higher intensity in regions 2 and 3 compared to PRF60. Additionally, at a higher strain rate, PRF60 demonstrates reduced intensity in regions 1, 2, and 3, which contrasts with the heightened intensity observed in regions 2 and 3 for OME1. It is important to note that the chemical reactivity of OME1 in region 1 is significantly weaker than that of PRF60, and its intensity is more sensitive to variations in strain rate. Furthermore, the steep increase in temperature during the flamelet ignition process occurs at a richer mixture as the strain rate increases, while the ignition of OME1 takes place in a much leaner mixture than PRF60, consistently remaining in the region where $\phi < 2$.

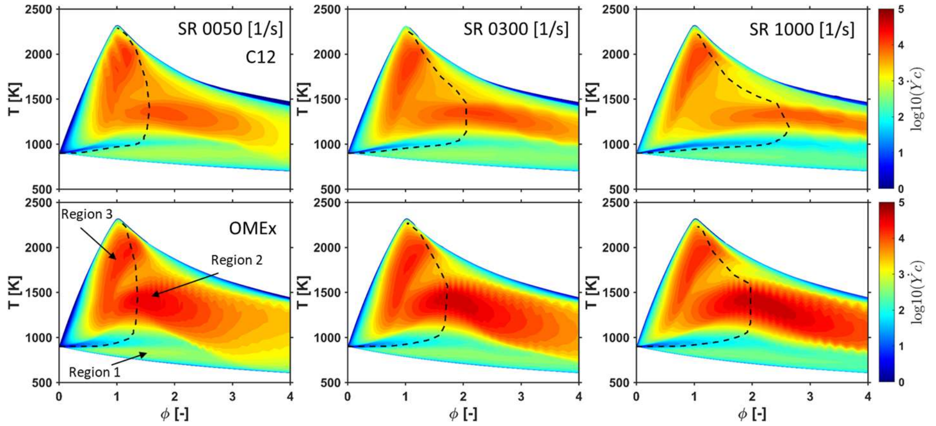

a. C12 (top) and OMEx (bottom)

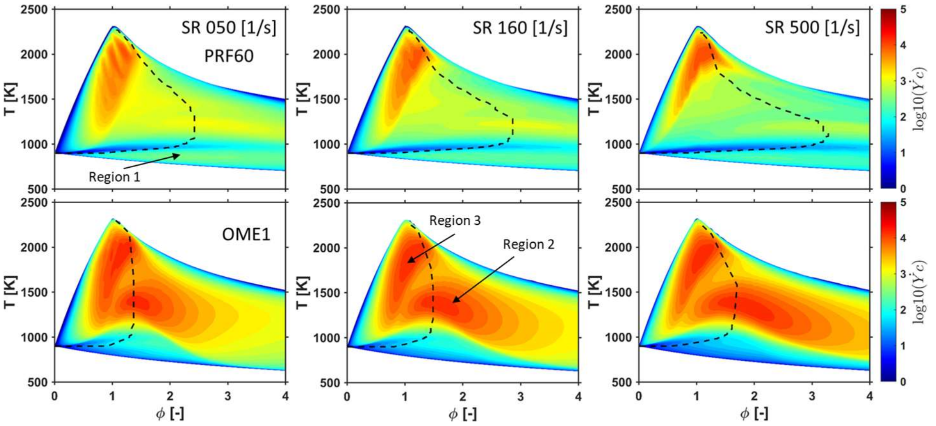

b. PRF60 (top) and OME1 (bottom)

Figure 6.4. Contours of chemical source term $\dot{Y}_c = \partial Y_c/\partial t$ displayed in temperature versus mixture fraction. Dashed black line superimposed on the contour is the evolution of maximum temperature at every 10 μs timestep. The vertical line is the stoichiometric ratio.

The profiles of flamelet ignition delay as a function of equivalence ratio are presented in Figure 6.5, which includes the low-temperature ID (denoted as LT-ID, defined as the instant when C > 0.1) and high-temperature ID (denoted as HT-ID, defined as the instant when C > 0.9). Note that equivalence ratio is used as independent variable instead of mixture fraction because of the different stoichiometric mixture fraction among all four fuels. Both the low- and high-temperature ignition delays for the investigated fuels exhibit a typical V-shape, with the minimum value occurring at a rich mixture. A detailed analysis of n-dodecane, OMEx, and OME1 based on a closed homogeneous reactor and the difference of OMEx and OME1 have been already reported in [191]. The main analysis will focus on the differences between C12 and

OMEx, PRF60 and OME1. The characteristics of C12 and PRF60 have been presented in Chapter 4 and 5, hence there will be no further discussion on that.

At the lowest strain rate, the shortest HT ignition delay among the fuels is consistent with the trend of fuel cetane number ($CN_{C12} > CN_{OME_x} > CN_{PRF60} > CN_{OME1}$), with the n-dodecane being the first one to be ignited, following by OMEx, then continue as PRF60, and finally OME1 is the longest one.

Across the entire equivalence ratio, C12 demonstrates a shorter LT ignition delay compared to OMEx, with the difference becoming smaller as the mixture approaches stoichiometry, and subsequently increasing in richer mixtures. However, C12 and OMEx shows the same HT ignition delays in lean mixtures, then, HT ignition delay of C12 becomes shorter as the mixture becomes richer, finally, the difference in HT ignition delay between C12 and OMEx becomes nearly constant in the range of $3 < \phi < 4$.

On the other hand, PRF60 and OME1 show similar LT ignition delays in the lean mixture, but the LT ignition delay of PRF60 drastically decreases as the mixture approaches the rich side. Consequently, a significant difference in LT ignition delay is found between PRF60 and OME1 in rich mixtures, which can be attributed to the weaker chemical intensity of OME1 in the low temperature region, as indicated in Figure 6.4. As for the HT ignition delay, a lower value is noted for OME1 before the mixture reaches the tipping point of $\phi = 1.2$. Beyond this point, the HT ignition delay of OME1 increases. Moreover, the discrepancies between OME1 and PRF60 are considerably greater than those observed between OMEx and C12 in terms of LT and HT ignition delay.

As an increase in strain rate, a wider and flatter profile is observed for LT and HT ignition delay across the equivalence ratio, particularly in the lean mixtures. The shortest LT ignition delay for OMEx remains nearly constant, while it is longer for OME1. When comparing OMEx and C12, the difference in LT ignition delay tends to be smaller, with the LT ignition delay of OMEx in the lean mixture ultimately being shorter than that of C12. Furthermore, the HT ignition delay of OMEx is consistently shorter than C12 across the entire equivalence ratios, which may explain the longer measured ID for C12 compared to OMEx under Nominal Spray A condition [24]. As for the comparison of low-reactivity fuels, PRF60 demonstrates a shorter LT ignition delay across the entire range of equivalence ratio, with greater discrepancies observed in rich mixtures. As suggested in Figure 6.4 (b), the chemical reactivity in the rich mixture of PRF60 is reduced while it is increased for OME1, therefore, the HT ignition delay of PRF60 becomes slightly longer than that of OME1 at the highest strain rate.

Figure 6.6 presents the flamelet ignition delay as a function of strain rate, where the ignition delay is the shortest HT-ID in the flamelet manifold at each strain rate. The left image presents the flamelet ID for the entire range of strain rate until the extinction limit, and the right images shorten the scale to 1000 1/s. For all the fuels, monotonically increasing trends of ID as a function of strain rates are found. Under the adopted chemical mechanisms, the auto-ignition limitation in strain rate is observed to be broader for oxygenated fuels. For the low-reactivity fuels (OME1 and PRF60), they show a similar ID at the small strain rates, then the HT-ID of OME1 is shorter at the large strain rates. For OMEx, the HT-ID is nearly constant in the range of strain rates less than 1000 1/s. However, C12 shows a larger sensitivity to strain rate, which is mainly due to the smaller range until extinction limit. In summary, there is a quite similar flamelet ID for hydrocarbon and oxygenated fuels. Note that the differences in the following calculated ID & LOL using Quasi-1D model should stem not only from this chemical behavior, but also from the difference in the difference in the mixing field distribution, which is consistent with the conclusions in [191] [248].

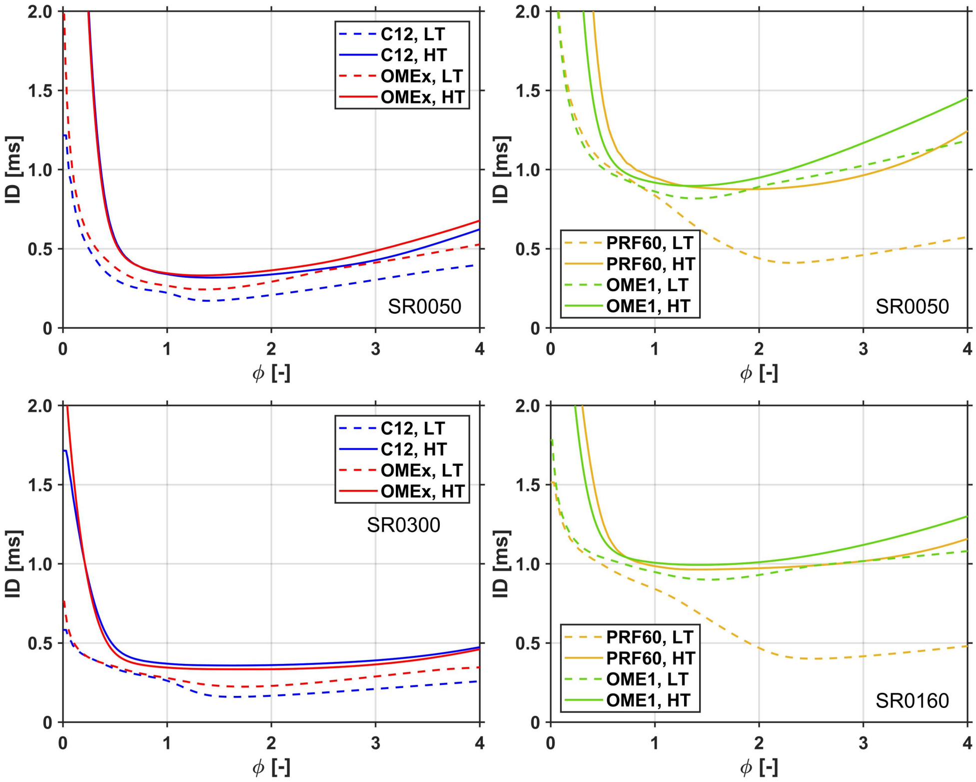

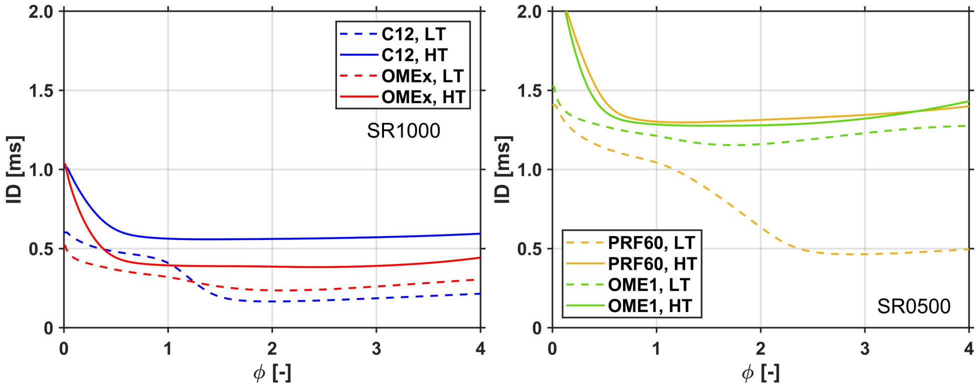

Figure 6.5. The evolution of low-temperature (LT) and high-temperature (HT) ignition versus equivalence ratio for C12 and OMEx (left) at strain rate 50, 300 and 1000 1/s, PRF60 and OME1 (right) at strain rate 50, 160 and 500 1/s.

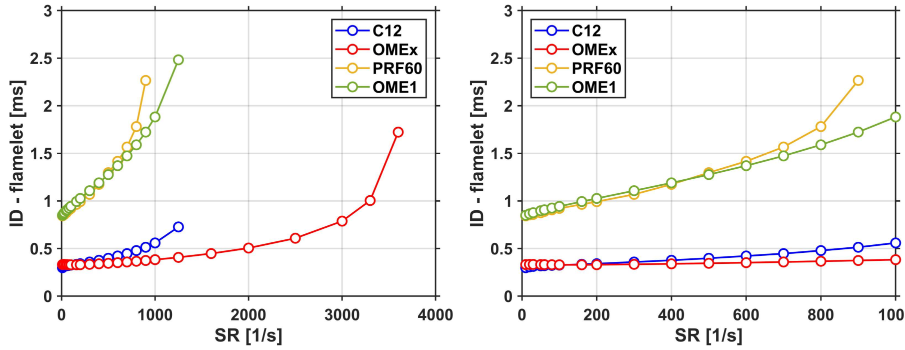

Figure 6.6. The profiles of flamelet ignition delay against strain rate for the investigated fuels. Left: full scale of strain rate until the extinction limit; Right: zoom-in scale in the range of 0 – 1000 1/s.

6.3.3. Effect of strain rate on Quasi-1D spray ignition

ID & LOL as a function of strain rate calculated by Quasi-1D model for the investigated four fuels are presented in Figure 6.7, where the ID follows the definition of the instant when Cmax exceeding 0.9 and LOL follows the criteria of minimum axial distance from the nozzle to the closest location where 14% of the maximum value of the mass fraction of OH in the spray. The experimental results are plotted as a dash-dot line with a light shadow, using the same color for clarity.

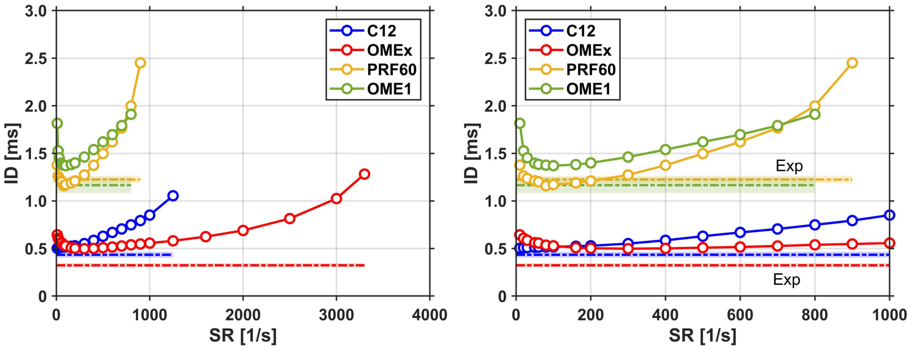

Figure 6.7. The profiles of ignition delay (left) and lift-off length (right) against strain rate for the investigated fuels from Quasi-1D modelling. The x-axis scale is limited to strain rate at 1000 1/s.

In contrast to the monotonic trend of flamelet ID increasing as the strain rate increases, the predicted ID for both oxygenated fuels exhibit a slightly V-shaped pattern, with the shortest value occurring at a strain rate of 100 1/s for OME1 and 300 1/s for OMEx. Moreover, the sensitivity of ID is more pronounced at low strain rates. It should be noted that ignition is not achieved at all the strain rates for the low-reactivity fuels. In particular, no ignition occurs for OME1 at above 800 1/s, and similarly for PRF60 above 900 1/s.

The sensitivity of ID to strain rate depends on the fuel, which results in a modification in the faster to ignite fuel as strain rate changes. In this sense, PRF60 ignites slightly earlier than OME1 until a strain rate value of 700 1/s, which is close to the no-ignition value. Similarly to flamelet ID, n-dodecane exhibits a shorter ID for strain rates below 100 1/s, with the opposite behavior at larger values.

The profiles of LOL against strain rate are observed to be consistent with the trend of ID, with the shortest value occurring at the same strain rate. At a constant strain rate value, oxygenated fuels show a longer LOL compared to hydrocarbon fuels, with a larger difference in LOL in the comparison between OME1 and PRF60. Therefore, no cross-over points exist for LOL.

Quasi-1D ID value overpredicts the experimental values for both OME1 and OMEx, with a similar difference observed between the measurements and the shortest ID across the strain rates. Meanwhile, LOL for both OMEx and OME1 also overpredicts measurements, but OME1 demonstrates a greater difference than that of OMEx.

To further clarify the difference in ignition process between flamelet and Quasi-1D model under the changed strain rates, the evolution of Tmax (maximum temperature across the domain) versus mixture fraction/equivalence ratio is presented in Figure 6.8. The characteristics of n-dodecane ignition predicted by Quasi-1D modelling have been examined in detail in Chapter 4. According to that, the ignition process of n-dodecane in the flamelet is described as a three-stage ignition, especially in moderate and high strain rates. The first stage ignition corresponds to the initial low temperature increase from 900 K to 1000 K, the second stage ignition is the steep increase at a constant mixture fraction. Soon after that, the third stage ignition ends up with a decrease of mixture fraction and temperature towards stoichiometry and Cmax close to steady state (C = 1). For OMEx, the flamelet evolution of Tmax in the first stage shows a lower slope compared to C12 as the fuel/air mixing approaches the stoichiometry. In the second stage, flamelet ignition for OMEx also takes place in the rich side, and the corresponding temperature increase is slightly larger compared to the same stage n-dodecane. Eventually, both mixture fraction and maximum temperature tend towards stoichiometry, similarly to n-dodecane.

In contrast to flamelets, Quasi-1D spray ignition for OMEx occurs at the lean side where f ~0.075, and the ignition process does not seem to be influenced by the strain rates. Moreover, leaner mixture (f < 0.075) is more favorable to be ignited. Then, the combustion reaches a steady state at the similar mixture fraction (f ~0.075), corresponding to approximate 2000 K. Finally, the ignition propagates to the richer mixtures (f > 0.075), and the mixture where f > fst is eventually ignited.

The flamelet ignition process for OME1 exhibits a similar behavior to that of OMEx, with the steep increase in Tmax occurring at a lower mixture fraction. In addition, Quasi-1D ignition for OME1 also demonstrates a lean ignition at three strain rates, with some sensitivity to strain rate that did not happen for OMEx.

In general, the ignition process of oxygenated fuels is predicted to begin at a lean mixture due to the long local residence time, and the ignition mixture fraction is observed to be higher than the corresponding hydrocarbon fuels. After the instant when Tmax > 1300 K (Ta + 400 K), the position of Tmax for C12 is near the stoichiometry, while it shows an ignition propagation to the richer mixture for OMEx, as a result of the strong reactivity in this rich region shown in Figure 6.4 (a). For the low-reactivity fuels, PRF60 and OME1 both exhibit an ignition propagation to richer mixture after the ignition, but PRF60 shows less sensitivity to strain rate in the ignition mixture fraction.

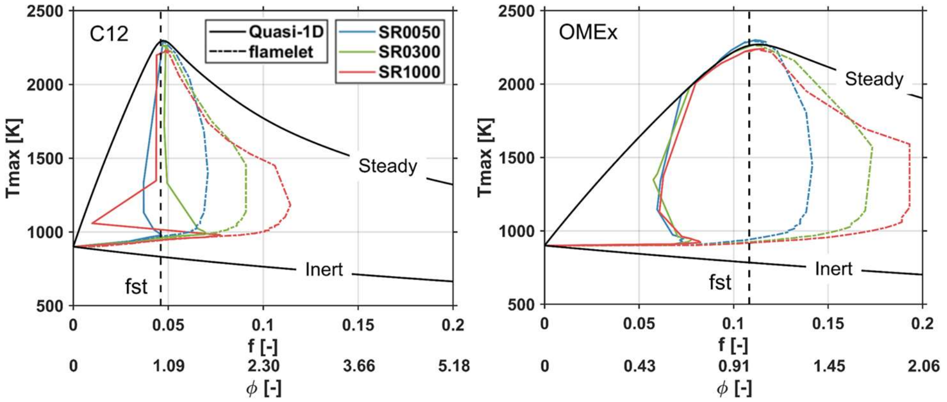

a. C12 & OMEx at strain rate 50, 300, 1000 1/s

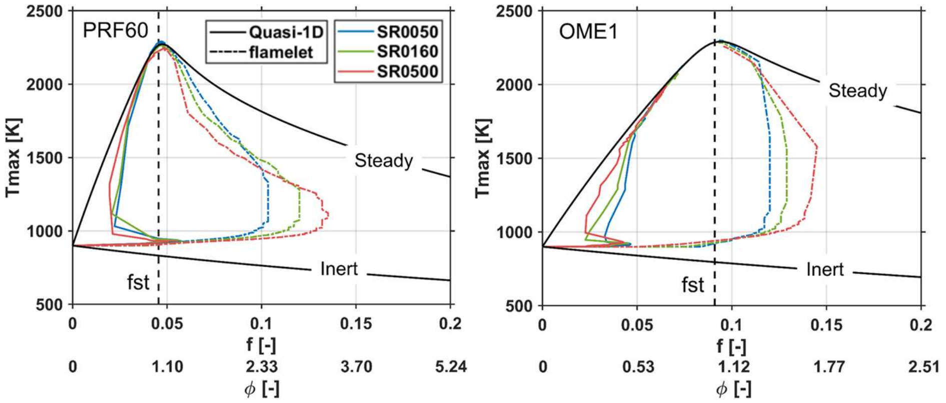

b. PRF60 & OME1 at strain rate 50, 160, 500 1/s

Figure 6.8. Maximum temperature as mixture fraction from flamelet (dash-dotted) and Quasi-1D model (solid) under nominal Spray A condition for the investigated fuels. The vertical dashed line represents the stoichiometric ratio.

As reported in Chapter 4, the ignition evolution in mixing trajectories shows similar three-stage process with a typical characteristic that the instant when the maximum temperature along the mixing trajectory reaches the value at the steady state under the corresponding mixture fraction. This characteristic defines the ignition delay for each trajectory, and the smallest one will be the ignition delay for the reacting spray. To further analyze the ignition process for the fuels under the effect of strain rate, the profile of temperature as mixture fraction at this instant is illustrated in Figure 6.9, covering five typical trajectories ranging from the spray center (r/R = 0.01) to the spray boundary (r/R = 0.83). The trajectory marked as dosh-dotted line represents the one that the ignition delay of trajectory is the shortest.

Similarly to n-dodecane results in Chapter 4, the ignition delay at SR = 50 1/s is determined by the trajectory at r/R = 0.55 with the ignition position occurring near the stoichiometry. Due to the short residence time at the trajectory for the cases close to the axis (e.g., r/R = 0.01) due to the highest local velocity, it is more difficult to be ignited than that of trajectory at r/R = 0.83. As the strain rate increases, the ignition delay is determined by both trajectories (r/R = 0.55 & 0.65) at SR = 300 1/s, and both trajectories (r/R = 0.55 & 0.83) at SR = 1000 1/s. Concerning OMEx, the earliest igniting trajectory is always the one at r/R = 0.55, which explains the nearly overlapped profiles of Tmax as f/ϕ among the strain rates shown in Figure 6.8. Meanwhile, this trajectory shows the shortest ignition at SR = 300 1/s, which is consistent with the observation of the profiles of ignition delay versus strain rate, as indicated in Figure 6.7. Additionally, the mixture along the trajectories at r/R = 0.65 & 0.83 is ignited faster as the strain rate increases, with a significant reduction at r/R = 0.83 (t = 2.2 ms to t = 1.2 ms). This observation highlights the effect of local residence time on the ignition in lean mixtures.

As for PRF60, the ignition delay of the spray is also determined by the same trajectory at r/R = 0.55 where the instant is the shortest. However, the instant is after that of C12 at 0.55 ms. Due to the similar mixing fields between n-dodecane and PRF60, a later ignition further away from the nozzle means that this occurs at a leaner mixture (f ~ 0.03). As for OME1, it also follows the observation that the trajectory of r/R = 0.55 determining the spray ignition delay. However, the ignition along all trajectories occurs in the lean mixtures.

As indicated in Figure 6.4, flamelet ignition process shows a hot-temperature ignition occurring in the rich mixture, due to the strong chemical reactivity. However, the ignition process in Quasi-1D model also includes the influence of residence time. As a balance of both factors, the earliest ignition happens along the trajectory of r/R = 0.55 for the four fuels at the three strain rates, hinting at a balance between a too short residence time on the axis and a too long one at high radial positions. The actual mixture value where ignition occurs depends on the strain rate, with ignition becoming leaner with higher strain rates.

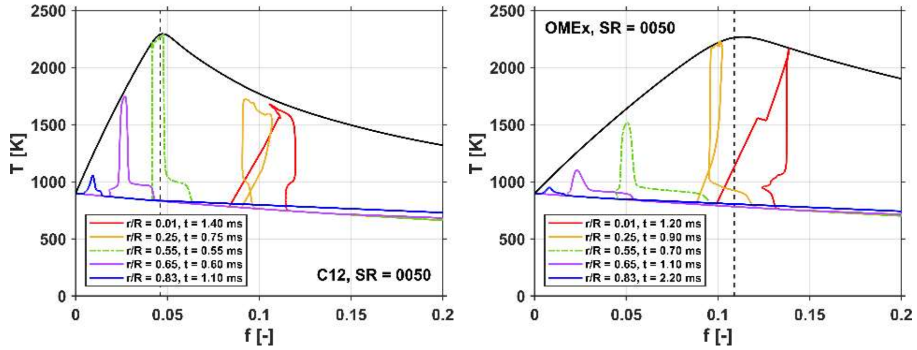

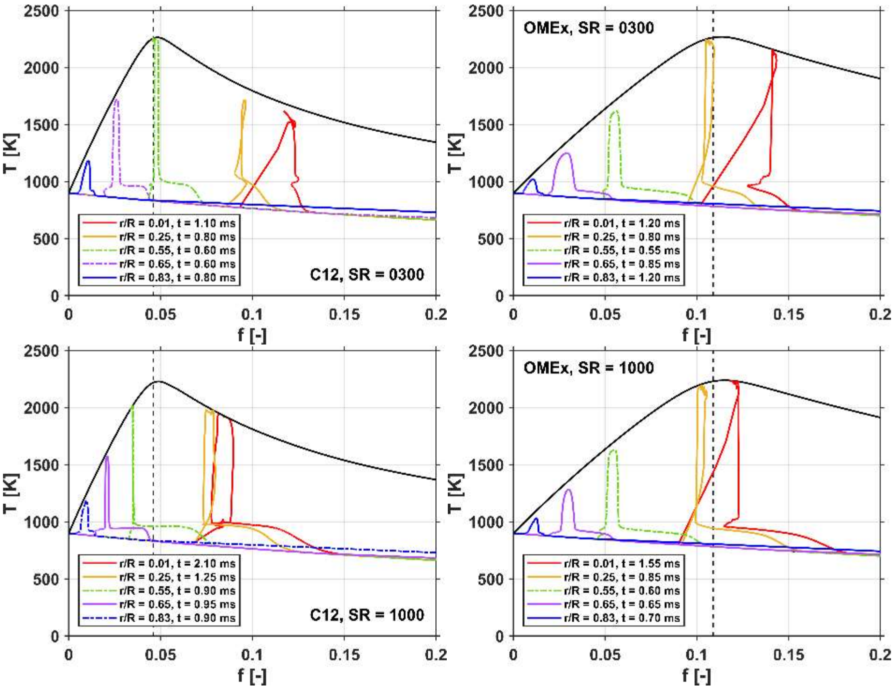

a. C12 (left) & OMEx (right) at strain rate 50 1/s (left), 300 1/s (middle), and 1000 1/s (bottom)

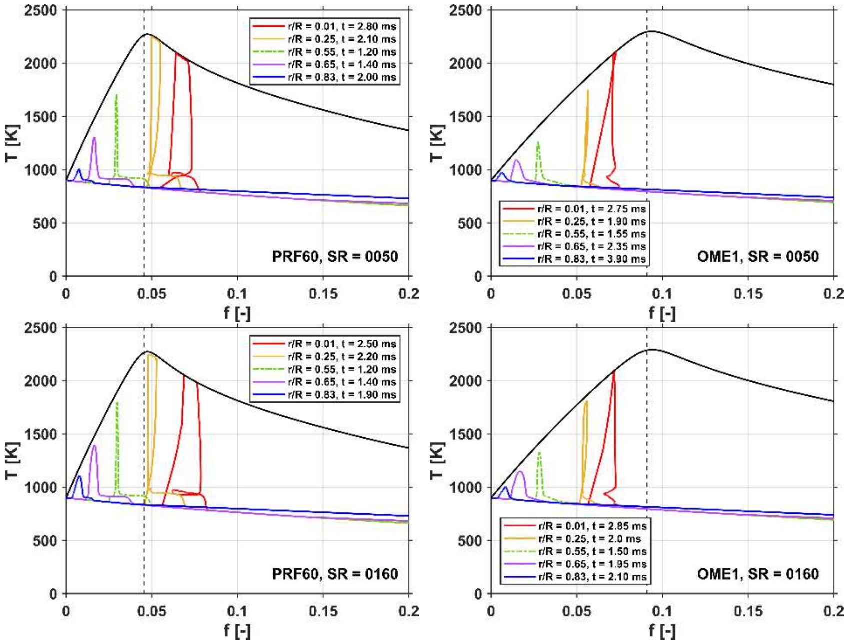

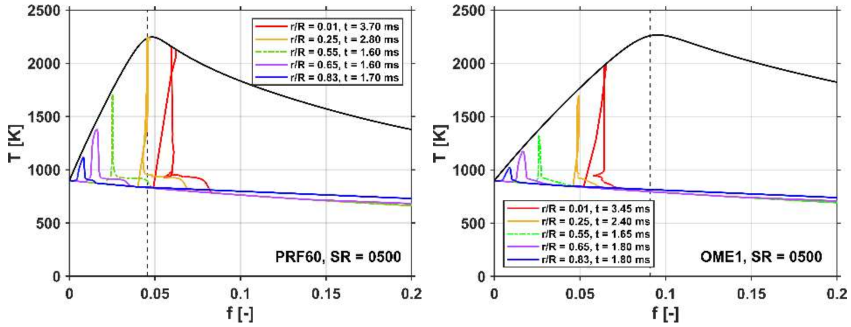

b. PRF60 (left) & OME1 (right) at strain rate 50 1/s (upper), 160 1/s (middle) and 500 1/s (bottom)

Figure 6.9. T – f profiles of at the ignition timing of five trajectories (r/R = 0.01, 0.25, 0.55, 0.65, 0.83) along the radial direction for the investigated fuels (C12 & OMEx, a; PRF60 & OME1, b). The dashed line is the earliest instant when reaching the steady state. The vertical line is the stoichiometric ratio.

Figure 6.10 presents the evolution of Cmax for the investigated fuels at three typical strain rates. As the strain rate varies, the appearance of the initial rise in Cmax is almost at the same instant for individual fuels. During the first-stage period, the Cmax of C12 shows a second acceleration after 0.25 ms ASOI, which can be explained by the ignition appearing other trajectories beside r/R = 0.55. Since the Cmax is dominated by the same trajectory, as indicated in Figure 6.9, the first-stage ignition shows a similar Cmax with the difference in the ignition period.

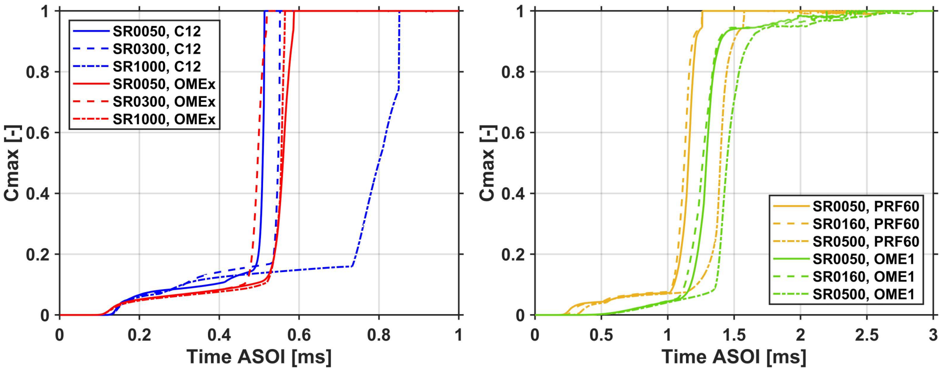

Figure 6.10. The evolution of Cmax for C12 & OMEx (left) and PRF60 & OME1 (right) under nominal Spray A condition for three strain rates.

As for OMEx, a typical two-stage ignition is also observed, with the appearance of the first-stage ignition slightly earlier than C12. Attributed to the small gap between the LT- and HT ignition delay derived from flamelet (Figure 6.5), OME1 experiences a continuous increase in Cmax after the initial rise appearing at 0.5 ms ASOI, indicating a single-stage ignition process.

From the discussion above, the choice of strain rate for the calculations of OMEx and OME1 can be determined by the predicted ID & LOL where is closest to the measured data. Consequently, SR = 100 1/s is selected for OME1 and SR = 300 1/s is for OMEx.

Imposed ignition propagation

Figure 6.11 presents a time-sequence of two-dimensional temperature fields during the ignition process, the comparison between n-dodecane and OMEx is shown in Figure 6.11 (a), PRF60 and OME1 are shown in Figure 6.11 (b). The image sequence shown in the column starts from the instant when Tmax exceeds 1300 K until the instant of steady combustion. The details of the analysis of n-dodecane have been reported in Chapter 4, thus, more discussion will focus on OMEx and OME1. For OMEx, the ignition was observed at the surface of $\phi = 0.5$ at a similar instant to n-dodecane (507 μs ASOI), in agreement with the observation in Figure 6.9. Meanwhile, the ignition also takes place longer distance compared to n-dodecane at the first instant, caused by the weak chemical intensity in the low temperature region. Furthermore, for OMEx, the larger gap in the chemical term between the low- and moderate-temperature regions results in a longer period from the initial ignition to the start of radial expansion (~600 μs ASOI). The temporal lift-off length of OMEx is also anticipated to be longer than that of n-dodecane, along with a greater distance where radial expansion begins to stabilize.

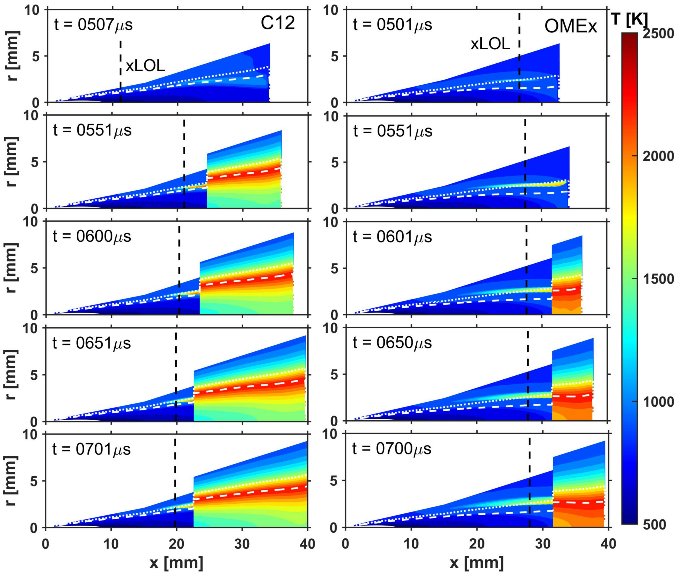

a. C12 & OMEx

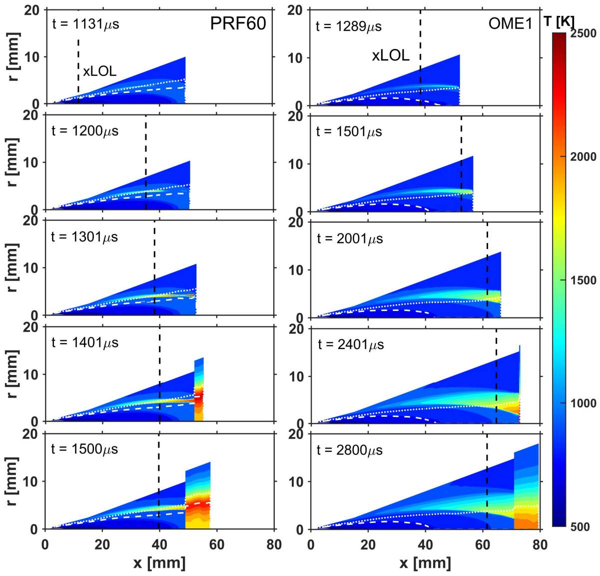

b. PRF60 & OME1

Figure 6.11. 2D contours of temperature along ignition process for the investigated fuels under Nominal Spray A condition. The vertical black line represents the temporal lift-off length. The dashed white line represents the surface of stoichiometric. The dotted line above the white dashed line represents the surface of $\phi = 0.5$.

For PRF60, ignition observed in the first image locates at the surface of $\phi = 0.5$, approximately 30 mm from the nozzle. As combustion progresses, the mixture downstream begins to ignite and diffuse towards the stoichiometry surface near the spray tip at 1301 μs ASOI. Subsequently, combustion near the spray tip reaches a steady state, indicating the start of radial expansion. The lift-off length then stabilizes at a distance of 40 mm with radial expansion commencing at 48 mm. In addition to the combustion in a fully steady state, ignition consistently occurs in the lean mixture before 1500 μs ASOI. In the case of OME1, ignition takes place at a later phase compared to PRF60, and it is also observed at a leaner mixture and a larger distance from the orifice. The highest temperature in the spray also occurs near the spray head. In addition, OME1 exhibits a longer duration from initial ignition at 1289 μs ASOI to the steady state after 2400 μs ASOI, consistent with the findings in Figure 6.10. The lift-off length stabilizes at 62 mm and radial expansion occurs downstream of the lift-off length defined by OH mass fraction.

In general terms, the ignition position is similar between the oxygenated and hydrocarbon fuels in the field of coordinate or called as mixture fraction. However, the difference on the distribution of equivalence ratio suggests that the ignition of oxygenated fuels tend to occur in leaner mixture compared to hydrocarbon fuels.

Using the selected strain rate, the validation on the reacting spray penetration as well as the ignition delay and temporal lift-off length by the Quasi-1D model using the imposed ignition propagation is illustrated in Figure 6.12. The measurement data origins from [24] [152] [234]. The inputs of spray angles and intact length lead to a good prediction to the spray penetration before ignition delay. After the ignition, besides the good agreement on the penetration of n-dodecane and OMEx, the penetration of PRF60 and OME1 is slightly overpredicted. As indicated in [182], ignition doesn't cause an acceleration to spray propagation when the PRF# number is over 40, which also explains the slight overprediction on OME1's penetration. One thing needs to be noted that the reduction in lift-off length at 2.8 ms ASOI of OMEx is caused by the ignition of lean mixture, and the starting of radial expansion becomes closer to the nozzle after an accumulation of C in the lean side. For OME1, the weak intensity of OH formation results in an increase in temporal LOL after the ignition, then, LOL stabilizes after 2.0 ms ASOI.

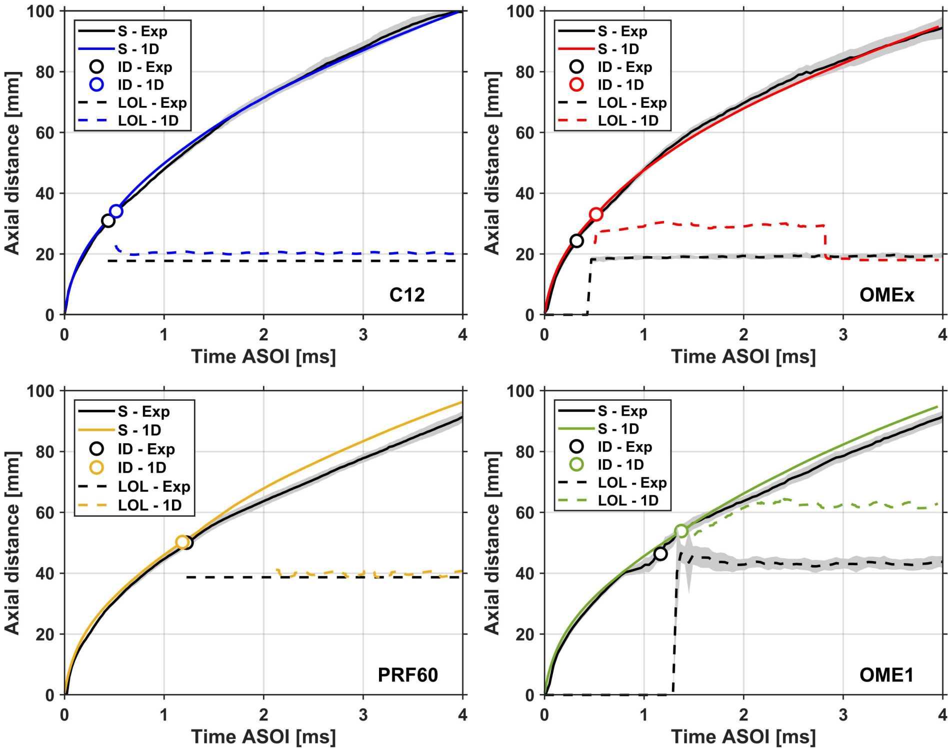

Figure 6.12. Reacting spray tip penetration, ignition delay, lift-off length for the investigated fuels under nominal Spray A condition

6.4 Parametric variations

To further evaluate the performance of Quasi-1D model on the ID & LOL prediction for oxygenated fuels, a comparison between it and hydrocarbon fuels at a similar cetane number is presented in Figure 6.13 in the type of simulation versus measurement. For most of the conditions, this model delivers a good prediction to ID within a discrepancy of 20% for n-dodecane, while this prediction for OMEx deviates more from the measurement than n-dodecane. Meanwhile, this deviation is reduced under the conditions of smaller nozzle diameter (compared to Spray D), higher ambient temperature (Ta = 1000 K), higher oxygen concentration (XO2 = 21%) and lower injection pressure. For the LOL prediction, the accuracy across the all conditions is similar between n-dodecane and OMEx, and it is better under the cases of higher temperature (Ta = 1000 K) and oxygen concentration (XO2 = 21%).

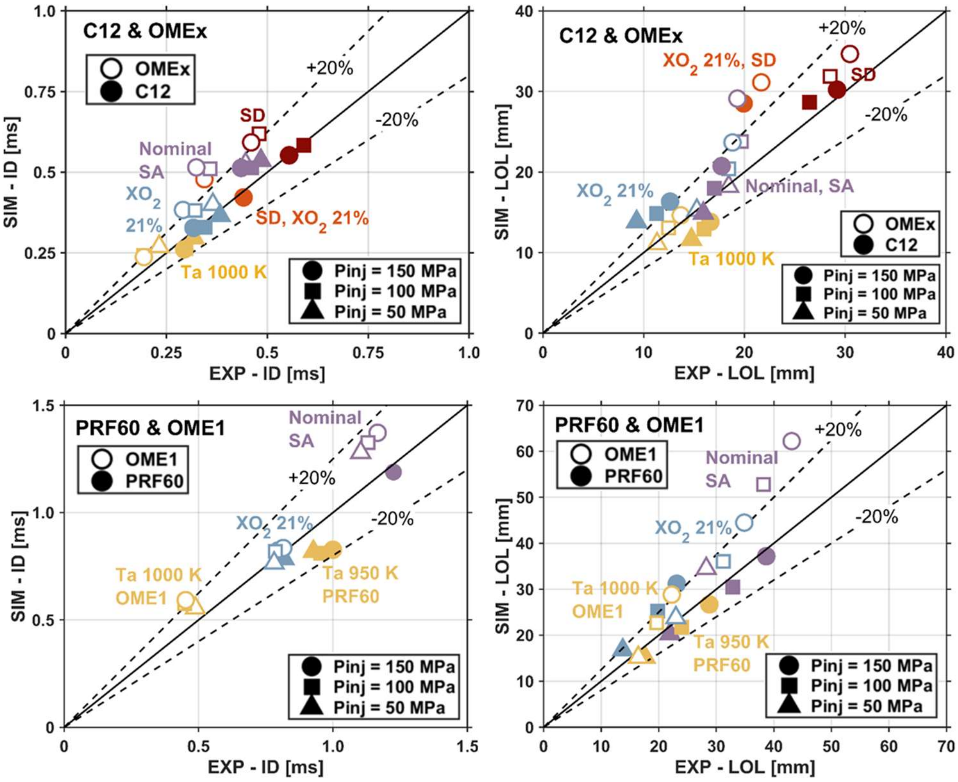

Figure 6.13. Validation of Quasi-1D model predictions of ignition delay (left) and lift-off length (right) for the investigated fuels (C12 & OMEx, upper; PRF00 & OME1, bottom) and operating conditions. Dashed diagonals correspond to a ±20% for ID and LOL. Solid marker: C12, PRF60; empty marker: OMEx, OME1. Circle marker: Pinj = 150 MPa; Square marker: Pinj = 100 MPa; Triangle marker: Pinj = 50 MPa

As for the comparison between PRF60 and OME1, the model accuracy in ID & LOL prediction is within the discrepancy of 20%, where the most accurate prediction is at the conditions of higher oxygen concentration (XO2 = 21%) for both fuels. Similar to the comparison of C12 and OMEx, hydrocarbon fuels tend to have an underestimation of ID at high ambient temperature, while this parameter is slightly overpredicted for oxygenated fuels. As for LOL prediction, the low chemical reactivity of OME1 under nominal Spray A condition causes the biggest deviation to experiment among all conditions. A similar observation to OMEx is also found that the deviation is reduced under a higher reactive ambient condition.

6.5 Summary/Conclusions

This chapter studies the performance of Quasi-1D model on the prediction of ignition process for oxygenated fuels containing OMEx and OME1 under the ECN recommended conditions. n-dodecane and PRF60 are also used as reference for hydrocarbon fuels. Single flamelet approach is adopted in the calculation. Throughout the findings, the conclusions are listed as follows:

- For inert Spray A, the little effect of fuel types on the vapor tip penetration is obtained, while the predicted liquid length is both slightly higher than the measurement for OMEx and OME1. A higher on-axis mixture fraction is observed for OMEx and OME1 due to fuel density differences. The oxygen components in OMEx and OME1 cause a longer residence time compared to hydrocarbon fuels along the surface of the same equivalence ratios.
- As the strain rate increases, the chemical reactivity of OMEx and OME1 exhibits a decreased chemical reactivity in the low-temperature region, an increased intensity in the moderate-high temperature region within rich mixtures, and a heightened intensity in the high-temperature region near stoichiometry. Additionally, a spanning profile of ignition delay as a function of equivalence ratio is observed for all fuels. At the highest strain rate, OMEx demonstrates a shorter high-temperature ignition delay compared to C12. OME1 displays a similar high-temperature ignition delay to PRF60, while its low-temperature ignition delay is significantly longer than that of PRF60.
- Across the various strain rates, a monotonic increase in flamelet ignition delay is noted for all fuels. OME1 and PRF60 show comparable flamelet ignition delays when the strain rate is less than 500 1/s. Similarly, OMEx and C12 demonstrate analogous flamelet ignition delays when the strain rate is below 200 1/s.
- The predicted ID & LOL by Quasi-1D model shows a consistent trend as a function of strain rate for the four fuels. The ID & LOL of OMEx is more

sensitive to strain rate at the low value and less sensitive at high strain rates compared to C12. In addition, oxygenated fuels show a longer LOL than hydrocarbon fuels at the entire strain rate.

- The predicted ID and LOL match well with the measurement for C12 and PRF60 at a low strain rate. However, the Quasi-1D model tends to overpredict the ID and LOL for both OMEx and OME1. Notably, OME1 exhibits a greater discrepancy in LOL predictions compared to OMEx across all strain rates.
- With varying strain rates, the ignition process of C12 was observed to occur near the stoichiometric ratio, while lean ignition was noted for the other fuels. As the strain rate increases, the ignition of OMEx shows similar evolutions characterized by the relationship between Tmax and mixture fraction, while the ignition of OME1 was found to occur at a leaner mixture. In addition to C12, the ignition delay predicted by the Quasi-1D model is determined by the ignition evolution along the mixing trajectory at $r/R = 0.55$. Consequently, the Cmax during the first-stage ignition remains nearly constant, regardless of changes in strain rate.
- The approach of imposed spread ignition allows for more accurate predictions of reacting sprays for high-reactivity fuels. It slightly overpredicts the behavior of low-reactivity fuels after the ignition delay. Among the Engine Combustion Network conditions, the Quasi-1D model provides reasonable predictions for ignition delay and lift-off length, with a deviation of within 20%. The most accurate predictions occur under conditions of high oxygen concentration for OME1 and high ambient temperature for OMEx.

Chapter 7

Conclusions and future works

Content

7.1. Introduction

This final chapter provides a summary of the research conducted throughout the thesis. It includes conclusions drawn from the various work undertaken to achieve the main objective of the thesis. At the conclusion of the chapter, the contribution of this thesis to 1D spray model are also offered. Additionally, the potential future research directions are discussed at the end of this chapter, highlighting new studies that could further improve accuracy and possible applicability.

7.2. Conclusions

As initially mentioned in Chapter 1, the main objective of this study is to develop a fully predictive approach for calculations in reacting spray/jets that integrate the 1D spray modelling approach with detailed chemistry. The fulfillment of this objective was categorized as two pathways, model improvement on the computational cost and prediction accuracy, and the model application on the effect of chemical mechanism, fuel reactivity and oxygen content on the combustion. The experimental database from CMT – Clean Mobility & Thermofluids was utilized for the model validation for the combustion metrics under various conditions recommended by Engine Combustion Network. From the literature review in Chapter 2, flamelet is a good solution to balance the trade-off relationship between computational cost and prediction accuracy when implying the detailed chemistry in 1D spray model. Following this idea, laminar flamelet was integrated into 1D spray model by adding the conservation of progress variable into the existing conservation equations of axial momentum and mixture fraction, with the detailed procedures of this integration and the optimizations given in Chapter 3. As a first step, the model description for a reacting turbulent spray was optimized to achieve an accurate prediction, as well as the procedures in overcoming the possible iteration failures. Conducted under the ECN Nominal Spray A condition fueled with n-dodecane, the main modifications in the model development are summarized in the following:

- The discretized control volume has been changed to be perpendicular to the spray axis. The spray penetration has also been reconstructed so that it remains the current iteration criteria while the iteration failure was solved, particularly in the low reactive conditions. Explicit solution for progress variable has been adopted, thereby, it realized a reduction in computational cost by two-thirds.
- The transient term at the inert state has been recalculated by means of a piecewise linear interpolation, resulting in a consistency with the tabulated evolution of progress variable across the range of equivalence ratio from lean to rich. As for the effect of liquid phase, it is assumed that no reactions

upstream of liquid length. Consequently, the prediction to ID is much improved with a slight overprediction to LOL under the constant strain rate.

- After the ignition timing, the spray downstream the LOL has been imposed to be fully ignited to balance the progress variable diffusion among the trajectories, with an accounting for radial expansion at ignition onset, which is an effect that is observed experimentally in the spray evolution. This modification enables a more accurate prediction of spray tip penetration as well as the spatial distribution of temperature and species, without affecting the prediction to ID and LOL.

After the initial steps, the model was optimized under the specific Spray A condition. The next objective in this thesis is to assess the performance of the model for a wide range of operating conditions and fuels. Before the implementation, the necessary step is to validate the inputs to 1D spray model on the prediction of inert spray. In Chapter 4, the reference fuel is n-dodecane, and the validation is firstly conducted by comparing the obtained quantities with measurement under ECN Nominal Spray A condition, comprising liquid and vapor penetration, mixture fraction and velocity along the axial direction and radial direction at three axial points. Then, good agreement was achieved in the liquid and vapor penetration under the lowest injection pressure when the same inputs are followed. As for Spray D, longer transition distance between the near-field and far-field spray angle is utilized. Concerning Primary Reference Fuels (Chapter 5) under Spray A conditions, a larger near-field spray angle is introduced to obtain a shorter liquid length compared to n-dodecane. Meanwhile, the other inputs remain the same as before. Last, with the same inputs, the trend of the predicted liquid length is in contrast to the measurements in the comparison between OMEx and C12, as well as the comparison between OME1 and PRF60 (Chapter 6). The adjustment in the near-field spray angle finally obtained good agreement with the measured vapor penetration.

After the validation on inert spray, the partial objective of model application was fulfilled with the following tasks: the investigation of influence of chemical mechanisms with the variations of strain rate on the combustion prediction, the model accuracy at various mixing conditions (Chapter 3 & 4), and the performance of ID and LOL predictions for fuels with various reactivities (Chapter 5) and oxygen content (Chapter 6). The conclusions have been established in their corresponding chapter, here, the main results are gathered to synthesize the contributions of this work to 1D spray model. The relevant findings are summarized as follows:

- **Assessment of chemical mechanisms on combustion process (Chapter 4)**

  The performance of three chemical mechanisms, named as Yao, LLNL and Narayanaswamy, was assessed under ECN Nominal Spray A condition. The calculation was conducted with a constant strain rate, which sweeps from an extremely low value to the extinction limit. The most relevant findings are:

- All three chemical mechanisms reveal a two-stage flamelet ignition process. The Yao mechanism exhibits greater chemical reactivity in the first stage, whereas the LLNL mechanism shows enhanced chemical reactivity in rich mixtures at intermediate temperatures. The Nara mechanism behaves similarly to the LLNL mechanism, albeit with reduced intensity. A comparable first-stage ignition delay was observed in Yao and LLNL solutions, while the difference on the lean side increased with the increasing strain rates. The second-stage ignition delay of the Yao and LLNL schemes are similar throughout the mixture fraction at low and medium strain rates. In contrast, the Nara mechanism displays the longest ignition delay in the first phase.
- The predicted ignition process by Quasi-1D model exhibits three distinct behaviors across the entire strain rates. As the strain rate increases, the retarded chemical reactivity results in a longer ignition delay at a low range of strain rates, accompanied by a transition in ignition from a near stoichiometric mixture (as observed in the Yao mechanism) or a slightly lean mixture (as observed in the LLNL mechanism) to a richer mixture. This transition is attributed to the shift in chemical reactivity in the moderate temperature region towards a richer side. At a higher strain rate, the long residence time in the lean area across the spray domains enhances the local ignition, contributing to a lean ignition and a reduced ignition delay in Yao solution. Conversely, this leads to an increase in the ignition delay with LLNL mechanism, which is accounted for the strong chemical reactivity near the stoichiometry that drives the high-temperature ignition occurring around the stoichiometry. In the case of the Nara mechanism, ignition takes place at a progressively leaner mixture at a higher strain rate, exhibiting a V-shaped ignition delay profile as the strain rate varies. This profile reflects a decrease in ignition delay due to the reduced flamelet low-temperature ignition delay in lean mixtures, followed by an increase attributed to lower chemical reactivity.
- For each chemical mechanism, the trend of the prediction ID is consistent with LOL as the variation of strain rate. At low strain rate, good match on the measurement in terms of ID & LOL is observed with Yao and LLNL mechanisms. However, the solution of Nara mechanism shows the overprediction to both ID & LOL across the whole range of strain rates. Summarized by the calculations under a wide range of conditions, LLNL is the preferred option among the three chemical mechanisms.

- **Performance of model integration with single and multiple flamelets (Chapter 3 & 4)**

  The comparison was conducted with LLNL mechanism under Nominal Spray A condition. The initial step is to validate the derived strain rates, followed by the analysis of combustion metrics with single flamelet at SR = 50 1/s and multiple flamelets at the strain rate ranging from 10 to 1000 1/s. The relevant findings are summarized as follows:

  - A simplified approach for the calculation of strain rate was developed and compared with recent DNS calculations of a turbulent constant density gas jet. Together with accurate predictions for on-axis velocity and mixture fraction, the Quasi-1D approach shows good predictions of strain rate for $r/x>0.07$. To address the significant underestimation observed in the inner regions, a constant value assumption was employed from the center to the peak.
  - As for the spray calculations, the use of multiple flamelets delivers an average behavior within the flamelet manifold strain rate range. In general, the use of multiple flamelets does not alter the occurrence of cool flame; however, it extends its duration. The predicted ignition delay (ID) aligns with the data from a single flamelet at a strain rate of approximately 300 1/s, while the predicted lift-off length (LOL) corresponds to a higher value of around 800 1/s. The ignition sequence is relatively similar between a single- and a multiple-flamelet, only relatively small differences are found. Considering the additional degree of freedom that the selection of a single strain rate offers, the latter approach has been selected for the calculations in the thesis.

- **Evaluation of model accuracy at various mixing conditions (Chapter 4)**

  In this section, the effect of mixing characteristics on combustion metric is explored by adjusting the injection pressure and orifice diameter. Both Yao and LLNL chemical mechanisms are utilized. With the further validations under various ambient conditions, the relevant findings are summarized as follows:

  - A lower fuel injection velocity at low injection pressure leads to a longer local residence time, which is approximately proportional to the square root of injection pressure ratios. The time of Spray D spent at specific equivalence ratios is approximately twice as long as that of Spray A, corresponding to the ratio of the nozzle diameter.
  - The relationship of modelled ignition delay/lift-off length and strain rate at both different mixing conditions mainly resemble the result under the nominal condition, with the less sensitivity as the variation of strain rate,

particularly in the solution of Yao mechanism. Good agreement in the measurement can be observed in the low strain rates for all the mixing conditions using both chemical mechanisms.

- Using the approach of imposed ignition spread with constant strain rate, excellent prediction on reacting spray penetration and on-axis mixture fraction can be achieved using both Yao and LLNL mechanisms. Meanwhile, with a reasonable strain rate, both chemical mechanisms can succeed in the reasonable prediction of ignition delay and lift-off length as the changed mixing conditions, which is consistent with the trend obtained from measurement. Under the various chamber ambient conditions, Quasi-1D model is also able to obtain the reasonable trends in prediction to ignition delay and lift-off length as the injection pressure increases. As for the prediction accuracy across vast conditions, LLNL mechanism is more favorable for the n-dodecane simulation in Quasi-1D model. Hence, this has been adopted for subsequent n-dodecane analysis.

- **Effect of fuel reactivity on combustion (Chapter 5)**

  Primary Reference Fuels are adopted in this study. The fuel reactivity characterized by the octane number ranging from 0 to 80 is adjusted by changing the blends of n-heptane/iso-octane. The similar stoichiometric ratio and fuel density among the fuels leads to a similar mixing field. After the model validations on ECN condition with constant strain rate, some relevant findings can be summarized as follows:

  - As for PRF00, an increase in strain rate results in a reduction in chemical reactivity, a longer flamelet ignition delay, a shift towards richer mixture and a reduced magnitude rise for the step of the steep temperature increase inside the flamelet-derived ignition process. Quasi-1D ignition delay and lift-off length as a function of strain rate show a V-shaped profile. Additionally, the first-stage ignition experiences a longer duration with a richer mixture, resulting in a richer hot-temperature ignition.

  - With a higher blend of iso-octane in PRFs, the weaker chemical reactivity leads to a longer flamelet-derived and Quasi-1D ignition delay, and its sensitivity to strain rate is also higher. The profiles of ignition delay and lift-off length as a function of strain rate are similar across different PRFs, leading to a consistent constant strain rate applied for calculations of all PRFs under the ECN Spray A conditions. In addition, ignition occurs at a leaner mixture due to the decreased fuel reactivity, along with a longer first-stage ignition duration.

- **Effect of Oxygen content on combustion (Chapter 6)**

In the section, the effect of oxygen content in fuels was studied by introducing the OME-type fuels. The assessment was conducted with two pairs of fuel, high-reactivity fuels including n-dodecane and OMEx; and low-reactivity fuels, including PRF60 and OME1. Following a similar analysis as in Chapter 4, some relevant findings can be summarized as follows:

- With the same injection pressure, similar mixing fields in terms of mixture fraction are observed for all fuels, while the oxygen component in OMEx and OME1 cause a shorter residence time compared to hydrocarbon fuels along the surface of same equivalence ratios.
- As for the flamelet ignition results, the higher chemical reactivity in the moderate- and high-temperature region of OMEx and OME1 contributes to a leaner flamelet ignition compared to n-dodecane and PRF60, respectively. For the same reason, OME1 and PRF60 exhibit comparable flamelet ignition delays within the strain rate lower 500 1/s. Similarly, OMEx and C12 demonstrate analogous flamelet ignition delays at the strain rate below 200 1/s.
- As for the Quasi-1D model results, the ignition of OMEx shows a similar trace in the evolution of maximum temperature against mixture fraction at the three typical strain rates, while OME1 demonstrates a leaner ignition as the strain rate increases. The relationships of ignition delay and lift-off length both show a V-shaped profile as the strain rate changes. Across the entire strain rate values, Quasi-1D model delivers an overpredicted ignition delay and lift-off length for both OMEx and OME1, with the greater discrepancies in lift-off length observed in OME1. The analysis of the ignition evolution along the trajectories shows that the ignition delay is dominated by the ignition happening along the trajectory at r/R = 0.55.

To highlight the model accuracy in the prediction of combustion metrics, the comparison of simulated and measured ignition delay and lift-off length for hydrocarbon (C12 & PRF) and oxygenated fuels (OMEx & OME1) is presented in Figure 7.1, which includes all the investigated conditions in this thesis. In global, the prediction is within a 20% deviation for most conditions. However, the prediction of ignition delay in the case of hydrocarbon fuels is slightly underestimated, while it is slightly overpredicted for the oxygenated fuels. As for the model accuracy on lift-off length prediction, a good match is observed under high-reactivity conditions, with slight overpredictions at the case of low temperatures. Overall, the advantages of low computational cost and accurate predictions can make it a valuable tool for the evaluation of effects of fuel reactivity and oxygen content on spray ignition and combustion, which is an important field nowadays within the transition to renewable fuels.

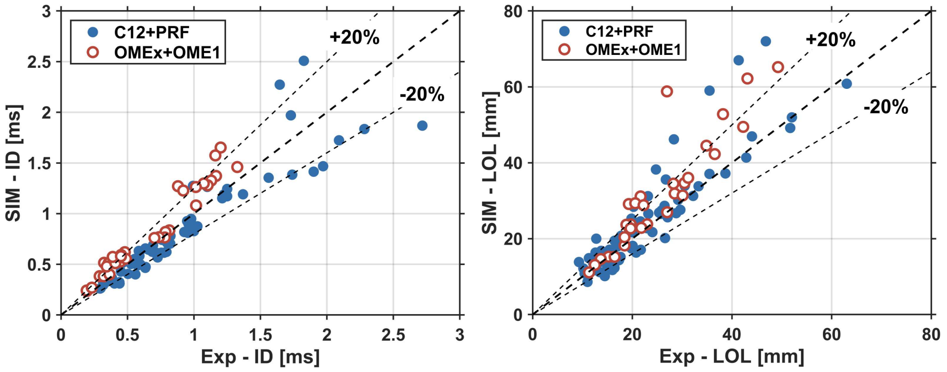

Figure 7.1. The performance of Quasi-1D model on the prediction to ignition delay (left) and lift-off length (right) for hydrocarbon (C12 + PRF) and oxygenated fuels (OMEx + OME1)

7.3. Future works

There is no doubt that there are still many shortcomings in the developed Quasi-1D model in this thesis. To further improve the model accuracy under the extended application scenario, the following proposals might be relevant to that end:

- In this thesis, laminar tables are utilized to describe the turbulent reacting spray. Consequently, the integration of a one-dimensional spray model with flamelet is established on the single variable, mixture fraction. However, this approach does not capture all the information of the combustion process which is tabulated in flamelet tables. To address this issue, introducing the parameter of variance of mixture fraction through empirical correlations may provide a more detailed description of the combustion process.

- In principle, employing multiple flamelets is feasible for the calculation of a case with long injection duration. Validations of the local strain rate has been conducted for an isothermal jet, whereas data for inert diesel-like sprays or reacting sprays remain unavailable. In addition, the simplified approach with a constant radial distribution around the centerline should be further examined to ensure reliable integration with the flamelets.

- Another possible route for improving the model accuracy is the direct integration with detailed chemical kinetics; however, the number of control volume should be reduced to effectively manage computational costs.

- Furthermore, the possible extension can be performed under transient ambient conditions, such as those occurring within the cylinder during engine operation. In this context, Quasi-1D model may also prove beneficial for engine calibration, particularly with the use of alternative fuels.

Bibliography

[1] IEA, "CO2 Emissions in 2022, IEA, Paris," 2023. [Online]. Available: https://www.iea.org/reports/co2-emissions-in-2022. [Accessed 6 9 2024].

[2] IEA, "Greenhouse Gas Emissions from Energy Data Explorer, IEA, Paris," 2024. [Online]. Available: https://www.iea.org/data-and-statistics/data-tools/greenhouse-gas-emissions-from-energy-data-explorer. [Accessed 6 9 2024].

[3] IEA, "Global Energy Review," 2020. [Online]. Available: https://www.iea.org/reports/global-energy-review-2020/oil. [Accessed 6 9 2024].

[4] H. Ritchie, P. Rosado and M. Roser, "Energy Production and Consumption," 2020. [Online]. Available: https://ourworldindata.org/energy-production-consumption. [Accessed 6 9 2024].

[5] IEA, "Electric Vehicles," [Online]. Available: https://www.iea.org/energy-system/transport/electric-vehicles. [Accessed 6 9 2024].

[6] S. Deng and Z. Mi, "A review on carbon emissions of global shipping," *Marine Development,* vol. 4, no. 1, 2023.

[7] "IMO's work to cut GHG emissions from ships," INTERNATIONAL MARITIME ORGANIZATION, 2023. [Online]. [Accessed 7 9 2024].

[8] WEICHAI, "Breaking World Records Four Times | Weichai Power Releases the World's First Diesel Engine with Base Engine Brake Thermal Efficiency of 53.09%," 20 4 2024. [Online]. [Accessed 18 9 2024].

[9] A. Krishnasamy, S. K. Gupta and R. D. Reitz, "Prospective fuels for diesel low temperature combustion engine applications: A critical review," *International Journal of Engine Research,* vol. 22, no. 7, pp. 2071-2106, 2021.

[10] T. Getachew and M. Dejene, "Low-Temperature Combustion in Diesel Engines," in *Diesel Engines - Current Challenges and Future Perspectives*, IntechOpen, 2023.

[11] A. Serra, R. Artal, J. Garcia-Amoros, E. Gomez and L. Philippe, "Circular zero-residue process using microalgae for efficient water decontamination, biofuel production, and carbon dioxide fixation," *Chemical Engineering Journal,* vol. 388, p. 124278, 2020.

[12] H. Pitsch, D. Goeb, L. Cai and W. Willems, "Potential of oxymethylene ethers as renewable diesel substitute," *Progress in Energy and Combustion Science,* vol. 104, p. 101173, 2024.

[13] H. Thomson, J. J. Corbett and J. J. Winebrake, "Natural gas as a marine fuel," *Energy Policy,* vol. 87, pp. 153-167, 2015.

[14] M. Altosole, G. Benvenuto, U. Campora, F. Silvestro and G. Terlizzi, "Efficiency Improvement of a Natural Gas Marine Engine Using a Hybrid Turbocharger," *Energies,* vol. 11, no. 8, 2018.

[15] B. Zincir and C. Deniz, "Methanol as a Fuel for Marine Diesel Engines," in *Alcohol as an Alternative Fuel for Internal Combustion Engines* , Springer, 2021.

[16] S. H. Hosseini , A. Tsolakis, A. Alagumalai, O. Mahian, S. S. Lam, J. Pan, W. Peng, M. Tabatabaei and M. Aghbashlo, "Use of hydrogen in dual-fuel diesel engines," *Progress in Energy and Combustion Science ,* vol. 98, p. 101100, 2023.

[17] Z. Xinyi, L. Tie, C. Run, W. Yijie, W. Xinran, W. Ning, L. Shiyan, K. Min and Y. Wenming, "Ammonia marine engine design for enhanced efficiency and reduced greenhouse gas emissions," *Nature Communications,* vol. 15, p. 2110, 2024.

[18] J. V. Pastor, J. Javier López, J. M. García and J. M. Pastor, "A 1D model for the description of mixing-controlled inert diesel sprays," *Fuel,* vol. 87, pp. 2871-2885, 2008.

[19] J. V. Pastor, J. M. Garcia-Oliver, J. M. Pastor and W. Vera-Tudela, "One-dimensional diesel spray modeling of multicomponent fuels," *Atomization and Sprays,* vol. 25, no. 6, pp. 485-517, 2015.

[20] J. Desantes, J. Pastor, J. García-Oliver and J. Pastor, "A 1D model for the description of mixing-controlled reacting diesel sprays," *Combustion and Flame,* vol. 156, no. 1, pp. 234-249, 2009.

[21] J. M. Garcia-Oliver, R. Novella, J. M. Pastor, L. Pachano and B. Naud, "A Quasi-1D Model for the Description of ECN Spray a Combustion Process," in *SAE International Journal of Advances and Current Practices in Mobility, 1974-1985*, 2020.

[22] J. Benajes, R. Payri, M. Bardi and P. Martí-Aldaraví, "Experimental characterization of diesel ignition and lift-off length using a single-hole ECN injector," *Applied Thermal Engineering,* vol. 58, no. 1-2, pp. 554-563, 2013.

[23] J. Pastor, J. García-Oliver, J. López and W. Vera-Tudela, "An experimental study of the effects of fuel properties on reactive spray evolution using Primary Reference Fuels," *Fuel,* vol. 163, pp. 260-270, 2016.

[24] J. V. Pastor, J. M. Garcia-Oliver, C. Mico and A. A. Garcia-Carrero, "An experimental study with renewable fuels using ECN Spray A and D nozzles," *International Journal of Engine Research,* vol. 23, no. 10, pp. 1748-1759, 2022.

[25] H. Park, Y. M. Wright, O. Seddik, A. Srna, P. Kyrtatos and K. Boulouchos, "Phenomenological micro-pilot ignition model for medium-speed dual-fuel engines," *Fuel,* vol. 285, p. 118955, 2021.

[26] J. B. Heywood, Internal Combustion Engine Fundamentals, McGraw-Hill Education, 2018.

[27] P. X. Pham, N. V. Pham, T. V. Pham, V. H. Nguyen and K. T. Nguyen, "Ignition delays of biodiesel-diesel blends: Investigations into the role of physical and chemical process," *Fuel,* p. 121251, 2021.

[28] Y. Zhang, S. Gao, Z. Zhang, W. Li, T. Yuan, D. Tan, L. Duan and G. Yang, "A comprehensive review on combustion, performance and emission aspects of higher alcohols and its additive effect on the diesel engine," *Fuel,* vol. 335, p. 127011, 2023.

[29] M. P. Musculus, P. C. Miles and L. M. Pickett, "Conceptual models for partially premixed low-temperature diesel combustion," *Progress in Energy and Combustion Science,* vol. 39, no. 2-3, pp. 246-283, 2013.

[30] S. Rabl, T. Davies, A. McDougall and R. Cracknell, "Understanding the relationship between ignition delay and burn duration in a constant volume vessel at diesel engine conditions," *Proceedings of the Combustion Institute,* vol. 35, pp. 2967-2974, 2015.

[31] J. E. Dec and C. Espey, "Chemiluminescence Imaging of Autoignition in a DI Diesel Engine," in *SAE Technical Paper 982685*, 1998.

[32] M. Krishnamoorthi, R. Malayalamurthi, Z. He and . S. Kandasamy, "A review on low temperature combustion engines: Performance, combustion and emission characteristics," *Renewable and Sustainable Energy Reviews,* vol. 116, p. 109404, 2019.

[33] M. P. B. Musculus and K. Kattke, "Entrainment waves in diesel jets," in *SAE Technical Papers, 2009-01-1355*, 2009.

[34] K. Luo, C. Shao, M. Chai and J. Fan, "Level set method for atomization and evaporation simulations," *Progress in Energy and Combustion Science,* vol. 73, pp. 65-94, 2019.

[35] H. Hiro and A. Masataka, "Structures of Fuel Sprays in Diesel Engines," in *SAE Technical Paper 900475*, 1990.

[36] G. J. Smallwood and O. L. Gulder, "Views on the structure of transient diesel sprays," *Atomization and Sprays,* vol. 10, no. 3-5, pp. 355-386, 2000.

[37] S. Elghobashi and G. Truesdell, "On the two-way interaction between homogeneous turbulence and dispersed solid particles II: turbulence modification.," *Physics of Fluids,* vol. 6, pp. 1405-1407, 1994.

[38] P. Jenny, D. Roekaerts and N. Beishuizen, "Modeling of turbulent dilute spray combustion," *Progress in Energy and Combustion Science,* vol. 38, pp. 846-887, 2012.

[39] H. v. Helldorff and G. J. Micklow, "Primary and secondary spray breakup modelling for internal combustion engine applications," *Journal of Multidisciplinary Engineering Science and Technology,* vol. 6, no. 4, pp. 9882-9894, 2019.

[40] G. Guo, Z. He, Y. Chen, Q. Wang, X. Leng and S. Sun, "LES investigations on effects of the residual bubble on the single hole diesel injector jet," *International Journal of Heat and Mass Transfer,* vol. 112, pp. 18-27, 2017.

[41] S. Krüger and G. Grünefeld, "Droplet velocity and acceleration measurements in dense sprays by laser flow tagging," *Applied Physics B,* vol. 71, pp. 611-615, 2000.

[42] D. Sedarsky, . E. Berrocal and M. Linne, "Numerical analysis of ballistic imaging for revealing liquid breakup in dense sprays," *Atomization and Sprays,* vol. 20, no. 5, pp. 407-413, 2010.

[43] R. Payri, G. Bracho, P. Marti-Aldaravi and A. Viera, "Near field visualization of diesel spray for different nozzle inclination angles in non-vaporizing conditions," *Atomization and Sprays,* vol. 27, no. 3, pp. 251-267, 2017.

[44] G. L. Martinez, G. M. Magnotti, B. W. Knox, C. L. Genzale, K. E. Matusik, D. J. Duke, C. F. Powell and A. L. Kastengren, "Quantification of Sauter Mean Diameter in Diesel Sprays using Scattering-Absorption Extinction Measurements," in *ILASS-Americas 29th Annual Conference on Liquid Atomization and Spray Systems*, Atlanta, 2017.

[45] G. L. Martinez, F. Poursadegh, G. M. Magnotti, K. E. Matusik, D. J. Duke, B. W. Knox, A. L. Kastengren, C. F. Powell and C. L. Genzale, "Measurement of Sauter mean diameter in diesel sprays using a scattering–absorption measurement ratio technique," *International Journal of Engine Research,* vol. 20, no. 1, pp. 6-17, 2019.

[46] M. Ghiji, L. Goldsworthy, P. Brandner, V. Garaniya and P. Hield, "Numerical and experimental investigation of early stage diesel sprays," *Fuel,* vol. 175, pp. 274-286, 2016.

[47] S. Som and S. Aggarwal, "Effects of primary breakup modeling on spray and combustion characteristics of compression ignition engines," *Combustion and Flame,* vol. 157, pp. 1179-1193, 2010.

[48] W. Zhang, H. Liu, C. Liu, M. Jia and X. Xi, "Numerical investigation into primary breakup of diesel spray with residual bubbles in the nozzle," *Fuel,* vol. 250, pp. 265-276, 2019.

[49] Y. Sun, Z. Guan and K. Hooman, "Cavitation in diesel fuel injector nozzles and its influence on atomization and spray," *Chemical Engineering and Technology,* vol. 42, no. 1, pp. 6-29, 2019.

[50] F. Duronio, A. D. Vita, L. Allocca and M. Anatone, "Gasoline direct injection engines – A review of latest technologies and trends. Part 1: Spray breakup process," *Fuel,* vol. 265, p. 116948, 2020.

[51] C. Arcoumanis and T. Kamimoto, Flow and Combustion in Reciprocating Engines, Springer Berlin Heidelberg, 2009.

[52] B. S. Higgins, C. J. Mueller and D. L. Siebers, "Measurements of Fuel Effects on Liquid-Phase Penetration in DI Sprays," in *SAE Technical Paper, 1999-01-0519*, 1999.

[53] D. L. Siebers, "Liquid-Phase Fuel Penetration in Diesel Sprays," in *SAE Technical Paper, 980809*, 1998.

[54] L. M. Pickett , C. L. Genzale and J. Manin, "Uncertainty quantification for liquid penetration of evaporating sprays at diesel-like conditions," *Atomization and Sprays,* vol. 25, pp. 425-452, 2015.

[55] M. Bardi, R. Payri , L. M. C. Malbec, G. Bruneaux, L. M. Pickett, J. Manin, T. Bazyn and C. L. Genzale, "Engine combustion Network: comparison of spray development, vaporization, and combsution in different combustion vessels," *Atomization and Sprays,* Vols. 807-842, p. 22, 2012.

[56] D. L. Siebers, "Scaling Liquid-Phase Fuel Penetration in Diesel Sprays Based on Mixing-Limited Vaporization," in *SAE Technical Paper 1999-01-0528*, 1999.

[57] R. Payri, J. M. García-Oliver, M. Bardi and J. Manin, "Fuel temperature influence on diesel sprays in inert and reacting conditions," *Applied Thermal Engineering,* vol. 35, pp. 185-195, 2012.

[58] R. Payri, J. Gimeno, M. Bardi and A. H. Plazas, "Study liquid length penetration results obtained with a direct acting piezo electric injector," *Applied Energy,* vol. 106, pp. 152-163, 2013.

[59] J. Pastor, J. García-Oliver, J.-G. Nerva and B. Giménez, "Fuel effect on the liquid-phase penetration of an evaporating spray under transient diesel-like," *Fuel,* vol. 90, pp. 3369-3381, 2011.

[60] S. Kook and L. M. Pickett, "Liquid length and vapor penetration of conventional, Fischer-Tropsch, coal-derived, and surrogate fuel sprays at high-temperature and high-pressure ambient conditions," *Fuel,* vol. 93, pp. 539-548, 2012.

[61] J. D. Naber and S. Dennis L., "Effects of Gas Density and Vaporization on Penetration and Dispersion of Diesel Sprays," in *SAE Technical Paper 960034*, 1996.

[62] F. Sass, Kompressorlose Dieselmaschinen (Druckeinspritzmaschinen): ein Lehrbuch für Studierende, Springer, 1929.

[63] J. Dent, "A basic for the comparison of various experimental methods for studying spray penetration," in *SAE Technical Paper 710571*, 1971.

[64] N. Hay and P. Jones, "Comparison of the various correlations for spray penetration," in *SAE Technical Papers 720776*, 1972.

[65] P. Schweitzer, "Penetration of Oil Sprays," *Journal of Applied Physics,* vol. 9, pp. 735-741, 1938.

[66] A. Lyshevskiy, "The coefficient of free turbulence in a jet of atomized liquid fuel," NASA-TT-F-351, 1965.

[67] Y. Wakuri, M. Fujii, T. Amitani and R. Tsuneya, "Studies on the Penetration of Fuel Spray in a Diesel Engine," *Bulletin of JSME,* vol. 3, no. 9, pp. 123-130, 1960.

[68] G. Sitkei, Kraftstoffaufbereitung und Verbrennung bei Dieselmotoren, Berlin, Heidelberg: Springer, 1964.

[69] M. Parks, C. Polonski and R. Toye, "Penetration of Diesel Fuel Sprays in Gases," in *SAE Technical Paper 660747*, 1966.

[70] I. H. Oz, "Calculation of Spray Penetration in Diesel Engines," in *SAE Technical Paper 690254*, 1969.

[71] D. Taylor and B. Walsham, "Combustion Processes in a Medium-Speed Diesel Engine," in *Proceedings of the Institution of Mechanical Engineers*, 1969.

[72] J. Kostas, D. Honnery and J. Soria, "Time resolved measurements of the initial stages of fuel spray penetration," *Fuel,* vol. 88, pp. 2225-2237, 2009.

[73] J. Kostas, D. Honnery and J. Soria, "A correlation image velocimetry-based study of high-pressure fuel spray tip evolution," *Experiments in Fluids,* vol. 51, no. 3, pp. 667-678, 2011.

[74] Y. Liu, Z. Yuan, Y. Ma, J. Fu, R. Huang and J. Liu, "Analysis of spray combustion characteristics of diesel, biodiesel and their npentanol blends based on a one-dimensional semi-phenomenological model," *Applied Energy,* vol. 238, pp. 996-1009, 2019.

[75] J. M. Desantes, J. Arregle , J. J. Lopez and A. Cronhjort, "Scaling laws for free turbulent gas jets and diesel-like sprays," *Atomization and Sprays,* vol. 16, no. 4, pp. 443-473, 2006.

[76] J. Pastor, J. M. Garcia-Oliver, A. Garcia and V. R. Nareddy, "Characterization of Spray Evaporation and Mixing Using Blends of Commercial Gasoline and Diesel Fuels in Engine-Like Conditions," in *SAE Technical Papers 2017-01-0843*, 2017.

[77] K.-J. Wu, C.-C. Su, R. Steinberger, D. Santavicca and F. Bracco, "Measurements of the Spray Angle of Atomizing Jets," in *Transactions of the ASME*, 1983.

[78] D. Kumar and A. K. Agarwal, "Macroscopic spray characteristics of gasoline, methanol, and ethanol in direct injection spark ignition engine-like conditions," *Atomization and Sprays,* vol. 33, no. 11, pp. 25-43, 2023.

[79] L. M. Pickett, J. Manin, C. L. Genzale, M. P. B. Musculus, D. L. Siebers and C. A. Idicheria, "Relationship Between Diesel Fuel Spray Vapor Penetration/Dispersion and Local Fuel Mixture Fraction," in *SAE International Journal of Engines*, 2011.

[80] M. Blessinger, J. Manin, S. A. Skeen, M. Meijer, S. Parrish and L. M. Pickett, "Quantitative mixing measurements and stochastic variability of a vaporizing gasoline direct-injection spray," *International Journal of Engine Research,* vol. 16, no. 2, pp. 238-252, 2015.

[81] T. C. Klima, A. Peter, S. Riess, M. Wensing and A. S. Braeuer, "Quantification of mixture composition, liquid-phase fraction and - temperature in transcritical sprays," *The Journal of Supercritical Fluids,* vol. 159, p. 104777, 2020.

[82] O. Park, R. A. Burns, O. R. Buxton and N. T. Clemens, "Mixture fraction, soot volume fraction, and velocity imaging in the soot-inception region of a turbulent non-premixed jet flame," *Proceedings of the Combustion Institute,* vol. 36, no. 1, pp. 899-907, 2017.

[83] A. Hsu, V. Narayanaswamy, N. Clemens and J. Frank, "Mixture fraction imaging in turbulent non-premixed flames with two-photon LIF of krypton," *Proceedings of the Combustion Institute,* vol. 33, no. 1, pp. 759-766, 2011.

[84] M. Mansour, H. Imam, K. A. Elsayed, A. Elbaz and W. Abbass, "Quantitative mixture fraction measurements in combustion system via laser induced breakdown spectroscopy," *Optics and Laser Technology,* vol. 65, pp. 43-49, 2015.

[85] Y. Ren, A. Kreischer, F. Cameron and H. Pitsch, "Quantitative measurement of mixture fraction in counterflow diffusion flames by laser-induced breakdown spectroscopy," *Combustion and Flame,* vol. 241, p. 112130, 2022.

[86] R. Bilger, "The structure of turbulent nonpremixed flames," *Symposium (International) on Combustion,* vol. 22, no. 1, pp. 475-488, 1989.

[87] N. Peters, Turbulent Combustion, Cambridge University Press, 2000.

[88] J. Desantes, R. Payri, J. Garcia and F. Salvador, "A contribution to the understanding of isothermal diesel spray dynamics," *Fuel,* vol. 86, no. 7-8, pp. 1093-1101, 2007.

[89] M. Meijer, J. Galle, L. Somers, J. Griensven and S. Verhelst, "High-speed characterization of ECN spray a using various diagnostic techniques," in *SAE International Journal of Engines*, 2013.

[90] B. Higgins, D. Siebers and A. Aradi, "Diesel-Spray Ignition and Premixed-Burn Behavior," in *SAE Technical Paper 2000-01-0940*, 2000.

[91] H. S. Sim, N. Maes, L. Weiss, L. M. Pickett and S. A. Skeen, "Detailed measurements of transient two-stage ignition and combustion processes in high-pressure spray flames using simultaneous high-speed formaldehyde PLIF and schlieren imaging," *Proceedings of the Combustion Institute,* vol. 38, no. 4, pp. 5713-5721, 2021.

[92] H. S. Sim, N. Maes, L. M. Pickett, S. A. Skeen and J. Manin, "High-speed formaldehyde planar laser-induced fluorescence and schlieren to assess influences of injection pressure and oxygen concentration on Spray A flames," *Combustion and Flame,* vol. 253, p. 112806, 2023.

[93] S. A. Skeen, J. Manin and L. M. Pickett, "Simultaneous formaldehyde PLIF and high-speed schlieren imaging for ignition visualization in high-pressure spray flames," *Proceedings of the Combustion Institute,* vol. 35, no. 3, pp. 3167-3174, 2015.

[94] L. M. Pickett, D. L. Siebers and C. A. Idicheria, "Relationship between ignition processes and the lift-off length of diesel fuel jets," in *SAT Technical Paper 2005-01-3843*, 2005.

[95] E. Shim, H. Park and C. Bae, "Comparisons of advanced combustion technologies (HCCI, PCCI, and dualfuel PCCI) on engine performance and emission characteristics in a heavyduty diesel engine," *Fuel,* vol. 262, p. 116436, 2020.

[96] D. L. Siebers and B. Higgins, "Flame Lift-Off on Direct-Injection Diesel Sprays Under Quiescent Conditions," in *SAE Technical Paper 2001-01-0530*, 2001.

[97] F. Payri, J. V. Pastor, J.-G. Nerva and J. M. Garcia-Oliver, "Lift-Off Length and KL Extinction Measurements of Biodiesel and Fischer-Tropsch Fuels under Quasi-Steady Diesel Engine Conditions," in *SAE International Journal of Engines*, 2011.

[98] T. Xuan, Z. Sun, A. I. EL-Seesy, Y. Mi, W. Zhong, Z. He, Q. Wang, J. Sun and R. M. El-Zoheiry, "An optical study on spray and combustion characteristics of ternary hydrogenated catalytic biodiesel/methanol/n-octanol blends; part I: Spray morphology, ignition delay, and flame lift-off length," *Fuel,* vol. 289, p. 119762, 2021.

[99] N. Maes, M. Meijer, N. Dam, B. Somers, H. B. Toda, G. Bruneaux, S. A. Skeen, L. M. Pickett and J. Manin, "Characterization of Spray A flame structure for parametric variations in ECN constant-volume vessels using chemiluminescence and laser-induced fluorescence," *Combustion and Flame,* vol. 174, pp. 138-151, 2016.

[100] O. T. Kaario, S. Karimkashi, A. Bhattacharya, V. Vuorinen, M. Larmi and X.-S. Bai, "A comparative study on methanol and n-dodecane spray flames using Large-Eddy Simulation," *Combustion and Flame,* vol. 260, p. 113277, 2024.

[101] T. Xuan, H. Li, Y. Wang, Y. Chang, M. Jia, Z. He, Q. Wang, J. Cao and R. Payri, "A conceptual model of polyoxymethylene dimethyl ether 3 (PODE3) spray combustion under compression ignition engine-like conditions," *Combustion and Flame,* vol. 261, p. 113296, 2024.

[102] F. G. Chmela and G. C. Orthaber, "Rate of Heat Release Prediction for Direct Injection Diesel Engines Based on Purely Mixing Controlled Combustion," in *SAE Technical Paper 1999-01-0186*, 1999.

[103] D. Jung and D. N. Assanis, "Multi-Zone DI Diesel Spray Combustion Model for Cycle Simulation Studies of Engine Performance and Emissions," in *SAE Technical Paper 2001-01-1246*, 2001.

[104] R. Finesso, E. Spessa, E. Mancaruso, L. Sequino and B. M. Vaglieco, "Assessment of a New Quasi-Dimensional Multizone Combustion Model for the Spray and Soot Formation Analysis in an Optical Single Cylinder Diesel Engine," in *SAE International Journal of Engines*, 2013.

[105] J. M. Desantes, J. M. Garcia-Oliver, J. M. Pastor and A. Pandal, "A comparison of diesel sprays CFD modelling approaches: DDM versus Σ-Y Eulerian atomization model," *Atomization and Sprays,* vol. 26, no. 7, pp. 713-737, 2016.

[106] S. Hoyas, J. M. Pastor, D. Khuong-Anh, J. M. Mompó-Laborda and F. Ravet, "Application and Evaluation of the Eulerian-Lagrangian Spray Atomization (ELSA) Model on CFD Diesel Spray Simulations," in *SAE Technical Paper 2011-37-0029*, 2011.

[107] W. Ning, R. D. Reitz, R. Diwakar and A. M. Lippert, "An Eulerian-Lagrangian spray and atomization model with improved turbulence modelling," *Atomization and Sprays,* vol. 19, no. 8, pp. 727-739, 2009.

[108] J. García-Oliver, X. Margot, M. Chávez and A. Karlsson, "A combined 1D3D-CFD approach for reducing mesh dependency in Diesel spray calculations," *Mathematical and Computer Modelling,* vol. 54, no. 7-8, pp. 1732-1737, 2011.

[109] H. Hiroyasu and T. Kadota, "Development and use of a spray combustion modeling to predict diesel engine efficiency and pollutant emissions (Part 1 Combustion Modeling)," *Bulletin of JSME,* vol. 26, no. 214, pp. 569-575, 1983.

[110] H. Hiroyasu, T. Kadota and M. Arai, "Development and use of a spray combustion modeling to predict diesel engine efficiency and pollutant emissions* (Part 2 Computational Procedure and Parametric Study)," in *Bulletin of the JSME*, 1983.

[111] C. Poetsch, H. Ofner and E. Schutting, "Assessment of a multi zone combustion model for analysis and prediction of CI engine combustion and emissions," in *SAE 2011 World Congress and Exhibition 2011-01-1439*, 2011.

[112] M. P. Musculus, "Entrainment waves in decelerating transient turbulent jets," *Journal of Fluid Mechanics,* vol. 638, pp. 117-140, 2009.

[113] J. Desantes, R. Payri, F. Salvador and A. Gil, "Development and validation of a theoretical model for diesel spray penetration," *Fuel,* vol. 85, no. 7-8, pp. 910-917, 2006.

[114] J. M. García-Oliver, L. M. Malbec, H. B. Toda and G. Bruneaux, "A study on the interaction between local flow and flame structure for mixing-controlled Diesel sprays," *Combustion and Flame,* vol. 179, pp. 157-171, 2017.

[115] J. M. Garcia-Oliver, R. Novella, J. M. Pastor and J. Cao, "Quasi-1D Analysis of n-Dodecane Split Injection Process," in *SAE Technical Paper 2022-01-0506*, 2022.

[116] A. Doudou, "Turbulent flow study of an isothermal diesel spray injected by a common rail system," *Fuel,* vol. 84, pp. 287-298, 2005.

[117] A. Joshi and W. Schreiber , "An experimental examination of an impulsively started incompressible turbulent jet," *Experiments in Fluids ,* vol. 40, pp. 156-160, 2006.

[118] G. Abramovich, "Chapter 5: Jet of an Incompressible Fluid in a Coflowing External Stream" The Theory of Turbulent Jets, Cambridge, MA: The MIT Press, 1963.

[119] C. Barro, M. Parravicini and K. Boulouchos, "Neat polyoxymethylene dimethyl ether in a diesel engine; part 1: Detailed combustion analysis," *Fuel,* vol. 256, p. 115892, 2019.

[120] M. Xu, Y. Cui and K. Deng, "One-dimensional model on liquid-phase fuel penetration in diesel sprays," *Journal of the Energy Institute,* vol. 89, pp. 138-149, 2016.

[121] J. M. Desantes, J. J. Lopez, J. M. Garcia and J. M. Pastor, "Evaporative diesel spray modeling," *Atomization and Sprays,* vol. 17, no. 3, pp. 193-231, 2007.

[122] L. M. Pickett, J. Manin, R. Payri , M. Bardi and J. Gimeno, "Transient rate of injection effects on spray development," in *SAE Technical Paper 2013-24-0001*, 2013.

[123] J. V. Pastor, R. Payri, J. M. Garcia-Oliver and J.-G. Nerva, "Schlieren measurements of the ECN-spray a penetration under inert and reacting conditions," in *SAE Technical Papers 2012-01-0456*, 2012.

[124] J. Manin, M. Bardi, L. M. Pickett and R. Payri, "Boundary condition and fuel composition effects on injection processes of high-pressure sprays at the microscopic level," *International Journal of Multiphase Flow,* vol. 83, pp. 267-278, 2016.

[125] CMT - Clean Mobility & Thermofluids, "VIRTUAL INJECTION RATE GENERATOR," [Online]. Available: https://www.cmt.upv.es/#/ecn/download/InjectionRateGenerator/InjectionRateGenerator. [Accessed 21 09 2024].

[126] C. P. Koci, R. P. Fitzgerald, V. Ikonomou and K. Sun, "The effects of fuel–air mixing and injector dribble on diesel unburned hydrocarbon emissions," *International Journal of Engine Research,* vol. 20, no. 1, pp. 105-127, 2019.

[127] A. S. Cheng and C. J. Mueller, "Conceptual Investigation of the Origins of Hydrocarbon Emissions from Mixing-Controlled, Compression-Ignition Combustion," in *SAE International Journal of Engines, 2017-01-0724*, 2017.

[128] C. Beatrice, G. D. Blasio, E. Mancaruso, L. Sequino and B. M. Vaglieco, "Characterization of Combustion and Emissions in Light-Duty Diesel Engines Using High-Glycerol-Ethers/Diesel Blends," in *SAE Technical Paper 2015-24-2445*, 2015.

[129] A. Zhang, A. Montanaro, L. Allocca, J. Naber and S.-Y. Lee, "Measurement of Diesel Spray Formation and Combustion upon Different Nozzle Geometry using Hybrid Imaging Technique," in *SAE International Journal of Engines*, 2014.

[130] F. R. Westlye, M. Battistoni, S. A. Skeen, J. Manin, L. M. Pickett and A. Ivarsson, "Penetration and combustion characterization of cavitating and non-cavitating fuel injectors under diesel engine conditions," in *SAE Technical Paper 2016-01-0860*, 2016.

[131] J. V. Pastor, J. M. Garcia-Oliver, A. Garcia and A. M. López, "An Experimental Investigation on Spray Mixing and Combustion Characteristics for Spray C/D Nozzles in a Constant Pressure Vessel," in *SAE Technical Paper 2018-01-1783*, 2018.

[132] R. P. Fitzgerald, C. Gehrke, K. Svensson and G. Martin, "A New Validation of Spray Penetration Models for Modern Heavy Duty Diesel Fuel Injectors," in *SAE Technical Paper 2017-01-0826*, 2017.

[133] J. V. Pastor, R. Payri, J. M. Garcia-Oliver and F. J. Briceno, "Analysis of transient liquid and vapor phase penetration for diesel sprays under variable injection conditions," *Atomization and Sprays,* vol. 21, no. 6, pp. 503-520, 2011.

[134] J. M. Desantes, J. M. Garcia-Oliver, A. Garcia and T. Xuan, "Optical study on characteristics of non-reacting and reacting diesel spray with different strategies of split injection," *International Journal of Engine Research,* vol. 20, no. 6, pp. 606-623, 2019.

[135] L. Liu, N. Horibe and T. Ishiyama, "Combustion modelling for a diesel engine with multi-stage injection using a stochastic combustion model," *Proceedings of the Institution of Mechanical Engineers, Part D: Journal of Automobile Engineering,* vol. 228, no. 5, pp. 518-534, 2014.

[136] L. Long, M. Xiuzhen and F. Magagnato, "Extended modeling of decelerating turbulent jets for diesel spray's penetration after end-of-injection," *Fuel,* vol. 199, pp. 324-331, 2017.

[137] R. Sangras, O. Kwon and G. Faeth, "Self-Preserving Properties of Unsteady Round Nonbuoyant Turbulent Starting Jets and Puffs in Still Fluids," *Journal of Heat and Mass Transfer,* vol. 124, no. 3, pp. 460-469, 2002.

[138] Z. Bao, N. Horibe and T. Ishiyama, "A Study on Diesel Spray Characteristics for Small-Quantity Injection," in *SAE Technical Paper 2018-01-0283*, 2018.

[139] L. Liu, Y. Peng, X. Ma, N. Horibe and T. Ishiyama, "Phenomenological modeling of diesel spray with varying injection profile," *Proceedings of the Institution of Mechanical Engineers, Part D: Journal of Automobile Engineering,* vol. 233, no. 11, pp. 2780-2790, 2019.

[140] X. Zhou, T. Li, Z. Lai and Y. Wei, "Modeling diesel spray tip and tail penetrations after end-of-injection," *Fuel,* vol. 237, pp. 442-456, 2019.

[141] J. Xue, T. E. Grift and . A. C. Hansen, "Effect of biodiesel on engine performances and emissions," *Renewable and Sustainable Energy Reviews,* vol. 15, pp. 1098-1116, 2011.

[142] J. E, M. Pham, D. Zhao, Y. Deng, D. Le, W. Zuo, H. Zhu, T. Liu, Q. Peng and Z. Zhang, "Effect of different technologies on combustion and emissions of the diesel engine fueled with biodiesel: A review," *Renewable and Sustainable Energy Reviews,* vol. 80, pp. 620-647, 2017.

[143] Y. Zhang, Y. Zhong, S. Lu, Z. Zhang and D. Tan, "A Comprehensive Review of the Properties, Performance, Combustion, and Emissions of the Diesel Engine Fueled with Different Generations of Biodiesel," *Processes,* vol. 10, no. 6, p. 1178, 2022.

[144] Q. Cheng, H. Tuomo, O. T. Kaario and L. Martti, "Spray dynamics of HVO and EN590 diesel fuels," *Fuel,* vol. 245, pp. 198-211, 2019.

[145] A. García, J. Monsalve-Serrano, B. Heuser, M. Jakob, F. Kremer and S. Pischinger, "Influence of fuel properties on fundamental spray characteristics and soot emissions using different tailor-made fuels from biomass," *Energy Conversion and Management,* vol. 108, pp. 243-254, 2016.

[146] G. Lequien, S. Skeen, J. Manin, L. M. Pickett and O. Andersson, "Ignition Quality Effects on Lift-Off Stabilization of Synthetic Fuels," in *SAE International Journal of Engines, 2015-01-0792*, 2015.

[147] J.-G. Nerva, C. L. Genzale, S. Kook, J. M. Garcia-Oliver and L. M. Pickett, "Fundamental spray and combustion measurements of soy methyl-ester biodiesel," *International Journal of Engine Research,* vol. 14, no. 4, pp. 373-390, 2013.

[148] J. Manin, S. Skeen, L. M. Pickett, E. Kurtz and J. E. Anderson, "Effects of Oxygenated Fuels on Combustion and Soot Formation/Oxidation Processes," in *SAE International Journal of Fuels and Lubricants*, 2014.

[149] M. Yinjie, H. Sheng, H. Ronghua, Z. Yu and X. Shijie, "Spray and evaporation characteristics of n-pentanol–diesel blends in a constant volume chamber," *Energy Conversion and Management,* vol. 130, pp. 240-251, 2016.

[150] V. Scharl, T. Lackovic and T. Sattelmayer, "Characterization of ammonia spray combustion and mixture formation under high-pressure, direct injection conditions," *Fuel,* vol. 333, p. 126454, 2023.

[151] R. Payri, J. M. García-Oliver, G. Bracho and J. Cao, "Experimental characterization of direct injection liquid ammonia sprays under non-reacting diesel-like conditions," *Fuel,* vol. 362, p. 130851, 2024.

[152] R. Payri, J. M. García-Oliver, T. Xuan and M. Bardi, "A study on diesel spray tip penetration and radial expansion under reacting conditions," *Applied Thermal Engineering,* vol. 90, pp. 619-629, 2015.

[153] J. Benajes, R. Novella, A. Garcia, V. Domenech and R. Durrett, "An investigation on mixing and auto-ignition using diesel and gasoline in a direct-injection compression-ignition engine operating in PCCI combustion conditions," in *SAE International Journal of Engines*, 2011.

[154] J. Benajes, S. Molina, A. García, E. Belarte and M. Vanvolsem, "An investigation on RCCI combustion in a heavy duty diesel engine using in-cylinder blending of diesel and gasoline fuels," *Applied Thermal Engineering,* vol. 63, pp. 66-76, 2014.

[155] J. J. Lopez, J. M. García-Oliver, A. García and V. Domenech, "Gasoline effects on spray characteristics, mixing and auto-ignition processes in a CI engine under Partially Premixed Combustion conditions," *Applied Thermal Engineering,* vol. 70, pp. 996-1006, 2014.

[156] P. G. Valladolid, P. Tunestål, J. Monsalve-Serrano, A. García and J. Hyvönen, "Impact of diesel pilot distribution on the ignition process of a dual fuel medium speed marine engine," *Energy Conversion and Management,* vol. 149, pp. 192-205, 2017.

[157] J. Monsalve-Serrano, G. Belgiorno, G. D. Blasio and M. Guzmán-Mendoza, "1D simulation and experimental analysis on the effects of the injection parameters in methane–diesel dual-fuel combustion," *Energies,* vol. 13, no. 14, p. 3734, 2020.

[158] L.-M. Malbec, W. E. Eagle, M. P. B. Musculus and P. Schihl, "Influence of Injection Duration and Ambient Temperature on the Ignition Delay in a 2.34L Optical Diesel Engine," in *SAE International Journal of Engines*, 2015.

[159] E. Mancaruso, R. Marialto, L. Sequino and B. M. Vaglieco, "Comparison of spray characteristics measured in an optical single cylinder diesel engine with 1D model," in *SAE Technical Paper 2014-01-1424*, 2014.

[160] E. Mancaruso, L. Sequino and B. Vaglieco, "Analysis of the pilot injection running Common Rail strategies in a research diesel engine by means of infrared diagnostics and 1d model," *Fuel ,* vol. 178, pp. 188-201, 2016.

[161] D. Ruth and J. O'Connor, "Development and Verification of Reduced-Order Model for Diesel Spray Penetration and Spreading during Wall Impingement," in *SAE Technical Paper 2017-01-0814*, 2017.

[162] A. A. Osorio, A contribution to 1D Modeling of Diesel Sprays and Combustion, Mechanical engineering [physics.class-ph]. École centrale de Nantes, 2019.

[163] J. E. Peraza, F. J. Salvador, J. Gimeno and S. Ruiz, "ECN Spray D visualization of the spray interaction with a transparent wall under engine-like conditions. Part I: Non-reactive impinging spray," *Fuel,* vol. 307, p. 121699, 2022.

[164] G. S. Wood, K. C. Kwok, N. A. Motteram and D. Fletcher, "Physical and numerical modelling of thunderstorm downbursts," *Journal of Wind Engineering and Industrial Aerodynamics,* vol. 89, no. 6, pp. 535-552, 2001.

[165] J. Vlachopoulos, "Velocity and temperature profiles in compressible turbulent wall jets," *The Canadian Journal of Chemical Engineering,* vol. 49, no. 1, pp. 44-50, 1971.

[166] A. A. Osorio, X. Tauzia and A. Maiboom, "Development of a wall jet model dedicated to 1D combustion modelling for CI engines," *International Journal of Spray and Combustion Dynamics,* vol. 13, no. 3-4, pp. 146-163, 2021.

[167] J. Desantes, J. García-Oliver, T. Xuan and W. Vera-Tudela, "A study on tip penetration velocity and radial expansion of reacting diesel sprays with different fuels," *Fuel,* vol. 207, pp. 323-335, 2017.

[168] L. Pickett, J. Caton, M. Musculus and A. Lutz, "Evaluation of the equivalence ratio-temperature region of diesel soot precursor formation using a two-stage Lagrangian model," *International Journal of Engine Research,* vol. 7, no. 5, pp. 349-370, 2006.

[169] J. E. Broadwell and A. E. Lutz, "A Turbulent Jet Chemical Reaction Model: NOx Production in Jet Flames," *Combustion and Flame,* vol. 114, no. 3-4, pp. 319-335, 1998.

[170] B. W. Knox and C. L. Genzale, "Reduced-order numerical model for transient reacting diesel sprays with detailed kinetics," *International Journal of Engine Research,* vol. 17, no. 3, pp. 261-279, 2016.

[171] A. Catania, R. Finesso and E. Spessa, "Diagnostics of mixing process dynamics, combustion and emissions in a euro v diesel engine," in *SAE Technical Paper 2011-24-0018*, 2011.

[172] R. Finesso and E. Spessa, "Analysis of combustion and emissions in a EURO V diesel engine by means of a refined quasi-dimensional multizone diagnostic model," in *SAE International Journal of Engines*, 2012.

[173] T. K. Lee, H. Min and H. H. Song, "Study on Auto-Ignition Characteristics of High Pressure Methane Jet for Compression Ignition Engine Application," in *SAE Technical Paper 2018-01-0274*, 2018.

[174] G. Ma, X. Tauzia and A. Maiboom, "One-dimensional combustion model with detailed chemistry for transient diesel sprays," *Proceedings of the Institution of Mechanical Engineers, Part D: Journal of Automobile Engineering,* vol. 228, no. 4, pp. 457-476, 2014.

[175] X. Tauzia, A. Maiboom and G. Ma, "A 1D Model for Diesel Sprays under Reacting Conditions," in *SAE Technical Paper 2015-24-2395*, 2015.

[176] A. Aljure, X. Tauzia and A. Maiboom, "Comparison of Eulerian and Lagrangian 1D Models of Diesel Fuel Injection and Combustion," in *SAE Technical Paper 2017-24-0006*, 2017.

[177] A. Aljure, X. Tauzia and A. Maiboom, "Heat Release Rate Modeling Improvement in an Eulerian 1D Diesel Combustion Model," in *SAE Technical Paper 2018-01-1127*, 2018.

[178] A. Y. Deshmukh, M. Davidovic, T. Grenga, R. Lakshmanan, L. Cai and H. Pitsch, "A Reduced-order Model for Turbulent Reactive Sprays in Compression Ignition Engines," *Combustion and Flame,* vol. 236, p. 111751, 2022.

[179] A. Deshmukh, T. Grenga, M. Davidovic, L. Schumacher, J. Palmer, M. Reddemann, R. Kneer and H. Pitsch, "A reduced-order model for multiphase simulation of transient inert sprays in the context of compression ignition engines," *International Journal of Multiphase Flow,* vol. 147, p. 103872, 2022.

[180] A. Saha, A. Deshmukh, T. Grenga and H. Pitsch, "Physics-based reduced-order modeling of flash-boiling sprays in the context of internal combustion engines," *International Journal of Multiphase Flow,* vol. 171, p. 104673, 2024.

[181] J. M. Desantes, R. Payri, J. M. Garcia-Oliver and F. Salvador, "A contribution to the understanding of isothermal diesel spray dynamics," *Fuel,* vol. 86, no. 7-8, pp. 1093-1101, 2007.

[182] W. M. Vera-Tudela Fajardo, An experimental study of the effects of fuel properties on diesel spray processes using blends of single-component fuels, Ph.D thesis, Universitat Politècnica de València, Departamento de Maquinas y Motores Termicos, 2015.

[183] D. P. Schmidt, M. Arienti, J. M. Garcia-Oliver and J. M. Pastor, "Assessment of the mixing-limited hypothesis with first-principles simulation results," *Physics of Fluids,* vol. 34, no. 12, p. 123328, 2022.

[184] C. K. Westbrook, W. J. Pitz, O. Herbinet, H. J. Curran and E. J. Silke, "A comprehensive detailed chemical kinetic reaction mechanism for combustion of n-alkane hydrocarbons from n-octane to n-hexadecane," *Combustion and Flame,* vol. 156, no. 1, pp. 181-199, 2009.

[185] R. Payri, J. M. Garcia-Oliver, F. Salvador and J. Gimeno, "Using spray momentum flux measurements to understand the influence of diesel nozzle geometry on spray characteristics," *Fuel,* vol. 84, pp. 551-561, 2005.

[186] T. Xavier, M. Alain and M. Quanqin, "A 1D Model for Diesel Sprays under Reacting Conditions," in *SAE Technical Paper 2015-24-2395*, 2015.

[187] H. Pitsch and M. Ihme, "An Unsteady/Flamelet Progress Variable Method for LES of Nonpremixed Turbulent Combustion," in *43rd AIAA Aerospace Sciences Meeting and Exhibit – Meeting Papers*, 2005.

[188] J. F. Winklinger, Implementation of a Combustion Model based on the Flamelet Concept and its Application to turbulent reactive Sprays, PhD thesis, Departamento de Maquinas y Motores Termicos, Universitat Politecnica de Valencia , 2014.

[189] F. Williams, "Recent Advances in Theoretical Descriptions of Turbulent Diffusion Flames," in *Turbulent Mixing in Nonreactive and Reactive Flows*, S. N. B. Murthy. Boston, MA: Springer New York, 1975, pp. 189-208.

[190] J. M. Desantes, J. M. Garcia-Oliver, R. Novella and E. J. Perez-Sanchez, "Application of an unsteady flamelet model in a RANS framework for Spray A simulation," *Applied Thermal Engineering,* vol. 117, pp. 50-64, 2017.

[191] J. Benajes, J. M. Garcia-Oliver, J. M. Pastor and D. D. Leon-Ceriani, "Unsteady Flamelet modeling study on OMEx-type fuels under Engine Combustion Network Spray A conditions," *Fuel,* vol. 331, p. 125458, 2023.

[192] B. Naud, R. Novella, J. M. Pastor and J. F. Winklinger, "RANS modelling of a lifted H2/N2 flame using an unsteady flamelet progress variable approach with presumed PDF," *Combustion anf Flame,* vol. 162, no. 4, pp. 893-906, 2015.

[193] N. Peters, "Laminar diffusion flamelet models in non-premixed turbulent combustion," *Progress in Energy and Combustion Science,* vol. 10, no. 3, pp. 319-339, 1984.

[194] J. M. Desantes, J. M. Garcia-Oliver, R. Novella and L. Pachano, "A numerical study of the effect of nozzle diameter on diesel combustion ignition and flame stabilization," *International Journal of Engine Research,* vol. 21, no. 1, pp. 101-121, 2020.

[195] F. Payri, J. M. Garcia-Oliver, R. Novella and E. Perez-Sanchez, "Influence of the n-dodecane chemical mechanism on the CFD modelling of the diesel-like ECN Spray A flame structure at different ambient conditions," *Combustion and Flame,* vol. 208, pp. 198-218, 2019.

[196] V. Aparece-Scutariu, Investigation on spatial and temporal characteristics of scalar dissipation rate in non-reacting and reacting turbulent jets, Ph.D Dissertation, The University of Edinburgh, 2021.

[197] V. Aparece-Scutariu and D.-h. Shin, "Spatial characteristics and modelling of mixture fraction variance and scalar dissipation rate in steady turbulent round jets," *International Journal of Heat and Fluid Flow,* vol. 98, p. 109048, 2022.

[198] N. Panchapakesan and J. Lumley, "Turbulence measurements in axisymmetric jets of air and helium. Part 1. Air jet," *Journal of Fluid Mechanics,* vol. 246, pp. 197-223, 1993.

[199] T. Poinsot and D. Veynante, Theoretical and Numerical Combustion, R.T. Edwards Inc., pp.522, 2005.

[200] D. A. Feikema, D. Everest and J. F. Driscoll, "Images of dissipation layers to quantify mixing within a turbulent jet," *American Institute of Aeronautics snd Astronautics,* vol. 34, no. 12, pp. 2531-, 1996.

[201] P. A. Libby and K. Bray, "Implications of the laminar flamelet model in premixed turbulent combustion," *Combustion and Flame,* vol. 39, no. 1, pp. 33-41, 1980.

[202] N. Peters and F. A. Williams, "Liftoff characteristics of turbulent jet diffusion flames," in *20th Aerospace Science Meeting*, Orlando, 1982.

[203] E. J. P. Sanchez, Application of a Flamelet-based Combustion Model to Diesel-like Reacting Sprays, Doctoral Thesis, Universitat Politecnica de Valencia, 2018.

[204] J. C. Ong, K. M. Pang, X.-S. Bai, M. Jangi and J. H. Walther, "Large eddy simulation of n-dodecane spray flame: Effects of nozzle diameter on autoignition at varying ambient temperature," *Proceedings of the Combustion Institute,* no. 38, pp. 3427-3434, 2021.

[205] J. C. Ong, Y. Zhang, S. Xu, J. H. Walther, X.-S. Bai and K. M. Pang, "Large eddy simulation of n-dodecane spray flame: Effects of injection pressure on spray combustion characteristics at low ambient temperature," *Proceedings of the Combustion Institute,* no. 39, pp. 2631-2642, 2023.

[206] D. Li, Z. He, T. Xuan, W. Zhong, J. Cao, Q. Wang and P. Wang, "Simultaneous capture of liquid length of spray and flame lift-off length for second-generation biodiesel/diesel blended fuel in a constant volume combustion chamber," *Fuel,* vol. 189, pp. 260-269, 2017.

[207] K. Narayanaswamy, P. Pepiot and H. Pitsch, "A chemical mechanism for low to high temperature oxidation of n-dodecane as a component of transportation fuel surrogates," *Combustion and Flame,* vol. 161, no. 4, pp. 866-884, 2014.

[208] T. Yao, Y. Pei, B.-j. Zhong, S. Som and T. Lu, "A hybrid mechanism for n-dodecane combustion with optimized low-temperature chemistry," in *9th US National Combustion Meeting, Cincinnati, OH, The Combustion Institute*, 2015.

[209] H. Wang, Y. Ra, M. Jia and R. D. Reitz, "Development of a reduced n-dodecane–PAH mechanism and its application for n-dodecane soot predictions," *Fuel,* vol. 136, pp. 25-36, 2014.

[210] L. Cai, H. Pitsch, S. Y. Mohamed, V. Raman, J. Bugler, H. Curran and S. Mani Sarathy, "Optimized reaction mechanism rate rules for ignition of normal alkanes," *Combustion and Flame,* vol. 173, pp. 468-482, 2016.

[211] L. Pachano, CFD modelling of combsution and soot production in diesel sprays, Uniersitat Politecnica de Valencia, Departamento de Maquinas y Motores Termicos, Doctoral Thesis, 2020.

[212] P. Rahnama, A. Maghbouli, H. Bao, A. Vasavan, R. Novella and B. Somers, "Generalizing progress variable definition in CFD simulation of combustion systems using tabulated chemistry models," *Applications in Energy and Combustion Science,* vol. 14, p. 100132, 2023.

[213] ECN, "Diesel Data Search," [Online]. Available: https://ecn.sandia.gov/ecn-data-search/. [Accessed 07 03 2024].

[214] "Engine Combustion Network," 2024. [Online]. Available: https://ecn.sandia.gov/.

[215] Y. Pei, E. R. Hawkes, M. Bolla, S. Kook, G. M. Goldin, Y. Yang, S. B. Pope and S. Som, "An analysis of the structure of an n-dodecane spray flame using TPDF modelling," *Combustion and Flame,* vol. 168, pp. 420-435, 2016.

[216] A. Wehrfritz, O. Kaario, V. Vuorinen and B. Somers, "Large Eddy Simulation of n-dodecane spray flames using Flamelet Generated Manifolds," *Combustion and Flame,* vol. 167, pp. 113-131, 2016.

[217] A. Maghbouli, B. Akkurt, T. Lucchini, G. D'Errico, N. G. Deen and B. Somers, "Modelling compression ignition engines by incorporation of the flamelet generated manifolds combustion closure," *Combustion Theory and Modelling,* vol. 23, no. 3, pp. 414-438, 2019.

[218] H. Bao, H. Y. Akargun, D. Roekaerts and B. Somers, "The inclusion of scalar dissipation rate in modeling of an n-dodecane spray flame using flamelet generated manifold," *Combustion and Flame,* vol. 249, p. 112610, 2023.

[219] N. Maes, S. A. Skeen, M. Bardi, R. P. Fitzgerald, L.-M. Malbec, G. Bruneaux, L. M. Pickett, K. Yasutomi and G. Martin, "Spray penetration, combustion, and soot formation characteristics of the ECN Spray C and Spray D injectors in multiple combustion facilities," *Applied Thermal Engineering,* vol. 172, p. 115136, 2020.

[220] Z. Shi, F. Liu, W. Shang, Y. Li, C. Sun and M. Zhu, "Numerical study on the influence of injection pressure on the ignition and combustion of n-dodecane spray at cold-start conditions," *Fuel,* vol. 264, p. 116882, 2020.

[221] U. Eguz, S. Ayyapureddi, C. Bekdemir, B. Somers and P. d. Geoy, "Manifold resolution study of the FGM method for an igniting diesel spray," *Fuel,* vol. 113, pp. 228-238, 2013.

[222] P. Kundu, M. M. Ameen and S. Som, "Importance of turbulence-chemistry interactions at low temperature engine conditions," *Combustion and Flame,* vol. 183, pp. 283-298, 2017.

[223] G. Kalghatgi and B. Johansson, "Gasoline compression ignition approach to efficient, clean and affordable future engines," *Proceedings of the Institution of Mechanical Engineers, Part D: Journal of Automobile Engineering,* vol. 232, no. 1, pp. 118-138, 2017.

[224] L. Hildingsson, G. Kalghatgi, N. Tait, B. Johansson and A. Harrison, "Fuel octane effects in the partially premixed combustion regime in compression ignition engines," in *SAE Technical Paper 2019-01-2648*, 2009.

[225] V. Manente, B. Johansson and W. Cannella, "Gasoline partially premixed combustion, the future of internal combustion engines?," *International Journal of Engine Research,* vol. 12, no. 3, pp. 194-208, 2011.

[226] C. Jiang, G. Huang, . G. Liu, Y. Qian and X. Lu, "Optimizing gasoline compression ignition engine performance and emissions: Combined effects of exhaust gas recirculation and fuel octane number," *Applied Thermal Engineering,* vol. 153, pp. 669-677, 2019.

[227] S. Vijai Shankar Bhavani, S. Muhammad, A.-Q. Khalid, A. Nour, A. Issam, A. Ahfaz, C. Sukho, R. William, M. Kai and S. Mani, "Primary reference fuels (PRFs) as surrogates for low sensitivity gasoline fuels," in *SAE Technical Paper 2016-01-0748*, 2016.

[228] J. Badra, Y. Viollet, A. Elwardany, H. G. Im and J. Chang, "Physical and chemical effects of low octane gasoline fuels on compression ignition combustion," *Applied Energy,* vol. 183, pp. 1197-1208, 2016.

[229] W.-Q. Han and C.-D. Yao, "Research on high cetane and high octane number fuels and the mechanism for their common oxidation and auto-ignition," *Fuel,* vol. 150, pp. 29-40, 2015.

[230] Q. Zhou, T. Lucchini, G. D'Errico, R. Novella, J. M. García-Oliver and X. Lu, "CFD analysis of combustion and emission characteristics of primary reference fuels: from transient Diesel spray to heavy-duty engine," *Fuel,* vol. 301, p. 120994, 2021.

[231] G. Zhai, S. Xing, A. Yuen, G. Yeoh and Q. Chan, "Spray and combustion characteristics of gasoline-like fuel under compression-ignition conditions," *Energy & Fuels,* vol. 34, no. 12, pp. 16585-16598, 2020.

[232] G. Zhai, S. Xing, A. Srna, A. Wehrfritz, S. Kook, E. R. Hawkes and Q. N. Chan, "Ignition and flame stabilisation of primary reference fuel sprays at engine-relevant conditions," *Combustion and Flame,* vol. 233, p. 111620, 2021.

[233] "NIST Chemistry WebBook, SDR69," National Institute of Standards and Technologies, [Online]. Available: https://webbook.nist.gov/cgi/cbook.cgi?ID=142-82-5. [Accessed 01 05 2024].

[234] R. Payri, J. M. Garcia-Oliver, R. Novella, J. M. Pastor, D. Lopez-Pintor and W. Shang, "Application of an Optimized Mechanism of Primary Reference Fuel to Single Hole Sprays," in *32nd European Conference on Liquid Atomization & Spray Systems*, Napoli, 2023.

[235] M. Mehl, W. J. Pitz, C. K. Westbrook, K. Yasunaga, C. Conroy and H. J. Curran, "Autoignition behavior of unsaturated hydrocarbons in the low and high temperature regions," *Proceedings of the Combustion Institute,* vol. 33, no. 1, pp. 201-208, 2011.

[236] K. E. Niemeyer, C.-J. Sung and M. P. Raju, "Skeletal mechanism generation for surrogate fuels using directed relation graph with error propagation and sensitivity analysis," *Combustion and Flame,* vol. 157, no. 9, pp. 1760-1770, 2010.

[237] Q. Zhou, T. Lucchini, G. D'Errico, R. Novella, J. M. Garcia-Oliver and X. Lu, "CFD Modeling of Reacting Diesel Sprays with Primary Reference Fuel," in *WCX World Congress Experience*, 2021.

[238] N. Jean-Guillaume, An assessment of fuel physical and chemical properties in the combustion of a Diesel, Doctoral Thesis, Universitat Politecnica de Valencia, 2013.

[239] H. Liu, Z. Wang, Y. Li, Y. Zheng, T. He and J. Wang, "Recent progress in the application in compression ignition engines and the synthesis technologies of polyoxymethylene dimethyl ethers," *Applied Energy,* Vols. 233-234, pp. 599-611, 2019.

[240] M. Härtl, P. Seidenspinner, E. Jacob and G. Wachtmeister, "Oxygenate screening on a heavy-duty diesel engine and emission characteristics of highly oxygenated oxymethylene ether fuel OME1," *Fuel,* vol. 153, p. 328–335, 2015.

[241] D. Goeb, M. Davidovic, L. Cai, P. Pancharia, M. Bode, S. Jacobs, J. Beeckmann, W. Willems, K. A. Heufer and H. Pitsch, "Oxymethylene ether – n-dodecane blend spray combustion: Experimental study and large-eddy simulations," *Proceedings of the Combustion Institute,* vol. 38, pp. 3417-3425, 2021.

[242] J. M. Ngugi, S. Richter, M. Braun-Unkhoff, C. Naumann and U. Riedel, "A study on fundamental combustion properties of oxymethylene ether-1, the primary reference fuel 90, and their blend: Experiments and modeling," *Combustion and Flame,* vol. 243, p. 111996, 2022.

[243] J. V. Pastor, J. M. Garcia-Oliver, C. Mico, A. A. Garcia-Carrero and A. Gomez, "Experimental study of the effect of hydrotreated vegetable oil and oxymethylene ethers on main spray and

combustion characteristics under engine combustion network spray A conditions," *Applied Sciences,* vol. 10, no. 16, p. 5460, 2020.

[244] J. V. Pastor, A. Garcia, C. Mico and F. Lewiski, "Simultaneous high-speed spectroscopy and 2-color pyrometry analysis in an optical compression ignition engine fueled with OMEX-diesel blends," *Combustion and Flame,* vol. 230, p. 111437, 2021.

[245] "Spray A Nozzle Geometry," Engine Combustion Network, [Online]. Available: https://ecn.sandia.gov/diesel-spray-combustion/target-condition/spray-a-nozzle-geometry/. [Accessed 22 05 2024].

[246] F. Wiesmann, L. Strauß, S. Rieß, J. Manin, K. Wan and T. Lauer, "Numerical and Experimental Investigations on the Ignition Behavior of OME," *energies,* vol. 15, p. 6855, 2022.

[247] J. V. Pastor, J. M. Garcia-Oliver, C. Micó and F. J. Tejada, "Comparison of the Diffusive Flame Structure for Dodecane and OMEXFuels for Conditions of Spray A of the ECN," *SAE Int. J. Advances & Curr. Prac. in Mobility,* vol. 3, no. 1, pp. 402-411, 2020.

[248] J. V. Pastor, J. M. Garcia-Oliver, C. Mico and F. J. Tejada, "Characterization of the oxymethylene ether fuels flame structure for ECN Spray A and Spray D nozzles," *Applied Energy,* vol. 332, p. 120475, 2023.

[249] "Enerxico database," Clean Mobility Thermofluids, [Online]. Available: https://www.cmt.upv.es/#/ecn/download/Enerxicodata/Enerxicodata.

[250] L. Cai, S. Jacobs, R. Langer, F. v. Lehn, K. A. Heufer and H. Pitsch, "Auto-ignition of oxymethylene ethers (OMEn, n = 2–4) as promising synthetic e-fuels from renewable electricity: shock tube experiments and automatic mechanism generation," *Fuel,* vol. 264, p. 116711, 2020.

[251] CMT - Clean Mobility & Thermofluids, "Spray C/D Rate of injection," 2024. [Online]. Available: https://www.cmt.upv.es/#/ecn/download/nozzlecharac/ncSprayCDRateOfInj.

[252] R. Payri, A. Garcia, V. Domenech, R. Durrett and A. Plazas, "An experimental study of gasoline effects on injection rate, momentum flux and spray characteristics using a common rail diesel injection system," *Fuel,* vol. 97, pp. 390-399, 2012.

[253] L. Strauß, S. Rieß and M. Wensing, "Mixture formation of OME3−5 and 1-Octanol in comparison with diesel-like Dodecane under ECN Spray A conditions," *Frontiers in Mechanical Engineering,* vol. 9, 2023.

[254] S. Jacobs, M. Döntgen, A. B. Alquaity, W. A. Kopp, L. C. Kröger, U. Burke, H. Pitsch, K. Leonhard, H. J. Curran and K. A. Heufer, "Detailed kinetic modeling of dimethoxymethane. Part II: Experimental and theoretical study of the kinetics and reaction mechanism," *Combustion and Flame,* vol. 205, pp. 522-533, 2019.